Surface Analysis of the Negative Electrode in Lithium-Sulfur Secondary Batteries

Dissertation

im Fachbereich 08 – am Physikalisch–Chemischen Institut –
der Justus–Liebig–Universität Giessen

vorgelegt von: Hauke Metelmann

Erstgutachter: Prof. Dr. Jürgen Janek

Zweitgutachter: Prof. Dr. Bernd Smarsly

September 2017

Contents

List of Abbreviation

ASF	Atomic Sensitivity Factor
CSF	Cathode Surface Film
DME	1,2-dimethoxyethane
DOL	1,3-dioxolane
FTIR	Fourier-Transform Infrared Spectroscopy
FWHM	Full Width at Half Maximum
LIB	Lithium-Ion Battery
LiTFSI	Lithium bis(trifluromethylsulfonyl)imide
OCV	Open Circuit Voltage
PSSM	Polysulfide Shuttle Mechanism
RSF	Relative Sensitivity Factor
SEI	Solid Electrolyte Interphase
SEM	Scanning Electron Microscopy
SIMS	Secondary Ion Mass Spectrometry
ToF-SIMS	Time-of-Fight Secondary Ion Mass Spectrometry
UHV	Ultra High Vacuum
UPS	Ultraviolet Photoelectron Spectroscopy
XPS	X-ray Photoelectron Spectroscopy
XRD	X-ray Diffraction

List of Figures

List of Tables

1. Motivation

Today, the fossil energy resources are the most applied energy carrier, however, oil is believed to reach its maximum rate of extraction, the peak oil, from the wells within these years. The disposability of oil will shrink in the future and only disputable methods like fracking and deepwater drilling may provide sufficient supply of fossile energy carriers for the economy. Besides the decline of the fossil energy carriers, the exhaust products of the combustion engines are unhealthy and also lead to the global warming phenomenon which is why many countries try to decrease their CO_2 pollution by law. Considering these concerns, the utilization of fossil energy sources is questioned these days and novel ways to overcome the fossil energy sources are focused on. For stationary energy applications like room lightening, air conditioning, or electric radiators, the change to regenerative energy sources is inevitable to replace the coal as energy source. However, regenerative energy sources have the disadvantage of producing electricity nonuniformly due to weather conditions like an alternating wind speed and changing insolation during the daytime. To compensate the also nonuniform consumption of energy, there has to be an efficient storage network for the huge amounts of excess energy. Likewise, novel solutions are considered for the mobile applications and the electromobility is deemed to be the future replacing the combustion engine. For both stationary and mobile applications, battery devices may be utilized to storage and dispense the energy.

The electrochemical battery stores electricity by a chemical conversion or intercalation. The state-of-the-art technology is the Lithium-Ion Battery (LIB) which is utilized in mobile devices like notebooks, shavers, cellular phones, various electrical tools and also electric vehicles. However, this technology utilizes costly transition metals and may not provide sufficient storage capacity for an acceptable range of about 500 km for a commercially available electric car. Therefore, novel battery systems with a higher specific energy density are investigated within the electrochemistry community and by the chemical and the automotive industry. Particularly, the battery system based on sulfur as positive electrode material is of interest because the material is abundant, inexpensive, and non-toxic. There are companies like SION Power or OXIS Energy that are specialized on the development of lithium-sulfur batteries. Also, many chemical companies like the BASF or LG Chem which are focusing on the role as supplier for the necessary chemical components, especially the electrolyte compounds, are also researching lithium-sulfur batteries. Indeed, the lithium-sulfur battery is not fully understood and many drawbacks are not overcome

by a complete control of the battery chemistry yet.

In this thesis, the focus is set on the surface analysis of the negative electrode, the lithium metal electrode, in the mentioned lithium-sulfur battery system. Lithium is a reactive material that causes side reactions besides the cell reaction of lithium and sulfur to lithium sulfide. These side reactions render a crucial drawback of the lithium-sulfur cell and necessarily need to be kept in check. However, the formation of a surface film on the lithium electrode, the Solid Electrolyte Interphase, by the side reactions is deemed to be beneficial since they intrinsically prevent further reactions of the lithium metal with the electrolyte. Therefore, the side reactions with the electrolyte, generally applied in lithium-sulfur cells, are investigated with X-ray Photoelectron Spectroscopy and Secondary Ion Mass Spectrometry as surface analytical tools in this work.

2. The Lithium-Sulfur Battery

The interest in the lithium-sulfur battery system is based on its high specific energy density illustrated in the so-called *Ragone-plot* (figure 2.1). Indeed, the lithium-sulfur system suffers from many drawbacks that prevents the commercialization of the cell system, just as for the lithium-oxygen battery with an even higher specific energy. The physical and chemical properties of the lithium-sulfur cell are discussed in detail in this chapter.
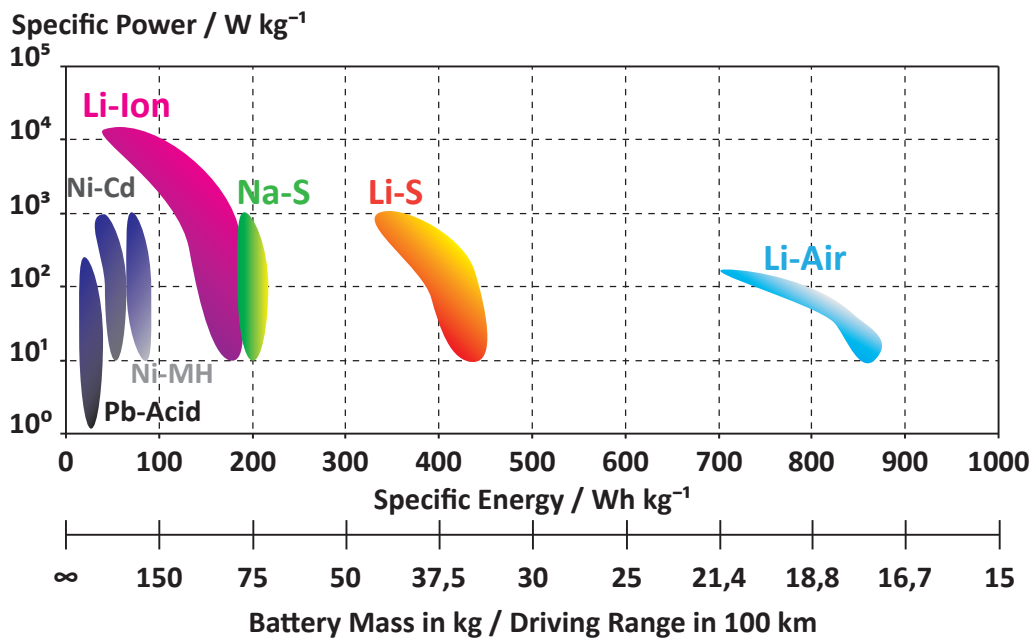
Figure 2.1.: The Ragone-plot depicts the electrochemical capability of particular battery systems (compare Ref. [1][2][3]), also translated for the electromotive application by the required battery mass for 100 km driving range.

Two parameters render the specific energy of a battery system: the cell voltage and the cell capacity. The lithium-sulfur system stands out due to its high theoretical cell capacity of $1672\,\mathrm{mA}\,\mathrm{g}_{\mathrm{sulfur}}^{-1}$, however, it exhibits a comparably low cell voltage of only 2.1 V. In table 2.1 the electrochemical cell characteristics for the lithium-sulfur battery and some custom Lithium-Ion Batterys (LIBs) are specified for comparison. In contrast to LIBs where primarily only one electron is involved in the reaction at the positive electrode, each sulfur atom is able to accept two electrons to form sulfide species. Furthermore, elemental sulfur (S_8) has a lower density than the

transition metal oxides ($LiMeO_x$) or phosphates ($LiMePO_4$) utilized in LIBs [4][5]. In conclusion, this leads to a higher capacity for lithium-sulfur cells than for LIBs, however, for a comparison, it also has to be pointed out that the cycling of a lithium-sulfur battery generally starts in the charged state, whereas LIBs have to be charged from the discharged state so that the volumetric and the gravimetric capacity are related to the volume and mass of the discharged phase respectively. Therefore, the specific capacity for lithium-sulfur has to be normalized to the final discharge product lithium sulfide (Li_2S) that is listed in table 2.1 as well. Besides these cell setup properties there are strong deviations in the chemistry compared to LIBs (compare section 2.1).

Table 2.1.: Overview of the theoretical cycling performance for lithium-sulfur batteries and selected LIBs; a) mass density according to Ref. [5], b) cell parameters and mass density according to Ref. [4]:

Cell System	Specific Capacity / Ah kg⁻¹	Cell Voltage / V	Specific Energy / Wh kg⁻¹	Volumetric Energy / Wh dm⁻³
S_8 Li_2S	1672 1167	2.1	3510 2450	7270[a] 4020[a]
$LiFePO_4$	169[b]	3.5[b]	590	2130[b]
$LiMn_2O_4$	148[b]	4.05[b]	600	2580[b]
$LiCoO_2$	274[b]	3.9[b]	1070	5450[b]

From the early investigations of the lithium-sulfur cell [6][7][8] till today the cell setup and the insights about the cell chemistry have advanced vastly, however, the cell chemistry is still not fully understood. The improvement of the cell components is still in an ongoing development so that the drawbacks of the cell are overcome. The current lithium-sulfur cell systems (see figure 2.2) typically consist of a liquid electrolyte (section 2.2), a carbon-sulfur composite as positive electrode (section 2.3), and lithium metal as negative electrode (section 2.4). Furthermore, a permeable membrane called separator keeps both electrodes apart from each other so the occurrence of short circuits inside the cell is prevented in the first place. As current collectors, copper, nickel, or stainless steal is commonly applied for the negative electrode and aluminum, sometimes primed with carbon, for the positive electrode. The dimensions and detailed compositions of each component vary a lot within the literature. Due to this, it is difficult to draw a clear comparison of the electrochemical performance for the presented cell configurations. Besides the bulk components of the cell, the electrode interfaces have an important influence on lithium-sulfur batteries because the redox mechanisms at both electrode surfaces are crucial for the the cell performance. Also, the electrolyte decomposes at both electrode interfaces and form a surface film in the process. At the lithium metal electrode this film is called

Lithium Metal Electrode   **Electrolyte + Separator**   **Carbon– Sulfur Electrode**

Solid Electrolyte Interphase (SEI)   **Cathode Surface Film (CSF)**
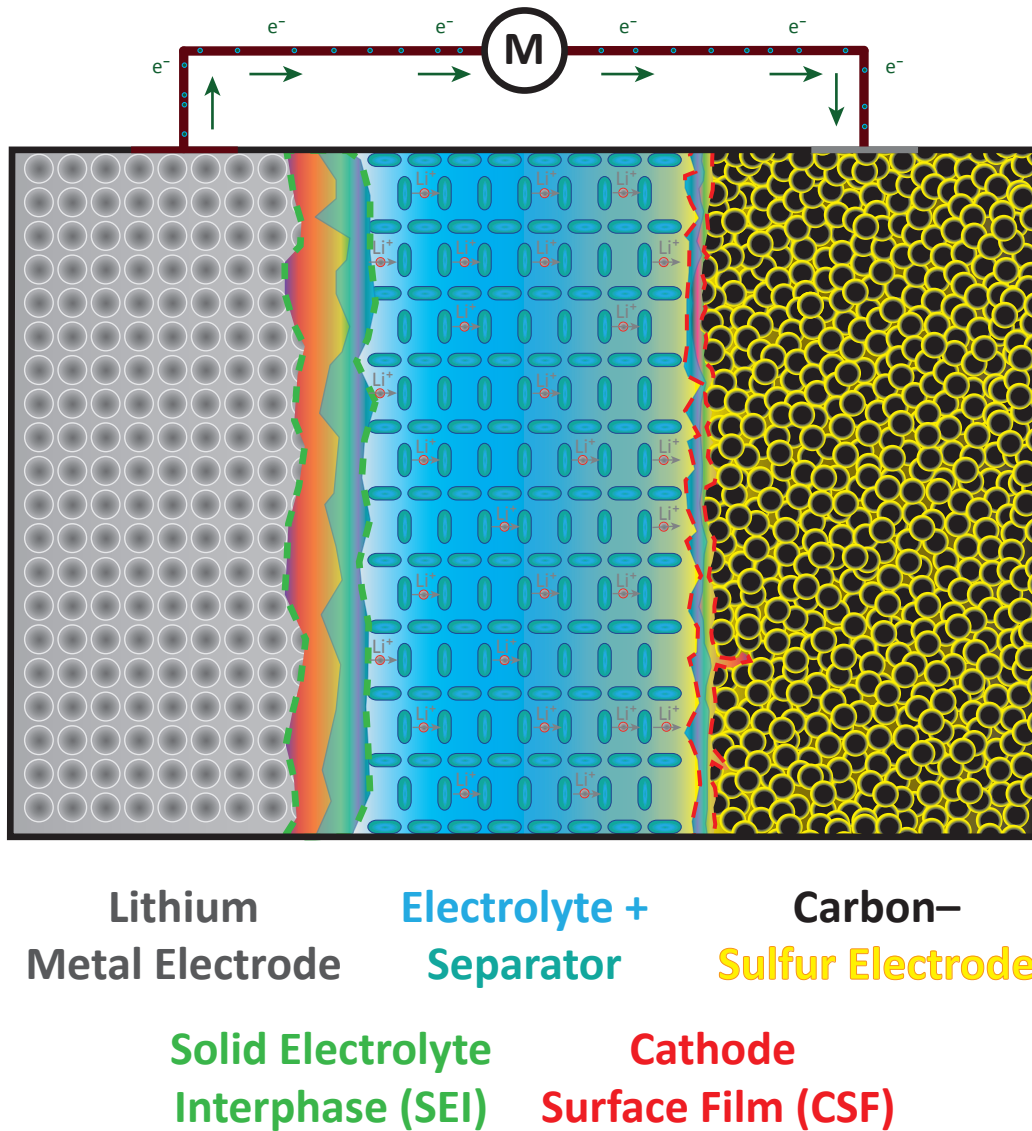
Figure 2.2.: Schematic illustration of a lithium-sulfur battery cell. During discharge, the electrons are moving through an outer circuit while the lithium cations diffuse or migrate through the electrolyte from the negative electrode, a lithium metal foil, to the positive electrode, a carbon-sulfur composite. Thereby, the surface films on the electrodes, particularly on the lithium metal, are vital for an enhanced cycling performance and the reversibility of the electrode reactions. Also, it has to be pointed out that the Cathode Surface Film covers particles deep inside the electrode as well since the electrolyte is able to intrude into the carbon-sulfur composite through the porous structure.

SEI; at the carbon-sulfur composite it is denoted as Cathode Surface Film (CSF). The formation and alteration of both layers during the cycling procedure represent significant processes for the cell performance. Therefore, the properties of these films are decisive for the improvement of the cell performance. An artificial arrangement of the SEI and CSF is desirable to suppress malfunction. The properties and investigations of the SEI will be discussed in section 2.5 in detail. Since the CSF is not investigated in this work, the CSF is only briefly described in section 2.3.

2.1. Basic Cell Properties of a Lithium-Sulfur Cell

In this section, the cell reactions inside the lithium-cell are described in detail and the effect on the cell performance is discussed afterwards. Eventually, alternative approaches for the standard cell setup, depicted in figure 2.2, like a completely liquid cell, a *redox-flow cell*, and a cell made of solids, an *all-solid-state cell*, are briefly mentioned in the last paragraph of this section.

Conversion Reactions of the Lithium-Sulfur Cell System

While the lithium cations intercalate and deintercalate into and off the cathode and anode in LIBs, elemental sulfur is transformed at the positive electrode by a conversion reaction with lithium to lithium sulfide and vice versa in a lithium-sulfur battery. More precisely, there are multiple phase transitions from solid elemental sulfur to solid lithium sulfide via *lithium polysulfides* that are soluble in the electrolyte. In equation 2.1 - 2.5 the elementary reactions from elemental sulfur to lithium sulfide and the total reaction in equation 2.6 are shown. These equations take polysulfide species from acknowledged literature [9][10] as a basis. Still, details of the reactions and their specific contribution to the total cell reaction are debated in literature [11].

$$6\,Li^+ \quad + \quad 3\,S_8 \quad + \quad 6\,e^- \quad \rightleftharpoons \quad 3\,Li_2S_8 \tag{2.1}$$

$$2\,Li^+ \quad + \quad 3\,Li_2S_8 \quad + \quad 2\,e^- \quad \rightleftharpoons \quad 4\,Li_2S_6 \tag{2.2}$$

$$4\,Li^+ \quad + \quad 4\,Li_2S_6 \quad + \quad 4\,e^- \quad \rightleftharpoons \quad 6\,Li_2S_4 \tag{2.3}$$

$$12\,Li^+ \quad + \quad 6\,Li_2S_4 \quad + \quad 12\,e^- \quad \rightleftharpoons \quad 12\,Li_2S_2 \tag{2.4}$$

$$24\,Li^+ \quad + \quad 12\,Li_2S_2 \quad + \quad 24\,e^- \quad \rightleftharpoons \quad 24\,Li_2S \tag{2.5}$$

$$48\,Li^+ \quad + \quad 3\,S_8 \quad + \quad 48\,e^- \quad \rightleftharpoons \quad 24\,Li_2S \tag{2.6}$$
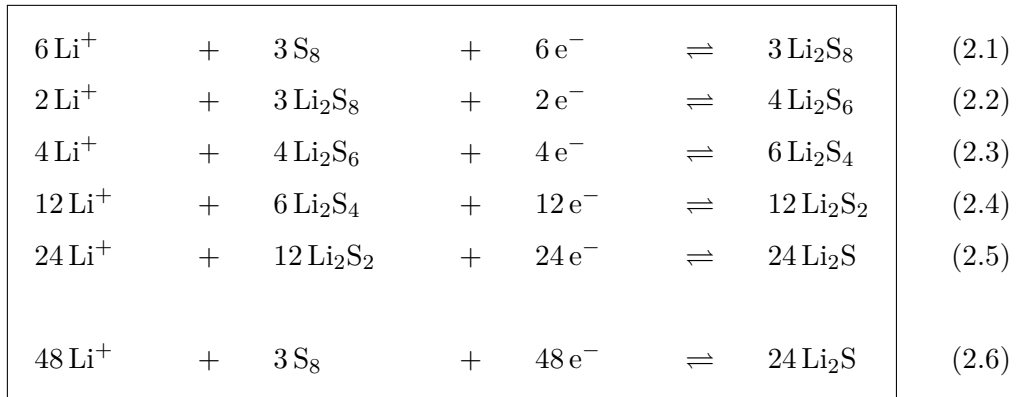
The elementary reactions already point out some crucial aspects of the lithium-sulfur battery. If one of the reactions is aborted by a parasitic reaction all the subsequent reactions cannot take place and, thus, the full cell capacity cannot be achieved anymore. Also, half of the capacity is accumulated in the last elementary reaction (2.5); on the contrary, only one quarter is accumulated in the first three reaction steps (2.1 - 2.3) which renders the importance of the last elementary reaction for the sulfur utilization.

Another aspect rendered by the elemental reactions is the electron consumption per reaction. The most polysulfide molecules normalized on one electron participate in equation 2.2: during discharge, $\frac{3}{2}\,Li_2S_8$ per electron participate in the reaction; during charge, even $2\,Li_2S_6$ per electron are consumed for the same reaction. In contrast,

the first reaction only converts $\frac{1}{2}$ sulfur species per electron. Thus, for the different reactions, in which different amount of polysulfies are converted to new polysulfides, the kinetics are affected sterically or diffusively so that the the reaction 2.1 is presumably the fastest and the reaction 2.2 the slowest. Beyond that, the cell kinetics play a decisive role for a full conversion of the active material [9].

In conclusion, the physical and chemical properties of all the sulfur species have a crucial influence on the performance, however, the quantitative or qualitative analysis of the dissolved polysulfides is sophisticated due to a multiplicity of factors of influence. The influence of the dissolved polysulfides on the cell components and the cell performance is more facile to investigate. In subsection 2.2.2, the most remarkable effect of the polysulfides, the Polysulfide Shuttle Mechanism, is described in detail.
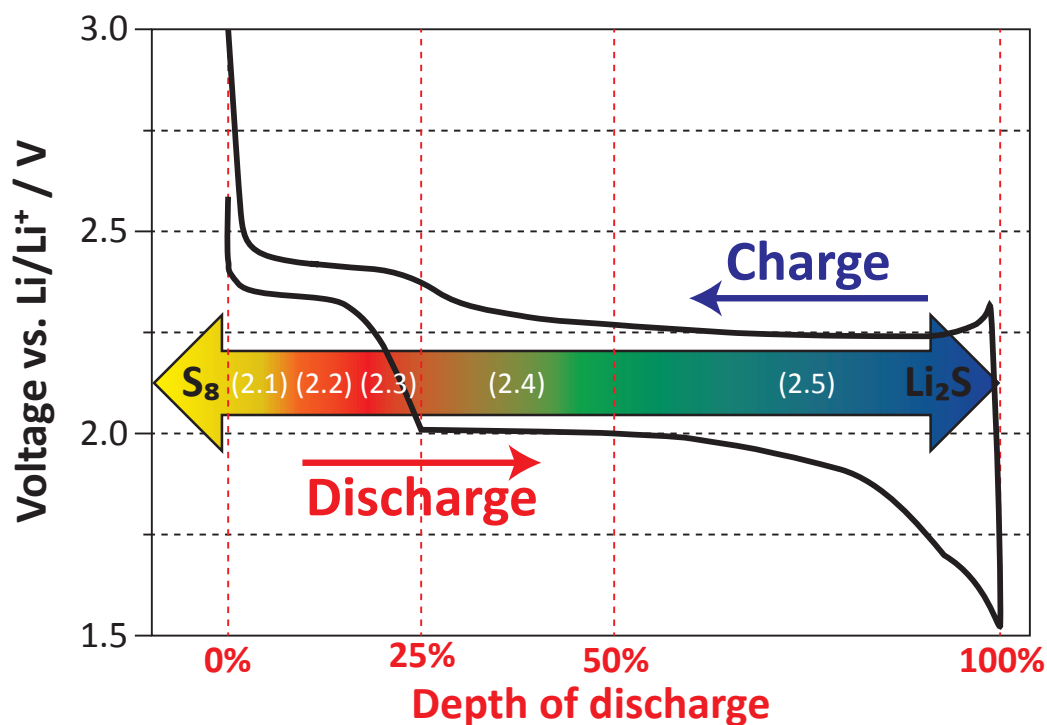
Figure 2.3.: Cycling profile of a lithium-sulfur battery: The different regions of the profile are related to the elementary reactions on page 7.

Cycling Performance

The abovementioned elementary reactions from sulfur to lithium sulfide have a specific influence on the cell characteristics as well. Not all elementary reactions occur at the same cell voltage which can be seen in the typical charge and discharge profile in figure 2.3. It consists of an upper plateau at about 2.3 V attributed to the first three reaction steps and a lower plateau at about 2.0 V for the forth and fifth reaction step.

Besides the abovementioned elementary reaction, equilibrium reactions between the already presented polysulfide species and other intermediate polysulfide species like Li_2S_3, Li_2S_5, Li_2S_7, or Li_2S_9 take place in the electrolyte [12]. By these equilibrium reactions the lower plateau voltage is stabilized so that the Gibb's phase rule is not violated. These equilibrium reactions may be suppressed at low temperatures [13]. Then, multiple potential steps are visible in the discharge profile. Nevertheless, the lithium-sulfur system is proposed to be low temperature compatible, however, at the cost of a vanishing upper plateau with decreasing temperature [13].

Cell Setup Modifications

There are several alternative approaches besides the above described cell setup (compare figure 2.2) to reach the applicability of the lithium-sulfur system. For instance, the redox flow battery concept consists of a setup in which the polysulfide species are dissolved within the electrolyte. After the reaction at the positive electrode, the formed polysulfide products are flown away and fresh polysulfide reactants can react electrochemically at the electrode. By a continous exhange with a tank reservoir the capacity of a cell is only limited by the size of the reservoir [14]. However, redox flow cells have a comparable low volumetric energy density [15] and, therefore, they are not relevant for mobile and electromotive applications. This reduces the utilization of redox flow cells to stationary utilization. Spefically, a significant challenge of the lithium-sulfur redox flow cells is the tuning of the flow rate due to the altering viscosity depending on the polysulfide concentration and their chain length [15].

Another important approach is given by the application of a solid electrolyte as a membrane to hold back dissolved sulfur species at the positive electrode. Here, the interfaces with other cell components like the liquid electrolyte or lithium seems to be challenging as the reaction with those components leads to the degradation of the surface and, hence, to a high interfacial resistance [16][17].

All-solid-state lithium-sulfur batteries with a solid electrolyte have also been reported. They exhibit similar interfacial resistances between the solid electrolyte and the lithium electrode or the carbon-sufur composite like for the membrane [17]. Commonly, a glass ceramic made of P_2S_5 and Li_2S is utilized as solid electrolyte in the all-solid-state cells [18][19]. Here, one of the main challenges is rendered by the facility of diffusion paths for electrons and lithium ions inside the positive electrode composite in an equal measure. Another aspect of this cell setup is the volume expansion and contraction of the positive electrode during the charge/discharge cycle which is constrained by the solid electrolyte. To still ensure the structural integrity of the cell components, nanosized particles have to be applied in the structure of the positive electrode [19][20]. Also, this volume expansion may further limit the sulfur content within the positive electrode compared to the liquid electrolytes [19]. Due to this and due to the vanishing of the upper plateau (compare Ref. [19]) the specific

energy density is significantly lowered in the all-solid-state setup compared to liquid electrolytes.

2.2. The Electrolyte

During the cycling of the cell, the lithium ions migrate back and forth the spatially separated electrodes through an *electrolyte* while the electrons flow along an outer circuit generating electrical power (see figure 2.2). The electrolyte is the medium in which the ion transportation takes place. A hindered ion transfer between the electrodes leads to a higher cell resistance, thus, a higher *overpotential* that leads to a lower discharge voltage and a higher charging voltage. Therefore, the conductance of the electrolyte is important, particularly for power applications with high currents. There are various types of electrolytes: liquid electrolytes, gel polymer electrolytes, ionic liquids, and solid electrolytes. While the commonly utilized liquid electrolytes, ionic liquids, and polymer electrolytes possess a ionic conductivity in the range of $10^0-10^1\,\mathrm{mS\,cm^{-1}}$ [21][22], the solid electrolytes exhibit a significantly lower ionic conductivity in the range of 10^{-5}–$10^0\,\mathrm{mS\,cm^{-1}}$ [20][23]. Due to the strong temperature dependency of the conductivity, polymer electrolytes and solid electrolytes may be utilized at elevated temperature to enhance the ion conductivity [20][22].

The experiments in this thesis are based on a liquid electrolyte, prepared from an organic solvent and a conducting salt. Therefore, this type of electrolyte is discussed in detail in the following subsection. The Polysulfide Shuttle Mechanism, a predominant malfunction phenomenon of the sulfur-based cell systems, is described at the end of this section.

2.2.1. Liquid Electrolytes

Liquid electrolytes can be classified into aqueous and non-aqueous electrolytes. Due to the strong side reaction of lithium with water under formation of lithium hydroxide, hydrogen and heat, only non-aqueous electrolytes are applied within lithium-sulfur batteries. Commonly, the non-aqueous electrolyte for lithium-sulfur cells consists of a mixture of ether-based solvents and a fluoriated lithium salt. Primarily *1,2-dimethoxyethane (DME)* and *1,3-dioxolane (DOL)* are utilized as solvents and lithium-1,1,1-trifluoro-N-[(trifluoromethyl)sulfonylmethanosulfonimide] (IUPAC name) is utilites as conducting salt (compare figure 2.4) [2]. In literature, another notation is generally utilized for the conducting salt: *Lithium bis(trifluro-methylsulfonyl)imide (LiTFSI)*. Due to this, LiTFSI is also the applied notation throughout this thesis.

Altenatively, longer glymes than DME may be utilized as well [24][25][26]. The application of carbonate-based solvents are not suitable for lithium-sulfur batteries since they are attacked nucleophilic by polysulfides, particularly by those with a short chain length [27].
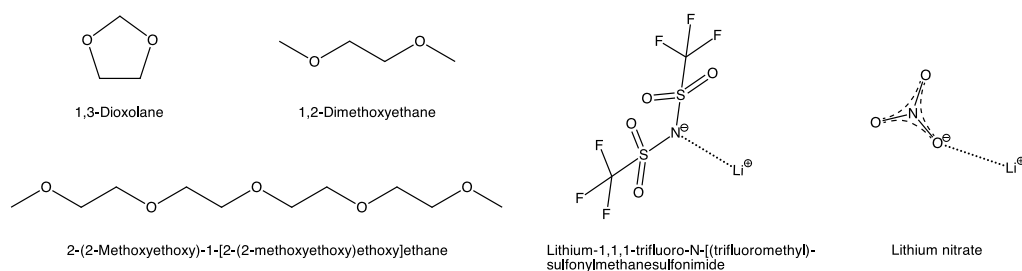
Figure 2.4.: Overview of the solvents and salts typically utilized in lithium-sulfur
battery cells

The application window for electrolytes is primarily set by side reactions at the electrodes, the so-called *electrochemical window*, and the phase transition of the solvents at the boiling point or melting point, the *thermal window*. The melting, boiling, and additionally the flash point of the typically utilized organic solvents for the lithium-sulfur cells are depicted in table 2.2. Both solvents exhibit a low flash point which renders a safety issue for the application and that is a reason why triglyme and tetraglyme [28] may be utilized instead of DME. Indeed, the solvents react with the surface of the electrodes, however, the lithium-sulfur cells perform within the electrochemical window of the commonly utilized electrolyte.

Concerning the cell performance, two electrolyte parameters contribute to the mobility of lithium cations in the electrolyte: on the on hand, the *relative permittivity* that describes how the electrolyte polarization is affected by an outer electric field; on the other hand, the *viscosity* that resembles the friction caused by neighboring molecules. For the optimization of both parameters a mixture of solvents is commonly applied to the cells. These paramater are listed in table 2.2 for DME and DOL as well. The relative permittivity is also proposed to have an influence on the maximum chain length of the polysulfides that can be formed in the solvents [29]. Moreover, both parameters also depend on the solvation of the cation and anion of the utilized salt. Thereby, the ability of the solvents to solvate the cation and the anion of the salt is reflected by the *donor number* and the *acceptor number* respectively [30]. The appropriate amount of salt with a distinct solvent mixture has to be determined experimentally and generally lies within the range of about 1 to 3 M salt [25]. For DME, the donor number yields $23.9\,\text{kcal}\,\text{mol}^{-1}$ and the acceptor number yields $10.2\,\text{kcal}\,\text{mol}^{-1}$ [31]. As far as to the author's knowledge, there are no donor and acceptor numbers exists for DOL. Also, the donor number reflects the solubility of the polysulfides as the amount of polysulfides increases with incremental donor number [29]. Another important aspect for lithium-sulfur battery is rendered by the redox behavior of the polysulfides depending on the solvents. With DOL-rich electrolytes, the final discharge product is proposed to be Li_2S_2 so that only 50 % of

the sulfur is utilizable for the application of DOL alone [8]. Also, the low viscosity of DOL is necessary to prevent the formation of a dense lithium sulfide layer at the outer region of the positive electrode [25].

Table 2.2.: Overview of physical parameters for typical lithium-sulfur solvents after a) Ref. [31] and b) Ref. [32]

Solvent	Viscosity / 10^{-3} Pa $\cdot$ s	Relative Permittivity / $A^2 \cdot s^4 \cdot kg^{-1} \cdot m^{-3}$	Melting Point / °C	Boiling Point / °C	Flash Point / °C
DME	0.455[a]	7.2[a]	-58[b]	84[b]	-2[b]
DOL	0.6[a]	7.34[a]	-26.4[b]	74[b]	-5[b]

For battery safety considerations the flash point of the electrolyte is very important, also shown in table 2.2. To increase the flaming point, electrolyte additives are commonly applied to suppress free radicals (see Ref. [33]).

Furthermore, electrolyte additives are utilized to modify the surface layer formation of the electrodes, particularly of the negative electrode, to enhance the cell performance [34]. The most familiar one in lithium-sulfur batteries is lithium nitrate that seems to be indispensable for superior cycling performance. Its modification of the electrode will be discussed in detail in subsection 2.5.2. Furthermore, shuttle mediators like metallocenes [35], thiosulfate [36], or other [14][37] may be utilized to enhance the lithium sulfide re-oxidation during charging.

Another concept is the application of an electrolyte with highly concentrated LiTFSI that leads to the formation of a protective SEI layer. Thereby, the growth of dendrites and ongoing corrosion of the electrode is prevented which is proposed to be a beneficial approach despite the lower ionic conductivity of the electrolyte due to the increment of the viscosity [38].

2.2.2. The Polysulfide Shuttle Mechanism

As already mentioned, the various polysulfides (Li_2S_2 to Li_2S_8) are soluble in the liquid electrolyte. One direct consequence out of this behavior is an increase of the electrolyte's viscosity depending on the amount of the dissolved polysulfides [25][39]. Furthermore, the higher viscosity increases the electrolyte resistance [40]. However, the effect with the largest impact resulting out of this solubility is given by the *Polysulfide Shuttle Mechanism (PSSM)*, a phenomenon that concerns the applicability of lithium-sulfur cells gravely.
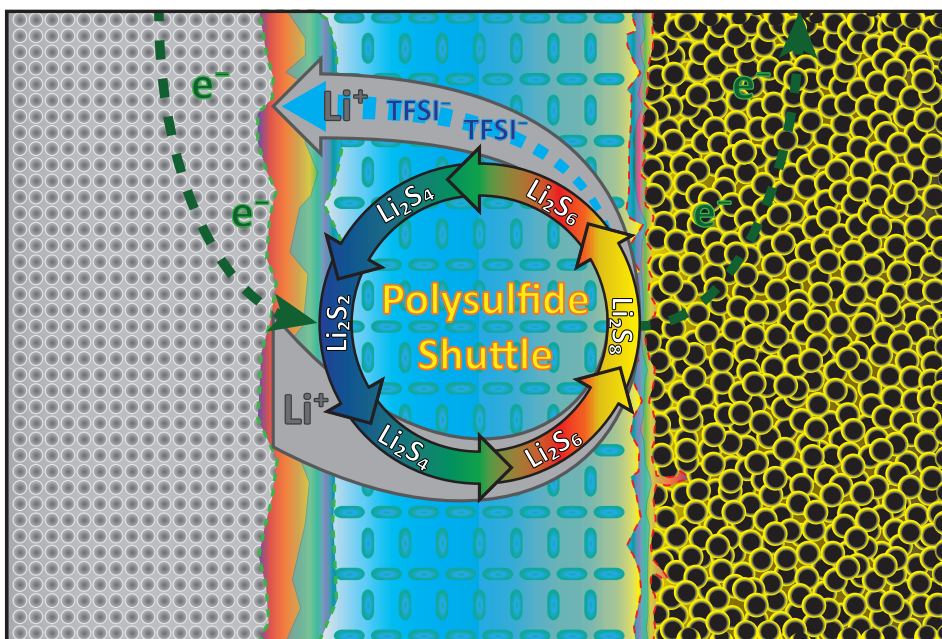
Figure 2.5.: Schematic of the PSSM: during the charge of the cell long chain polysulfides diffuse to the negative electrode where they are reduced to short chain polysulfides accepting electrons and lithium ions. These short chain polysulfides migrate back to the positive electrode where they are re-oxidized to long chain polysulfides dispensing electrons and lithium ions. Then, these long chain polysulfides may diffuse to the negative electrode once again creating the shuttle phenomenon. The dispensed lithium ions at the positive electrode are supposedly transported back to the negative electrode by the conducting salt while the yielded electrons result in an ongoing charging current.

During the discharge, a one time shuttle takes place between the positive and negative electrode. The polysulfides with a long chain length (e.g. Li_2S_8) migrate or diffuse to the negative electrode where they are reduced by lithium metal to shorter chains (e.g. Li_2S_2) or even solid lithium sulfide. As lithium sulfide can barely be re-oxidized, this reduction also leads to a loss of active material and the lithium

sulfide passivates the surface of the negative electrode during the process. However, the growing passivation of the negative electrode results in a lower reduction potential at the interface to the liquid electrolyte. Therefore, the further reduction of the polysulfides to solid lithium sulfide is prohibited by the surface coverage after a period of time. Then, the electrolyte may be considered as a catholyte and the dissolved polysulfides are reduced according to the cell reaction (equation 2.1 - 2.5) at the positive electrode. The ongoing reduction process of the polysulfides within the electrolyte can also be observed analytically by examination of the sulfur species at an additional membrane mounted on top of the positive electrode [41].

On the contrary, the charging capacity may increase till infinity due to an ongoing shuttle mechanism depicted in figure 2.5. The longer polysulfides diffuse from the positive electrode to the negative electrode where they get reduced to shorter polysulfides similar to the discharge process. Likewise these shorter polysulfides migrate back to the positive electrode but, during charge, the positive electrode has a lower oxidation potential and therefore the shorter polysulfides can be re-oxidized to polysulfides with a longer chain length. This oxidation process leads to an excess of lithium cations at the positive electrode that thereupon migrate back to the negative electrode supposedly along with the salt anions. Also, electrons are yielded by this re-oxidation process at the positive electrode that contribute to the charging current of the outer circuit, moreover leading to the overcharge process [13]. Strictly speaking, the PSSM consists of four interconnected cyclic processes: the sulfur shuttle, the lithium stripping and deposition cycle, the electron current, and the salt shuttle (not completely depicted in figure 2.5).

Primarily, the shuttle influences the cell performance by a poor Coulombic efficiency because the prolonged charging capacity exceeds the discharge capacity by up to 120-200 times overcharge [13]. Indeed, the shuttle may be a good overcharge protection mechanism but the cell performance suffers exceedingly by it. Also, this overcharge leads to a heating of the cell [13], presumably due to side reactions amplified by the shuttle mechanism. Furthermore, the passivation of the negative electrode with sulfur species leads to a loss of active material. If this passivation is not mechanically and chemically stable, this process leads to a steady capacity fading of the cell. In general, the aging of a lithium-sulfur batter cell is accelerated by the PSSM and, therefore, it renders an important, undesirable process.

There are different approaches to prevent the PSSM:

- Negative electrode protection: the most prominent approach is the utilization of electrolyte additives, particularly oxidizing agents that react with the sulfidic species at the negative electrode to form sulfur-oxygen compounds. These compounds prevent the reduction of longer chain polysulfides to shorter chains. Thereby, the PSSM is interrupted. Primarily, the addition of lithium nitrate into the electrolyte is considered for this application [42] and will be discussed in subsection 2.5.2 in detail.

- Membrane approach: the application of a physical barrier, a membrane, for the polysulfides between the electrodes enables a lithium transfer but retains the polysulfides at the positive electrode and prevents them from reacting with the negative electrode. Solid electrolytes may be utilized as membrane. They separate the electrolyte at the negative electrode, the *anolyte*, and the electrolyte at the positive electrode, the *catholyte*, from each other [16].

- Positive electrode retention: a further approach is the retention of the polysulfides within the porous structure of the sulfur-containing electrode. By this, they cannot dissolve from the positive electrode which will be discussed in the following section.

Still the PSSM remains a challenge for the lithium-sulfur battery system since none of the upper approaches have been successfully applied for a cell setup with a liquid electrolyte so far. This prevents an infinite or long-term cycling performance of the cell system.

2.3. The Positive Sulfur Electrode

The utilization of sulfur as active material for the positive electrode offers many advantages for the battery application. Its low density and the acceptance of two electrons per atom provide a high volumetric and gravimetric energy density. However, sulfur, the various lithium polysulfides, and lithium sulfide are electronically isolating so that a conducting host is necessary for the transformation of sulfur to lithium sulfide and vice versa. Furthermore, a porous material system is essential to address the maximum amount of sulfur by electrons and lithium ions. The best suited material properties that matches these requirements are exhibited by porous carbons with a graphitic structure that can be facilitated conveniently and low priced as well. Besides carbon, other materials like a porous nickel [43] matrix or layered manganese oxide [36] are also considered as sulfur host. By combining the host material and the sulfur, either through ball mixing or melt infiltration of the sulfur, a composite powder is produced. Commonly, this powder is then processed to a slurry by dispersion of the particles together with a solvent and a binder. Eventually, the slurry is coated onto an aluminum current collector by a doctor blade and then dried till the solvent is evaporated completely.

Most research efforts for lithium-sulfur batteries is concerned with the improvement of the carbon host for sulfur by an optimized pore structure so that a maximum fraction of sulfur may be utilized. Likewise, the PSSM is suppressed by a best possible sulfur retention within the pores. Also, the electronic conductivity of the various carbon materials is considered as an important factor for the sulfur utilization. Indeed, there have been various types of carbon utilized for lithium-sulfur batteries: graphen [44], carbon blacks [45][46], carbon nanotubes, and carbon fiber cloth.

Concerning the sulfur retention capability, a high surface area is favored for carbon blacks, however, the mechanical stabilty of the positive electrode suffers by the application of carbon blacks which manifests itself in a brittle electrode structure [46]. Another approach to enhance the polysulfide retention capability of the positive electrode is given by blending additives into the carbon-sulfur composite fabrication, for example, $Mg_{0.6}Ni_{0.4}O$ [26] or Al_2O_3 [28], also to improve the sulfur utilization catalytically as well. Furthermore, a stronger binding of the sulfur to the the carbon matrix may be achieved by a co-polymerization of the elemental sulfur with aromatic compounds, dissolved into the electrolyte, via the inverse vulcanization method [44][47].

Indeed, there are also drawbacks that prevent the utilization of sulfur. For instance, it is reported that the application of an oxidizing agent like lithium nitrate leads to the partially oxidation of the sulfur species at the positive electrode leading to an irreversible formation of sulfur-oxygen compounds [48].

To enhance the electronic conductivity carbons can also be doped with substitutes like nitrogen [49], oxygen, or sulfur into the carbon matrix.

A thick *Cathode Surface Film (CSF)* is proposed to cause a similar behavior like the utilization of a solid electrolyte [50]. Thereby, the CSF is particularly formed at a lower discharge voltage of 1 V for which the reduction capability of the positive electrode is enhanced.

There are serveral reviews that examine the cell performance in dependence on the different carbon structures [51] or on the different fractions of carbon, sulfur, and binder [24], however, the electrolyte is not standardized so a consistent comparison is barely achieved. Also, the sulfur loading plays a decisive role and is sometimes not considered properly. As already mentioned at the beginning of this chapter, a systematic and comprehensive view on the cell performance considering the different cell components has not been reported in literature yet.

2.4. The Negative Electrode

The alkali metal lithium is in principle a preferred material in battery systems because of its high gravimetric and volumetric capacity. The capacity results from the low density caused by the small atomic radius; also, the small ionic radius and the single charge of the lithium ion results in high ionic mobility, however, the lowest of all alkali metals [52]. Moreover, lithium has the lowest electrochemical potential with -3.0 V against the Standard Hydrogen Electrode (SHE). Therefore, the application of lithium exhibits an exceeding energy density and also an excellent power density. However, there are several drawbacks concerning the application of lithium metal. Since lithium has a very low electrochemical potential it reacts spontaneously with other species. This leads to impairing side reactions with the electrolyte. Hence, a detrimental "drying" of the electrolyte and thermal runaways are possible effects which result in the stall of the cell or maybe even cause flamings or explosions. Therefore, it is crucial to lower this reactivity to improve the cell lifetime and the safety issues.

Primarily, there are three different approaches to suppress the reactivity:

- One approach is the intrinsic modification of the SEI layer, formed by the electrolyte decomposition, to prevent further reaction of the negative electrode. To functionalize the surface layer the electrolyte is mixed with suitable additives so that electrons cannot be transferred from the lithium metal electrode to the electrolyte.

- The deposition of an artificial layer, commonly a solid electrolyte, on the lithium metal electrode or the deposition of lithium metal on a solid electrolyte is also considered. However, solid electrolytes are also reduced by lithium metal. This leads to decomposition of the solid electrolyte and, thereby, high interfacial resistance can occur (compare section 2.5).

- Another possibility is the application of lithium intercalation compounds or alloys which restrict the reactivity by a lower chemical potential of lithium, however, these materials have a slightly higher electrochemical potential (compare Ref. [1]).

In the following subsection, the application of lithium metal is discussed in more detail due to its relevance for the lithium-sulfur battery system (compare Ref. [17]). Eventually, the *rocking chair* material carbon and the alloy material silicon are described by their properties and functionality, and their possible application in lithium-sulfur battery systems is discussed.

2.4.1. The Lithium Metal Electrode

In general, a thin foil of lithium metal is utilized as negative electrode in lithium-sulfur cells. Because of its softness and stickiness the cell can be assembled easily, though, the lithium foil is usually not very planar. Also, the foil is roughened furthermore by scratching the surface with a ceramic knife to remove the native oxidized surface. This rough surface might entail in an inhomogenenous surface potential on the microscale that results in an nonuniform stripping and deposition process of lithium and different chemical reactions. To overcome this drawback, an enhanced stack pressure can be applied to the cell assembly which leads to higher surface tension and thereby to a denser and tighter lithium stripping and deposition [53][54]. A grave drawback of lithium metal is the formation of dendrites, small crystalline needles or whiskers, which grow during the deposition process due to the nonuniform exchange current densities at the electrode surface. By the electric field between the electrodes these dendrite needles may grow straight to the positive electrode, get in contact with the active material, and thereby shortcut the cell chemically which may lead to a thermal runaway or fire [53]. By the co-deposition of metals (Na, Mg, Ca, Sr, Ba) the dendrite growth may be suppressed because the incorparation of these metals into the surface is proposed to lower the exchange current density and create a physically hindrance for the dendrite growth due to lattice mismatch [55]. An investigation of the nucleation of lithium on stainless steel by Stark et al. [56] also identifies the suppression of lithium nuclei growth due to sodium co-deposition without alloying in the process. Also pointed out by this investigation, the SEI hinders the nuclei to agglomerate so that fresh surface area may be generated. The surface can further react with the electrolyte which decreases the coulombic efficiency. Furthermore, the application of cesium and rubidium salts are proposed to prevent dendrite growth by a *"self-healing electrostatic shield (SHES)"* mechanism in which these alkali metals align as positive ions Cs^+ or Rb^+ around the negatively polarized dendrite nuclei and thereby prevent further deposition of Li^+ [57], however, this effect is supposed to be incompatible with ionic liquids [55]. Another approach to lower the exchange current density is the minimization or diminishment of the capacitive surface charge by the application of *shuttle mediators* [53]. These shuttle mediators are molecules dissolved in the electrolyte that can be reduced or oxidized at the surface with a redox potential slightly lower than the Open Circuit Voltage (OCV) of the cell.

By applying an artificial overlayer, the lithium metal electrode may be protected from reacting with the electrolyte. Thereby, the required physical properties of the overlayer are the same as for the SEI created by the intrinsic reaction with the electrolyte during the cycling of a cell (compare section 2.5). For instance, an aluminum oxide layer deposited with atomic layer deposition (ALD) is proposed to be a suitable candidate to form a protective barrier against the air, the electrolyte, or

polysulfides [58].

Another important aspect of the lithium metal electrode is the the large volume change from the charged to discharged state and vice versa. This effect impairs a mechanically stable formation of the SEI [53] and is one of the critical effects in cells with high sulfur loading.

2.4.2. Alternative Lithium-containing Electrode Materials

There are various types of negative electrode materials besides lithium metal, however, only a few have been utilized for lithium-sulfur batteries due to the relatively low potential of the sulfur electrode. The alternative materials for lithium metal like tin, antimony, or titanate usually hold a lower potential, a lower capacity, and exhibit a volume expansion as well [59]. Therefore, they are not well applicable with sulfur in general. Indeed, there are some reports about graphite and silicon which will be discussed briefly in this subsection.

The Graphite Electrode

The graphite electrode has been investigated most and is applied in LIBs commercially. Thereby, the lithium ions are intercalated between the graphene sheets in subsequent steps and, hence, produce a volume expansion of about 7%. The application of a graphite host lowers the electrochemical potential of lithium by $0.66\,\mathrm{V}$ and, therefore, also the reactivity of lithium. Due to the low potential of the sulfur electrode (compare table 2.1), this may result in a loss of $1/3$ energy density compared to lithium metal. Also, the graphite electrode has a much lower gravimetric capacity of $378\,\mathrm{mAh/g}$ than the capacity of $3862\,\mathrm{mAh/g}$ for the lithium metal electrode. However, a much less excess amount of lithium is needed by the application of graphite than for lithium metal in lithium-sulfur cells [17].

Also, graphite is commonly used with carbonate-based solvents like ethylene carbonate (EC), propylene carbonate (PC), or diethyl carbonate (DEC) which are not suitable for lithium-sulfur batteries due to the reaction with polysulfides [27]. The utilization of ether-based solvents, however, leads to exfoliation of graphite sheets by co-intercalation of lithium with solvent molecules between the sheets. This may be overcome with the application of novel binder materials for the graphite electrode [60].

The Silicon Electrode

Silicon has already been applied successfully in lithium-sulfur batteries [44]. During charging the lithium and the silicon forms an alloy that is conductive. By this, a very high capacity similar to lithium metal may be achieved during cycling. Furthermore, there is no diminution of the cell voltage in contrast to the graphite electrode.

However, the silicon-lithium alloy expands by about 300 % during charging which requires nanostructuring of the material. The surface of silicon is usually covered with a silicon oxide or fluoride layer. This layer is believed to form a stable SEI on those nanoparticles and, therefore, prevents further corrosion of the electrode.

2.5. Solid Electrolyte Interphase

A lot of investigations have been conducted to characterize and understand the electrode surface reactions for various materials and applications. These side reactions at the surface may be considered malicious for the battery application due to an increment of the overpotential and a loss of active material on the one hand. On the other hand, a protective character for the electrode may be yielded by this passivation of the electrode. Since the first proposal of the *Solid Electrolyte Interphase (SEI)* as such a functional passivation layer for lithium in non-aqueous electrolytes by Peled and Yamin [61] in 1979, the knowledge about functional passivation films has increased significantly. Particularly for the graphite electrode, intensive research has been conducted which has led to the commercialization of the Lithium-Ion Batterys (LIBs). An extensive summary of the hitherto existing literature was presented by Balbuena and Wang in 2004 [62]. Admittedly, the formation, growth, and chemical alteration of the SEI are still not fully understood, not to mention of its physical properties. The limits of the investigation are set by the analytical techniques that can barely probe the thin and reactive structure on a microscopic scale. Therefore, the advances in the analytical techniques likewise lead to a greater understanding of the SEI composition and properties. For graphite as negative electrode material, the SEI is in the range of several tens nanometer (see Ref. [63][64]), for lithium metal the whole SEI layer may be serveral tens of micrometer thick (compare Ref. [38][65]).

A detailed overview of the SEI literature is given in the following subsections. First, the general SEI build-up is described which is then rendered for the lithium-sulfur battery in more detail. Eventually, the hitherto approaches and considerations of the SEI investigation are presented, however, the SEI in lithium-sulfur electrodes has not been investigated intensively yet. Therefore, the literature for the SEI analysis is represented as a more general overview, also to achieve a better understanding of the analytical approach utilized in this work.

2. The Lithium-Sulfur Battery

2.5.1. General Solid Electrolyte Interphase Properties

An electrode made of lithium is strongly reactive and affects the liquid electrolyte as a reducing agent. The reduced electrolyte species adsorb at the electrode surface and instantly form a layer made out of decomposition products (see figure 2.6). This layer is denoted as Solid Electrolyte Interphase (SEI) in general.
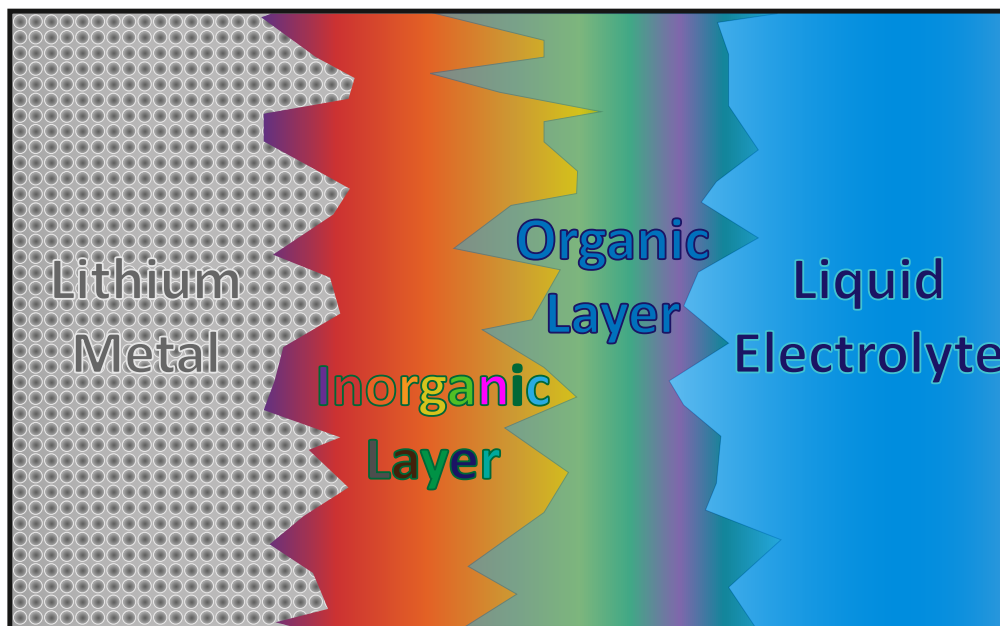
Figure 2.6.: Schematic of a typical SEI: While the inorganic layer consists of strongly reduced electrolyte species, the organic layer primarily consists of solvent decomposition products and precipitated products produced by side reactions. The color code of the layers will be utilized in the following chapters.

The SEI is proposed to be composed out of two distinct layers [21]: (1) a dense *inorganic layer* consisting of small crystals of strongly reduced species like LiF, Li_2O, Li_xC_y, or other lithium halides (LiCl, LiI), lithium chalcogenes (Li_2S, Li_2Se), or lithium pnictogenes (Li_3N, Li_3P, Li_3As) depending on the utilized electrolyte [66]. This layer stands out due to its high electronic insulation capability because of the high band gap of the mentioned compounds. However, not all these phases are excellent lithium ion conductors. Therefore, the composition of the electrolyte has to be considered and adjusted to ensure a sufficient lithium ion conductance in this inorganic layer. (2) At the electrolyte site of the SEI, the porous *organic layer* consists of solvent decomposition products like hydrocarbons, lithium alkoxides, lithium hydroxide, and lithium carbonate [21][66][67]. By polymerization of the solvent molecules, the organic layer contributes to the mechanical stability of the formed SEI [66].

An excellent SEI on the negative electrodes is decisive for the successful operation of cell system because the SEI adopts several functions within the cell. This functionality is ensured by distinct physical properties:

- **Lithium Ion Conductor:** An ideal SEI should have a transference number of unity for lithium ions and should conduct lithium ions like a typical solid electrolyte. If no other ions, especially anions, are transmitted through the SEI the lithium electrode is protected from further corrosion. Additionally, the ion diffusion through the SEI is expected to be the rate determining step for the surface kinetics so that a high cell resistance or overpotential may be attributed to a limiting lithium ion conductance of the SEI, particularly for high charge or discharge currents.
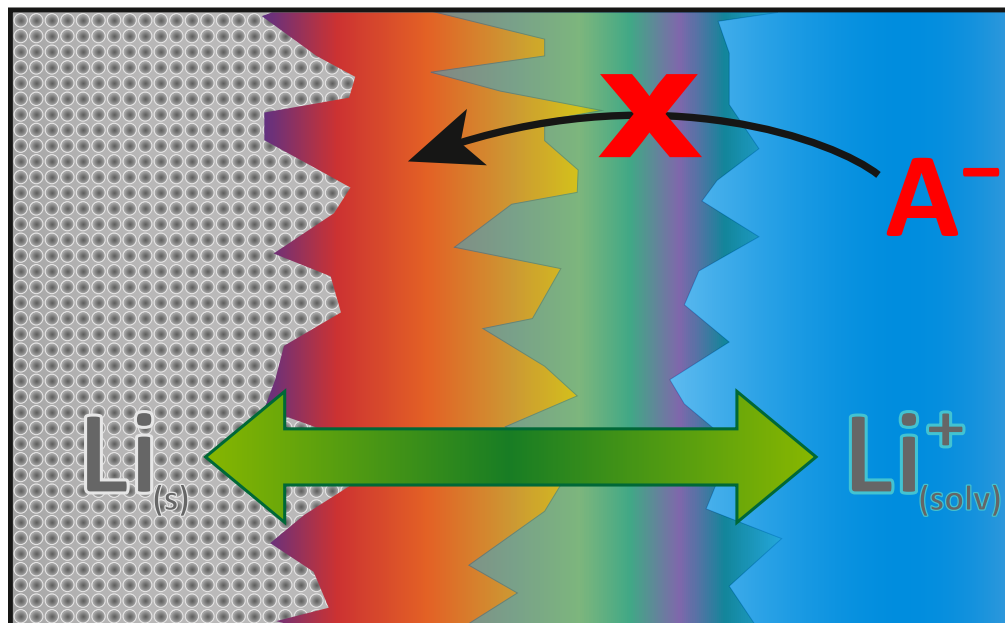
Figure 2.7.: Ion conductance capability of the SEI: An ideal SEI only conducts lithium ions to the electrode surface where they can be deposited. The electrolyte species, particularly anions, are not supposed to pass the SEI so further corrosion of the electrode is prevented by the layer.

- **Electronic Insulation:** Ideally, the SEI should be electronically insulating for several reasons. First, if electrons are conducted through the electrode surface the electrolyte species may be reduced and then decompose. This leads to electrolyte drying and finally to malfunction of the battery cell [45]. Furthermore, during the charging process lithium ions can be reduced to lithium metal within the SEI layer structure so that the SEI becomes more electronically conductive and dendrites can grow. Also noted, an insulating SEI has a huge surface charge during polarization of the cell due to the conservation of electrons at the surface which may lead to faster kinetics.
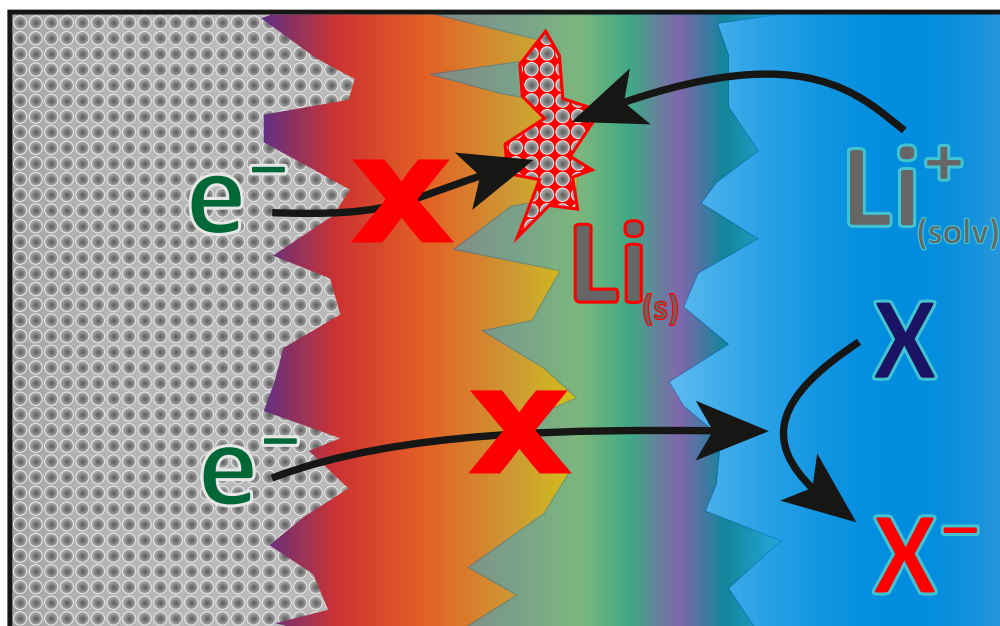
Figure 2.8.: Electronic insulation capability of the SEI: If the SEI is not electronic insulating the lithium ions may adsorb as lithium metal within the passivation. Also, the electrons can diffuse or tunnel through the passivation layer and reduce the electrolyte species by an ongoing process.

- **Mechanical Stability:** During charge and discharge the volume of the electrode expands and constricts respectively. Thereby, mechanical stress is induced to the SEI that might lead to a breakdown of the SEI. Repeating breakdowns lead to ongoing reaction of the lithium metal electrode with the electrolyte causing the drying of the electrolyte and the growth of dendrites at the free sites of the SEI as well. Also, the inorganic salts of the SEI can seclude or dissolve from the surface [68]. These secluded or dissolved species might malfunction other cell components like the separators, current collectors, or the positive electrode.
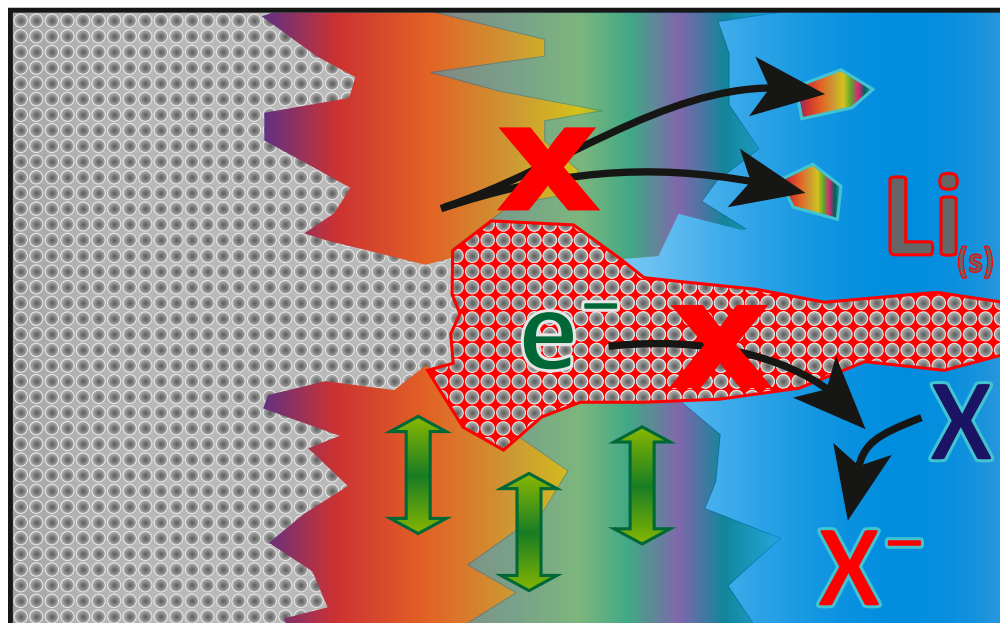
Figure 2.9.: Mechanical stability of the SEI: A mechanically stable SEI ensures the electrode protection capability during the cycling of the cell for which the electrode expands and constricts by lithium deposition and dissolution respectively. Otherwise, the passivation breaks down, inorganic particles may seclude into the electrolyte, fresh lithium surface gets in contact with the electrolyte species, and the polarized electrode offers a preferential spot for the lithium deposition by which dendrites may be formed.

2.5.2. The Solid Electrolyte Interphase in Lithium-Sulfur Cells

The abovementioned physical and chemical properties of the SEI are also considered for the SEI in lithium-sulfur cells described in this subsection. Thereby, the reported literature for the electrolyte components DME, DOL, LiTFSI, the sulfur species, and the electrolyte additive lithium nitrate are summarized individually.

The reaction of 1,2-dimethoxyethane with lithium was investigated by Aurbach et al. [67]. They proposed that the primary reaction products are lithium methoxide and ethylene: First, an electron transfers from a lithium atom to a solvent molecule generating a radical anion that is stabilized by the formed lithium cation. In a second step, this radical anion decomposes to lithium methoxide and an ethyl methyl radical that undergoes a second electron transfer generating an additional lithium methoxide and ethylene. Furthermore, the solvent DME exhibits a slow reaction with the bulk lithium but a fast reaction with the freshly deposited lithium. For the bulk lithium, a well detectable film is formed after over a week while the film for the electrochemically deposited lithium is already substantiated after several hours. Also, they asserted that there is no conversion or growth of the thin film formed by DME.

On the other hand, a decomposition of 1,3-dioxolane to lithium formate, lithium carbonate, and lithium alcoxides was detected by Fourier-Transform Infrared Spectroscopy (FTIR) at the lithium metal surface [69]. Furthermore, it was also proposed that DOL polymerizes at the lithium metal electrode by a reaction with alkoxides that are present at the surface [42]. These polymers are considered to be elastomers that mechanically stabilize the SEI on lithium metal [66].

In contrast to the solvent, the conducting salt LiTFSI seems to be stable against the lithium metal electrode [21][70]. The salt cannot penetrate through the native lithium oxide layer on the foil so that only HF [21] or the later incorporation of LiTFSI may lead to the formation of lithium fluoride; a possible reaction mechanism can be seen in Ref. [42]. The application of fluorinated solvents may likewise lead to lithium fluoride as a decomposition product at the negative electrode. This lithium fluoride is proposed to form a dense protection layer which prevents the PSSM, however, the formation of this layer also leads to a high overpotential in the first cycles [71].

The SEI in lithium-sulfur cells is influenced by the PSSM discussed in subsection 2.2.2. Therefore, the deposition of lithium sulfide and lithium polysulfides can be detected by X-ray Photoelectron Spectroscopy (XPS) [39][72]. The reaction of the polysulfides with the electrode surface is proposed to lead to a dense layer that prevents further reactions with the electrolyte [72]. Furthermore, the appearance of polysulfides in an electrolyte is believed not only to form a dense and smooth layer but also to prevent the growth of lithium dendrites [73].

An important electrolyte additive is lithium nitrate. This compound works as an oxidizing agent, particularly for the lithium polysulfides [22][42], which leads to a dense, protective layer at the lithium electrode that prevents further corrosion of the electrode by sapping the electron transfer at the surface of the negative electrode. Therefore, lithium nitrate is proposed to suppress the PSSM by the formation of an electronic insulating layer. Additionally, the Coulombic efficiency is significantly improved by adding lithium nitrate to the electrolyte. Furthermore, the roughness of the surface is smoothed by lithium nitrate so that dendrite formation may be suppressed, however, the SEI, influenced by lithium nitrate, seems to have a higher ionic resistance [22][74]. Similar results are yielded by pretreating the lithium foil with lithium nitrate [65] or by the application of lithim perchlorate as conducting salt which is likewise an oxidizing agent [75]. Additionally noted, the stability of lithium nitrate seems to be a crucial issue since lithium nitrate decomposes for a discharge voltage of $1.8\,\mathrm{V}$ at the positive electrode [76] and may irreversibly form sulfur-oxygen species [48]. Also, lithium nitrate is consumed in the redox reaction at the negative electrode so that its beneficial effect on the cell performance is limited by a certain number of cycles according to the utilized amount of lithium nitrate.

2.5.3. Approaches and Considerations for the SEI Analysis

In the following literature summary, a comprehensive introduction is stated for the SEI analysis. By this, a fundamental understanding of the challenges and their feasible solutions are provided. The literature embracing the SEI analysis is primarily concerned with the composition and structure of the SEI on the graphite electrode for Lithium-Ion Batterys. However, most of the analytical challenges are also faced in the investigation of the lithium metal electrodes in this thesis. The summary includes the contributions from the working group of Prof. Petr Novák, Prof. Kristina Edström, Prof. Emanuel Peled, Prof. Martin Winter, and further working groups. For this comprehensive literature summary, the insights of reviews are quoted for most instances since single articles usually discuss the application of the respective techniques only partially. In single articles, more attention is paid to the results for the actual composition and structure of the SEI which is already summarized in subsection 2.5.1 and 2.5.2.

Research from the Working Group of Prof. Petr Novák

Vetter et al. [77] pointed out that the SEI is supposedly formed during the first cycling and its conversion, stabilization, and growth proceeds in the following cycles. Also, electrolyte additives should not only enhance the formation process but also contribute beneficially to the aging mechanism of the SEI. They emphasized to track the aging mechanism and particularly their impact on the cell performance with impedance spectroscopy. By this technique, the resistance of the surface films on both electrodes can be determined and qualitative conclusions on the growth may be proposed with a low technical effort in view of time and cost.

Verma et al. [78] reviewed the SEI formation for graphite electrodes and typical Lithium-Ion Battery electrolytes. They also summarized all the applied techniques for the investigation of the SEI, particularly FTIR and XPS. For XPS, they pointed out that the modeling of the chemical composition requires precise knowledge of the battery system and good reference values for the verification as well. Therefore, various data of characteristic lines for primarily carbonaceous compounds were listed from a variety of literature for FTIR as well as XPS.

Research from the Working Group of Prof. Kristina Edström

Edström et al. [79] examined the influence of air exposure and sputtering on the graphite SEI with the XPS technique. They asserted that the contamination due to air exposure changes the composition of the SEI significantly and that a tightly sealed sample transfer is of particular importance. By sputtering with Ar^+ ions, the compounds lithium oxide and fluoride respectively emerged from the radiation

damage of lithium carbonate and the conducting salts $LiBF_4$ or $LiPF_6$ in the XPS spectra. Thereby, they showed that the occurrence of lithium oxide and lithium fluoride may not be unambiguously verified within the SEI.

Malmgran et al. [80] investigated the film on the positive as well as the negative electrode in a graphite/$LiFePO_4$ cell system with $LiPF_6$ in a EC/DEC (1:1) solvent via synchrotron XPS. By varying the X-ray energy, they acquired a conditional depth profile similar to the angle-resolved measurements (compare subsection 3.1.2). In the deeper regions of the SEI at the lithiated negative electrode they observed lithium fluoride, lithium oxide, and lithium carbide. The actual appearance of these compounds within the SEI was verified without the application of sputtering which may change the SEI drastically.

Philippe et al. [81] reviewed the results for the SEI analysis by the XPS technique, particularly by the application of syncrotron radiation. Thereby, the negative as well as the positive electrode materials and their surface films are discussed for different electrode materials. Particularly, this articles elucidates the approach to reveal the SEI composition by XPS in detail.

Research form the Working Group of Prof. Emanuel Peled

Peled et al. [82] investigated the lateral distribution of SEI components by Time-of-Fight Secondary Ion Mass Spectrometry (ToF-SIMS) with a lateral resolution of about 1 µm for the first time. By this, it was assumed that the SEI is homogeneously distributed on the basal plane of the utilized HOPG.

In a subsequent work, Peled et al. [70] analyzed the basal plane and the cross-section of different carbon materials with ToF-SIMS and XPS. By the intensity difference of the SIMS signals, they proposed that the SEI of the basal plane is richer in salt decomposition products of LiTFSI, $LiPF_6$, or $LiAsF_6$ and the cross-section is enriched with solvent decomposition products of ethylene carbonate and diethyl carbonate. Furthermore, the cross-section SEI was suggested to be thicker than for the basal plane due to the course of elemental signals in the depth profiles, however, neither XPS nor SIMS depth profiles are illustrated in the article.

Research from the Working Group of Prof. Martin Winter

Niehoff et al. [63] investigated the SEI with the XPS technique utilizing sputter depth profiling (SDP) to detect the species in the SEI. They first analyzed an untreated graphite electrode as well as an untreated graphite electrode in contact with the electrolyte in order to estimate the sputter-induced change respectively. Finally, a cycled graphite electrode was analyzed by sputtering depth profiling to reveal the SEI build-up. Thereby, the depth profiles were illustrated by detail spectra and tables of components and their fractions in the respective depth. By this, a model

for the SEI was created illustrating the prevailing compounds in a top and bottom layer.

Further Research of various Working Groups

Lu and Harris [83] analyzed the SEI layer structure by isotope labeling with ^{6}Li and detection with ToF-SIMS. For the outer layer of the SEI, they determined a thickness of about 5 nm under the assumption that the sputter rate of the SEI equals the sputter rate of silicon oxide. Furthermore, the inner layer was proposed to be dense and it also exhibited an enrichment of lithium oxide or lithium carbonate. Xiong et al. [72] analyzed the SEI of lithium metal for lithium-sulfur cells with the standard electrolyte DME/DOL plus LiTFSI with the XPS technique. They also sputtered the electrode surface with argon to yield a depth profile. By this, they observed a top layer primarily consisting of electrolyte decomposition products and a layer below that was proposed to exhibit primarily sulfidic species. However, the elemental distribution over the depth did not reflect this proposal of the SEI layer. They also examined the SEI for DME/DOL and lithium nitrate plus polysulfides with a similar approach [74]. Here, they observed a top layer of sulfite or oxidized sulfur species that should prevent further reaction of the electrolyte with the lithium electrode. On the other hand, the bottom layer consists of reduced polysulfide species and reduced lithium nitrate decomposition products. This composition was proposed to be favorable for a stable SEI in lithium-sulfur batteries.

The Resulting Approach for the SEI Analysis

Concluding the abovementioned literature, the investigation of the SEI is not facile since several aspects have to be considered to gain an image of the SEI structure and composition. This includes the preparation, the selected analysis techniques and their influence on the samples, and eventually the interpretation of the acquired data.

In this work, the preparation was conducted in a way that as little as possible contamination of the sample was achieved. Particularly, the contamination due to extraneous substances was excluded by a rigorous sample handling and by sealing the sample against air or atmosphere molecules (see section 3.4). As analytical techniques, XPS and SIMS were chosen for the investigation of the SEI since the XPS technique resembled a common SEI examination method for the chemical composition of the SEI (explained in section 3.1) and SIMS was deemed to give complementary insights into the spatial distribution of the compounds (explained in section 3.2). Furthermore, the influence of the radiation damage due to sputtering was preliminarily examined for pristine compounds (chapter 4) to estimate the conversion of the potential surface compounds in the later XPS analysis of the passivation by the sputter depth profiling. Also, the measurements yielded excellent XPS reference

data for the analyzed compounds which were utilized in the SEI analysis as well. Due to a novel conversion of the XPS data into an illustration in mole fraction (see section 3.4) this analysis was more comprehensive than the illustration in elemental distribution or peak fractions. With this knowledge, the SEI was investigated by the XPS and SIMS techniques in a systematic analysis. Therefore, negative electrodes were extracted out of lithium-sulfur cells with different cycle number (chapter 5). Eventually, the results of both techniques were consolidated from their complementary depiction.

Due to this, a comprehensive insight into the evolution of the SEI is yielded so that an authentic representation is proposed for the SEI structure and composition. Also, the influence of sample washing and unique features on this systematic analysis is considered and will be discussed in chapter 6 that adds insights to the SEI analysis beyond the common procedure. Finally, this approach will be reviewed and concluded in the last chapter 7.

3. Experimental Considerations for the SEI Analysis

In this Chapter, the utilized analytical techniques for the examination of the lithium surface, XPS and SIMS, are introduced. Both methods are complementary to each other providing divergent approaches for a surface sensitive examination of the top atomic layers. Due to this sensitivity, Ultra High Vacuum (UHV) conditions are required for the analysis. On the one hand, the UHV prevents primary and secondary beams from getting disturbed by the atmosphere in the analysis chamber which gives rise to more reduced signals, noisier backgrounds, or undesired contribution of atmosphere species. On the other hand, the surface coverage by atmosphere atoms is diminished (compare Ref. [84]). For both methods, local charging can occur in the analysis region due to the incident beam that ejects electrons from the surface. The arising positive charge has to be compensated by a connection to ground potential, the spectrometer itself, or by an electron gun which neutralize the positive charge with low energy electrons. Also, both methods are independent of the crystallinity of the examined samples and, therefore, the amorphous phases are equally detected as the respective crystal phases in the measurements.

The complementarity arises from the different inspection types and their physical limitations. The XPS technique examines the electronic structure of the material by the photoelectric effect and thereby the elemental composition and chemical bonding can be determined for a material. On the contrary, the SIMS technique analyzes the surface composition under negligence of the electronic structure with a much lower detection limit for elements and compounds. Also, the SIMS technique holds a greater spatial resolution than the XPS technique considering the utilization of laboratory machines.

Most properties and features in XPS spectra are treated well in literature. The evaluation of XPS data requires knowledge of these features so that consistent and reliable fits with reasonable spectral properties like the position or Full Width at Half Maximum (FWHM) of intensity peaks can be applied to evaluate the XPS data. The evaluation of SIMS measurements stands out due to the huge amount of data and complexity. For the analysis, systematic correlations are usually indispensable to understand the mass spectra. In addition, the understanding of specific features like the matrix effect and preferential sputtering are necessary to avoid misinterpretation of the depth profiles.

The fundamental functionality of the XPS and SIMS technique and the utilized machines are subsequently discussed in detail within the next sections. Furthermore, important aspects for the depth profiling are also rendered comprehensively. Eventually, the sample preparation for the measurements is described in the last section.

3.1. X-Ray Photoelectron Spectroscopy

The analysis technique X-ray Photoelectron Spectroscopy (XPS) stands out for its quantitative detection of the elemental distribution and the determination of compounds in the sample surface. Thereby, the analysis depth is about 10 nm and the detection limit is set in the ppt range which renders the method as exceedingly surface sensitive for the extensive chemical analysis of a sample.

This technique relies on the excitation of electrons with X-rays via the *photoelectric effect* and the subsequent quantitative detection of these electrons according to their binding energy of the electron orbital. A schematic of the whole process from the X-ray generation to the final illustration of the results is depicted in figure 3.1. The fundamentals of the analysis method and the respective machine components are briefly described in the following subsections.
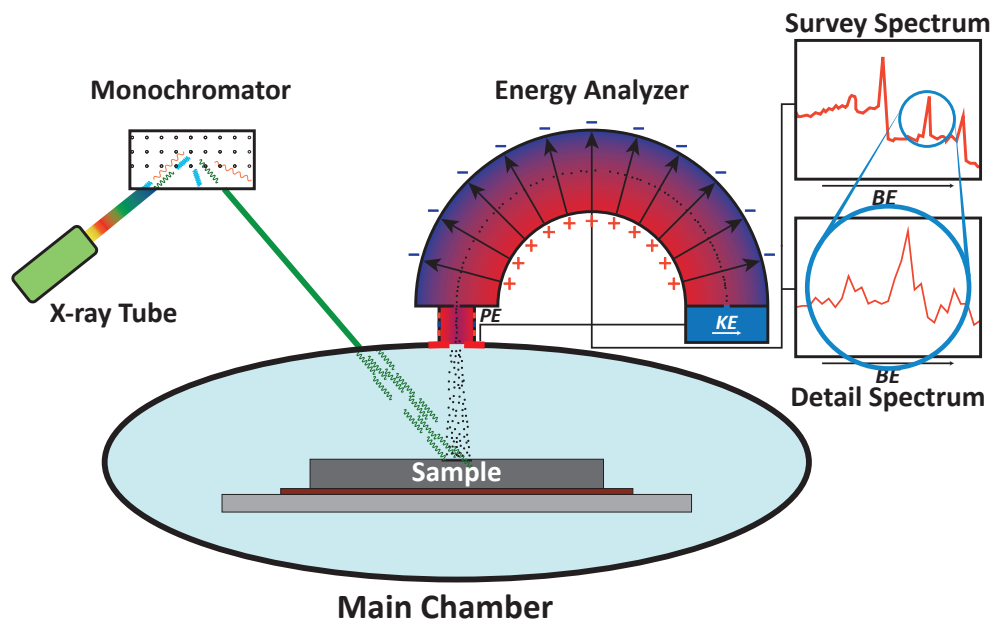
Figure 3.1.: Functionality of the XPS technique: Characteristic X-rays are generated by an X-ray tube of a certain anode material. To avoid the Bremsstrahlung and other undesired X-rays of different wavelengths the X-rays are filtered by a monochromator and afterwards are irradiated onto the sample surface. There, they transfer their energy to the electrons in the atom orbitals of the surface constituents which leads to the emission of the electrons out of the sample. These emitted electrons are collected and analyzed by their kinetic energy. Finally, the detected electrons of a specific energy are accumulated and their counts are plotted against the binding energy. By inspecting the characteristic lines or peaks in the spectra, the composition of the sample surface can be determined quantitatively.

3.1.1. Methodical Fundamentals of the XPS technique

In this subsection, the fundamental effect that is exploited for the XPS technique, the *photoelectric effect*, is described in detail. The Auger effect, another important process occurring during X-ray irradiation of a sample, is briefly considered as well. For deeper knowledge about XPS and Auger spectroscopy, the reader is referred to the fundamental literature of Briggs and Seah [85] and also Taglauer and Vickerman [86], for instance.

The Photoelectric Effect

During the photoelectric effect, photons or more precisely X-ray quanta of a distinct energy are irradiated onto a sample where they may interact with a core electron in an orbital of a surface atom. Thereby, the energy of a single quantum $h\nu$ is transferred to this electron that is specifically bound to the atomic nucleus by a binding energy BE. This results in the emission of the electron from the sample with a distinct kinetic energy E_{kin} that is characteristic for the according element to which the orbital belongs (compare figure 3.2). The general relation of the binding energy and the kinetic energy is given by:

$$E_{kin} = h\nu - BE - \underbrace{(\phi_S \pm \phi_{\text{neutralizer}})}_{machine} \tag{3.1}$$

The equation is adjusted by machine parameters like the work function of the spectrometer ϕ_S that is in contact with the sample. Additionally, most XPS machines enable charge neutralization of the sample surface by an electron beam which set the surface potential on a distinct value. Although the kinetic energy is analyzed, the intensity or counts of the electrons is plotted against the binding energy in general. There are two routines of obtaining a XPS spectrum (see figure 3.3).

By scanning the kinetic energy over a wide range and counting the electrons for the according energy each time, a XPS *survey spectrum* is taken. Here, the characteristic lines for each element are primarily observed for a sample. Since single lines are not necessarily unambiguous several lines are usually utilized to assert the identification and verification of these elements. Therefore, survey spectra are inevitable to recognize peak overlap and misinterpretation; additionally, survey spectra help to prevent the disregard of impurities in the sample analysis.

Furthermore, the binding energy for a distinct orbital depends on the chemical environment of the according atom. This phenomenon is called *chemical shift* and the minor energy differences are primarily resolved in the *detail spectra*. For this, a small specific energy range is examined for an existing chemical element of the respective sample. In the detail spectra, the binding energy changes to a higher value for a greater positive oxidation state and for a lower value for greater negative oxidation

Photoelectric Effect　　　　**Auger Effect**

O 1s　　　　O KL$_1$L$_2$

1s　　　　K

2s　　　　L$_1$

2p　　　　L$_2$
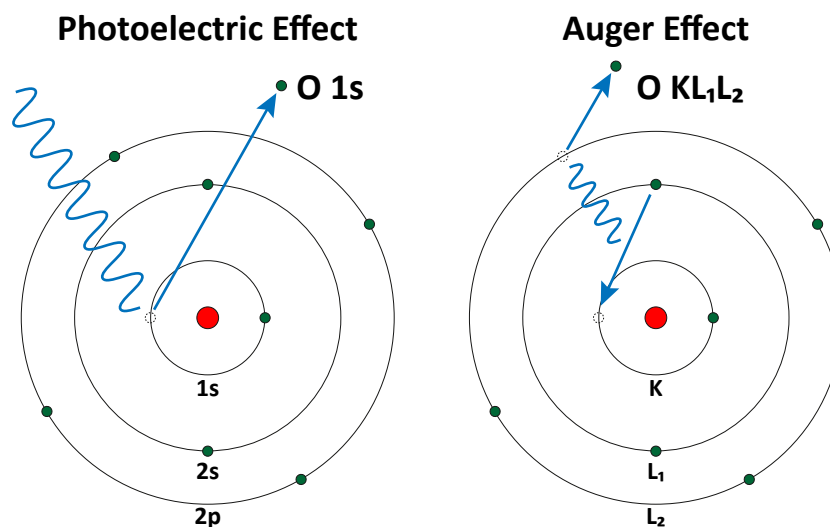
Figure 3.2.: *Photoelectric effect*: the energy of the incident X-ray is completely transferred to a core electron. The kinetic energy of the emitted electron is reduced characteristically by the binding energy of the atom orbital.
Auger effect: by the relaxation of an electron to lower empty atom orbital a sufficient amount of energy is dispensed so that an instantly absorption of this energy by another electron leads to the emission of a so-called Auger electron.

Auger Peaks　　**Photo-electron Lines**　　　　**S 2p**

Intensity / arb. units

F 1s

F KLL

O KLL

O 1s

S LMM　N KLL

C KLL

N 1s　C 1s

S 2s

S 2p

Li 1s

Li-S*-S

S-S^x-S

Li$_2$S

Imp

Binding Energy / eV

1200　900　600　300　0

168　165　162　159
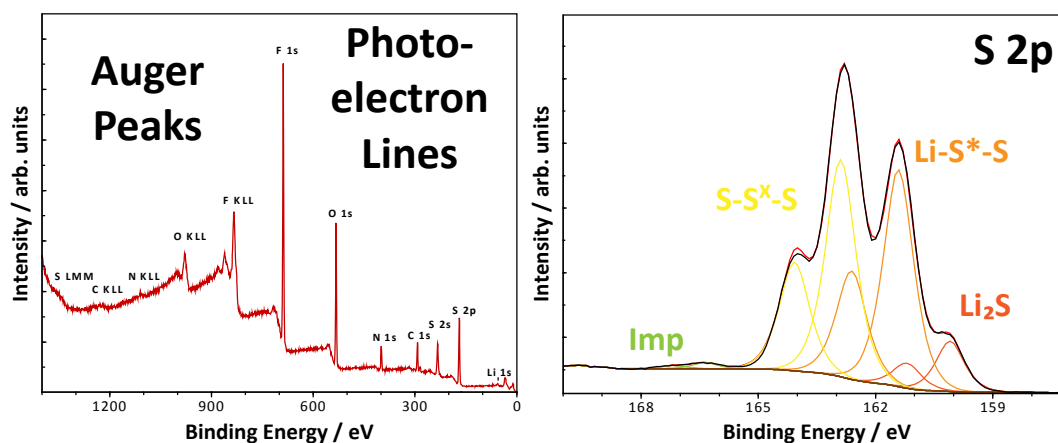
Figure 3.3.: In the *survey spectrum* of LiTFSI (left) all the utilized photo lines are visible. They are well separated from the Auger peaks observed at higher binding energies. By applying a lower pass energy, the single lines can be resolved more precisely so that different chemical components are differentiable from each other in a *detail spectrum* (right). Both types of spectra are generally illustrated as intensity in arbitrary units against the declining binding energy in eV.

state as rule of thumb. This shift is in the range of a few 0.1 eV up to 10 eV. Thereby, the oxidation state of an examined element is more significant for the magnitude of the chemical shift than the actual binding partner or the particular chemical environment. For instance, the binding energy of sulfur in lithium sulfate and LiTFSI is quite similar for the S 2p line.

To quantify the elements in the sample surface, the intensity in terms of the line area are related to each other. Thereby, some elements are more readily to detect than others due to their different cross-sections with the incident X-rays, e.g. lithium is difficult to detect and barely exhibits a peak above the noise level of a spectrum while fluorine shows a clear peak even for a small concentration. The general detection limit of XPS is in the ppt range. This varying ability to detect the different elements of the periodic table is reflected by so-called *Atomic Sensitivity Factors (ASFs)* which are listed in tables (compare Ref. [87]). For the quantification, these ASFs have to be taken into account for the relation of all the line areas LA_n to each other. An atomic concentration c_i of an element i is then given by:

$$c_i = \frac{\mathrm{LA}_i/ASF_i}{\sum_n \mathrm{LA}_n/ASF_n} \tag{3.2}$$

By considering all available elements with their precise binding energy and the corresponding intensities a full chemical composition can be disclosed and their mole fraction at the surface can be quantified.

The Auger Effect

Another process coming along with the photoelectric effect is the *Auger effect* that is also depicted in figure 3.2. The effect is described as follows: Due to the emission of a core electron a vacant state is left behind. Subsequently, this vacant state is occupied by an electron from a higher orbital and, thereby, the relaxation energy is dissipated either to an emitting photon or to an electron, likewise in an elevated orbital, that is then able to emit from the atom. The emission of this secondary electron is possible because the relaxation energy is greater than the binding energy for the secondary electron, denoted as Auger electron. Both the photon energy as well as the kinetic energy of the Auger electron are characteristic for the examined element and are utilized in the techniques X-ray fluorescence (XRF) or energy-dispersive X-ray spectroscopy (EDS) and Auger spectroscopy (AES,) respectively. The Auger peaks are assigned by their associated chemical element and a triple of letters utilized in the X-ray notation: first the vacant state, second the original orbital of the relaxing electron and third the orbital of the emitting electron; e.g. O $\mathrm{KL_1L_2}$ for the oxygen Auger peak (compare figure 3.2).

Notably, the Auger electrons are undesired in XPS spectra in most cases since their

peaks are broad and nonuniform. If there is an overlap with a photoelectric line existing the intensity of the Auger peak can barely be worked out so that a precise measurement is not possible. In a few cases the chemical shift of the Auger peak and the one of the photoelectric peak move in the opposite direction for the same compound providing an unambiguous criterion for the detection of this compound, however, this is not the case in this work. Likewise, the shape of an Auger peak might be a reference for a specific compound in the sample. The undesired Auger peaks can be shifted by utilizing an additional X-ray source with a different anode material or X-ray energy. The binding energy $BE \simeq h\nu - E_{kin}$ remains the same for the photoelectric effect as a higher photon energy also leads to a higher kinetic energy of the photoelectrons. In contrast, the binding energy $BE_{Aug} \simeq h\nu - E_{kin,Aug}$ changes with different X-ray energies since the kinetic energy $E_{kin,Aug}$ is constant for the Auger electrons. On this account, the intensity of the detected electrons is thus plotted against the kinetic energy in the Auger spectroscopy.

Further Features within a XPS Spectrum

There are several features possibly occurring in a XPS spectrum. First of all, the background of the spectrum arises from scattered photoelectrons that interact with the sample atoms and, thereby, dissipate energy. By this, the kinetic energy is reduced and accordingly the binding energy is increased leading to a higher background on the left side than on the right side of the photo peak (compare figure 3.3). This background has to be subtracted consistently for each photo line by application of an algorithm, e.g. created by Shirley or by Tougaard. Only after background subtraction, a mathmatical fit can be utilized and evaluated for the quantification of the elements or compounds.

Primarily, the non-scattered photoelectrons originate from about the first $10\,\text{nm}$; that is three times the mean free path length of the electron. However, this *escape depth* also depends on the kinetic energy E_{kin} of the electrons (compare Ref. [88]). For an overlayer and for a simultaneously huge difference in binding energy of the chosen elemental lines, originating from the sublayer, a falsified quantification may result for the composition of this sublayer due to overestimated detection of electrons with a lower binding energy and hence higher kinetic energy.

Due to the spin-orbit coupling a duplet structure can be resolved in the detail spectra for angular momentum quantum numbers $l = p, d, f, ...$. Thereby, the duplet consists of a small peak at higher binding energy and a huge peak at smaller binding energy. The reason for this splitting is the coupling of the spin $s \pm \frac{1}{2}$ with the respective angular momentum l: For $s = -\frac{1}{2}$, the electrons are stronger bound to the atom as for $s = +\frac{1}{2}$. Also, the magnetic quantum number for the total angular momentum m_j is less degenerated for $s = -\frac{1}{2}$ than for $s = +\frac{1}{2}$. This leads to a 1:2 ratio for $p_{1/2}$ to $p_{3/2}$, to a 2:3 ratio for $d_{3/2}$ to $d_{5/2}$, and a 3:4 ratio for $f_{5/2}$ to $f_{7/2}$ states.

A further feature is the appearance of so-called *shake-up satellites* that are caused by a two-electron process. The emission of a core electron, the primary photoelectron, also leads to a reorganization of the valence electrons which may involve an excitation, a "shake-up", to a higher unoccupied state for a secondary electron. The required energy for this excitation is subtracted from the kinetic energy of the emitted primary electron which results in a shift to a higher binding energy in the spectra and, therefore, satellite peaks are observed. This phenomenon occurs particularly for transition metals with unpaired electrons in the $3d$ or $4f$ shells. Also, an asymmetric tail of the peaks is observed for metallic solids by this excitation of valence electrons due to a continuous distribution of unoccupied states above the Fermie energy. Furthermore, not only single electrons can be excited but also collective oscillations of the conducting electrons, the plasmons, can occur in a metal. The energy of the different metal-characteristic oscillations reduces the kinetic energy of the emitted photoelectron as well.

3.1.2. General Instrumental Setup of a XPS Machine

A XPS machine consists of the X-ray generation device, the analysis chamber, and an installation for the energy separation and detection of electrons. In figure 3.1 the different sections are shown schematically. The different machine parameters determine the accuracy of the technique as well as the feasibility. The accuracy manifests itself in the FWHM of the photoelectron peaks. While the energy distribution of the emitted electron is of Lorentzian type, the machine appends a Gaussian distribution to this energy distribution, primarily by the X-ray energy distribution and the energy separation of the analyzer. Furthermore, the measurement of insulating samples due to surface charging renders a challenge in surface science for most instances and likewise for the XPS technique which has to be overcome by the machine setup. In general, the environment of the analysis chamber is decisive for the feasibility of measuring a sample. The individual components and their functions are now briefly described in the following paragraphs.

X-ray Generation

There are two possibilities to generate X-rays artificially: one is the X-ray tube invented by William Conrad Röntgen and the second is the utilization of the synchrotron radiation. While the X-ray tube creates radiation of a distinct energy depending on the anode material of tube, the X-rays originating from a synchrotron can be varied in their energy by changing the deflection devices of a particle accelerator. Also, the synchrotron X-rays have a much lower lateral resolution and usually comprises a higher photon density. Because of this and the pronounced definiteness of the snychrotron X-ray energy, the peaks in a XPS spectrum become very sharp.

Nevertheless, the X-ray tube is applied relatively effortless and, thus, a widespread analysis tool. Since synchrotron X-ray radiation has not been used for this thesis the reader is referred to corresponding literature [81] for a detailed description.

In a X-ray tube, electrons are emitted at a hot cathode and are accelerated by a high voltage till they strike the anode. There, they get decelerated inelastically by the atoms of the anode material. Thereby, they generate a continuous energy spectrum of photons, the Bremsstrahlung, and sharp lines at distinct energies which are characteristic for the anode material. Bremsstrahlung results from the interaction of the electron with the nucleus during passing its attraction field. On the contrary, the characteristic radiation of the anode material is generated by an electron transition process: An accelerated electron from the cathode transfers energy to an electron in a core state which is emitted from the material. The thereupon unoccupied core state is filled by an electron from a higher state. This transition leads to the emission of an X-ray quantum with a discrete energy. Because several transitions and hence the emission of different X-ray energies are possible within this relaxation process the various X-ray quanta are filtered by a monochromator through Bragg-reflection. By this, only coherent X-ray quanta of a distinct energy irradiate the sample. Thereby, additional peak satellites and the background intensity are suppressed in the XPS spectrum.

Typical anode materials for a X-ray tube are aluminum, magnesium, and zirconium with respective X-ray energies of 1486.6 eV, 1253.6 eV, and 2042.4 eV. Both aluminum and magnesium excels by their little energy width of 0.85 eV and 0.7 eV, respectively, while zirconium features an advanced escape depth for the examination of deeper surface regions due to its higher excitation energy.

The Analysis Chamber

In the analysis chamber or main chamber, the irradiation of the sample and the emission of electrons from the sample surface takes place, essentially. Beyond that, various sample modification tools may be applied to the analysis chamber to make different in situ operations feasible.

For instance, the measurement of insulating samples renders a challenge. Since X-rays are irradiated onto the sample and electrons are emitted, the sample becomes charged positively on a local level. This may cause a strong decline of the photoelectron current, shifting of the binding energy, or the total loss of signal in the worst case. To prevent sample charging an electron gun is usually utilized to irradiate the sample with low energy electrons of a few eV at the respective spot. Thereby, the formation of a positive charge is neutralized by the negative electrons. As a matter of course this electron beam should not alter the sample.

In this context, the chamber also has the functionality to maintain the composition of the sample surface and to avoid potential distorting effects. Most of these dis-

torting effects are inhibited by the application of UHV conditions so that nearly no atoms are present in the vicinity of the sample; id est, the mean free path of X-rays and photoelectrons is increased significantly compared to an atmosphere with many gas constituents. By this, the noise and the background intensity of a XPS spectrum is lowered and likewise the peaks of the atmosphere constituents do not contribute to the spectrum. Another issue is the re-covering of the surface by physical or chemical adsorption of the surrounding atmosphere species during sputter profiles.

Furthermore, by changing the angle between the sample surface and the X-ray beam a conditioned depth profile can be acquired for the maximum analysis depth of about 10 nm. It is conditioned because the analysis depth is just lowered in this angular resolved depth profile; id est, the concentration in the depth is yielded only after the mathematical subtraction of the concentration above. This method is denoted as *angle-resolved XPS (AR-XPS)* in literature.

The Electron Analysis and Detection

The emitted electrons from the sample surface are gathered by an aperture and then are decelerated. After this step the electrons enter the energy analyzer which usually consists of a semi-hemisphere capacitor. Only electrons are able to pass the analyzer which fulfill the following equation:

$$\mathrm{PE} = E_{kin} + \phi_{dec} \tag{3.3}$$

where PE is the so-called *pass energy* and ϕ_{dec} the decelerating voltage. A spectrum is recorded by fixing the pass energy and varying ϕ_{dec} so that electrons for different E_{kin} are transmitted through the analyzer.

The pass energy is an important machine parameter. For an elevated pass energy, the electrons have a high velocity and therefore spend less time in the analyzer. This enables a high count rate but also lowers the energy resolution since the electrons with a slightly higher energy only have a short time to get separated from the adjusted pass energy. In the case of a lower pass energy, the electrons have a lower velocity and, thus, the separation is enhanced. This leads to an improved energy resolution which is important to detect small differences in binding energy for the sample compounds. However, this leads to a much lower intensity because a huge amount of electrons cannot pass the analyzer. According to this, the transmission function of the analyzer proportionally increases with higher pass energy. Therefore, the pass energy has to be chosen carefully to obtain the desired information and accuracy either from the chemical shift via improved energy resolution or from the yield for the precise determination of low elemental concentrations with intensities close to the detection limit. Furthermore, a low peak intensity also leads to a bad signal to noise (S/N) ration. Of course, the S/N ratio may be improved by increasing the analysis time but this also leads to exorbitant measurement time without any

additional gain of information.

Finally, the electrons are counted at the detector which usually consists of a photomultiplier that amplifies a single electron impact event to an electronic pulse. The resulting pulse is then processed by the electronic and computational hardware which is eventually evaluated by the software of a PC.

3.1.3. The Utilized XPS Machine
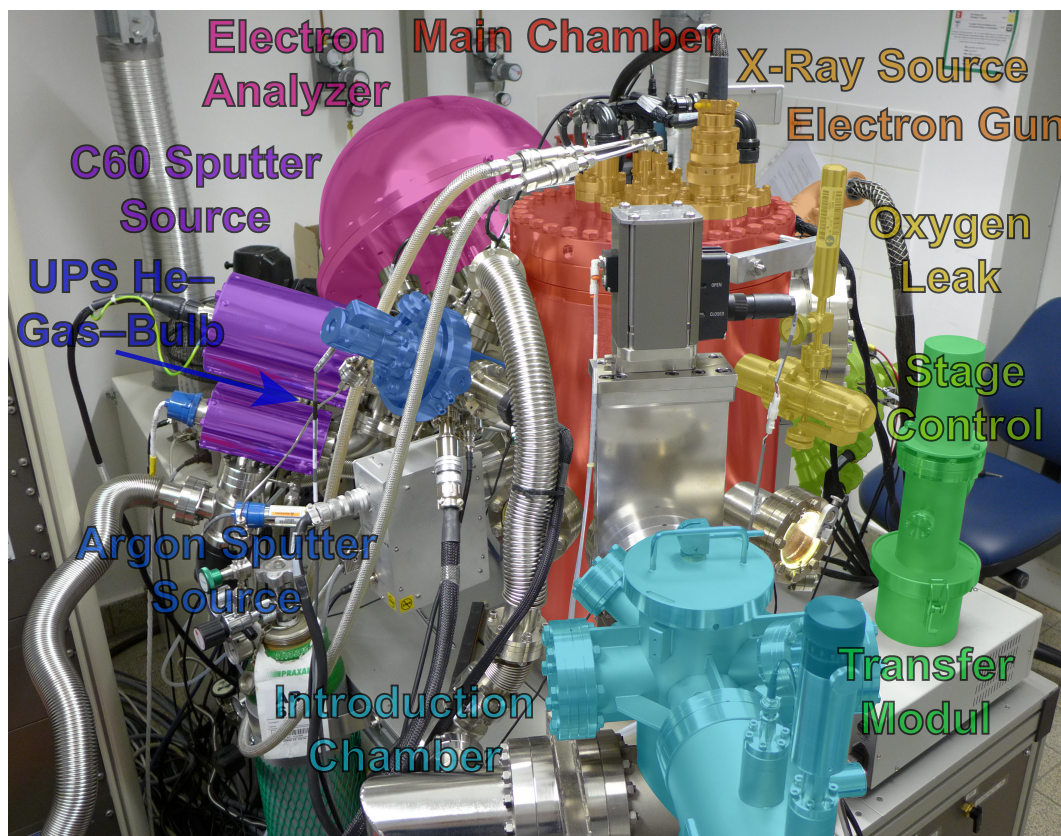
Figure 3.4.: The utilized XPS machine, PHI Versaprobe 5000 I, consisted of a laterally-resolving aluminum X-ray tube and a semi-hemispheric electron analyzer that were connected to the analysis chamber or main chamber. Beyond that, the machine featured different installations like argon and C_{60} sputter sources for depth profiling, a helium-gas-bulb for the UPS analysis of surface valence states, an oxygen leak primarily for the refreshment of the ion getter pump beneath the machine, and an electron gun for Auger spectroscopy and SEM pictures. The transfer module for the sealed transportation of samples from the glove box to the machine is also depicted on the right side.

The utilized *PHI Versaprobe 5000 I* XPS machine is depicted in figure 3.4. As special feature, it utilizes a focused X-ray beam with a lateral resolution below 10 µm. To achieve this lateral resolution, the electron beam is scanned over the aluminum

anode which generates a focused X-ray beam in the X-ray tube. This leads to a feasible analysis mode, the *high power mode*, for which an electron beam with a high current is scanned over an anode region of $200\,\mu m \times 1400\,\mu m$ rendering a high coherent X-ray photon density that is irradiated onto a similar sample area. This distributes the radiation exposure of the sample and simultaneously averages the surface composition over a great area.

Furthermore, the machine holds an argon and a C_{60} sputter gun for depth profiling of a sample. The argon gun is also used for the neutralization of the samples to neutralize the local negative charges while an electron source neutralize the local positive charges. For this neutralization, both sources are utilized in a low energy mode of $200\,eV$ for argon and several eV for the electrons so that the sample surface is set to a defined potential and the shift in the XPS spectra due to the surface potential remains relatively uniform.

There are several installed devices at the machine which are not utilized for the presentation of the results in this work. For instance, a helium gas bulb is available for UPS analyses of the valence band. Also, an electron gun may be used for SEM images and Auger spectroscopy in the sample investigation as well. Furthermore, the stage mounting the sample can be operated for various kinds of experiments. It can be heated up to $800\,°C$ with a heating current or cooled down to $-150\,°C$ with liquid nitrogen. However, for heating experiments the preservation of the UHV condition needs to be considered. Additionally, four contact measurements of electrochemical cells can be conducted simultaneously inside the analysis camber. All these tools of the machine may be utilized in potential consecutive experiments of this work or have been already used in other current research fields, for example, the alteration of the passivation by changing the temperature or four contact measurements for all-solid-state lithium-sulfur batteries.

In this work, the argon source was exclusively utilized for depth profiling. As the surface was continuously covered by the deposition of carbon during a test measurement of a lithium electrode with the C_{60} source a further application of this source was not considered for the later analysis. Furthermore, the lateral resolution was not exploited for the analysis of the samples due to the enhanced resolution of the complementary SIMS measurements. All measurements were neutralized during the spectra acquisition and the sputtering steps. After the measurements in the XPS machine the data were evaluated with the software CasaXPS.

3.1.4. Peak Coupling in the XPS Data Evaluation

Like every XPS evaluation software, CasaXPS allows the quantification of the elements and the fitting of peaks into the spectral lines. Both these features have already been applied for the investigation of the SEI (compare Ref. [72]). Exceptionally, the software CasaXPS features the possibility of *peak coupling*, a feasible

method of data processing that is applied throughout the whole XPS analyses in this thesis. By this method, the elemental distribution and the fitted peaks are combined and translated into a chemical phase distribution in mole fraction.

For the processing of the data to achieve the phase distribution, every detail spectrum of a single measurement was first selected and converted to one single spectrum by the software function *irregular merge*. Afterwards, the spectral line regions of the original detail spectra had to be set manually into this single spectrum and subsequently the peaks for each chemical element of the corresponding compound were fitted into these regions. Now, within the all-in-one spectrum all fitted peaks could be linked with each other by the application of the following universal formula:

$$\mathrm{PA}_y = \mathrm{PA}_x \cdot \underbrace{\frac{ASF_y \cdot T_y}{ASF_x \cdot T_x} \cdot \frac{\nu_y}{\nu_x}}_{\mathrm{CF}_y^x} \tag{3.4}$$

Here, PA_x is the reference peak area of the fitting component x and PA_y the resulting peak area of the fitting component y. The ASFs of every component are listed parameters taken from the literature (compare Ref. [87]). Furthermore, the transmission function through the analyzer depends on the kinetic energy of the electrons and thus on the peak position. Therefore, the values of the transmission function for the respective components, T_x and T_y, differed by up to $20\,\%$ for the maximum range between lithium and fluorine in this thesis; a factor that could not be neglected. However, if the peak areas of the same spectral line are linked the difference was below $0.01\,\%$. Indeed, this could be neglected but this was not executed due to preservation of consistency and to achieve the highest possible accuracy. Finally, the stoichiometric factors of the components ν_x and ν_y of the regarded compound also had to be taken into account. In conclusion, all factors were summarized to a single *coupling factor* CF_y^x that was applied in the area construction function filed in the CasaXPS software.

For the presented investigations in this thesis, the following routine was applied to the data processing. First, the fitted measurements had to be evaluated without the coupling factors to determine the coupling factors in the first place. Thereby, a special case of equation 3.4 had to be adopted for sulfur in this thesis. When sulfur was applied as reference the coupling factor CF_y^{S2p} included the peak area of both the $\mathrm{p}_{3/2}$ and $\mathrm{p}_{1/2}$ peaks as well as their individual transmission function values. Also, for the reference samples in chapter 4 the coupling factors were applied individually for each measurement while a template of average coupling factors was established for the SEI analysis in chapter 5. For this, every determined coupling factor from all the measurements of every depth profile was taken into account to obtain these average values. The standard deviation of the average values was below $0.01\,\%$ and therefore negligible. After the application, the spectra were fitted once again. By the subsequent evaluation of the fit data new coupling factors were calculated and com-

pared with the previous ones. For huge deviations the coupling factors were applied to the spectra iteratively. If the difference between the new ones and the previous ones became sufficiently low a repeated adjustment of the coupling factors was not reestablished.

After the final application of the coupling factors, still the output data could only be displayed in atomic concentration for each assigned peak, the standard report for XPS measurements. To obtain a phase distribution, the atomic concentrations of each compound were summed up and then divided by the number of atoms in the respective compound. This was sophisticated for the polysulfide compounds for which the average chain length $\overline{n}$ had to be calculated out of the respective sulfur peak areas of S^X and S^* (compare chapter 4.1.1). This calculation is described in equation 3.5. Additionally noted, peaks that could not be assigned to a distinctive compound like hydrocarbons (C-C/C-H) were just taken as measured and could not be divided by their unknown number of atoms in the unknown compound. This usually led to an overestimation of hydrocarbon compounds in the sample.

$$\overline{n} = \frac{2 \cdot \mathrm{PA}_{S^X}}{\mathrm{PA}_{S^*}} + 2 \tag{3.5}$$

At last, the resulting phase distribution was normalized so that all detected phases for a measurement yield $100\,\%$. By this, a graphical representation in mole fraction was finally achieved.

This method can be generalized for every measurement and is particularly feasible for the analysis of multiple chemical components where this reduced graphical representation still yields the integrated important information. The overall error caused by this transformation is assumed to be negligibly low. A disadvantage is the inclusion of peaks that cannot be distinctively assigned to a compound which may result in a misleading or distorted representation.

3.2. Time-of-Flight Secondary Ion Mass Spectrometry

The *Time-of-Fight Secondary Ion Mass Spectrometry (ToF-SIMS)* technique is based on the bombardment of the surface by primary ions, the striking out or sputtering of secondary ions, and a subsequent mass separation by their different flight time. Finally, the ions are detected, counted, and then processed by the computational electronics. A scheme of this alignment is shown in figure 3.5. The method stands out for its high concentration sensitivity with a detection limit for elements and compounds below ppm. Also, the technique is surface sensitive since primarily the top two monolayers contribute to the mass spectra. Besides, the analysis does not rely on the atomic or vibrational states in the analyzed solid material or its crystallinity, however, SIMS is a destructive technique that penetrates into the sample surface by removing the surface atoms. On the other side, this renders the imaging of the composition as depth profile possible.
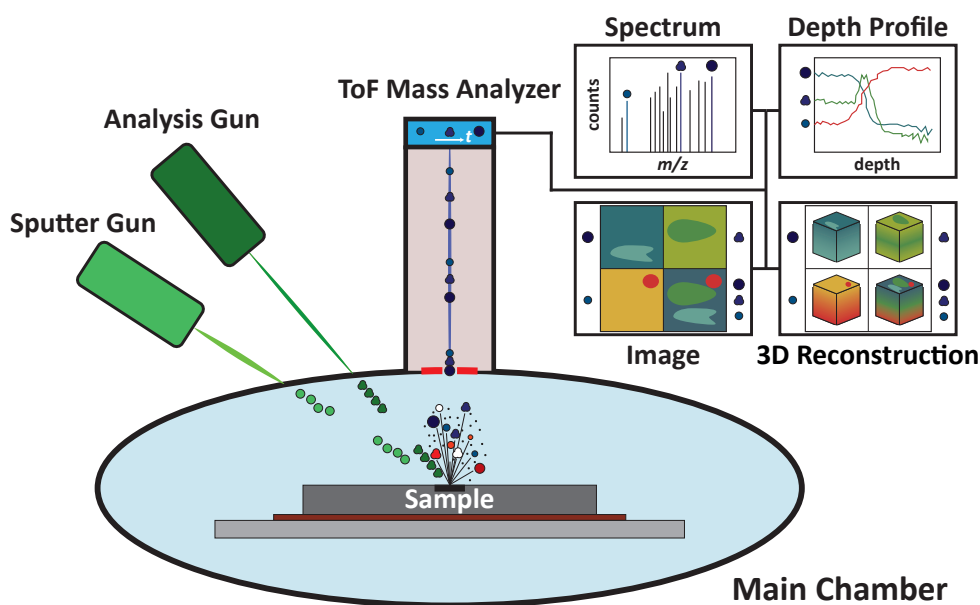
Figure 3.5.: Functionality of the SIMS technique: Primary ions of an analysis or sputter gun are focused on a sample by a voltage in the range of kV. These primary ions strike out surface atoms in a sputtering process. Besides electrons and uncharged neutral atoms, negatively and positively charged atoms and molecules, the secondary ions, are emitted from the sample surface and collected by an extraction voltage. Due to their diverging flight-times through the analyzer, the secondary ions are finally detected and counted on a time scale which can be transformed to a mass/charge scale. The data of the detected intensities can then be plotted as a mass spectrum, a depth profile, an image or a 3D reconstruction.

3.2.1. Methodical Fundamentals - The Matrix Effect

In this subsection, the sputtering process and the formation of secondary ions are explained in a breakdown description. Similar to XPS, the reader is referred to the fundamental literature for the SIMS technique particularly described by Vickerman, Brown, and Reed [89] or Taglauer and Vickerman [86]. Furthermore, Wilson, Stevie, and Maggie [90] summarized fundamental considerations for the depth profiling application of SIMS and also the application of *Relative Sensitivity Factor (RSF)* for the quantification of low concentrations up to ppb in a single phase material which is not feasible for heterogeneous material systems like the SEI layer in this work.

The Sputter Process

The fundamental process of the SIMS technique is the striking out or sputtering of surface ions or ionized molecules by the incident primary ions. Thereby, 95 % of the sputtered ions originate from the top two monolayers which makes the method exceedingly surface sensitive. In general, the energy of the primary ions is chosen in the range of keV so that a *collision cascade* is initiated in the surface region of the sample. Eventually, the energy is transferred to a surface atom that is then stroke out by this cascade. This process supplies the greatest sputtering yield Y, the ratio of sputtered particles divided by the incident primary particles. This is desirable for high secondary ion intensities and, thus, for an improved signal to noise ratio. By changing the angle of the incident primary ions to about 45 to 60° to the surface perpendicular, the sputtering yield is further increased for the collision cascade. For higher energies, the primary ion is widely implanted into the sample surface with a *thermal pulse*. Here, the atoms around the impact trajectory become unbound and collide with each other which leads to a strong mixing effect. Also, these collisions barely lead to a sputtering of surface atoms since less collision energy is transferred in the process (compare section 3.3). Obviously, the primary ions with a low energy barely possess sufficient energy to strike out surface atoms. The *linear cascade* is the lower limit for which surface atoms are sputtered. Here, the collision with the surface atoms propagates linearly through the constituents of the sample surface till it finally strikes out one single atom or molecule.

The Matrix Effect

For the understanding of the SIMS technique, the formation of secondary ions is fundamental since only charged particles are separated by their mass/charge ratio and detected afterwards. As for XPS, the detection depends on the species that is analyzed and sensitivity factors can be introduced to quantify the data. However, this requires the determination of distinct concentrations for each element in a respective homogeneous host material denoted as the *matrix* precluding the straightforward

application of quantification. The basic relation for an intensity of a secondary ion $I^{\pm}(m)$ of species m with a respective charge $+$ or $-$ is given by:

$$I^{\pm}(m) = \underbrace{I_p \cdot T}_{machine} \cdot \underbrace{Y_m \cdot P_m^{\pm} \cdot \theta_m}_{material} \tag{3.6}$$

The first part of this equation indicates a dependency on the utilized machine setup which is given by the applied primary ion current I_p and the transmission function T which generally holds no mass dependence for ToF-SIMS. For the comparison of SIMS data, it should be kept in mind that absolute intensities vary for different machine setups because of both machine parameters. A normalization to a certain intensity that is constant over the depth may improve the comparability. For materials with a layer system, however, the application of a normalization may not be feasible since the intensity of the impurity elements or compounds also depends on the matrix. This leads to a falsified display of most signals.

This relation to the material is expressed by the second part of equation 3.6. Both the sputtering yield Y_m and the ionization probability $P_m^{\pm}$ of the detected mass change with the matrix. While the sputtering yield may only vary about one order of magnitude for different elements, ionization probability varies about several orders of magnitude and significantly depends on the given matrix plus its surface composition. This dependence on the examined material is denoted as the *matrix effect*.

Three models are proposed for the ionization of secondary ions: the *bond breaking model*, the *electron tunnel model* and the *nascent molecular ionization model*. The bond breaking model treats the ionization probability by comparing the ionic character against the covalent character between a sputtered atom and a left-behind surface vacancy. Here, the ionization probability depends on the ionization potential of the sputtered atom and the electron affinity of left-behind vacancy at the surface. The more the difference the merrier is the formation of a secondary ion. As a consequence out of this model, oxygen primary ion sources are applied to increase the ionic character of the surface bonds that in turn increases the detection of positive ions [91]. In contrast, the electron tunnel model explains the probability of an electron to tunnel from the surface, formally reflected by the work function of the material, to the sputtered atom, formally reflected by its ionization potential or electron affinity, or vice versa. This effect is exploited by the utilization of cesium sources which lower the work function and, therefore, increase the tunnel probability of an electron from the surface to a sputtered atom that becomes a negative secondary ion [92]. Asides from this, cesium has a low electronegativity and therefore also increases the ionic character of the surface that attributes to the bond-breaking model analogously increasing the secondary ion yield. The third model, the nascent molecular ionization model, is similar to the bond breaking model but treats sput-

tered clusters, especially metal oxides, which separate due to the different velocity of the oxygen and the metal and then become single ions in the process. This model also emphasizes the application of an oxygen source for the detection of positive ions [93].

An important part of the SIMS technique is the mass separation, however, this varies with the utilized mass analyzer which is now discussed more detailed in the following subsection for a time-of-flight mass analyzer.

3.2.2. General Instrumental Setup of a ToF-SIMS Machine

In general, there are three different types of SIMS machines differing by their mass separation filter: Quadrupole-SIMS, Sector-Field-SIMS, and ToF-SIMS. In this work, a ToF-SIMS machine was utilized that is now described more in detail. However, for a deeper knowledge of all the mechanical components for every kind of SIMS the reader is referred to suitable literature. The ToF-SIMS technique stands out due to its high mass resolution, the quasi-simultaneous detection of all secondary ions' masses, and its low detection limit due to the high transmission of the analyzer.

For ToF-SIMS, the primary ion beam impacts the sample in pulses generated by choppers. This leads to a nearly simultaneous sputtering of the secondary ions in the analysis chamber. The properties of the analysis chamber are comparable with the XPS technique in subsection 3.1.2. After the sputtering process, the secondary ions are accelerated by an electric field to an equally high kinetic energy upon extraction from the sample. Afterwards, these ions can be separated by their flight-time because small particles with a lower mass have a higher velocity than large particles with a greater mass. Also, double-charged particles get twice the energy and, therefore, become as fast as single-charged particles with half the mass. Finally, by plotting the counts of the detected ions against the mass to charge ration m/z a continuous mass spectrum is generated with distinct peaks. The whole procedure from primary ion generation to secondary ion detection takes less than a millisecond and, therefore, fast and detailed spectra, maps and depth profiles can be imaged within a reasonable period of time.

The Ion Sources

The main purposes of the ion sources for a SIMS machine is the supply of a sufficient primary ion current that in turn enables a sufficient secondary ion yield. Basically, the ion sources can be categorized in three different ways: (1) enhancement of the ionization probability for secondary atoms to increase the formation of secondary ions, (2) avoidance of molecular fragmentation, and (3) enhancement of the sample imaging capability. As already discussed in the preceding subsection the utilization of cesium (Cs^+) and oxygen (O_2^+) is common to increase the yield for negative and

positive secondary ions, respectively. Metal ions like Ga^+ and Bi^+ exhibit an improved lateral resolution and cluster ions like Ar_{2500}^+, C_{60}^+, or Bi_3^+ exhibit a reduced fragmentation of surface compounds. In this work, only a cesium (Cs^+) and a bismuth (primarily Bi_3^+) source were utilized and the functionality of these sources are hence briefly summarized.

Primarily, the cesium source belongs into the first category. Within the source, cesium is vaporized by heating, then ionized at an anodic metal surface, and finally accelerated to the sputter-cathode by a high voltage. Depending on the application, this voltage is set appropriately: if the source is utilized as both sputter and analysis source the voltage commonly yields $6 - 20\,kV$ providing elevated sputter rates and secondary ions yields that are necessary for a SIMS machine with a low transmission for the mass analyzer, e.g. a quadrupole mass filter. A lower acceleration potential of about 0.5 to $2\,kV$ is applied when the cesium source is utilized exclusively as a sputter source to smoothly penetrate into the sample. Then, the source is usually applied together with a mass analyzers of a high transmission to yield comparable secondary ion intensities. Furthermore, cesium sources are very bright exhibiting currents of up to microamperes which makes it strongly feasible for the application as sputter source.

For bismuth sources, the metal is first melted and then gets ionized on a thin metal tip, the anode, under a strong electric field. Afterwards, the ions are accelerated to a cathode by a very high voltage of about $25\,kV$. Since the atoms of the liquid are still sticky to each other on the tip, cluster ions like Bi_3^+ and Bi_5^+ are also produced in a reasonable amount for the sample analysis. In contrast to the cesium gun, the bismuth gun is not very bright and currents of around $1\,pA$ for Bi^+ are achieved; cluster ions are even less likely to be generated. However, the higher mass and the higher total kinetic energy of the bismuth sources provide a sufficient secondary ion yield. In addition, the bismuth ions can be focused precisely leading to a lateral resolution down to $100\,nm$. By the application of cluster ions, the fragmentation of large compounds is decreased strongly so that the chemical information about bonding can be conserved moreover. This is especially important for the examination of organic molecules that consist of numerous atoms. The reason for the minor fragmentation is explained by the total kinetic energy of the cluster ion that is split among the single bismuth atoms upon impact on the sample. Thereby, the ion beam induces much less radiation damage to the sample. Furthermore, only one atom of the cluster stays ionized while the residual atoms are neutral resulting in a reduced ionization of sample because neutral atoms have a significant lower ionization capability than charged ions. In conclusion, the bismuth source belongs primarily to the second and third category and, therefore, represents a perfect analysis gun.

Mass Analyzer and Detection

The analysis arm consists of a extraction potential, a mass analyzer, and a detector for the single secondary ions. Whereas a quite low extraction voltage of several hundred volts is applied for Quardupole-SIMS to keep the ions long enough within the analyzer for the mass separation, for ToF-SIMS and Sector-Field the extraction voltage yields several kV because both techniques depend on the coherent kinetic energy of the secondary ions. As the sputtered secondary ions commonly yield kinetic energies of about 10 to 50 eV, a significantly higher potential of several kV achieves a deviation of a few percents for the kinetic energy considering all secondary ions at the entry into the mass separator.

In short, the *quadrupole mass filter* separates masses by a DC voltage overlapped by an AC voltages that are applied between two positive charged rods in the xz-plane and between two negative charged rods in the yz-plane. While the positive charged rods filter out the lower masses, the negative rods filter out the higher masses by electrostatic attraction and repulsion so that only one single mass to charge ration m/z passes through the analyzer. Since the voltages have to be set for every time a desired mass is ought to be detected, this analyzing method is slow and no simultaneous detection of ions is possible. In *sector-field spectrometers*, the ions are separated by passing through a magnetic field. Here, the centripetal force equals the magnetic force $\frac{m\vec{v}^2}{\vec{r}} = ze(\vec{v} \times \vec{B})$ leading to diverging curve radii for different mass to charge ratios. The scanning through the masses is much faster than for a quadrupole because the alteration of the magnetic field is faster and this method also allows utilization of multiple detection channels covering several radii simultaneously.

ToF-SIMS differentiate the mass to charge ratio by the flight-time. Hereby, the kinetic energy equals their electrostatic energy, given by the extraction potential. With $v = \frac{s}{t}$, the basic equation for the flight-time is:

$$t = \sqrt{\frac{ms^2}{2z \cdot eU}} \tag{3.7}$$

where m resembles the mass of the ion, s resembles the length of the analyzer, z resembles the charge of the ion, U resembles the extraction voltage and e the elemental charge. The equation can be trivially solved for m/z to convert the time spectrum into a mass spectrum. In practice, this conversion is conducted by selecting familiar masses in the spectrum as calibration points taking into account that surface charging for different samples may produce a different extraction voltage U; also noted, t is no linear function of U. To have a longer flight time that hence enhances time separation and thereby mass resolution, the ions have to fly through a long column. Furthermore, a ToF-SIMS analyzer usually contains a reflectometer enlarging the flight-length s of the analyzer by a counter-potential that reflects the ions at the top

of the column the way back down to the detector. The reflectometer also effects the ions as a time lens: ions with a slightly higher kinetic energy have to cover a longer distance as they are longer effected by the counter-potential than other sputter ions of slightly lower kinetic energy but of the same mass.

For Quadrupole-SIMS, a *channeltron* is typically utilized as the detector. It consists of a long twisted tube that acts as a photomultiplier for the incident ions. One mass-separated ion hits the high resistance surface within the channeltron tube striking out secondary electrons. Due to the applied potential between the entrance and the end of the tube, the secondary electrons are accelerated to the opposite wall of the tube striking out more tertiary electrons. By repeating the process multiple times, an electron avalanche accrues till the number of electrons are high enough (about 10^8) to be converted into an electronic signal that can be processed by a computer. Sector-Field-SIMS and ToF-SIMS utilize a *multichannel plate* consisting of a single plate with a vast number of micro-channels with radii of 5 to 20 µm acting similar to a channeltron. First, the mass-separated ion hits a high resistance surface striking out secondary electrons. Then, these electrons are multiplied within the channel to a magnitude of about 10^3. Finally, these electrons are detected on a phosphorous screen and converted into an electronic signal. A multichannel plate allows the detection of multiple events at the same time speeding up the measurement time. The refresh rate of such detector is below 1 ns which determines the maximum signals that can be counted. For the case of saturation, the mass peak becomes deformed; such signals are not customary for the interpretation of a measurement.

3.2.3. The Utilized ToF-SIMS Machine

For the analysis of the SEI, a ToF-SIMS machine from Ion ToF™, a ToF.SIMS[5] (see figure 3.6), was utilized in this work. The machine features a bismuth emitter for the analysis, a cesium and an oxygen gun for sputtering, and a C_{60} gun for both applications. To compensate surface charging, the machine provides the reduction of the surface by an oxygen leak valve for strongly insulating samples but since the measured lithium electrodes are considered as very conductive in general this leak was not not utilized; also, the oxygen leak might contaminate the analyzed surfaces unnecessarily.

Instead, an electron flood gun was used for the purpose of surface charge compensation in the case if the SEI might be insulating. The extraction potential was set for negative ion analysis to avoid the saturation and overlap of signals due to lithium Li^+ and its clusters (Li_2^+, Li_3^+, Li_4^+, ect.) that can be facilely ionized as secondary ions in a positive ion spectrum. For enhancing the negative ion yield, the cesium ion gun was utilized for sputtering. Furthermore, the bismuth analysis gun was set to Bi_3^+-clusters to obtain a lower fragmentation of greater molecules like for the conducting salt LiTFSI. The analysis and sputtering with C_{60} was also given a trial,

however, a comprehensive systematic examination had not been pursued due to the loss of lateral information compared to the bismuth gun. This resulted from the lower focusing capability of the C_{60} gun. Also, the C_{60} yielded a much lower sputter rate for inorganic samples .

The standard Ion ToF™ program SurfaceLab 6 was utilized for the evaluation of the recorded data. The software enabled the illustration of the data as mass spectrum. After the calibration of the mass spectrum by referencing characteristic peaks to their actual mass, numerous peaks were annotated with the according species. These peaks were further processed and illustrated as depth profiles, 2D maps that sum up the intensity over the whole depth, and 3D reconstructions. After evaluating all these assigned peaks and their appearance in the illustrations, the number was further confined to peaks with the supposedly highest relevance for the later analysis.

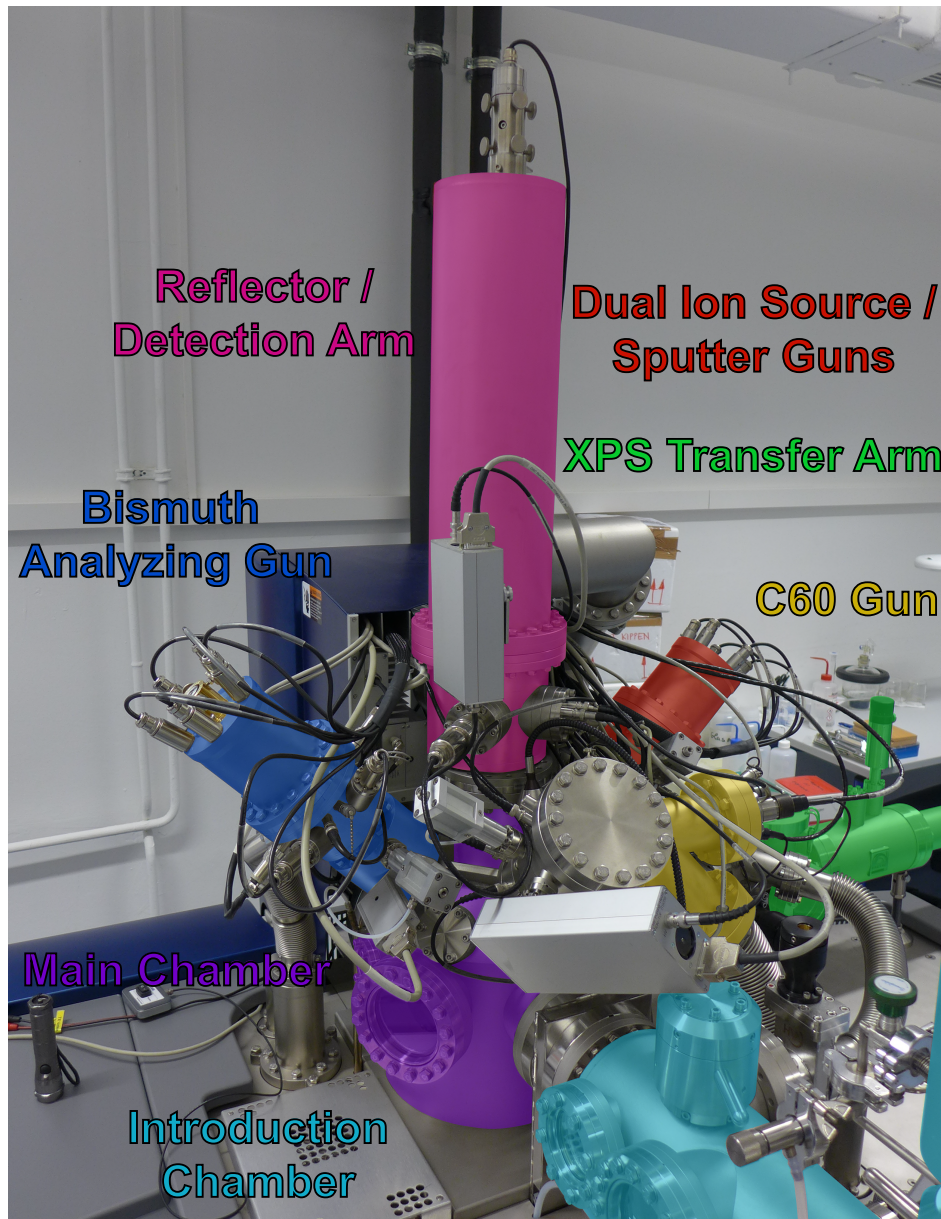Figure 3.6.: The utilized ToF-SIMS machine comprised a bismuth analyzing gun, a C_{60} gun that could be applied for analyzing and sputtering, and a dual ion source, consisting of a cesium and an oxygen gun. In the detection arm with the reflector at the the top, the sputtered ions are separated by their mass per charge ratio according to the required time for their flight through the device.

3.3. Depth Profiling Considerations

In the sputtering process described before, surface atoms are removed from the sample so that a fresh surface is unveiled. This fresh sample surface resembles the composition of a deeper level and can be analyzed again. By this, depth profiles can be obtained penetrating into deeper regions of the bulk. However, there are some differences between the acquired XPS and SIMS depth profiles which are explained in this section. Also, some phenomena contribute to the distortion of the depth profile compared to the intrinsic depth distribution of the constituent. These distorting phenomena include the sputtering of a rough surface, the mixing of atoms in the surface region, radiation damage, and preferential sputtering. These phenomena are described in this section as well and, eventually, the scaling of the depth from the sputter time in seconds to a depth axis in nm is discussed.
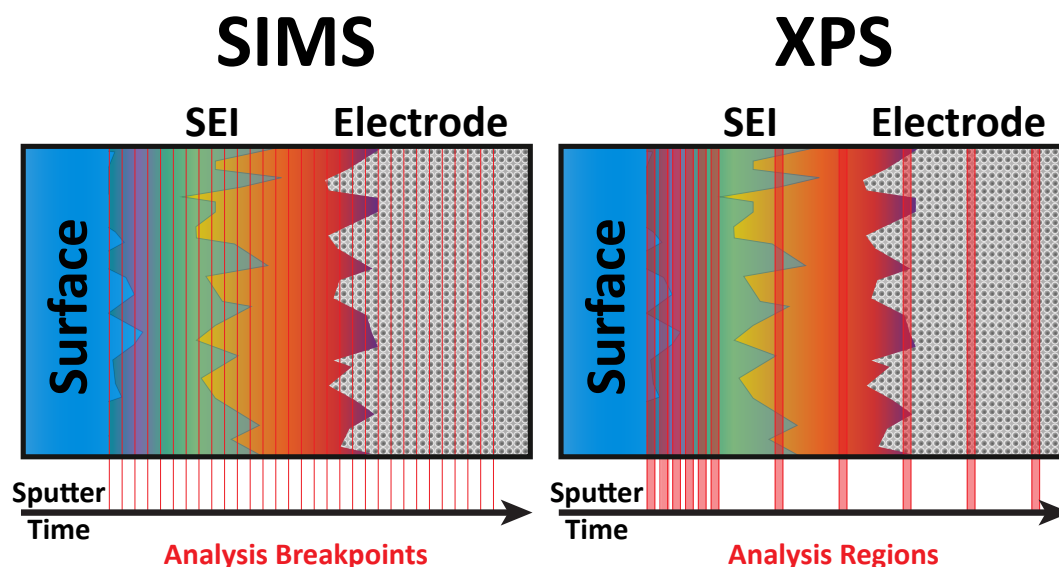
Figure 3.7.: The figure illustrates the different data acquisition of the XPS and SIMS technique. While for SIMS the data is recorded continuously in short intervals providing a high depth resolution, the XPS data has to be recorded in greater intervals since a single examination of the sputtered surface takes significantly more time. Additionally noted, the XPS data originates from the top 10 nm of the surface whereas the SIMS technique investigates the top two monolayers.

Data Acquisition

The data acquisition for both techniques, ToF-SIMS and XPS, is conducted in the way that analysis and sputtering are two separated steps during the depth profiling. While for the SIMS technique the surface is also slightly sputtered during the anal-

ysis, XPS is respected as non-destructive analysis method. However, the sputtering steps for XPS depth profiling can change the surface as well. Therefore, the influence of mixing and radiation damage on depth resolution have to be considered for both methods. Due to the strong difference in acquisition time for the SIMS (several seconds) and XPS analysis (several hours), the more frequent data acquisition for the SIMS technique leads to a significantly higher depth resolution as for the XPS technique considering a reasonable period of time.

Furthermore, the upper 10 nm of the surface are examined during a XPS measurement while the top two monolayers are detected in the SIMS analysis. Therefore, a XPS data acquisition at a certain depth describes the average composition of the next 10 nm and not the actual composition at this depth. On the contrary, the SIMS data resemble the actual depth composition more precisely. These differences in data acquisition are illustrated in figure 3.7 and have to be considered for the respective interpretation of the depth profiles.

Roughness Consideration

Furthermore, the roughness of a sample has a distorting influence particularly on the depth resolution of a SIMS depth profile. At the edges of heights and fissures the sputtering yield changes by the incident angle of the primary ions and, therefore, some regions are sputtered faster than others. Also, the surface tension changes at those areas which also leads to a locally altering sputtering yield.

This has an impact on a layer structure for which signals of an upper layer then may be found in deeper layers as well. Additionally, the interface becomes fuzzy so that the slope of dropping or raising layer-characteristical signals becomes more shallow and hence a distinct interface cannot be observed anymore. Therefore, an assumption of the the interface width, in which the layers mix with each other, is aggravated by the deposition process.

The indicators for a rough surface are the abovementioned smearing of the interface, the appearance of strong lateral intensity fluctuations, and the broadening of peaks in the mass spectrum. The reason for the latter one is explained by different flight times for different surface altitudes (compare equation 3.7). For instance, the sputtered ions of a far lower level of an exceedingly rough sample take more time to get to the detector and, thus, a shift to higher masses in the SIMS spectrum is observed. By this, great altitude differences on the sample can be craved out by the time distribution of a specific mass signals, particularly for particles or features with seize greater than 10 µm. This approach renders the detection of grains or holes and ridges or fissures on a surface possible if a reference signal for the planar is available within the lateral distribution. This method is utilized and described in section 6.2 where a fissure structure is evaluated.

For the XPS analysis, similar considerations may be applied to the analysis of the

data, however, the depth profiling exhibits a significantly lower depth resolution and the lateral resolution is not comparable to the SIMS technique, either. Therefore, the effects on a XPS depth profile are not as traceable as in the SIMS depth profile.

Radiation Damage

The radiation damage is described by the ion-solid interaction comprising the ionization along the incident ion trajectory, the displacement of lattice atoms in the sample, the consequential mixing of the surface region, and the different sputtering yields for different surface components. They are the fundamental distorting processes during sputtering that have an influence on the recorded data.

In the sputtering process, the incident ion dissipates its energy primarily by *nuclear stopping* that is described by a billiard-like thrust which leads to the already mentioned collision cascade. Furthermore, the atoms in the lattice can be excited or ionized by the interaction of their outer shell with the incident ion, denoted as *electronic stopping*, so that reactions in the sample region can be induced.

Briefly mentioned, the electronic stopping is pronounced when an ion holds an elevated kinetic energy which is primarily crucial for the ion implantation into a solid; the electronic stopping is of minor concern for a kinetic energy of several keV during sputtering. Here, the energy of the incident ion is dissipated by around one order of magnitude less for the electronic stopping than for the nuclear stopping, however, a significant change of the surface bonding to thermodynamically more stable compounds may also be induced by this.

Several phenomena may occur by the nuclear stopping. Essentially, the atoms are shifted off a relaxed state in the lattice by the incident ion. This leads to the excitement of phonons or even to the displacement of the trusted atom primarily generating an interstitial atom and a lattice vacancy, a *Frenkel defect*. Thereby, the typical displacement energy for an atom in a lattice amounts about 10 to 50 eV. In the energy range of the incident ions that is suitable for the sputtering process, *Schottky defects* may also occur; there, the generation of a vacancy leads to an attachment of a surface atom. The total number of vacancies created by the incident ion can be approximately calculated by the Kinchin-Pease model or by the later adaptions of this model.

As further consideration of the displacement, the surface region becomes amorphized after a period of sputtering due to changes in the chemical bonding. Additionally, the atoms within the surface region are mixed by their displacements, also into deeper regions of a material. Since some atoms are displaced or sputtered more facile than others due to their bonding and mass, an enrichment of specific species and a diminishment of other species may occur within the top surface layers. This process is denoted as *preferential sputtering* and may lead to falsified results for surface sensitive methods utilizing a sputtering process for the recording of a depth profile.

Both nuclear and electronic deceleration are described formally by the *Thomas-Fermi model* under the assumption that both types of stopping do not interact with each other significantly. The Thomas-Fermi model treads the electrons of an atom as a gas resulting in a screening potential and a screening length of the negative electrons around the positive atomic nucleus. Thereby, this model resembles a simple many-electrons system treatment that does not consider the single electron orbitals, distinct energy states, or the detailed structure of the atomic shell. Indeed, this information is of no concern for a collision event [94][95].

By expanding the model to multiple-collision events with the execution of several approximations and further models like the Kinchin-Pease model, the whole ion-solid interaction of an incident ion and a sample material can be simulated by a software like *Stopping and Rang of Ions in Matter (SRIM; www.srim.org)* utilized to estimated the effects of sputtering on the sample material in this work (see section A.2).

Depth Scaling

To translate the time scale for the data acquisition into a depth scale the sputter rate r_s has to be calculated by considering several individual machine and material parameters. The transformation function is expressed as follows:

$$d(t) = \underbrace{\frac{\frac{I_p}{e} \cdot Y_M \cdot n}{A_p \cdot \rho_M}}_{r_s} \cdot t \tag{3.8}$$

A theoretical approach to determine the sputter rate involves the ion-solid interaction simulation for the electronic and nuclear stopping mentioned above. By this, a value for the sputtering yield Y_M of a material M can be simulated in dependence of the energy and mass of the incident ion, the incident angle, the mass of the sputtered atom, and the density of the sample ρ_M. All the values for these quantities are known or can be approximated appropriately. The machine parameters I_p, n, and A_p are manually set for a measurement and can be altered so that the sputter rate is adjustable at will. In conclusion, all the parameters for the sputter rate are available and the sputter rate can be determined without any additional measurement.

Another, straightforward way to determine the sputter rate is rendered by the determination of the depth for a respective sputter crater subsequently to the actual SIMS or XPS measurement; the sputter rate is then obtained by dividing the depth by the total sputter time of the measurement. However, this approach requires a homogeneous sample during the profiling and an experimental setup to measure the depth which typically requires to sample the surface, for instance by a profilometer or an atomic force microscope (AFM). Due to the sticky and soft nature of lithium and the sensitivity of such sample probes, the determination of the depth is not fea-

sible particularly for rough surfaces. The heterogeneity of the SEI impedes its depth scaling as well. Therefore, these methods are not practical for lithium electrode examinations of battery cells and they can barely be found in literature.

3.4. Sample Preparation and Analysis Settings

In this section, the utilized sample preparation and analysis settings are described for the depicted experiments of the following sections. Thereby, the firstly elaborated preparation for the XPS measurements in the subsequent subsection is alike to the according sample preparation for the SIMS analysis described thereafter.

In general, the sample preparation was conducted in the way that contamination was suppressed as good as possible. During the preparation, a contamination could had originated from leaky vessels like glass bottles for the powders, electrochemical cells, or the transfer modules that all transported the respective samples outside the glove box. Inside the glove box, powder particles and volatile solvents might had been the primary cause for impurities. Another source for contamination might be the leakage of the introduction chamber at the XPS machine because the pumps had to be sealed off before opening the transfer module. On the contrary, the transfer for the SIMS machine module was opened while the turbo molecular pump was still running. During the measurements the residual gas inside the analysis chamber and sputtered particles might had covered the surface. Therefore, the number of presented samples were kept low and the distance between samples was chosen wide on the sample holder. For all measurements, the overall contamination due to external influences were minimized to a sufficient point so that no washing of the sample or cleaning the surface by sputtering was necessary.

3.4.1. Preparations and Settings for the XPS Measurements

The preparation for the examination with the XPS technique was kept uniform for every analyzed sample and was conducted inside a glove box filled with inert argon gas. First of all, double-sided adhesive tape was mounted onto the XPS sample holder. For the reference measurements (chapter 4), a thin indium foil piece was additionally applied on the tape. The powder particles of the different compounds were pressed into the supple foil to fix the powder on an inert substrate. The negative electrodes for the SEI analysis (chapter 5 and chapter 6) were obtained by dismantling the cells within the glove box and then fixating the negative electrodes on the double-sided adhesive tape.

Afterwards, the sample holder was stored inside a tight transfer module and locked out of the glove box. Subsequently, the transfer module was transported to the XPS machine and was mounted on top of the introduction chamber. The introduction chamber was evacuated to a reasonable pressure below 10^{-4} Pa. Then, the introduction chamber was unsealed from the pumping system and the transfer module, still filled with argon, was opened manually. By this, the introduction chamber was flooded with argon. Shortly after, the pumping was initiated once again to evacuate

the introduction chamber a second time. These steps were conducted very quick too prevent contamination due to the leakage of the introduction chamber. After reaching a reasonable pressure below 10^{-5} Pa, the sample holder was transferred from the introduction chamber to the analysis chamber.

Table 3.1.: List of machine parameters for the XPS analysis

Paramters	Reference Measurements	SEI Analysis Measurements
X-ray Setting (Survey Spectra)	200 µm (high power mode)	200 µm (high power mode)
Pass Energy (Survey Spectra)	187 eV	187.85 eV
Energy Step Size (Survey Spectra)	0.8 eV	0.8 eV
X-ray Setting (Detail Spectra)	200 µm (high power mode)	200 µm
Pass Energy (Detail Spectra)	23.5 eV	46.5 eV
Energy Step Size (Detail Spectra)	0.1 eV	0.1 eV
Sputter Energy (Ar⁺)	2 keV	2 keV
Sputter Area	2 x 2 mm²	2 x 2 mm²

For the examination of the samples the machine parameters were also maintained uniform. They are tabulated in table 3.1. At first, all samples were individually measured with a survey spectrum to ensure the absence of unintended impurities. As far as it could be asserted, no elements besides the typical compound constituents were detected. Likewise, strong changes due to the vacuum conditions could be excluded by the survey spectra. Afterwards, detail spectra for the reference measurements (chapter 4) or whole depth profiles for the SEI analysis (chapter 5) were recorded according to the respective analysis objectives. In the reference measurements, the low pass energy achieved a very high energy resolution. In contrast, an ordinary pass energy had to be applied for the SEI layer analysis to yield enough intensity for the diversity of compounds, however, the energy resolution remained excellent. Furthermore, the high power mode of the X-ray tube (compare 3.1.3) enabled an outstanding signal to noise ratio that was enhanced moreover by the application of numerous repeats and the subsequent averaging over all these measurements for the recording of each detail spectra. The sputtering setting was kept equally for the reference samples as well as for the lithium electrodes. The high voltage was chosen to get an improved sputter rate for the SEI analysis resulting in an examination within a reasonable period of time. Both spectra recording and sputtering were conducted with neutralization of the surface by a low energy irradiation of the surface with electrons and argon ions.

3.4.2. Preparations and Settings for the SIMS Measurements

The preparation inside the glove box was similar to the XPS measurements. First, the sample holder was prepared with conductive copper adhesive tape on which the

samples were mounted. Next, the sample holder was stored in the SIMS transfer module and locked out through the antechamber. Thereby, an evacuation was executed for a short period of time because this module was not as tight as the XPS transfer module. By the evacuation, an underpressure was induced inside the module which tightened the module chamber. After the momentary transport to the SIMS machine the module was inserted into the antechamber. As already mentioned the module could be opened while the turbo molecular pump was still running so a quick intrusion into the analysis chamber was possible and accessory contamination of the samples was avoided.

The settings for the SIMS machine were applied at the beginning of a measuring day and then kept for the whole day. First, the cesium gun was heated over an hour to sustain a constant current of about 50 nA. Meanwhile, the bismuth gun was heated just before the general calibration of the machine devices. Thereby, the software settings for the different parts of the machine were loaded and the currents of each gun were optimized at a Faraday cup on the sample holder by settling the apertures within the software. Likewise, the ion beam spot was focused and the screening of the sample was enhanced in uniformity and lateral resolution. Due to the overamplification of the ion yields for positive secondary ions in lithium-dominating samples the analyzer was set for negative ions to avoid or suppress a saturation of the detector. Another reason for this setting was the major interest in anions and their distribution within the electrode surface. The applied machine parameters can be reviewed in table 3.2. Then, the holder was moved to sample position and the height got auto-calibrated. As next step the sample surface was screened, the sputter beam focused to the middle of the screen, and then sputtered with a direct current for some time with a small cubic raster size ($200 - 300 \, \mu m$ edge length). Afterwards, a charge correction was conducted automatically to provide maximal secondary ion intensity for the depth profiling. Eventually, fresh spots on the sample were sought and, hereupon, the actual examination could be started with the typical analysis settings.

Table 3.2.: List of machine parameters for the SIMS analysis

Paramters	Analysis Gun	Sputter Gun
Primary Ion	Bi_3^+	Cs^+
Primary Ion Energy	25 keV	0.5 keV
Primary Ion Current	$0.3 - 0.5$ pA	$40 - 60$ nA
Raster Size	100 x 100 μm^2 / 128 x 128 pixel	500 x 500 μm^2
Sputter Time	–	2 / 5 seconds

3.4.3. Cell Settings of the Cycling Experiments

In chapter 5 and chapter 6, the lithium electrodes of cycled cells are investigated with the XPS and SIMS technique and the resulting data is evaluated. The whole preparation and the cycling of the cells were conducted by Artur Schneider at the Battery and Electrochemistry Laboratory (BELLA) of the Karlsruhe Institute of Technology (KIT). For a consistent evaluation of the data, the cell preparation had to be uniform or without any signification variation. Therefore, the utilized lithium-sulfur cell setup for the systematic investigation of the SEI formation and alteration is described in this subsection and the different cycling behavior are illustrated briefly. The lithium-sulfur cells consisted of a lithium metal foil as negative electrode, an electrolyte with a solvent mixture of DME and DOL (1:1) and a content of $0.325\,\mathrm{M}$ LiTFSI and $0.675\,\mathrm{M}$ LiNO$_3$, a Celgard EK2040 polyethylene separator, and a carbon-sulfur composite electrode as positive electrode. The carbon-sulfur composite consisted of $60\,\%$ sulfur, $17.5\,\%$ Super C65 (Timcal) plus $17.5\,\%$ Printex (Orion), that is $35\,\%$ carbon black, and $5\,\%$ Selvol 425 (Sekisui), a polyvinyl alcohol (PVA) binder. All these components of the positive electrode were dissolved with water to create a slurry which was then coated onto a primed aluminum foil. Thereby, the thickness of the electrode film amounted to $63 \pm 3\,\mathrm{\mu m}$ after a drying process so that a loading of about $2.1\,\mathrm{mg_{sulfur}/cm^2}$ was achieved. Eventually, all the cell components were assembled in a tight pot cell that could be dismantled easily after the cycling.

Concerning the cycling routine, the cells firstly rested for 24 hours and then were cycled with a discharge and charge rate of C/50 (with $1\mathrm{C} = 1672\,\mathrm{mA\,g_{sulfur}^{-1}}$) during the first cycle. Afterwards, the cells were cycled with C/5 for the discharge and C/8 for the charge step. Moreover, the cells rested for 15 minutes after they were charged to $2.5\,\mathrm{V}$ after each cycle; the discharge step terminated at a voltage of $1.7\,\mathrm{V}$.

For the systematic analysis of the the SEI evolution, cells with cycle number of 1, 2, 5, 24, 51, and 90 were analyzed with the XPS and SIMS technique. Up to five cycles, different cells with same cycle number were examined with those techniques, respectively. The investigation of the cell with twenty-three cycles failed for the XPS technique due to machine problems. For the long-term cycling, only one cell with fifty-one and ninety cycles were analyzed in both methods by cutting the electrodes in half.

In table 3.3 and 3.4, the cycling performance is illustrated briefly to give benchmark values of the capacity for the charge and the discharge of the cells with different total cycle numbers. All the cells exhibited a reasonable cycling performance. Notably, the discharge and charge capacity for the last cycle of the cell with fifty-one cycles differed from each other indicating a certain amount of self-discharge capacity at this point that could be retrieved during the charge. For the cell with 90 cycles, a malfunction cycling behavior was observed for the detailed capacity course which is explicitly depicted in figure 3.8. Also noted, the cycling performance of the washed

samples, discussed in chapter 6, exhibited an almost identical cycling performance as the here depicted cells.

Table 3.3.: List of benchmark values for the *discharge capacity* of the cells with different cycle numbers

Discharge	Capacity / mAh g⁻¹					
Sample	1. Cycle	2. Cycle	5. Cycle	24. Cycle	51. Cycle	90. Cycle
1 Cycle	1369					
2 Cycles	1224	967				
5 Cycles	1213	900	894			
24 Cycles	1228	962	962	882		
51 Cycles	1292	974	990	977	480	
90 Cycles	1189	917	919	911	845	781

Table 3.4.: List of benchmark values for the *charge capacity* of the cells with different cycle numbers

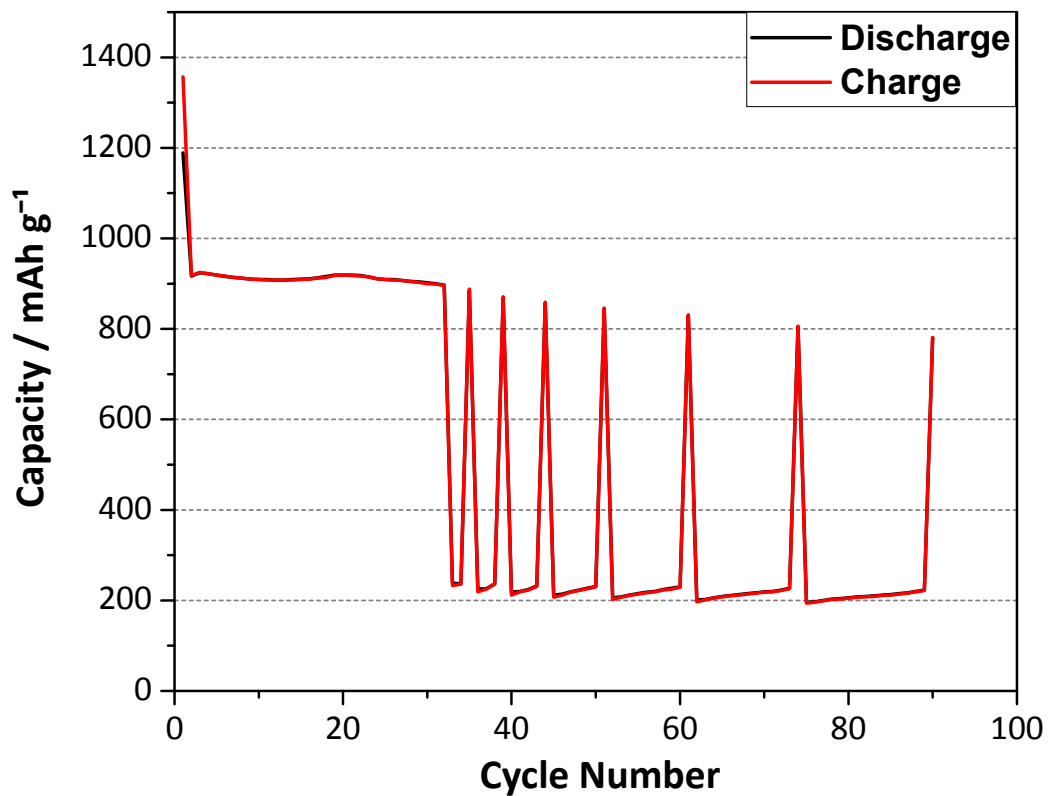| Charge	Capacity / mAh g⁻¹					
Sample	1. Cycle	2. Cycle	5. Cycle	24. Cycle	51. Cycle	90. Cycle
1 Cycle	1491					
2 Cycles	1380	965				
5 Cycles	1401	913	899			
24 Cycles	1388	963	963	880		
51 Cycles	1432	977	989	976	839	
90 Cycles	1357	918	919	911	846	781

Figure 3.8.: The cycling performance of the cell with ninety cycles exhibits a drop to about $240\,\mathrm{mA\,g^{-1}}$ during the 33rd cycle; the cell remained in this low region just above $200\,\mathrm{mA\,g^{-1}}$ besides for some exceptions at the 35th, 39th, 44th, 51st, 61st, 74th, and the 90th cycle.

4. Preliminary XPS Investigation and Consideration

In this chapter typical SEI compounds are investigated prior to the analysis of the cell components. Thereby, a better understanding of these compounds and their sputtering characteristics is achieved for the subsequent SEI analysis. Numerous pristine species were first measured and then irradiated with the argon sputter source to cause comparable damage as the depth profiling measurements of the SEI.

These pre-measurements of pristine substances allowed the precise determination of their peak positions in the respective detail spectra that were later utilized for the compound templates. In these templates, the peak intensities for each respective compound were linked so that the application of a phase distribution instead of the XPS-typical element distribution was feasible (after section 3.4). Later, these templates were applied as one unified and standardized fitting template to all the ex-situ XPS spectra in the depth profiles of the negative electrode. By this, the mole fraction of the phases in the surface region can be illustrated quantitatively.

After the analysis of the pristine samples, a sputtering step was applied to each sample, respectively. Thereby, the samples were irradiated by the argon gun for five minutes. Then, the record of detail spectra was performed with the same parameters as for the pristine samples once again. Eventually, a comprehensive perception of potentially sputter-introduced signals was yielded and, therefore, an insight about the reliability of emerging signals during a depth profile was obtained by these sputter experiments .

In the first section, the results for every examined compound are presented and briefly discussed. In conclusion, a summarizing overview and discussion of all compounds is rendered in the second section.

4.1. Experimental Results

For the analysis of the reference samples the detail spectra of the associated elements were examined for each compound. Furthermore, the detail spectrum of carbon was always utilized for adjusting the sample charging of each measurement. In general, this charge correction of the pristine sample operated satisfactorily by setting the hydrocarbon peak to $284.8\,\mathrm{eV}$ because the surface was usually contaminated with

residual hydrocarbons. After the sputtering process, these carbon species were removed largely so that significant peaks of the pristine sample were additionally utilized as reference position for the charge correction.

This section is further subdivided into the examination of sulfur species that are relevant for the later analysis of the passivation by polysulfide species originating from the positive electrode on the one hand. On the other hand, the investigation of typical surface compounds originating from the reaction of the negative electrode with the electrolyte constituents is described in another subsection. This subdivision is advantageous to clarify general questions for the later SEI analysis.

Every compound examination consecutively comprises the detected sample impurities, the peak positions, the applied peak coupling, the affect of sputtering, and a concluding discussion.

4.1.1. Sulfur Species

The hypothesis for the analysis of the sulfuric species was the clarification of if it is possible to obtain a discrimination criterion in the XPS spectra for the chain length of the polysulfides species and lithium sulfide. If so, how reliable and accurate is this criteria for the later examination of the negative electrodes in which the SEI layer might consists of either rather oxidized, long polysulfide chains or tend to contain lithium sulfide, the reduced product of those polysulfide chains. For this, the compounds lithium sulfide, lithium tetrasulfide, and lithium sulfate were examined assuming them to be characteristic compounds for the SEI analysis.

Lithium Sulfide

The lithium sulfide (Li_2S) powder was synthesized by David Westfal from the working group of Prof. Dr. Bensch at the Christian-Albrechts-Universität in Kiel. In the synthesis, elemental lithium and sulfur were stoichiometrically dissolved in ammonia and, subsequently, the formed product just dried out of the brine. Finally, the product was transported in a sealed case till it reached the glove box in Gießen where it was opened without getting into contact with air.

As it can be seen in figure 4.1, the sample exhibited a small amount of impurities labeled *Imp* at a binding energy of about $166.5\,\mathrm{eV}$ for the $S\,2p_{3/2}$ that can be attributed to thiols or sulfur-oxygen compounds. Furthermore, polysulfides were found at the surface, characterized by the terminal sulfur Li-S*-S and the bridging sulfur S-S^X-S of a polysulfide chain (for a detail discussion see the following paragraph on page 73). The ratio of the amount of lithium sulfide to the amount of polysulfides is graphically depicted in the Li 1s spectrum and yielded approximately $8.5:1$. The polysulfides might originated from the synthesis or from the oxidation of lithium sulfide due to the reaction with atmospheric species.

In the spectra, lithium sulfide could be clearly distinguished from other sulfuric species because of the chemical shift for lithium sulfide to a very low binding energy of 160.2 eV for the sulfur and 54.4 eV for the lithium component. The peaks for the polysulfides were examined at higher binding energies for both Li 1s and S 2p spectra.
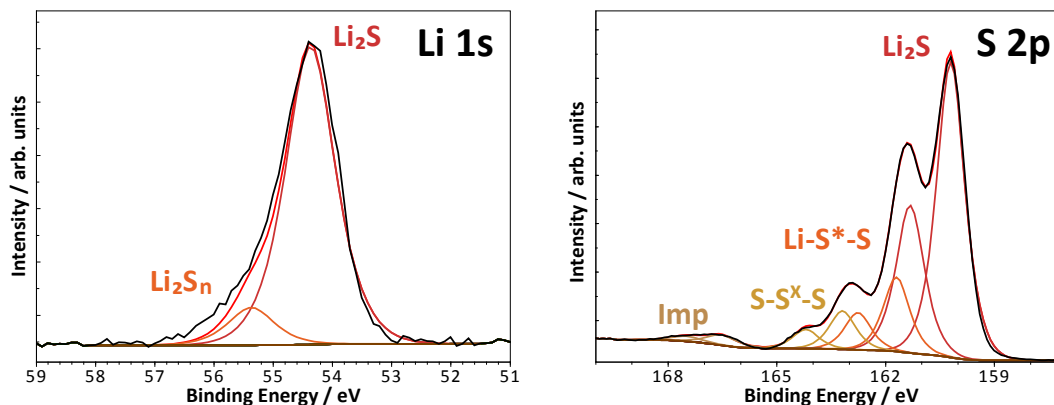

Figure 4.1.: The depicted Li 1s and S 2p spectra of the pristine lithium sulfide sample reveal a small amount of impurities and polysulfide species Li_2S_n.

For lithium sulfide, the attributed lithium intensity was referenced to the respective sulfur intensity by equation 3.4; a similar coupling was applied between the lithium and the terminal sulfur for the polysulfide content. The slightly lacking intensity of the fit at about 56 eV in the Li 1s spectrum could presumably be attributed to the already mentioned surface contamination which was not further linked in the spectra. After the sputtering of the sample, the impurity concentration vanished completely in the S 2p spetrum (see figure 4.2) as, by now, the fit suited perfectly to the spectrum in the Li 1s line. This indicated that the applied coupling between the peaks operated successfully here and is exceedingly trustworthy. The ratio of lithium sulfide to polysulfides decreased to about 5 : 1 after the sputter step took place. This change could be explained by preferential sputtering since the sputtering yields represented by $Y_{Li} = 4.67\,Li/Ar^+$ (lithium atoms per incident argon ion) and $Y_S = 1.81\,S/Ar^+$ for the utilized machine setup led to a depletion of lithium. The deviation of the sputtering yield from the 2 : 1 ratio was reasonable for the change from a 8.5 : 1 to a 5 : 1 ratio. A more significant change in the ratio would be expected if other effects, for instance the sublimation of species, might have played a role during the measurement.

The peaks for lithium sulfide in the Li 1s and S 2p spectra are found at about 160.2 eV and 54.4 eV binding energy respectively. The impurity concentration is negligible so that the peaks are determined very precisely. The peak positions are in good agreement with the literature [39][96].
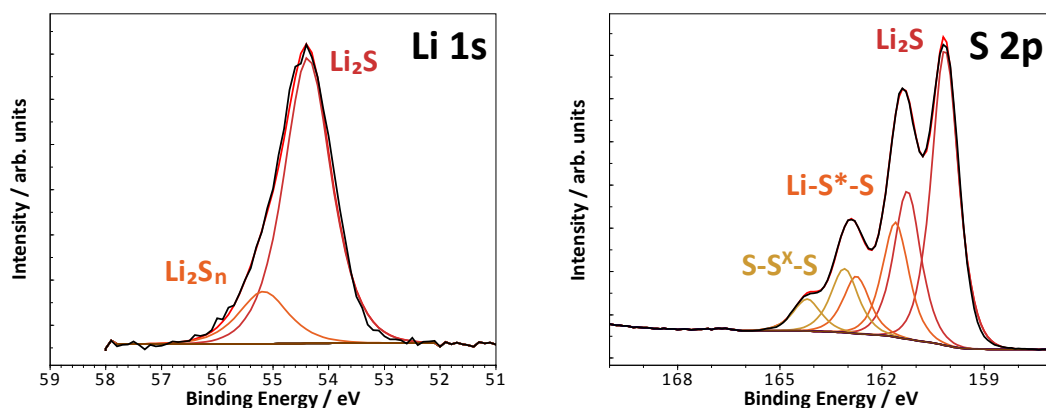
Figure 4.2.: The fits for the Li 1s and S 2p spectra of the sputtered lithium sulfide matched perfectly with the experimental data. Also, the fraction of impurities labeled Imp vanished while the fraction of polysulfides Li_2S_n apperently increases compared to the pristine sample as it can be seen directly by the peak ratio in the Li 1s spectrum.

Lithium sulfide resembles the most reduced lithium-sulfur species within a lithium-sulfur cell which occurs at the positive sulfur electrode for a deep discharge and is also found close to lithium metal electrode due to the migrating sulfur species (compare subsection 2.2.2). To reach the corresponding region of the SEI where lithium sulfide can be found sputtering of the surface is inevitable. The spectra of the sputtered sample (see figure 4.2) reveals that sputtering does not falsify the detection of lithium sulfide significantly despite of the preferential sputtering of lithium. However, it still needs to be clarified if sputtering of the polysulfides or other sulfur-containing species also lead to a considerable formation of lithium sulfide to assure an unambiguous detection of lithium sulfide.

Lithium Tetrasulfide

Lithium tetrasulfide (Li_2S_4) was synthesized by Yuandong Wu (AG Bensch) similar to David Westfal's synthesis of lithium sulifde.

A marginal impurity concentration likewise to the measurement of pristine lithium sulfide was observed for this sample (see figure 4.3). Furthermore, lithium sulfide was present at the sample surface with a considerable amount. Due to the precise measurement of lithium sulfide before, however, the respective lithium sulfide peaks could be calculated off the spectra precisely. By this, the final peak positions of lithium tetrasulfide were measured accurately. As origin for lithium sulfide, side products due to the synthesis, side reactions with atmospheric species, or sublimation of the sulfur into the UHV were considered. The latter case was also reported by Mycroft et al. [97] for elemental sulfur, though, the here observed peaks exhibited no significant loss of sulfur that can be attributed to this sublimation. A very intense hydrocarbon concentration primarily suggested the contamination by atmospheric species, most likely originating from preparation of the samples in the glove box.

Like every polysulfide with a chain length of greater than two, the XPS spectrum of lithium tetrasulfide consisted of one peak for the terminal sulfur (Li-S*-S), bound to one lithium and one sulfur atom, and one peak for the bridging sulfur (S-S^X-S), covalently bound to two neighboring sulfur atoms. The measurement exhibited almost the as expected $2:2$ ratio for terminal to bridging sulfur before the intensities of those peaks were locked to this ratio for the depicted measurement. Thereupon, the peaks for terminal sulfur and bridging sulfur were observed at $161.4\,\mathrm{eV}$ and $162.9\,\mathrm{eV}$ binding energy in the S 2p line and at $55.2\,\mathrm{eV}$ in the Li 1s line.
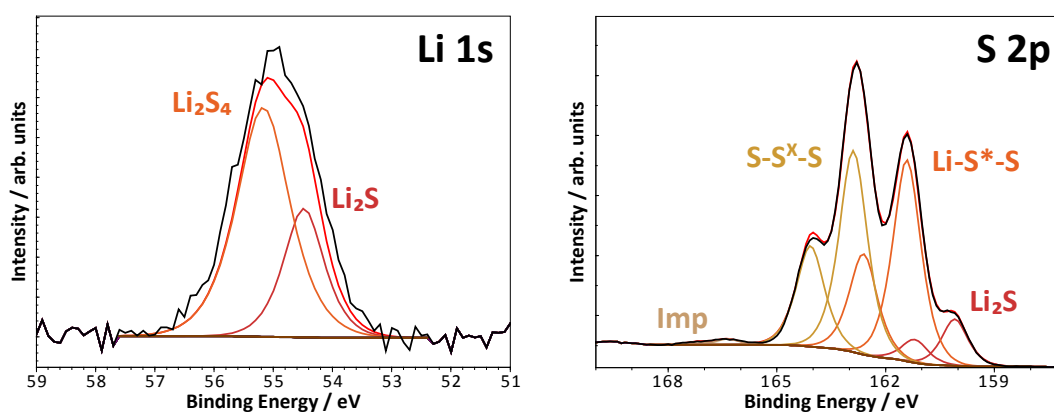

Figure 4.3.: The measurement of the pristine lithium tetrasulfide sample already exhibits a significant amount of lithium sulfide as it can be seen in the Li 1s line. In the S 2p spectrum, the characteristical peaks of terminal sulfur S* and bridging sulfur S^X are visible.

The same coupling as for lithium sulfide was applied for lithium tetrasulfide. To fix the ration of terminal sulfur to bridging sulfur, an additional coupling was added between those components. Like for the analysis of lithium sulfide, the Li 1s fit lacked

some intensity compared to measurement for the pristine sample and, likewise, this intensity gap vanished by sputtering. Similarly, this endorsed the previous assumption about the excellent quality of the peak coupling.
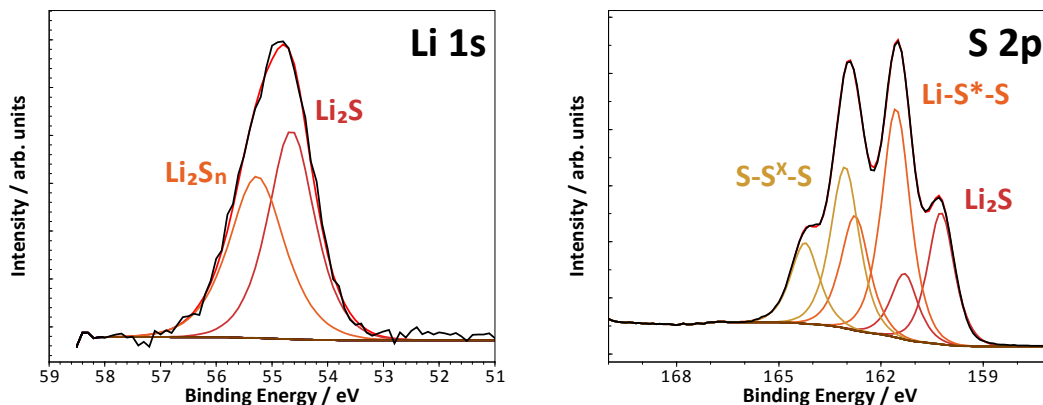

Figure 4.4.: The high amount of the impurity phase lithium sulfide entails in a considerable peak in the Li 1s spectrum. In general, the sputter process leads to an increment in reduced species of lithium tetrasulfide.

Furthermore, the sputtering of the sample led to an increase of the fraction of lithium sulfide and the ratio of terminal to bridging sulfur changed to $7:5$. This alteration of ratio resembled a loss of sulfur and the formation of reduced polysulfides composed of two or three sulfur atoms. This reduction could not only be explained by preferential sputtering since the sputtering yields for lithium and sulfur were represented by $Y_{Li} = 1.96 \, \mathrm{Li/Ar^+}$ and $Y_S = 3.33 \, \mathrm{S/Ar^+}$, respectively, meaning sulfur was sputtered only a little bit less intensively than lithium.

Besides the additional detection of lithium sulfide, the peaks for lithium tetrasulfide are obtained at sharp positions due to the preceding measurement of lithium sulfide. The assignment of the peaks at $161.4 \, \mathrm{eV}$ and $162.9 \, \mathrm{eV}$ in the sulfur S 2p line has been unclear in literature so far. Oei [98] reported the differentiation of terminal and bridging sulfur for the XPS analysis already in 1973, however, at false binding energy positions. Novel investigations of Demir-Cakan et al. [39], Liang et al. [36], and Smart et al. [96] agree more accurately with the strongly emphasized assignment for terminal and bridging sulfur in this work. Other research groups like Su et al. [41] suggest distinct polysulfides (Li_2S_4 and Li_2S_6) at those peak positions or Aurbach et al. [42] and Diao et al. [48][74] assign the peaks with thiosulfate and tetrathionate. However, thiosulfate does not hold a peak for bridging sulfur and, instead, possesses a sulfate peak in the typical region between 168-$170 \, \mathrm{eV}$ (compare the following paragraph on page 76ff). Here, this sulfate peak is not observed in the S 2p line. Furthermore, the terminal sulfur of thiosulfate is presumably detected at a slightly higher binding energy than for the presented peak of the terminal sulfur of lithium tetrasulfide due to the –I effect of the neighboring SO_3 group and comprises a

1:1 ratio to a sulfate peak as well (compare Ref. [36]). Nevertheless, the here asserted peaks for the polysulfide species are measured very accurately despite the lithium sulfide contamination and, therefore, only a significant difference of several $0.1\,\text{eV}$ from the determined peak positions supposedly indicates non-polysulfidic species in the later SEI analysis.

Lithium Sulfate

The here presented analysis of the pristine lithium sulfate was conducted on a powder sample purchased from Sigma-Aldrich. The powder was dried before the introduction into the glove box.

Due to the drying procedure, adsorbed water was barely observed in the O 1s spectrum (see figure 4.5). Also, no other impurities could be accounted for the compound so that the sample was respected as extremely pure and, thus, a particularly accurate analysis could be conducted.
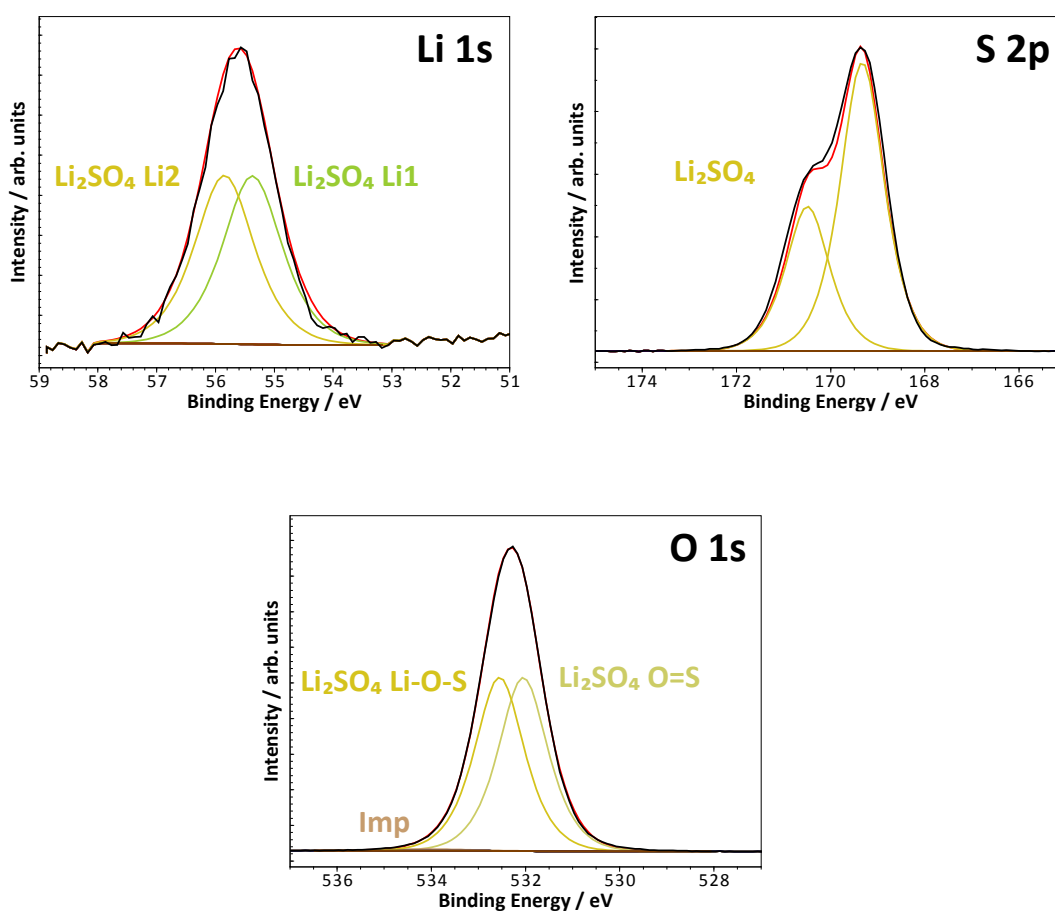

Figure 4.5.: The spectra of pristine lithium sulfate show a perfect fit for each spectral line. While the S 2p line exhibits one single peak the oxygen and lithium line are fitted with two peaks, respectively, indicating two different chemical environments for these components. There is barely any adsorbed water (labeled Imp) observed.

The sulfur S 2p spectrum yielded a peak at 169.3 eV binding energy that resembled a typical sulfate S^{+VI}-peak. Both the lithium Li 1s and the oxygen O 1s spectra were fitted with two peaks, respectively. A first approach with a single-peak fit resulted in unreasonably large FWHMs for both lines. Indeed, a closer look into the crystallographic data for lithium sulfate revealed that the two lithium atoms could

be distinguished (see figure A.1). Also, the separation into two kind of oxygen atoms, probably resembling the Li-O-S and the O = S oxygen bonding within the lithium sulfate molecule, was reasonable and could be explained by the X-ray Diffraction (XRD) data. Thus, this was rendered by the application of two peaks in the O 1s line.

Like for the sulfide species, the sulfur intensity was utilized as reference for the oxygen and lithium peaks of lithium sulfate. This relationship was applied for the peaks of lithium sulfite as well. The pristine sample of lithium sulfate showed an excellent agreement of the fit with the experimentally acquired spectrum. For the sputtered sample, a similar assumption could be made, however, the applied fit became much too sophisticated to resemble a reliable indication for the quality of the established peaks.
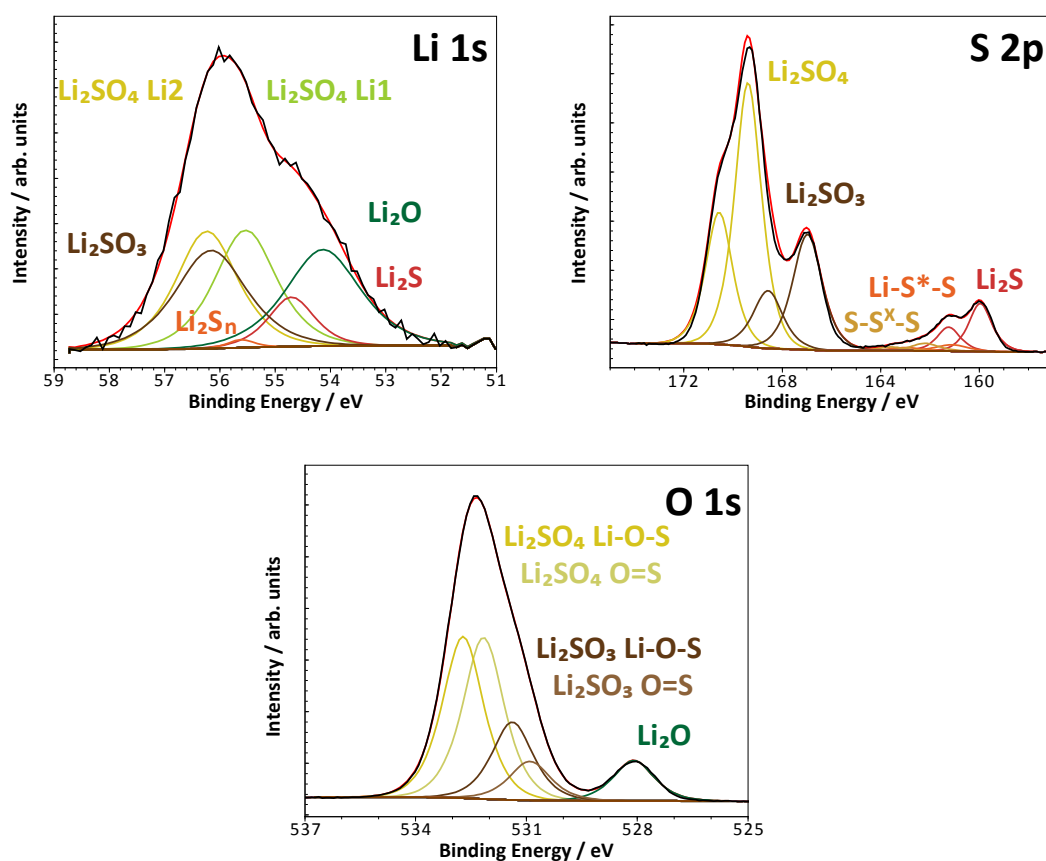

Figure 4.6.: After sputtering, all three spectra exhibit multiple peaks of several new components due to the strong decomposition of lithium sulfate to lithium oxide, lithium sulfite, and sulfide species.

After sputtering, lithium sulfate underwent a vast decay. Despite the still clear visible lithium sulfate peak, sulfite and sulfide species were observed in the S 2p spectrum of the sputtered sample. These species indicated a strong reduction process of the S^{+VI}-sulfur. The simulated sputtering yields $Y_{Li} = 2.47 \, \mathrm{Li/Ar^+}$, $Y_S = 1.01 \, \mathrm{S/Ar^+}$,

and $Y_O = 4.76 \, O/Ar^+$ revealed a preferential sputtering of lithium and oxygen that could explain this transformation due to radiation damage. Also, a loss of oxygen off the compound was traced by the formation of lithium oxide that was fitted with its oxygen intensity as reference for the respective lithium peak. The lithium oxide fit was consistent to other observations of lithium oxide formation particularly depicted in the subsection 4.1.2. Additionally, lithium sulfite was fitted with two oxygen peaks with a 2:1 ratio for Li-O-S to $O = S$. However, due to the absence of crystallographic reference data for lithium sulfite the lithium peak was fitted with a single peak. As it can be seen in figure 4.6, the Li 1s fit became intricate so that a reliable two-peak solution would also not lead to an improvement in accuracy due to an increase of the variance at the same time.

The peaks for lithium sulfate are precisely determined at 169.3 eV in the S 2p line, at 55.3 and 55.9 eV in the Li 1s line, and at 532.1 and 532.6 eV in the O 1s line. If the average of each two-peak solution is calculated, all peaks agree with the assigned peaks of Contarini et al. [99]. They also observed a degradation of lithium sulfate due to sputtering with Ar^+ with an energy of 4 keV and detected similar peaks after sputtering. The here suggested two-peak solution has not been reported in XPS literature yet. The more reliable FWHMs and the crystallographic data are in favor of the presented fit solution.

While the applied lithium sulfite peaks are fitted as reasonable as possible and can be utilized in the later battery component analysis, they are measured as sputtering decomposition product and, therefore, admittedly lack accuracy. Nevertheless, the peak positions of lithium sulfite are likewise in good agreement with Ref. [99], however, the sulfite peaks are not assigned distinctively in this article.

As already mentioned, lithium-sulfur-oxygen compounds may be formed by oxidation of the polysulfides. Then again, this examination of lithium sulfate indicates that lithium polysulfides and lithium sulfide are also formed by sputtering of oxygen-rich sulfur compounds. This leads to the conclusion that the assumed oxidation of sulfur species competes with this reduction due to the sputtering process. Particularly, the oxidation of sulfur species plays an important role for the electrolyte additive lithium nitrate in lithium-sulfur batteries which will be discussed in detail in section 5.2.
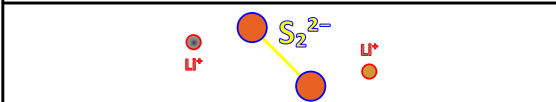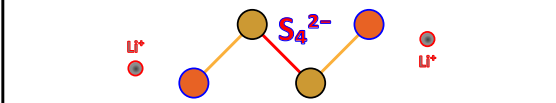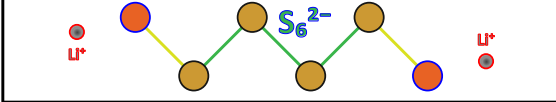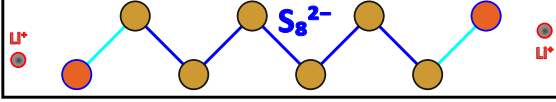
Conclusion - Sulfuric Species

The reported measurements of the sulfuric species yield insight for the following analysis of the negative electrode. Thereby, the determined XPS parameters of the pristine compounds are in good agreement with the literature. The sputtering revealed the appearance of new chemical components for the later SEI analysis and also facilitates the assumption about the influence of the radiation damage.

Sputtering of the sample seems to have a minor influence on lithium sulfide and polysulfides, however, a significant decomposition can be observed for lithium sulfate. As the sputter measurements suggest, the compound lithium sulfide tends to oxidize slightly while lithium tetrasulfide, resembling polysulfides in general, and lithium sulfate tend to get reduced due to sputtering. These trends compete with against each other, however, the degree of reduction for lithium tetrasulfide due to sputtering is greater than degree of oxidation for lithium sulfide. On this account, the fraction of lithium sulfide is presumably overestimated in the XPS depth profiles if oxidized sulfur species are also observed after sputtering.

The ambiguous addressing of the terminal and bridging sulfur peak has to be kept in mind for the later analysis. The appearance of lithium thiosulfate may be realistic if an oxidizing agent was used within the cell, however, the depicted spectra also suggest the assignment of lithium polysulfides and lithium sulfite for the same peaks. This ambiguity remains unsolved in this work, however, the interpretation, assuming lithium polysulfides and lithium sulfite, is regarded as more realistic and will be applied in the further interpretation of the XPS spectra.

Table 4.1.: List of polysulfides and their number of terminal and bridging sulfur

Polysulfide		Terminal Sulfur	Bridging Sulfur
S_2^{2-}		2	0
S_4^{2-}		2	2
S_6^{2-}		2	4
S_8^{2-}		2	6

Nevertheless, the question remains how a spectrum of a negative electrode may be interpreted in terms of the polysulfide chain length analysis. In table 4.1.1 the proposed polysulfides (compare page 7) and their numbers of terminal and bridging sulfur atoms are depicted. As it is already explained in section 3.4, the ratio of terminal to bridging sulfur yields an average chain length and, by this, a general tendency of reduction or oxidation can be determined for the comparison within and between the depth profiles of the different cells. Also noted, the amount of polysulfides is only set by the amount of terminal sulfur. Admittedly, the bridging sulfur cannot be assigned distinctively to the terminal sulfur so that various combinations of the different polysulfides with variable amounts are possible. However, a potential distribution may be assumed under consideration of the measurement systematics and cell chemistry (also compare Ref. [100]). A proposed composition of polysulfides needs to fulfill boundary conditions to be reliable. For instance, reduced sulfur species are more likely to be observed at the positive electrode in a discharged state than in a charged state. Accordingly, the distribution ought to shift to lower polysulfide chain lengths in the spectrum and longer chains shall not be proposed in a significant amount anymore.

A final aspect, but not further pursued in this work, is the observation of peak positions for different polysulfides. For longer chain lengths the charge of the terminal sulfur is supposed to have a smaller effect on the bridging sulfur. Then, the bridging sulfur is supposed to shift to higher binding energies and become more like elemental sulfur oberserved at a binding energy of 164.0 eV [101]. By this, a tendency for the chain length may be derived as well. However, this approach requires highly resolved XPS spectra that cannot not be provided by a conventional XPS machine but my be obtained by synchrotron XPS analysis. Still, a polysulfide distribution or composition for the analysis of the SEI is barely achievable due to the peak overlapping of the close peaks, presumably.

4.1.2. Electrolyte Species

While the sulfur species are of note due to the Polysulfide Shuttle Mechanism (PSSM), the examination of the electrolyte species and their potential decomposition products is fundamental because of their behavior as oxidizing agent and because of the question how the electrolyte decomposes at the negative electrode.
For this reason, typical SEI constituents were analyzed to get a detailed preview for the subsequent battery cell analysis. First, lithium carbonate, lithium methoxide, and lithium ethoxide were examined to get an insight into the solvent decomposition. Secondly, the electrolyte additive lithium nitrate and the salt LiTFSI were investigated. Besides, several secondary references were obtained for the later SEI analysis by these accurate measurements.
All pristine samples in this subsection were purchased from Sigma-Aldrich and heated under medium vacuum conditions before the introduction into the glove box.

Lithium Carbonate
The pristine sample of lithium carbonate exhibited a significant amount of impurity compounds (see figure 4.7). Unfortunately, these impurities were of organic nature. The glove box atmosphere, possibly containing volatile solvent species, was considered as most likely source for this contamination. By this, the surface of the lithium carbonate particles had reacted with these atmospheric species and eventually formed carbonic acid, carboxylic acid, lithium hydride or lithium hydrogen carbonate by a substitution reaction.
As it can be seen in the Li 1s spectrum, lithium carbonate was supposedly the major lithium containing compound in the sample. However, also lithium hydrogen carbonate could be proposed and was presumably the reason for the lack of intensity in this spectra. The reason for the suggested fitting solution with lithium carbonate plus carbonic acid and without lithium hydrogen carbonate was to keep the degree of complexity low for the oxygen O 1s spectrum and, thereby, to decrease the variance of the fitting routine. Like for lithium sulfate, the crystallographic data (see figure A.2) for lithium carbonate show two equivalent oxygen atoms with the same distance to the carbon atom resembling the alkoxide bonding Li-O-C and one atom with a shorter distance resembling the carbonyl bonding $C = O$, respectively. Therefore, two oxygen peaks with a 2:1 ratio were applied for the corresponding alkoxide and carbonyl groups. This ratio was also utilized for carbonic acid observed in the sample. Due to the impurities the fitting was sophisticated and, therefore, not as distinctive as for the previously shown sulfur species. In particular, the difference between the lithium carbonate peak and carbonic acid peak was diminutive in the C 1s spectrum yielding 289.9 eV for lithium carbonate, 289.5 eV for carbonic acid respectively. Likewise, the oxygen peaks within the O 1s line were determined

at 531.7 eV (alkoxide group) and 531.2 eV (carbonyl group) for lithium carbonate close-by of 532.3 eV (hydroxide group) and 531.2 eV (carbonyl group) for carbonic acid.

The intensity coupling between the individual lines, utilizing the carbon signals as reference, worked out satisfactorily besides the lack of intensity in the lithium Li 1s spectrum. As already mentioned, lithium hydrogen carbonate was a negligible, though, potential constituent that might fill in this lack of intensity. By sputtering of the sample, the hydrogen-containing impurities vanished almost completely and the peak coupling enhanced significantly. On the contrary, lithium hydroxide or lithium peroxide and lithium oxide emerged after sputtering resembling good secondary references. For lithium hydroxide/lithium peroxide, the lithium peak was set as the reference for the oxygen peak, whereas for lithium oxide the oxygen peak, which is very distinct in the O 1s detail spectrum (compare figure 4.8), resembled the reference for the lithium peak.
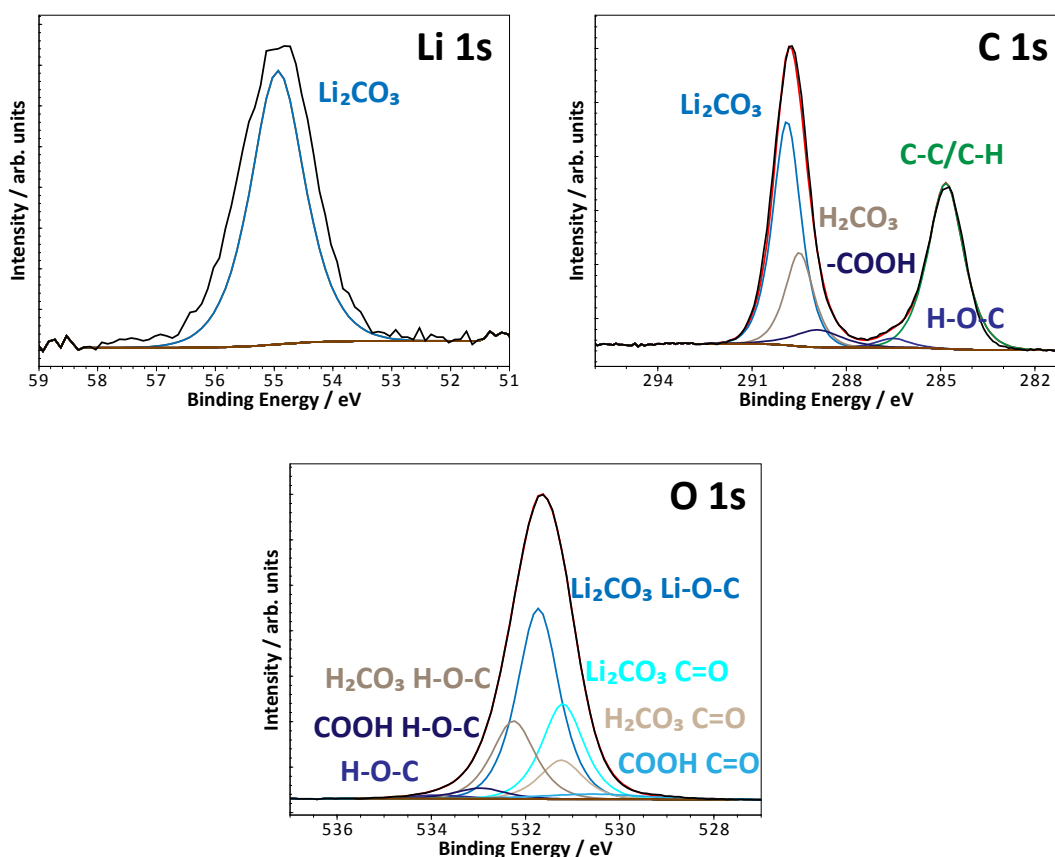

Figure 4.7.: The prestine lithium carbonate sample exhibits a significant amount of hydrogen-containing impurities like carbonic acid, carboxylic acid, alcohols, and hydrocarbons. The lack of intensity in the Li 1s spectrum may be due to the disregard of lithium hydrogen carbonate, presumably.
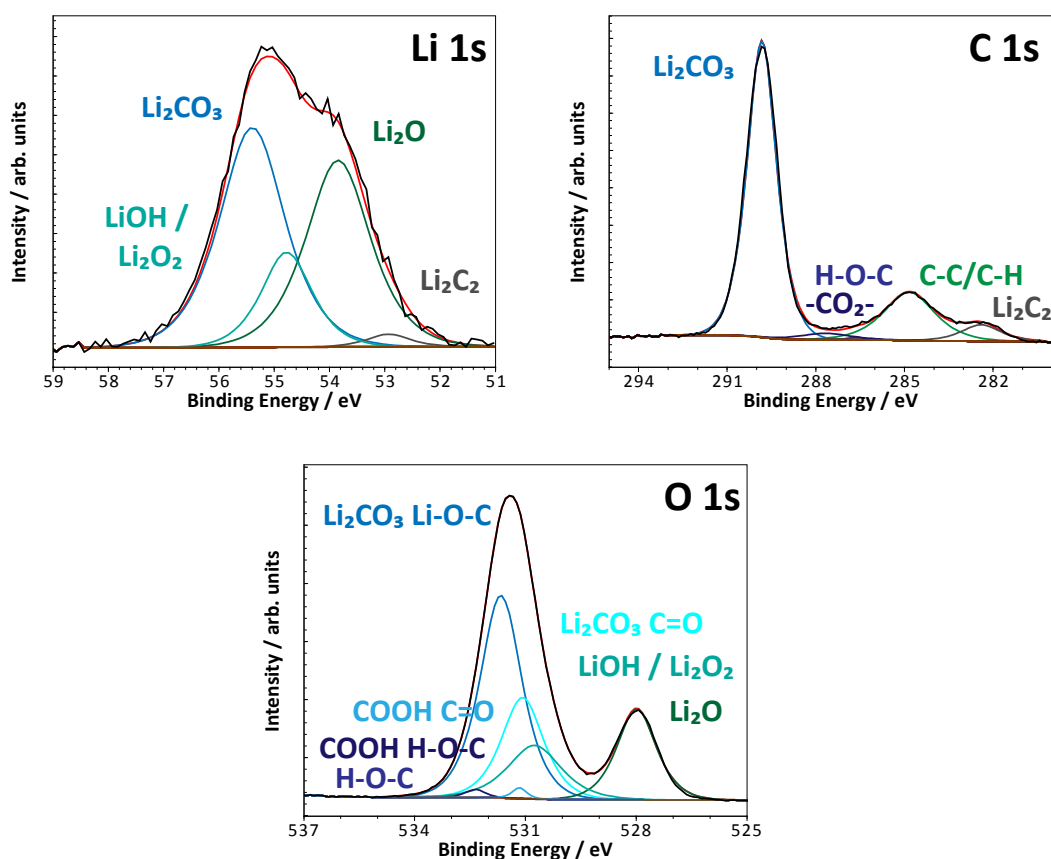
Figure 4.8.: The hydrogen-containing compounds nearly vanish in the detail spectra of the sputtered lithium carbonate sample; lithium peroxide is also more suggested than lithium hydroxide for this sample. On the contrary, reduced compounds like lithium oxide and lithium carbide emerge in the spectra.

Due to sputtering the C 1s spectrum became much clearer for lithium carbonate. The intensity of the impurity phases decreased in this spectrum, however, new phases like lithium carbide were formed by the radiation damage. Further impurity phases were the already mentioned lithium hydroxide/lithium peroxide and lithium oxide as it can be seen in the Li 1s spectrum of figure 4.8. The hydrogen loss was observed for every previously mentioned compound with hydrogen so that alcohol groups or carboxylic acid (-COOH) could not be detected anymore and also the C-C/C-H peak, representing hydrocarbon compounds in general, decreased significantly. A deeper look into the sputtering yields for pure lithium carbonate, $Y_{Li} = 2.86 \, \text{Li/Ar}^+$, $Y_O = 4.03 \, \text{O/Ar}^+$, and $Y_C = 0.52 \, \text{C/Ar}^+$, revealed a potential loss of oxygen and lithium while simultaneously carbon would accumulate at the surface. This might also explain the formation and detection of lithium carbide due to the sputtering process. Furthermore, while the C 1s spectrum became very distinct for lithium carbonate, the impurity phase lithium hydroxide/peroxide contributed to the O 1s

line by a significant amount. In addition, lithium hydroxide/peroxide together with lithium oxide considerably stood out within the Li 1s spectrum. Despite all these new impurity peaks in those spectra after sputtering, the coupling factors and positions of the carbonate peaks were obtained more precisely than for the pristine sample.

The peaks for lithium carbonate are obtained at 289.9 eV in the C 1s line, at 54.9 eV in the Li 1s line, and at 531.7 eV and 531.2 eV in the O 1s line. These results agree with the literature [99][101]; but like for lithium sulfate, the different oxygen binding energies representing the alkoxide and the carbonyl group have not been reported yet. The determination of the secondary references is impeded due to rivaling peaks of other compounds. The sputtering process leads to a reduction of lithium carbonate resulting in the formation of lithium oxide and lithium carbide. Also, lithium hydroxide and lithium peroxide are found at the same peak position [102] in the sputtered sample, however, lithium peroxide is proposed for lithium carbonate due to the lack of hydrogen. Furthermore, the decomposition of lithium carbonate to lithium oxide and carbon dioxide is also proposed in literature [79][99]. Therefore, the detection of lithium oxide would mean a similar formation of carbon dioxide gas and a strong loss of carbon and oxide for the sample which is not supported unambiguously by the elemental quantification (compare table 4.3).

In literature, the appearance of lithium carbonate in the SEI is often assumed to originate form carbonate esters as solvent constituent, and parasitically formed due to atmospheric CO_2 [42]. However, carbonate esters are not utilized in this work and an influence of CO_2 on the later SEI analysis can be excluded. In the following alkoxide examination lithium carbonate is also observed in a small amount as sputtering product. Thus, a careful interpretation of the existence of lithium carbonate is required for a more reliable SEI model.

Lithium Methoxide

Like lithium carbonate the sample of lithium methoxide exhibited a small amount of atmospheric impurities probably originating from volatile solvents or water vapor. The reaction of these species with lithium methoxide possibly entailed the formation of lithium hydroxide, however, only a minor amount could be discovered so that the fit was only slightly biased.
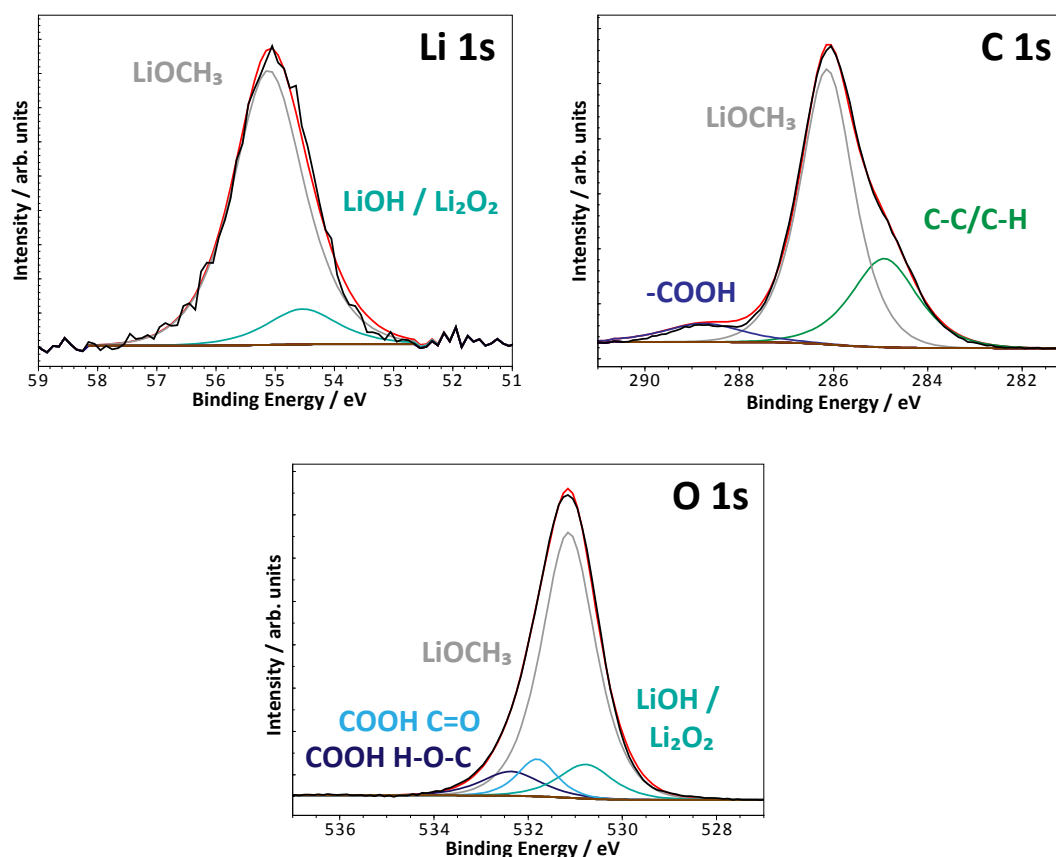

Figure 4.9.: Various compounds are visible in the lithium, carbon, and oxygen spectra of the pristine lithium methoxide sample. Their origin can be explained by the reactions with atmospheric species like volatile solvents or water. Still, the lithium methoxide peak is prevailing in all the three spectra.

Here, the charge correction was difficult because the C-C/C-H peak overlapped with the huge alkoxide peak at 286.1 eV in the C 1s spectrum (see figure 4.9). This position was determined closely to the position of a customary alcohol group. Additionally, the positions of the -COOH, C-C/C-H, and LiOH peaks were considered as references for the charge correction. Still, the applied fit was not unambiguous: the presence of alcohols could be assumed moreover. Then, the lithium methoxide intensity would decrease and lithium hydroxide/lithium peroxide would increase to compensate the lack of intensity in the Li 1s spectrum along with a simultaneous

increment in the O 1s line. Though, the alcohol content in the lithium carbonate measurement (compare figure 4.7) is also negligible low and, due to this, it is not suggested to have an impact on the lithium methoxide analysis as well; therefore, this fit solution was not considered.

The presented fit and peak coupling performed very well, however, this was also due to the assumption of lithium hydroxide/peroxide as constituent at the surface. For the sputtered sample, the fit became complex and, therefore, an assumption about the quality of the peak coupling could barely be appointed for these fits.
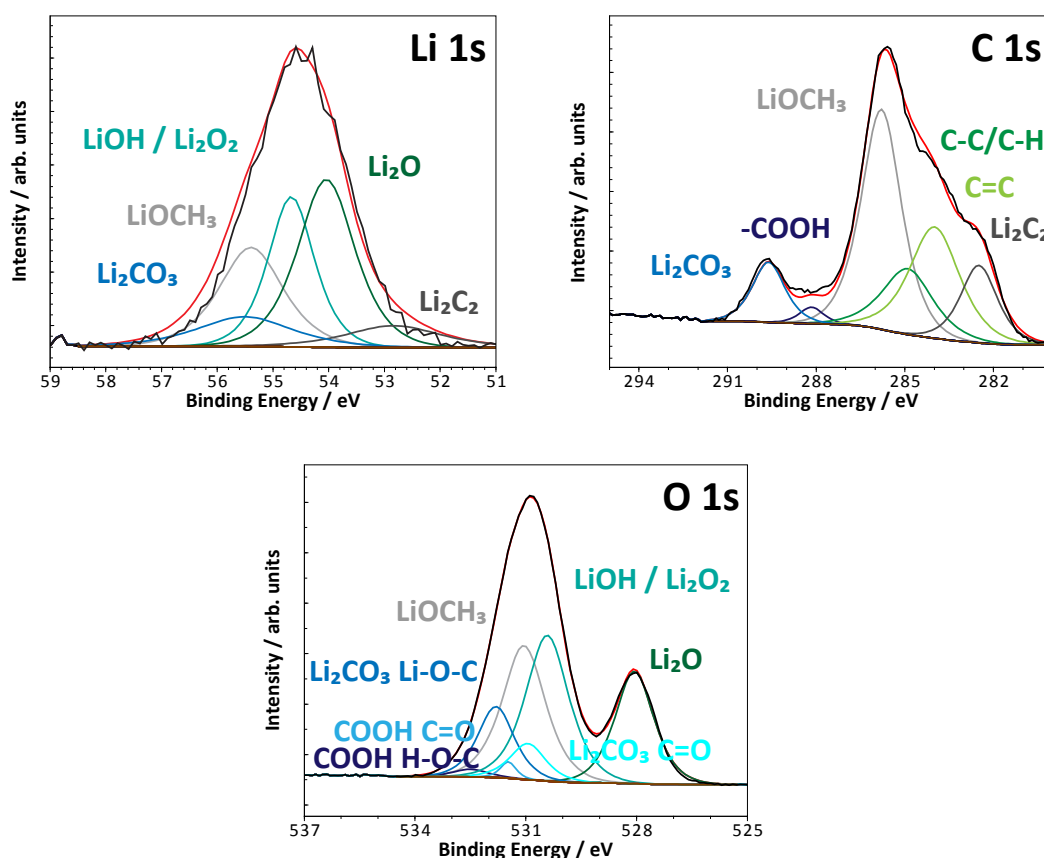

Figure 4.10.: Sputtered lithium methoxide reveals new species that are created by the reduction of the carbon, e.g. lithium carbide, but also by an oxidation process to lithium carbonate.

The sputtering had a huge impact on the sample due to a strong decomposition and a simultaneous surface cleaning of the pristine impurities (see figure 4.10). Due to the decomposition, lithium carbonate, lithium hydroxide/peroxide, lithium oxide, aromatic carbon, and lithium carbide were formed in the sputtering process. Despite the implementation of these constituents, the fit was still not perfect as it can be seen for lithium carbide in the Li 1s spectrum or for the overall match of the C 1s line. Due to the ambiguity between several lithium and hydrogen compounds, already discussed in the paragraph concerning lithium carbonate (compare page 81ff), the fit

might be under-determined. However, the application of additional components was not regarded as reasonable for the reliability of the overall fit. The decomposition of lithium methoxide due to sputtering led to both oxidation (lithium carbonate) and reduction (lithium carbide, aromatic carbon) of the carbon atom. However, the reduction prevailed overall as it can be seen in the spectra.

The peaks for lithium methoxide are determined at 286.1 eV in the C 1s line, at 531.1 eV in the O 1s line, and at 55.1 eV in the Li 1s line. This is in good agreement with the assignment by Malmgren et al. [80] and Stephan et al. [101] for lithium alkoxides (Li-O-R). The fit for the pristine sample exhibits several impurity constituents, however, the prevailing peaks of lithium methoxide are suggested to yield an accurate determination of their corresponding peak positions despite the slightly higher complexity of the fit. By sputtering the sample, new phases like lithium carbonate and lithium oxide appear with a significant contribution to the spectra. Thereby, an oxidation as well as a reduction of the compound takes place, however, the reduction prevails. Indeed, the ambiguous behavior leads to the suggestion that alkoxides may also become oxidizing agents for other species during the sputtering process, maybe for sulfide species as well. The dominance of the reduction process is also rendered by the sputtering yields $Y_{Li} = 0.85 \, \text{Li}/\text{Ar}^+$, $Y_O = 0.74 \, \text{O}/\text{Ar}^+$, and $Y_C = 0.30 \, \text{C}/\text{Ar}^+$, and $Y_H = 2.04 \, \text{H}/\text{Ar}^+$ under consideration of the respective oxidation numbers. Hereby, the loss or gain of electrons was insignificant at first instance due to the charge neutralization of the surface by the machine. Furthermore, for lithium methoxide the formation of lithium hydroxide is more suggested than the formation of lithium peroxide due to the presence of hydrogen in the methyl group. Considering the arguments of the discussion above, the detection of alkoxides in the later battery analysis is particularly intricate due to the ambiguity with alcohols. Likewise, the sputtering-induced alteration of lithium methoxide comprises a vast decomposition. Therefore, the distinct detection of lithium methoxide is rendered impossible, particularly if lithium methoxide does not abound exceedingly in comparison to other SEI constituents.

Lithium Ethoxide

The pristine sample of lithium ethoxide exhibited similar impurities like lithium methoxide, however, the concentration of lithium hydroxide/peroxide was much more intensive, as it can be seen in figure 4.11. The relative amount of carboxylic acid almost remained the same as for lithium methoxide indicating a constant surface contamination. This endorsed the thesis that both alkoxides were very sensitive to atmospheric species and reacted with them at their surface.
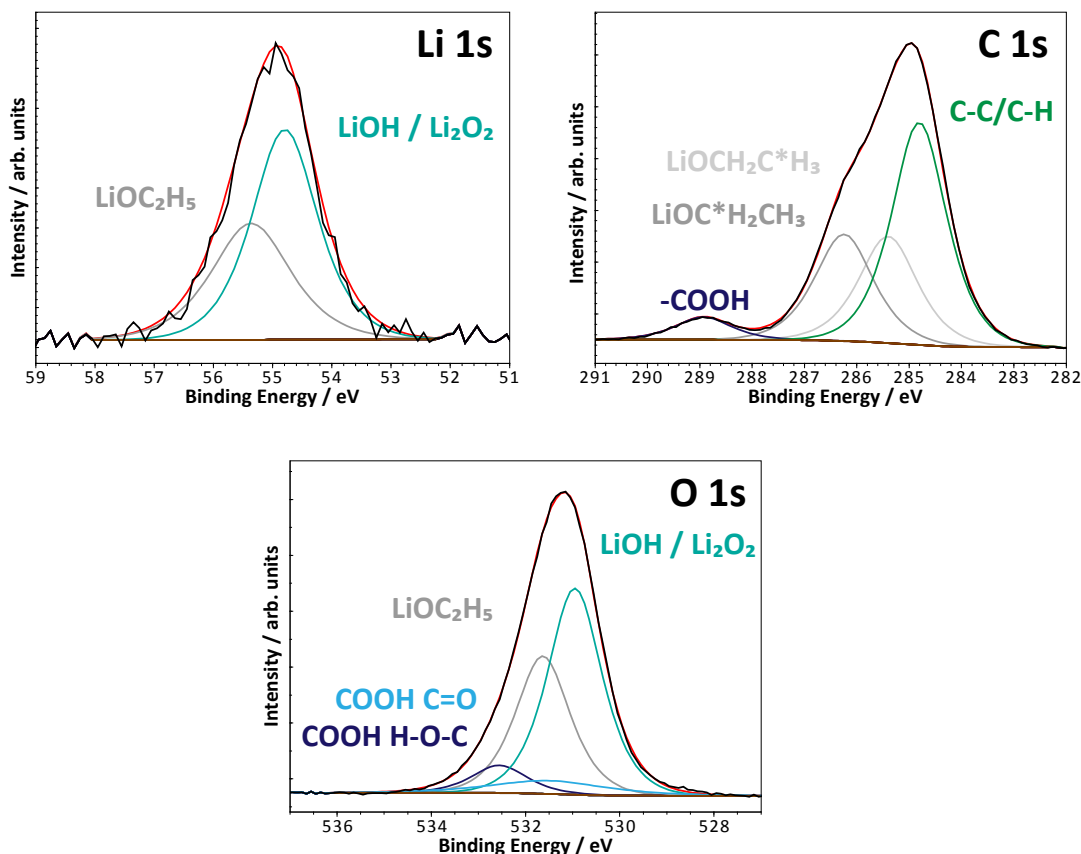

Figure 4.11.: The prisitine sample of lithium ethoxide exhibits similar impurities like for lithium methoxide (compare figure 4.1.2). The methyl group of lithium ethoxide is set by a 1:1 intensity ratio coupling with the alkoxide group.

Again, the application of the charge correction was difficult due to the overlap of peaks in the C 1s spectrum. Particularly, the methyl group of lithium ethoxide overlaps with the C-C/C-H peak which affects the accuracy of the charge correction. A chemical shift to a slightly higher binding energy was applied for the carbon atom of the methyl group due to the negative induction of the alkoxide group on the methyl group. This induction effect was assumed to be approximately $0.3\,\mathrm{eV}$ consulting the capacious data gained by Beamson and Briggs [103] for various polymers. The peaks of the methyl group and the alkoxide group were linked in the way that they ex-

hibited an equal intensity. The fit might be incomplete, again, since the presence of alcohols was not considered for the fit of lithium ethoxide similar to lithium methoxide.

For lithium ethoxide, the carbon attached with the alkoxide and the methyl group was used as reference signal. Due to the strong surface contamination, no reliable assumption for the quality of the peak coupling could be made despite the perfect match of the fit with the spectra.
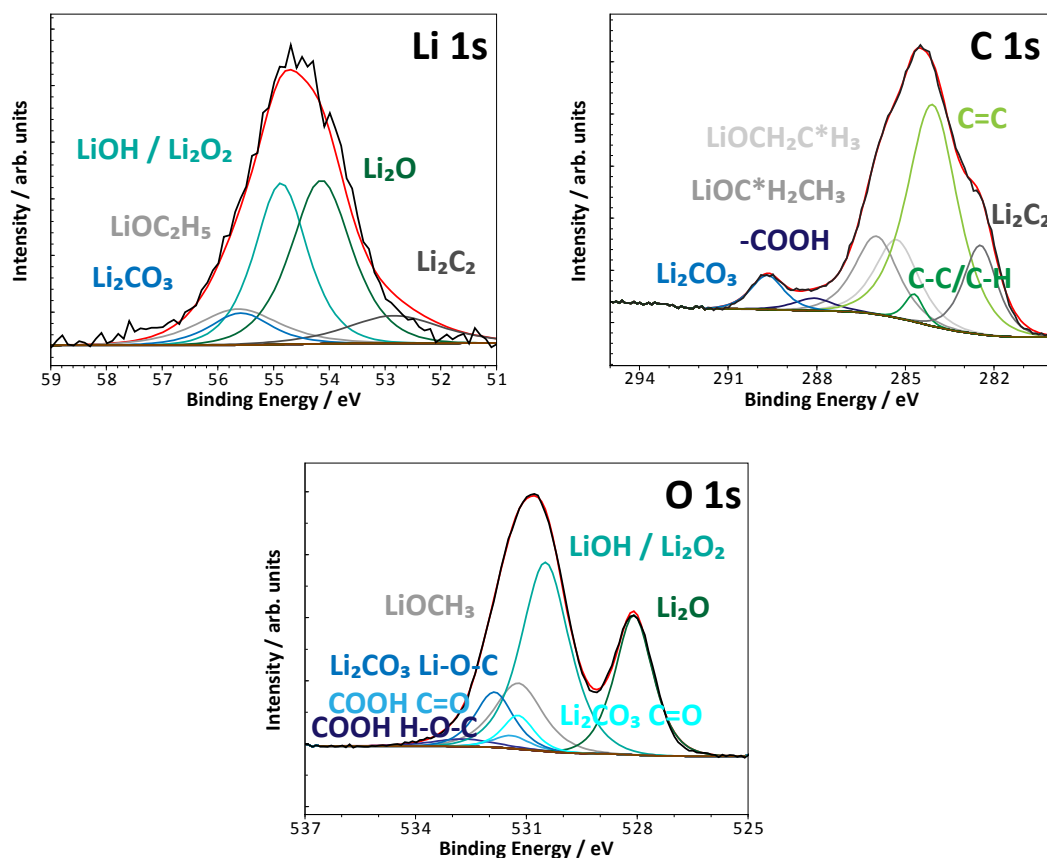

Figure 4.12.: The fractions for lithium hydroxide, lithium oxide, and reduced hydrocarbons prevail in the spectra of the spuittered lithium ethoxide sample. Like for lithium methoxide (compare figure 4.9), a reduction and an oxidation of carbon is observed which leads to the formation of lithium hydroxide and lithium carbonate, respectively.

After sputtering of lithium ethoxide the detail spectra exhibited lithium carbonate, lithium carbide, and lithium oxide in a comparable fraction to the sputtered lithium methoxide sample. On the contrary, the fraction of aromatic carbons increased for lithium ethoxide at the same time.

The peaks for lithium ethoxide are observed at 55.4 eV in the Li 1s line, at 531.7 eV in the O 1s line, and at 286.2 eV (LiOC*H$_2$CH$_3$) or 285.4 eV (LiOCH$_2$C*H$_3$) in the C 1s line, however, the latter one is a restricted value, set according to a referenced value from Beamson and Briggs [103]. Notably, the peak positions are very similar to lithium methoxide. The determined sputtering yields, $Y_{Li} = 0.65$ Li/Ar$^+$, $Y_O = 0.56$ O/Ar$^+$, and $Y_C = 0.43$ C/Ar$^+$, and $Y_H = 2.50$ H/Ar$^+$, render a less pronounced preferential sputtering of hydrogen than for lithium methoxide. However, the higher fraction of aromatic carbon for lithium ethoxide may be explained by the already present carbon-carbon bond that has to be formed for lithium methoxide.

The challenges pointed out for lithium methoxide in the SEI analysis are the same for lithium ethoxide. The higher fraction of lithium hydroxide, which presence is rather presumed than lithium peroxide as for lithium methoxide due to the same reason, in the pristine sample suggests a higher ability to decompose in the presence of other solvent molecules or water. The sputtering step results in the same redox behavior as for lithium methoxide so lithium ethoxide can either behave as an oxidizing or as reduction agent as well. As for lithium methoxide, a reliable detection of lithium ethoxide is rendered impossible for a depth profile.

Lithium Nitrate

The pristine sample of lithium nitrate barely exhibited any impurities (see figure 4.13). A minor fraction of lithium nitrite and an inferior fraction of solvent, adsorbed to the surface of the powder crystals, were detected in the spectra.
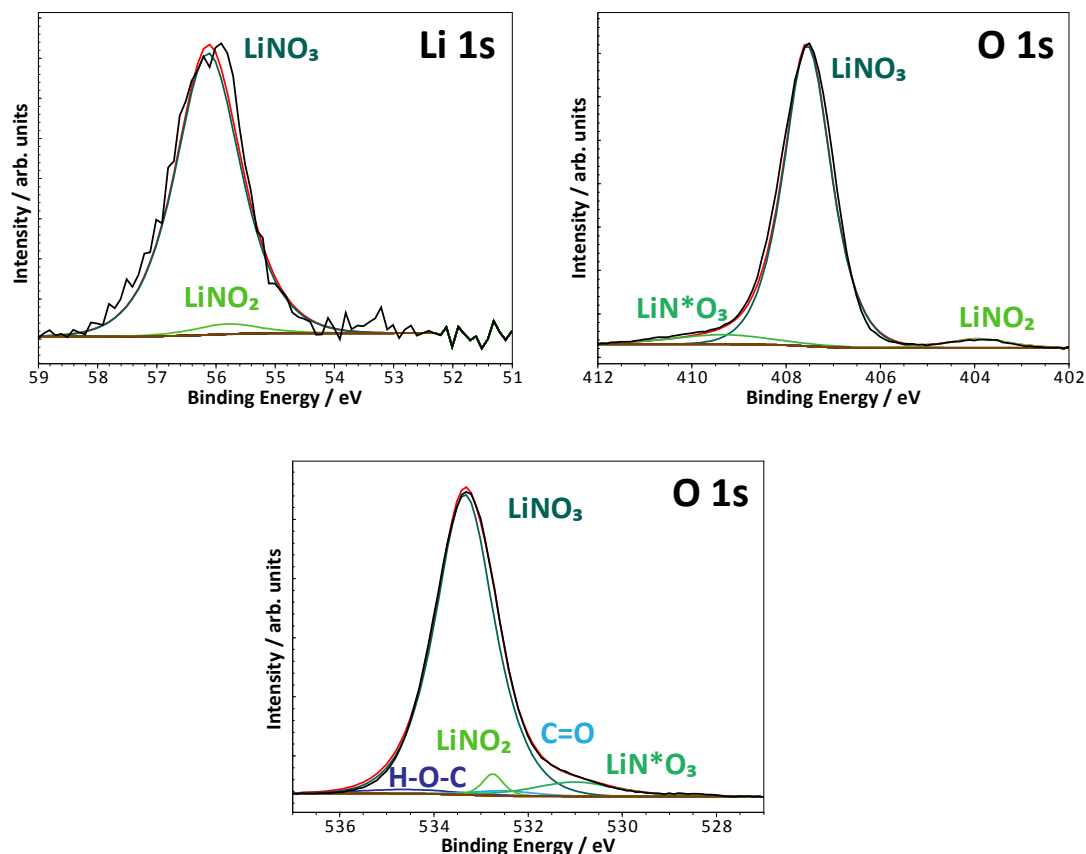

Figure 4.13.: The N 1s spectrum of the pristine lithium nitrate sample reveals three components: lithium nitrate prevails over lithium nitrite and a presumed activation of the lithium nitrate compound that also exists in the sample. Furthermore, a small fraction of carbonaceous impurites is visible in the O 1s line.

The nitrate peak in the N 1s line had a tail aligned to higher binding energies that was assigned without an existing reference. However, it was assumed that the tail was the result of an excited nitrate species labeled LiN*O$_3$ in the spectrum. Also, the O 1s tails out to to a lower binding energy suggesting an excitation of oxygen as well. The tail could also be fitted by applying an asymmetric fit to the elemental components of LiNO$_3$ which is equivalent to the depicted solution in figure 4.13. A differentiation for the oxygen peaks like for lithium sulfate or lithium carbonate was not applied because of the absence of a variation in binding length of the three neighboring oxygen atoms with the centered nitrogen atom in the crystallographic data. Also, lithium nitrate possesses a mesomerism turning all oxygen atoms equal

in the compound. Besides the fitting of the tail, the spectra could be fitted sharply enabling a precise measurement of the peak positions.

The peak coupling offered a precise fitting of the sample spectra utilizing the N 1s peak of lithium nitrate and nitrite as reference. The minor impurity fraction leads to an excellent quality of the applied peak coupling for the pristine sample. By sputtering, the fit of the spectra became difficult and assumptions about the quality of the fit or the applied peak coupling became sophisticated.
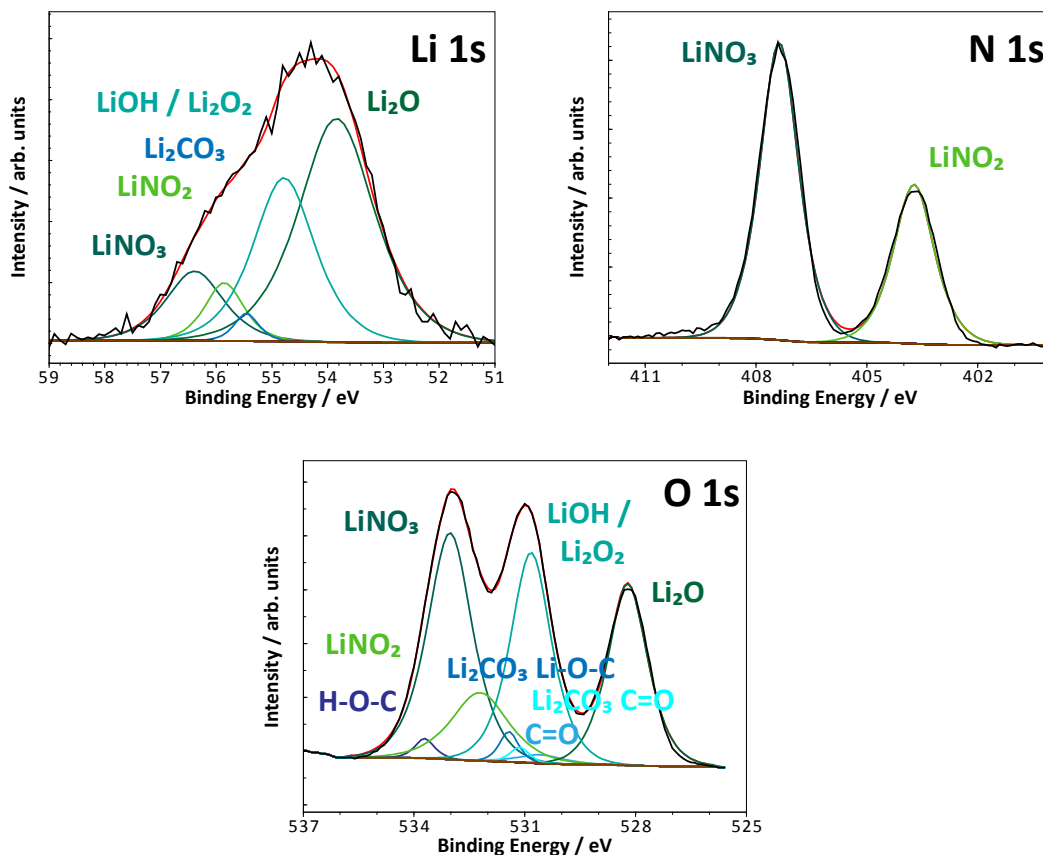

Figure 4.14.: In the spectra of the sputtered lithium nitrate sample various new compounds appear compared to the pristine sample. Besides the impurity compounds lithium carbonate and lithium peroxide, the sputtering decomposition products lithium nitrite and lithium oxide emerge at the surface.

After sputtering, a great amount of the lithium nitrate decomposed to lithium nitrite, lithium oxide and lithium hydroxide/lithium peroxide (compare figure 4.14). Thereby, the 29:1 ratio for lithium nitrate to lithium nitrite changed significantly to a 2:1 ratio. The fractions of lithium oxide and hydroxide/peroxide, illustrated in the Li 1s spectrum of figure 4.14, were large, however, the peak overlap impeded the utilization of secondary reference peak positions slightly in this measurement.

For lithium nitrate, spectral peaks are observed at $56.1\,\text{eV}$ in the Li 1s line, $407.6\,\text{eV}$ in the N 1s line, and at $533.3\,\text{eV}$ in the O 1s line. These results agree well with the results from Aduru et al. [104] that also reveal a vast decomposition of lithium nitrate due to sputtering by Ar^+ ions with an energy of $4\,\text{keV}$. $Y_{Li} = 1.82\,\text{Li/Ar}^+$, $Y_N = 1.73\,\text{N/Ar}^+$, and $Y_O = 5.21\,\text{O/Ar}^+$ are the determined sputtering yields revealing an intense release of oxygen which may also be assisted by volatile nitrogen oxides. For a formation of lithium hydroxide two possibilities are proposed as the hydrogen source: the trapping of residual hydrogen within the UHV and the mixing process of the hydrogen from the hydrocarbons with the lithium nitrate components due to the ion bombardment. Both explanations are not satisfying in view of the high fraction of lithium hydroxide. Thus, the assignment of the peaks with lithium peroxide (Li_2O_2) is probably more reasonable for lithium nitrate (compare Ref. [104]).

Nevertheless, the strong distinction of lithium nitrate and lithium nitrite renders the potential observation of the reduction process for lithium nitrate and simultaneous oxidation of sulfur species possible, however, the sputtering of the sample reveals that lithium nitrate also gets reduced under argon bombardment so that the attribution to a possible redox mechanism within a lithium-sulfur cell may not be unambiguous.
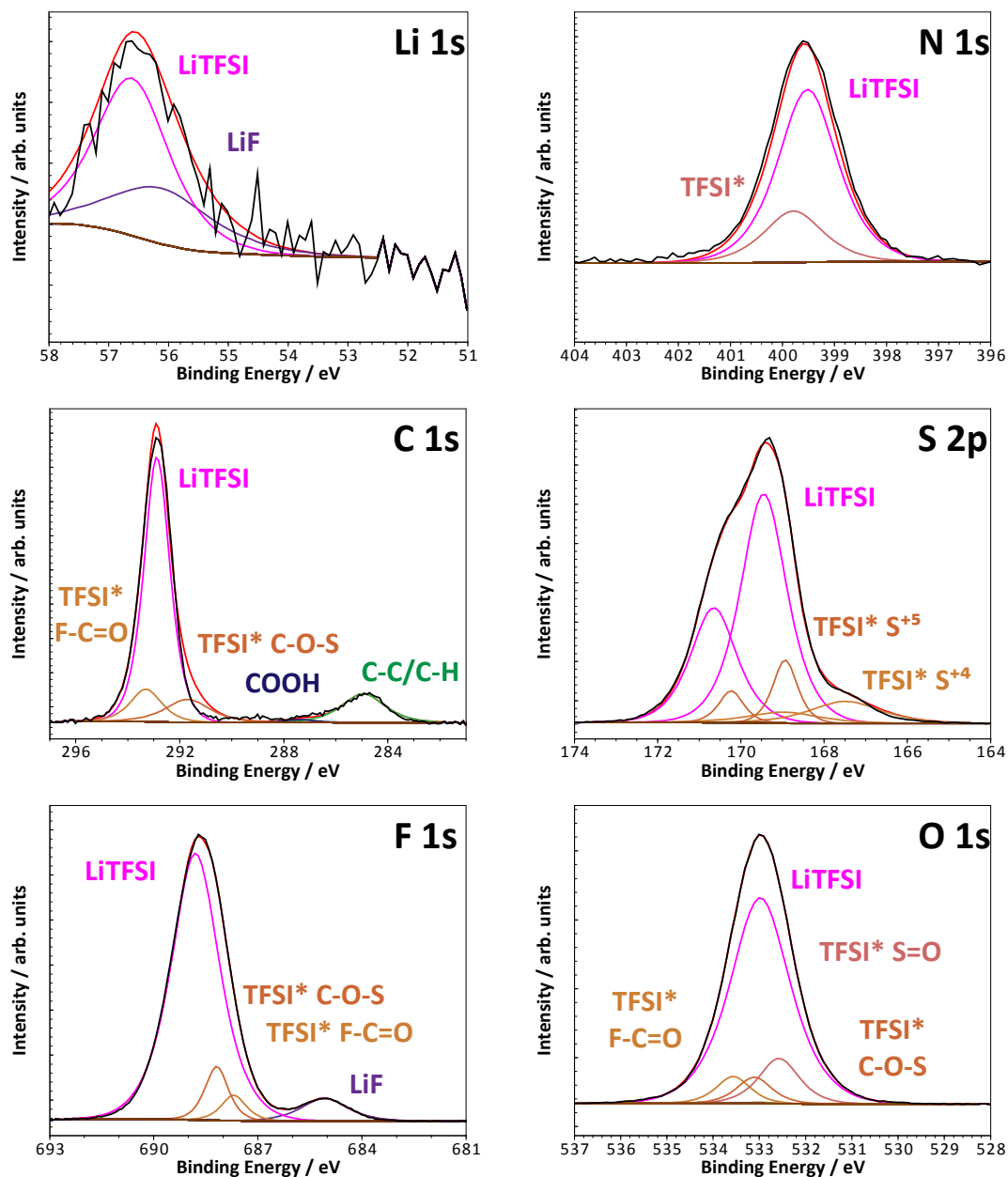
Lithium Bis(trifluoromethylsulfonyl)imide

Figure 4.15.: The spectra of LiTFSI show the decomposition of the pristine sample to lithium fluoride. The proposed pseudo compound TFSI*, which is a neutral molecule, already exhibits an inadequacy in the C 1s line, however, the overall fit matches the experimental data very well despite of this.

At last, Lithium bis(trifluromethylsulfonyl)imide (LiTFSI) was examined. The impurity concentration was hard to judge since LiTFSI decomposed under X-ray irradiation forming a significant surface fraction of lithium fluoride. Also, the LiTFSI powder is strongly hygroscopic and, therefore, surface reaction with water or solvents led to biased spectra, which impeded a precise analysis of LiTFSI.
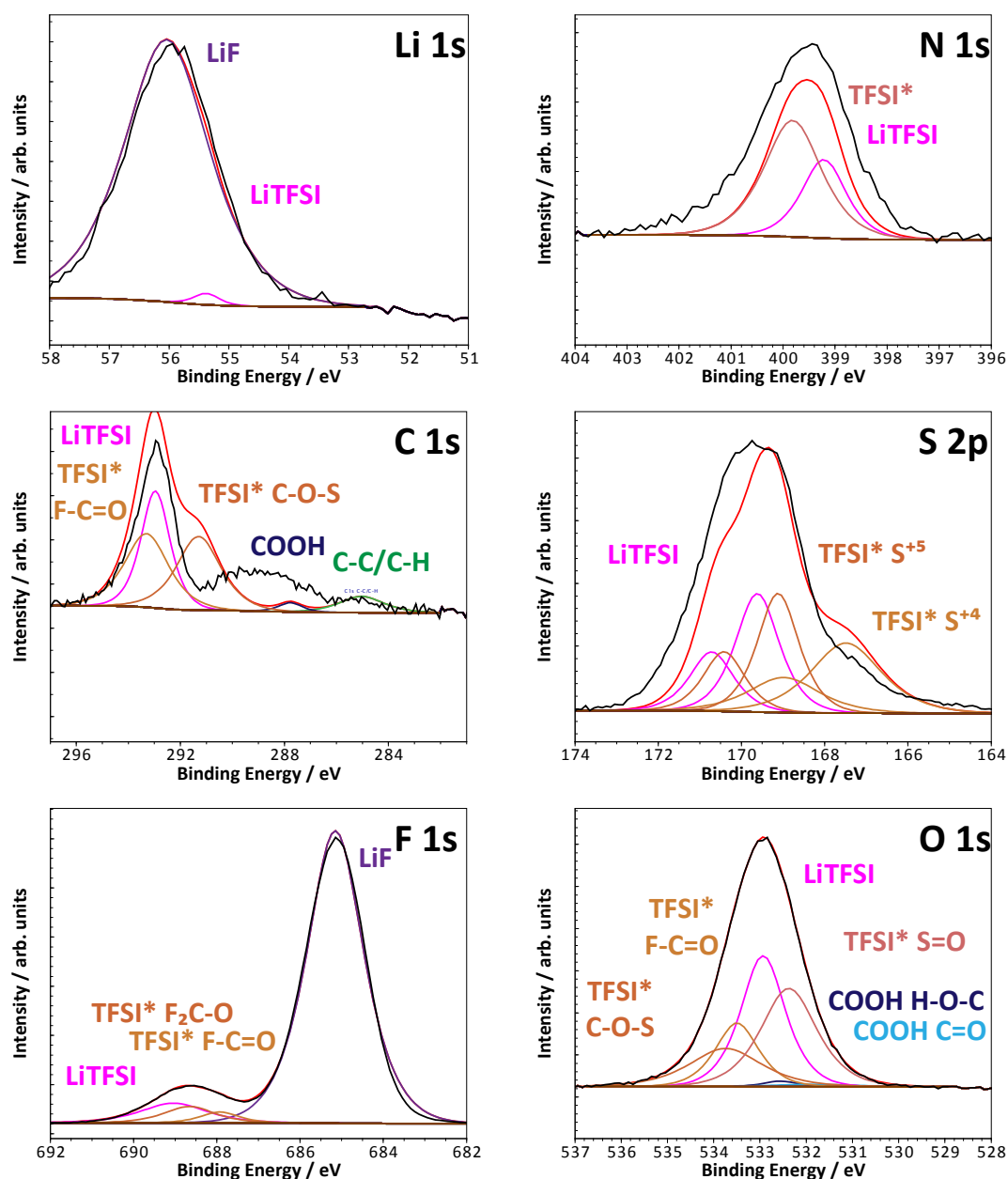
Figure 4.16.: By sputtering, LiTFSI is primarily decomposed to lithium fluoride. Other decomposition products like the proposed pseudo compound TFSI* are also observed, however, their total fraction at the surface is low. Also, the nitrogen, the carbon, and the sulfur spectra suggest more decomposition products than the proposed TFSI* that cannot be identified alone by XPS.

As shown in figure 4.15, an artificially constructed compound labeled with TFSI* was fitted into the spectra and consisted of OFC-S^{+IV}O-N^0-S^{+V}OO$_{epox}$-CF$_2$ components. This hypothetical species was proposed to include all the decomposition products of LiTFSI in a single compound. Several approaches to fit the spectra by other combinations of potential decomposition products with a fixed peak coupling

failed and were as reasonable as the above suggested peaks. For instance, one approach took into account the detected LiTFSI molecule fragments from the SIMS analysis but a suitable fit for the XPS spectra was not obtained as well.

The precise peak coupling for LiTFSI was not successful due to the high fraction of impurities in most spectra. The sulfur S^{+VI} in the sulfonyl group was believed to be most reliable reference for LiTFSI and, therefore, it was utilized as reference for the peak coupling. The TFSI* peaks were also linked with mediocre success and its functional failure as exclusive decomposition product can be seen in the spectra after the sputtering process in figure 4.16.

After the sputtering step, LiTFSI was degraded and lithium fluoride became the prevailing compound as it can be seen in the Li 1s spectrum of figure 4.16. While some spectra like the Li 1s line, the F 1s line, and the O 1s line were well fitted, the remaining lines exhibited a mismatch of the fit curve to the experimental intensity due to under-determination of possible decomposition products on the one hand and overestimation of signals, particularly for the TFSI* components because of the applied peak coupling, on the other hand. In a nutshell, the chemical reaction induced by radiation damage could not be well described.

The LiTFSI molecule consists of all the elementals that are found in the lithium-sulfur cells for the later SEI analysis anyhow, except for fluorine since no fluorine-containing binder was used for the positive electrode. The measured peak positions for the lithium cation at 56.6 eV, the imide group at 399.5 eV, the sulfonyl sulfur at 169.5 eV, the sulfonyl oxygen at 533.0 eV, the trifluoromethyl carbon at 292.9 eV, and the fluorine constituents at 688.8 eV agree with the literature [105]. The artificially combined TFSI* pseudo compound consists of peaks at 399.9 eV (-N-), at 168.9 eV (S^{+V}), at 167.5 eV (S^{+IV}), at 532.6 eV (S=O), at 533.6 eV, 687.7 eV, 293.3 eV (OFC), and at 533.1 eV, 291.7 eV, 688.2 eV ($O_{epox}CF_2$), respectively. However, the contamination of the sample prevents an accurate determination of the peak positions. The strong decomposition of the sample does not allowed to use the XPS as method to detect the conducting salt in deeper regions. By inducing radiation damage, LiTFSI decomposes to lithium fluoride with binding energies at 685.2 eV for the F 1s line and at 56.1 eV for the Li 1s line (comparable with Ref. [80][87][106]) and other degraded products quickly.

This decomposition effect might even be more pronounced in the present of excess lithium at the negative electrode surface. Unfortunately, the peak positions of the decomposition products of LiTFSI appear in the same spectral ranges like LiTFSI itself.

Conclusion - Electrolyte Species

The analysis of the electrolyte salts and of potential reaction products of the solvent with lithium metal discloses many effects for the subsequent SEI analysis. Indeed, the peak position for the examined compounds and for many secondary references are obtained by these measurements, however, the analysis seems to be much more sophisticated than for the sulfur species. Also, the sputtering of the samples has a vast impact on the spectra for all examined species.

As for the sputter analysis of sulfur species a reduction process can generally be expected for all electrolyte species. Lithium carbonate transforms to lithium oxide and various reduced carbonaceous species similar to the examined lithium methoxide and lithium ethoxide. The conducting salt LiTFSI primarily converts to lithium fluoride and the sputtering of lithium nitrate leads to the formation of lithium nitrite and lithium oxide. Lithium hydroxide or lithium peroxide seems to be an impurity found in every compound after sputtering. For the alkoxides a formation of lithium hydroxide may be more realistic while for lithium nitrate and lithium carbonate the presence of lithium peroxide is primarily suggested.

A direct detection of lithium alkoxides and also LiTFSI is rendered impossible due to their decomposition. At least, the decomposition products of LiTFSI, particularly lithium fluoride, may give a hint on its occurrence. Indeed, lithium carbonate and lithium nitrate also lead to a huge fraction of decomposition products at the surface, however, their peaks are distinctive, and together with their decomposition products the pristine compound can be traced back. Lithium carbonate itself may also be formed by the sputtering of lithium alkoxides; this formation occurs by the reaction of alkoxides with carbon dioxide to lithium alkyl carbonats or by the reaction of lithium oxide with carbon dioxide to lithium carbonate [67]. The ambiguity of those products may only be solved by considering other signals as well, however, this seems to be sophisticated as well.

The lithium oxide formation of the lithium alkoxides, lithium carbonate, and lithium nitrate suggest an oxygen-releasing behavior so that they may account for an oxidizing agent within the SEI depth profile. Under these oxygen-enriched conditions, the hydrogen within the hydrocarbons may primarily lead to the formation of lithium hydroxide during the examination of the negative electrode, however, a partial formation of lithium peroxide may also be considered.

4.2. Summary and Discussion

In conclusion of this section, the information of all preliminary XPS measurements is summarized and presented in an overview. This summary and discussion consists of the determined peak positions, the quantification data for the pristine and sputtered samples, and finally the calculated sputtering yields. The applied peak coupling shows a remarkable performance and contributes to an enhanced gain of information out of the samples. Thereby, the commonly assumed maximum error of $\pm 10\,\%$ for a XPS analysis can be undercut exceptionally as well.

First, the acquired peak position are depicted in table 4.2, listed for every compound, and by figure 4.17, illustrating the peak positions in the spectral lines. The tabulated data are average values of the peak positions considering the already discussed measurements with indium as the substrate for each powder sample as well as additional measurements with lithium foil as substrate (compare subsection 3.4.1). This ensures a greater statistical credibility for the determined peak positions.

The lithium peaks range from 52.83 eV for lithium carbide to 56.41 eV for lithium nitrate, whereas the most lithium compounds have peaks in the range from 55 to 56 eV. Therefore, compounds outside of this interval are easier to be distinguished.

Table 4.2.: Overview of all determined peak positions in eV for the binding energy

Compound	Li 1s	S 2p	C 1s	N 1 s	O 1s (C1)	O 1s (C2)	F 1s	Li/C 1s (C2)
Sulfur Species								
Li₂S	54.44	160.19						
Li-S*-S	55.16	161.59						
S-Sˣ-S		163.14						
Li₂SO₄	55.27	169.22			533.36	531.99		55.86
Electrolyte Species								
Li₂CO₃	55.25		289.95		531.79	531.21		
LiOCH₃	55.24		285.96		531.19			
LiOC₂H₅	55.68		286.05		531.49			285.25
LiNO₃	56.41			407.45	533.17			
LiTFSI	56.20	169.57	292.98	399.39	533.03		689.01	
Secondary References								
LiNO₂	55.95			403.79	532.58			
Li₂O	53.99				528.09			
LiOH / Li₂O₂	54.82				530.66			
LiF	56.08						685.16	
Li₂SO₃	56.19	166.90			531.52	530.88		
Li₂C₂	52.83		282.49					
C = C			284.06					

Concerning the sulfur component, the only ambiguity may be the observation of a peak at about 169 eV where lithium sulfate as well as the conducting salt is found. The same applies for their decomposition products Li₂SO₃ and the artificially artifi-
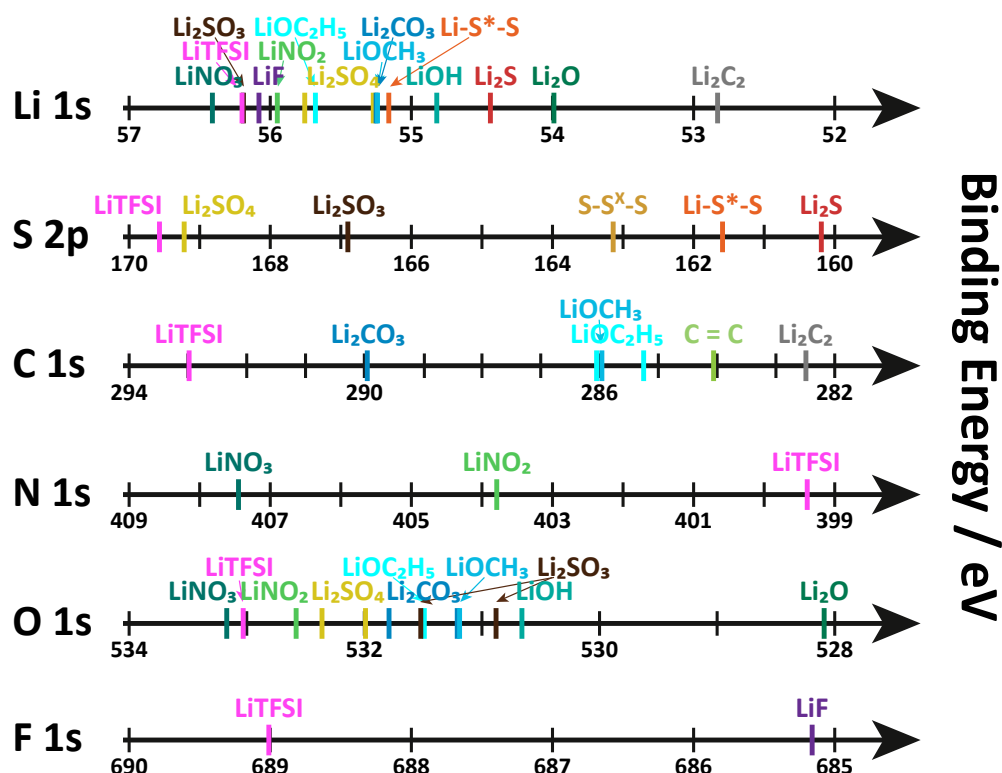
Figure 4.17.: Overview of all peak positions from the reference samples illustrated by their appearance in the respective photoelectron lines.

cially constructed TFSI* compound (compare page 94ff, not listed). Fortunately, the essential sulfur species, lithium sulfide and the lithium polysulfides, can be detected distinctively and may be analyzed the way as it is already discussed on page 79f.

For carbonaceous compounds, the impossibility of hydrogen detection impedes the unambiguous determination of most compounds. Lithium alkoxides and alcohols are observed close-by and likewise lithium carbonate, lithium hydrogen carbonate, and hydrogen carbonate are hard to specify solely. Another ambiguity is the carboxylic acid group that is marked COOH in the spectra in subsection 4.1.2, likewise not listed. Other fitting possibilities with similar binding energy are COOLi, an ester group, or an orthoester group (compare Ref. [103]). For the following SEI analysis, the compounds Li_2CO_3, COOH, and C-O-H label these discussed ambiguities as they are the most presumably present compounds. Besides, LiTFSI, lithium carbide, and aromatic carbons are determined distinctively.

Table 4.3.: Quantification table of the pristine and sputtered reference samples in % for their phase and element fraction

	Phase Distribution				Element Distribution			
	Prstine		Sputtered		Pristine		Sputtered	
Li_2S	53.1	Li_2S	78.5	Li_2S	Li1s Region	55.2	Li1s Region	59.1
	6.8	Li_2S_n	15.0	Li_2S_n	S2p Region	31.1	S2p Region	38.9
	35.1	C-C/C-H	6.5	C-C/C-H	C1s Region	3.7	C1s Region	2.0
Li_2S_4	10.8	Li_2S	43.5	Li_2S	Li1s Region	31.9	Li1s Region	47.5
	17.4	Li_2S_4	42.3	Li_2S_n	S2p Region	41.8	S2p Region	48.3
	63.4	C-C/C-H	15.1	C-C/C-H	C1s Region	26.3	C1s Region	4.2
	3.4	C-O-H	1.1	C-O-H				
Li_2SO_4	66.1	Li_2SO_4	45.1	Li_2SO_4	Li1s Region	25.6	Li1s Region	35.9
	2.1	C-O-H	21.7	Li_2SO_3	S2p Region	14.1	S2p Region	13.6
	31.8	C-C/C-H	3.2	C-C/C-H	O1s Region	53.7	O1s Region	49.9
			0.6	Li_2S_n	C1s Region	6.6	C1s Region	0.6
			7.1	Li_2S				
			22.3	Li_2O				
Li_2CO_3	62.8	Li_2CO_3	34.9	Li_2CO_3	Li1s Region	28.6	Li1s Region	43.4
	25.4	H_2CO_3	29.2	Li_2O	O1s Region	51.2	O1s Region	43.3
	2.9	C-C/C-H	9.7	C-C/C-H	C1s Region	20.2	C1s Region	13.3
	2.9	C-O-H	0.2	C-O-H				
	8.0	COOH/ester	0.3	COOH/ester				
			23.4	$LiOH/Li_2O_2$				
			1.3	Li_2C_2				
$LiOCH_3$	61.3	$LiOCH_3$	23.5	$LiOCH_3$	Li1s Region	28.3	Li1s Region	39.5
	6.2	COOH/ester	1.1	COOH/ester	O1s Region	34.1	O1s Region	34.9
	24.6	C-C/C-H	8.8	C-C/C-H	C1s Region	37.6	C1s Region	25.6
	7.9	$LiOH/Li_2O_2$	25.7	$LiOH/Li_2O_2$				
			3.8	Li_2C_2				
			14.9	C = C				
			4.5	Li_2CO_3				
			17.7	Li_2O				
$LiOC_2H_5$	21.4	$LiOC_2H_5$	10.2	$LiOC_2H_5$	Li1s Region	25.3	Li1s Region	40.4
	4.4	COOH/ester	1.5	COOH/ester	O1s Region	30.8	O1s Region	39.9
	42.0	C-C/C-H	1.5	C-C/C-H	C1s Region	43.9	C1s Region	29.7
	32.2	$LiOH/Li_2O_2$	29.1	$LiOH/Li_2O_2$				
			4.5	Li_2C_2				
			33.3	C = C				
			2.9	Li_2CO_3				
			17.0	Li_2O				
$LiNO_3$	62.6	$LiNO_3$	14.5	$LiNO_3$	Li1s Region	9.0	Li1s Region	42.9
	2.2	$LiNO_2$	8.2	$LiNO_2$	N1s Region	18.2	N1s Region	8.0
	33.1	C-C/C-H	7.0	C-C/C-H	O1s Region	52.6	O1s Region	45.9
	1.1	C-O-H	30.8	Li_2O	C1s Region	10.2	C1s Region	3.2
	2.9	COOH/ester	1.6	COOH/ester				
			1.1	Li_2CO_3				
			36.8	$LiOH/Li_2O_2$				
LiTFSI	46.9	LiTFSI	1.3	LiTFSI	Li1s Region	6.4	Li1s Region	39.0
	12.7	TFSI*	2.2	TFSI*	N1s Region	6.8	N1s Region	2.5
	16.8	C-C/C-H	0.4	C-C/C-H	S2p Region	12.5	S2p Region	3.6
	22.8	LiF	95.9	LiF	O1s Region	25.2	O1s Region	6.2
	0.6	COOH/ester	0.2	COOH/ester	C1s Region	13.7	C1s Region	2.9
					F1s Region	25.4	F1s Region	45.8

The separated binding energies of the nitrogen species $LiNO_2$, $LiNO_3$, and LiTFSI (compare figure 4.17) enables a distinct detection of those compounds. For oxygen, only lithium oxide stands out for the examined compounds. Indeed, lithium hydroxide/peroxide appears at a lower binding energy as well, however, it is close-by to all the other oxygen-containing compounds, observed between 531 and 533 eV. Additionally noted, lithium hydroxide competes with lithium peroxide at the same position. Under consideration of the hydrogen abundance in the respective region of the cell, it has to be suggested which one is more reasonable. For the quantification in the subsequent SEI analysis, the peak intensities are referred to lithium hydroxide which is believed to be more reasonable. An alternative quantification referring to lithium peroxide halves the mole fraction of lithium hydroxide and, thereby, increases the fractions of all other existing compounds slightly (compare section 3.4). At last, the fluorine in LiTFSI is separated by nearly 4 eV from lithium fluoride. The decomposition products of LiTFSI like TFSI* appear at lower binding energies, however, still widely separated from lithium fluoride.

In consideration for the following electrode analysis, the development or changes of oxidation states can be traced by the described compounds in this section. Thereby, the salt decomposition and the reduction of the solvents by the negative electrode as well as the redox mechanism of lithium nitrate are reflected by the shifts to components with lower or higher binding energies in the spectral lines, respectively. Additionally noted, most inorganic salts are distinctively detectable whereas an unambiguous assignment of the carbonaceous species turns out to be rather difficult.

For a deeper understanding of the surface changes, the phase distribution and the element distribution of the pristine and the sputtered compounds are listed in table 4.3.[1] As it can be noticed in the phase distribution, nearly all sample exhibit a high fraction of hydrocarbons at the surface of the pristine samples that vanish for all non-carbonaceous compounds after sputtering. Of course, this is also resembled by the element distribution where a decline of the C 1s fraction is visible in a same manner.

Considering the element distribution, a general enrichment of lithium is observed by sputtering for all compounds. Against this, the calculated sputtering yields (compare table 4.4) disclose a preferential sputtering of lithium that leads to a depletion of lithium at the surface. This is reasonable since lithium has a low mass compared to the other considered atoms. Indeed, the increment of lithium content in the actual experiments above can be explained by the measuring process in which a negative surface potential is applied by the neutralizer or by the preferential loss of sulfur or carbon along with their oxides due to their volatile behavior [99]. This is also indicated by the elemental distribution of LiTFSI: the SO_2 group as well as the CF_3

---

[1]The depicted values only resemble the measurements with indium as substrate, however, the samples with lithium as substrate exhibit similar results.

group are volatile so that only the sputtering-induced lithium fluoride remains at the surface. Similar assessments can be applied for the remaining of lithium sulfide, lithium oxide, and lithium carbide at the surface by simultaneous loss of S_xO_y, N_aO_b, and CO_2 for lithium sulfate, lithium nitrate, and lithium carbonate.

A detailed view at the phase distribution columns discloses that the sputter process has its most crucial impact on the conducting salt LiTFSI that is almost completely converted to lithium fluoride. This prevents a direct detection of LiTFSI as well as lithium fluoride during the depth profiling of the sample. Likewise, lithium nitrate is strongly decomposed to lithium oxide and most likely lithium peroxide. Also, a slight formation of lithium nitrite is observed. On the contrary, the decay of lithium sulfate due to sputtering is rather slight although it leads to the formation of lithium sulfite, lithium sulfide, and lithium polysulfides. Thereby, the lithium oxide formation of about 20 % for lithium sulfate is comparable with the one of lithium alkoxides; in contrast, lithium carbonate and lithium nitrate yield a fraction of about 30 % lithium oxide after the sputter process. This is a remarkable observation for the later detection of lithium oxide in the electrode samples. The sputtering decomposition of the carbonaceous species is not as crucial as for lithium nitrate and LiTFSI, but still notable. Thereby, lithium carbide and aromatic carbons are observed which may further react to lithium carbide by the presence of excess lithium in the SEI layer of the negative electrode. Also, the formation of lithium hydroxide instead of lithium peroxide is rather suggested for sputtering the alkoxides.

All the listed compounds in table 3.1 plus the TFSI* and COOH peaks were utilized as template in the later SEI analysis.

Table 4.4.: Sputtering yields of several relevant compounds in atoms/Ar^+:
The preferentially sputtered (red), the ordinary sputtered (light and dark orange) and the reluctantly sputtered components (green) are depicted according to the simulations in the appendix A.2. .

Compound	Lithium	Sulfur	Carbon	Nitrogen	Oxygen	Fluor	Hydrogen
Sulfur Species							
Li₂S	4.67	1.81					
Li₂S₄	1.96	3.33					
Li₂SO₄	2.47	1.01			4.76		
Electrolyte Species							
Li₂CO₃	2.86		0.52		4.03		
LiOCH₃	0.85		0.30		0.74		2.04
LiOC₂H₅	0.65		0.44		0.56		2.50
LiNO₃	1.82			1.73	5.21		
LiTFSI	0.40	0.70	0.30	0.38	1.53	2.32	
Secondary References							
Li	4.70						
Li₂O	5.85				2.70		
LiOH	2.57				2.33		1.77
LiF	4.97					4.79	
LiH	2.68						2.23
Li₂C₂	3.21	1.15					

5. Systematical Analysis of the SEI at the Lithium Electrode

In this chapter, the fundamental processes are described that lead to the formation and alteration of the SEI at the lithium metal electrode, the negative electrode. The propagating aging of the negative lithium electrode and its mechanism are revealed by the examination of samples with different cycle number up to the point whereupon the cell loses its storage capability. Thereby, the different chemical products, observed by XPS and SIMS, disclose this progression and permit the formulation of redox mechanisms at the surface that are decisive for the degradation process during the charge and discharge of the cell. Additionally, the products assemble in a layer structure that is rendered by the XPS depth profiles and particularly by the SIMS analysis.

To extract quantitative information about the formation mechanism the conversion to mole fraction was applied to XPS depth profiles (compare section 3.4). This quantitative view on the decomposition products at the surface exceeds the qualitative view, generally depicted in literature. For this, the peak positions of the compounds from the previous chapter (see table 4.3) were applied to the individual spectra of the depth profile. The peak coupling was set accurately by inspection of all detail spectra data. Thereby, an average coupling value from all the date was applied for the respective compounds that exhibited a marginal variance. Concentrations beyond the ppt range were neglected. On the one hand, they were not significant enough and on the other hand they were located within the noise background in many cases yielding misinformation about the actual concentration. Since the XPS depth profiles suffered from the radiation damage due to sputtering the quantitative analysis had to be handled with caution. This will be discussed in detail in the concluding discussion of this chapter.

The SIMS results complemented the view on the structure and composition of the SEI layer, however, SIMS could not be utilized as a quantitative method due to the matrix effect. Instead, SIMS revealed the layer structure more distinctively and illustrated a deeper qualitative view on the constituents of the SEI by the signal course characteristics of the various secondary ions. The major drawback of the SIMS analysis was that it could not detect lithium metal explicitly. In contrast to the XPS detection, SIMS allowed to detect hydrogen within the SEI layer.

Eventually, some notations were introduced to describe the layer system for the
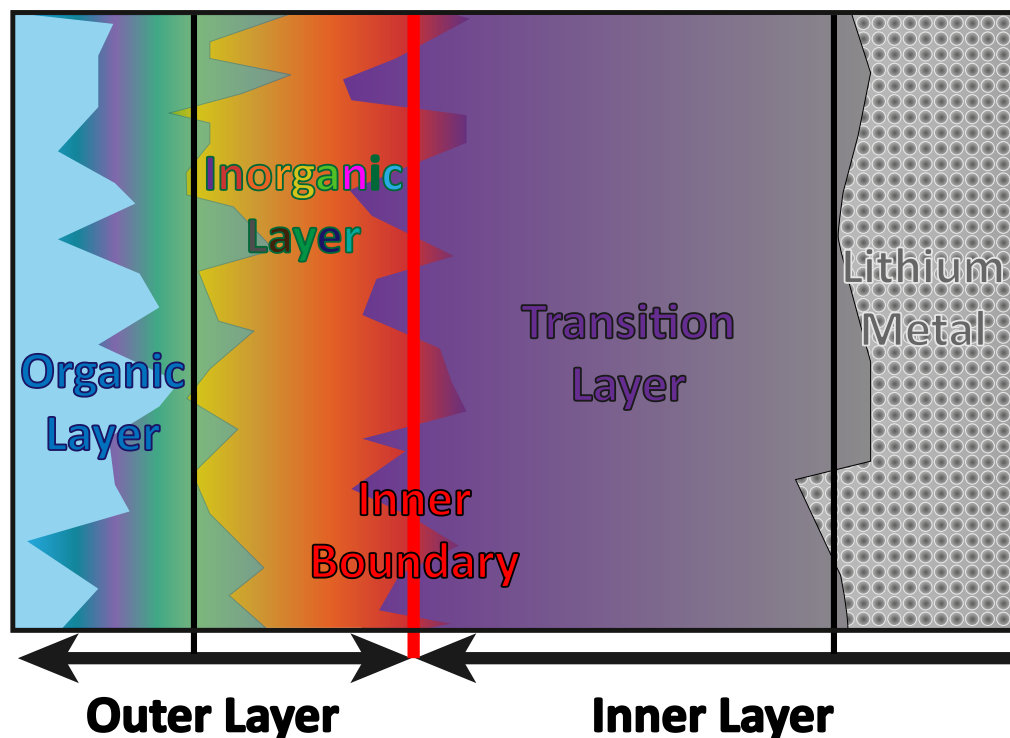
Figure 5.1.: The applied notation for the SEI layer structure is illustrated for the XPS and SIMS analysis. While SIMS can resolve the individual layer, XPS allows only to distinguish between the outer layer, comprising the organic and inorganic layer, and the inner layer, comprising the transition layer and the lithium metal electrode.

joint interpretation of the XPS and SIMS results because the sputter rates of both techniques were not comparable. The applied notation is depicted in figure 5.1. In general, the SEI consisted of an *organic layer* and *inorganic layer* composed of respective chemical substances. However, the boundary between those layers was barely resolvable in the XPS analysis. Therefore, these layers were denoted synoptically as *outer layer* in the later discussions of the XPS depth profiles. Beneath the outer layer, an *inner layer* was observed that consisted of the residual products from the previous cycles, forming the here defined *transition layer*, and the native lithium electrode. The intersection from outer to inner layer was additionally denoted as *inner boundary*. On the contrary, the SIMS experiments could resolve the organic, the inorganic, the transition layer, and the electrode distinctively for most instances and respective regions were assigned accordingly. At last, the term *SEI layer* comprises the organic, inorganic, and transition layer for SIMS or outer and inner layer for XPS as one entity for the deposition of extrinsic products on top of the lithium electrode.

This negative electrode itself exhibited several impurities and the depth profiles did not reach 100 % lithium metal in XPS or a solely lithium signal in SIMS, however,

some indicators like steady signals and high lithium metal revealed that the native surface of the lithium electrode or at least the electrochemical accessible region for lithium was reached.

Also noted, the elaborated color code of the individual compounds from the previous chapter 4 was applied to the XPS depth profiles in this chapter as well and the schematics for the proposed SEI likewise follow this color code. The SIMS analysis was plotted with a slightly different color code for the individual signals, particularly for the sulfur species. The regions were highlighted with a blue color for the organic layer, the stained color gradient for the inorganic layer, a color gradient from violet to grey for the transition layer, and a gray background for the native lithium electrode in the SIMS depth profiles, similar to build-up in figure 5.1. Complementary, the outer layer was denoted with the same stained color code as for the inorganic layer and the inner layer was illustrated with the same color gradient as the transition layer in the XPS depth profiles. The inner boundary was highlighted with a red line in the XPS depth profile and likewise the end of the inorganic layer and therefore the end of the SEI was marked with a red line in the SIMS profiles.

5.1. Examination of the SEI Formation and Alteration

To understand the formation and aging mechanism of the SEI and the simultaneously impairing side reactions at the surface, various lithium electrodes of different cells with different cycle numbers were analyzed with the SIMS and the XPS technique. Thereby, all cells were stopped in the charged state, for which the SEI growth could be observed in particular. For the depicted SIMS results, spots with barely no surface feature like fissures, holes, and particle clusters were selected to primarily point out the general SEI formation mechanisms. These surface features could not be excluded for the XPS measurement settings since the lateral resolution of the X-rays was not sufficient enough to reveal surface impurities. Furthermore, the analysis area was greater for XPS than for SIMS so that the probability for these impurities was higher as well. The examination of the pristine SEI layer and the analysis of special cases, occurring during this formation, are discussed separately within the current and the following chapter 6, respectively.

For the illustration of the XPS depth profiles, a separation into two figures was applied for the measured compounds to depict the whole detection range down to the ppt range in an appropriate manner. Thereby, the first one illustrates the phase fractions above 10 % in the range from zero to just above the maximal mole fraction on a linear scale; the second one depicts the phase fractions between 0.1 % and 10 % on a logarithmic scale. The SIMS depth profiles were divided as well, however, in a different manner. Here, the individual segments of a figure contain the respective layers with all their attributed signals representing their composition.

5.1.1. The SEI after the First Cycle

The first cycle of a battery cell resembles the initial stage for the SEI formation and is crucial for the further processes at the surface of the negative electrode. Hereby, the native lithium foil gets into contact with the electrolyte and, for the first time, is influenced by the whole migration and diffusion mechanism that accomplish the mass transport within the cell. Depending on the structure of the positive electrode, the amount of sulfur within the SEI layer of the negative electrode may hint at the quality of the restraining capability of the carbon-sulfur matrix. Therefore, the first cycle yields consequential information about the adsorbed products that partake in the formation mechanism of the SEI.
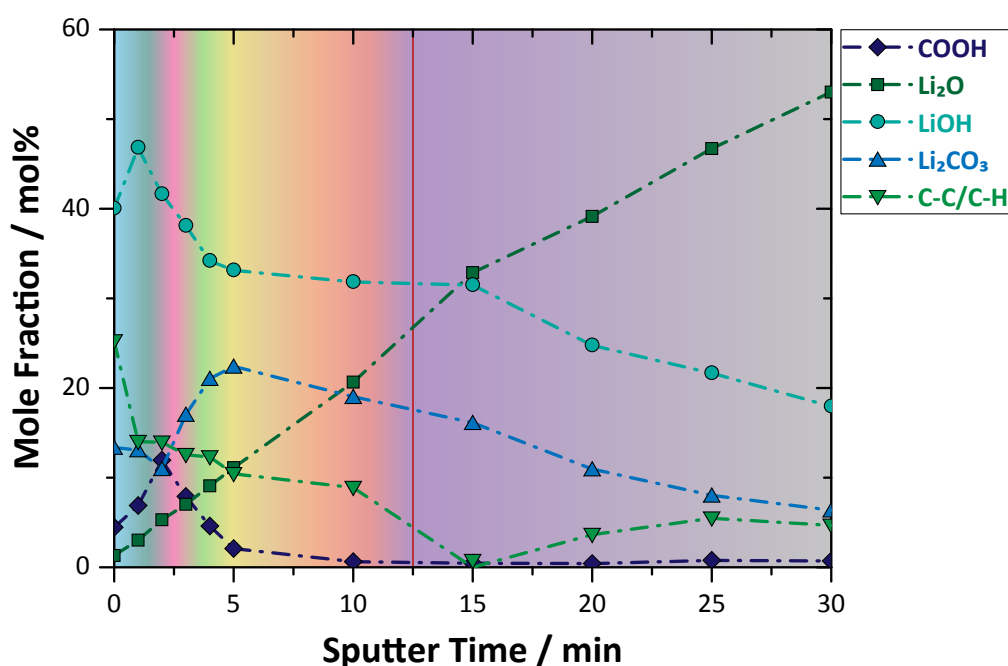
Figure 5.2.: In the XPS depth profile of the first cycle analysis the prevailing compounds are of organic nature. While in the outer layer lithium hydroxide is primarily observed, lithium oxide is dominant in the inner layer, which agrees with literature for a common SEI build-up [67]. The appearance of more lithiated or more reduced species deeper inside the sample surface can be observed generally. The inner boundary between the outer layer (stained color gradient) and inner layer (gradient from violet to grey) is marked with a red line.

As mentioned, the XPS depth profiles were subdivided into a minor and major mole fraction range. The first glance on the XPS depth profile of the major phases (figure 5.2) revealed lithium hydroxide, lithium oxide, lithium carbonate, hydrocarbons, and the carboxylic acid group as the prevailing compounds of the SEI after the first cycle. In general, the outer layer consisted of reaction products indicating the reaction of the lithium electrode with the solvent while the inner layer consisted of more lithiated

or reduced species of those solvent decomposition products which are formed by the pursued reaction with lithium. For instance, lithium hydroxide dominated the outer layer peaking at over 40 % mole fraction after the first sputter step. In the sequential sputtering of the sample the fraction decreased to about 30 % at the inner boundary (compare figure 5.2) and to less than 20 % after the final sputter step at 30 min. Meanwhile, the mole fraction of lithium oxide increased from about 1 % at the top surface steadily to about 50 % after the final sputter step becoming the prevailing compound deep within the sample surface. Also, the fraction of lithium carbonate reached its maximum of about 20 % at about 5 min of sputtering and, thereby, contributing significantly to the outer layer. On the contrary, the mole fraction of the carboxylic acid group showed a maximum at 2 minutes sputter time with a fraction of about 10 %. Furthermore, the mole fraction of hydrocarbons started over 20 % at the top surface, instantly decreased to about 10 % after the first sputtering step, and then steadily decreasing to the low percentage range within the inner layer. In contrast, the mole fraction of lithium carbide increased steadily in the inner layer from the ppt range which is illustrated in figure 5.3, the distribution of minor phases with low mole fraction.
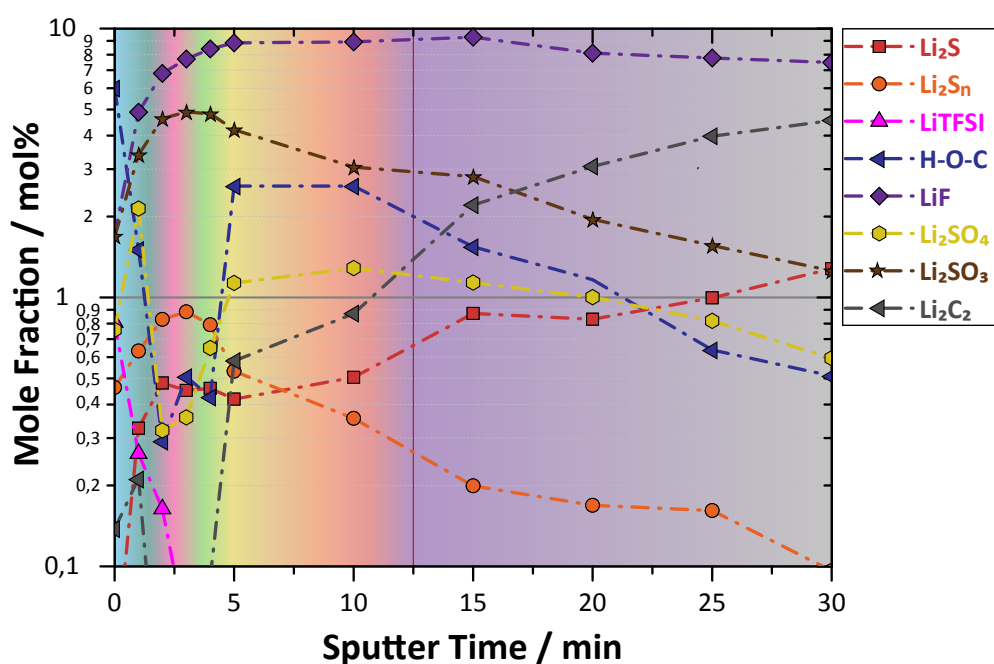
Figure 5.3.: Below 10 %, the XPS depth profile of the minor phases reveals a peaking of oxidized sulfur species in the outer layer and an increment of the reduced species lithium sulfide in the inner layer similar to the observations for the depth profile of the major phases.

Examining the depth profile of the minor concentrations, similar opposing characteristics could be found for the residual detected phases. For example, the mole fraction of lithium polysulfides Li_2S_n and lithium sulfite exhibited a maximum within the

outer layer and then decreased smoothly in the depth. Meanwhile, the fraction of lithium sulfide Li_2S increased from the sub-ppt range to about one percentage over the same range. As last significant consideration, the lithium salt LiTFSI yielded about one percent at the surface, then quickly dropped down below the detection limit after 3 min of sputtering. On the contrary, the concentration of lithium fluoride rose from about 1 % at the top surface to about 7 % complementary to LiTFSI. Additionally noted, lithium metal was absent or could not be detected in a significant amount in the XPS depth profile. Likewise, the signals of lithium nitrate and nitrate behaved unsteady because they were at or below the detection limit and, due to this, they are not plotted in the figures above.

In the SIMS depth profile (figure 5.4), the organic and inorganic layer could be distinguished very precisely. The corresponding signals for the organic layer, C_2 and CH_3O, peaked at a sputter time of about 15 seconds. All inorganic compound signals like the TFSI signal for the conducting salt, the NO_z signals resembling the electrolyte additive lithium nitrate, and every sulfur or sulfur-oxygen signal (S_xO_y) displayed their maximum at a sputter time of 35 s, characterizing the inorganic layer. Also, the CO_3 signal exhibited its highest intensity at this point indicating the chemical reaction of the ether solvents to lithium carbonate at the lithium surface.
After 35 s, all signals besides the Li_2 signal were dropping with advancing sputter time disclosing the transition to the native lithium electrode. Since a steady state of all the signals including Li_2 was reached quite instantly beyond the inorganic layer, this region was considered as the lithium metal electrode. Due to this, no interlayer between the inorganic layer and the electrode was accounted for the layer system and no further layer was expected after 200 s moreover.
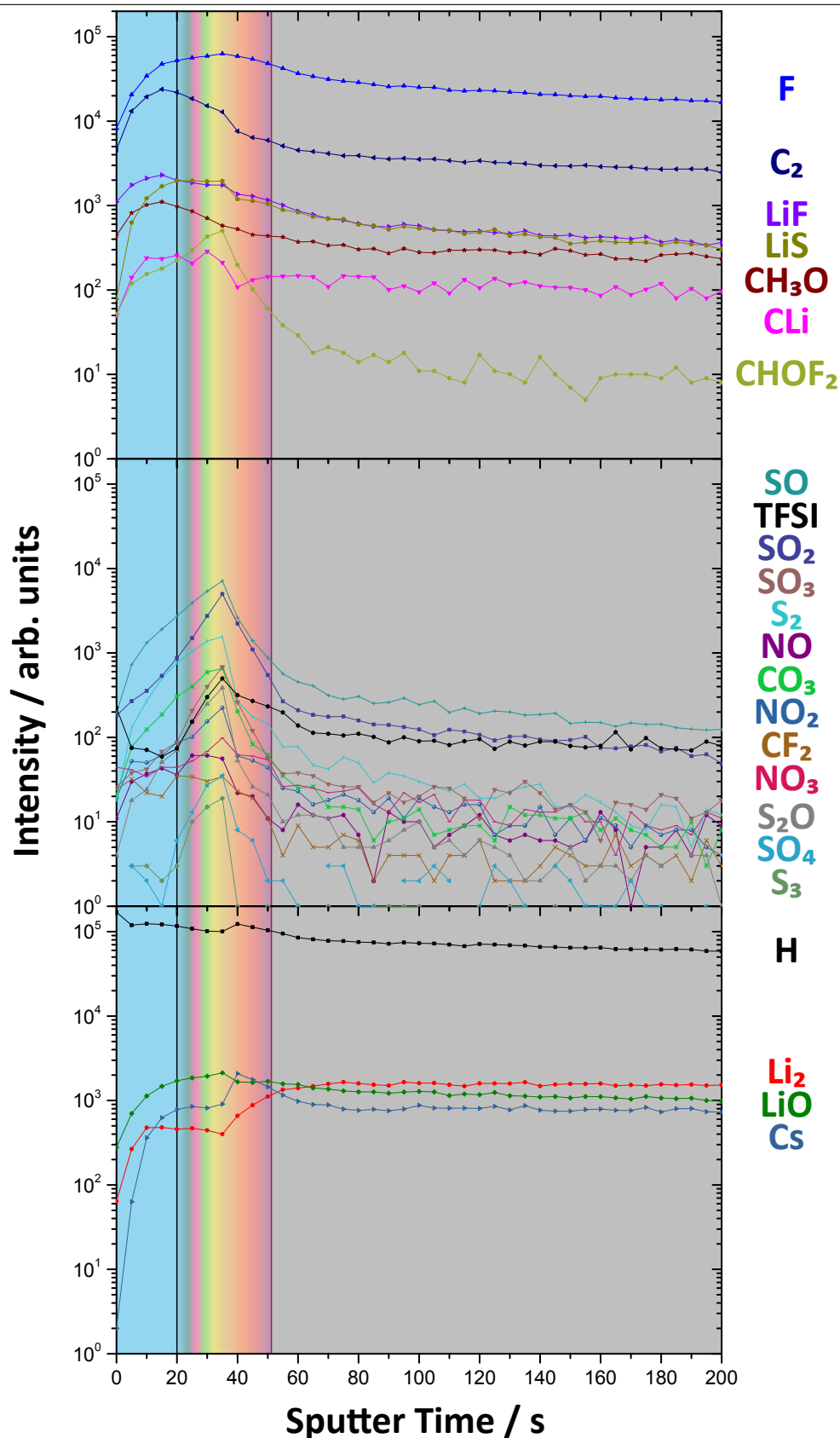
Figure 5.4.: Generally, the depicted SIMS depth profiles are subdivided into the signals attributed to the solvent and potentially dissolved species (top), the signals for the salts LiTFSI, LiNO₃, and sulfur-oxygen compounds (middle), and the signals characterizing the electrode and tracers for the layer structure (bottom). After the first cycle, the layer structure is primarily reflected by C_2, S_xO_y, and Li_2 respectively.

Concluding the XPS and SIMS results for the first cycle, the chemical and structural analysis of the SEI match each other complementary. The outer layer can be clearly distinguished into an organic layer at the top and an inorganic layer below. In the XPS depth profile, the organic layer exhibits high fractions of hydrocarbons and lithium hydroxide that originate from the reaction of the solvents with the lithium electrode, presumably. Here, the presence of lithium peroxide instead of lithium hydroxide is less probable due to the high fraction of hydrogen, also depicted in the SIMS depth profile (figure 5.4), as already discussed in the previous chapter. Indeed, the only possible sources for hydrogen in the utilized cell setup are the solvent molecules, the intrinsic impurities within the solvent, and the carbon matrix of the positive electrode. However, the solvent is assumed to be the pronounced origin of hydrogen-containing signals. Therefore, the relatively constant H signal may be attributed to the decomposition of the solvent and a subsequent fast diffusion into the SEI where hydrogen presumably forms lithium hydride or lithium hydroxide. As already pointed out, the formation of lithium hydride cannot be detected in a XPS measurement because hydrogen itself is not detectable by the XPS technique. Due to this, an unambiguous detection of hydrogen compounds is rendered impossible, also in the concluding consideration of the XPS and SIMS results.

Notably, lithium carbonate exhibits an elevated intensity in both analysis methods. Indeed, the formation of lithium carbonate can be explained by the sputtering of alkoxides (compare subsection 4.1.2), however, this may not be the only cause for the existence of lithium carbonate because then the complementary SIMS depth profile likewise has to feature an elevated CH_3O signal in the inorganic layer similar to the CO_3 signal as well. This is not the case and the sputter experiments in the previous chapter 4 do not suggest a formation of lithium carbonate to that extent. Therefore, an alternative formation mechanism has to be proposed. It is believed that the solvents 1,3-dioxolane or 1,2-dimethoxyethane undergo a reaction either with the oxidizing agent lithium nitrate or with other solvent decomposition products. Particularly, 1,3-dioxolane is considered as reactant to form lithium carbonate since it posses an acetal carbon that is already bound to two oxygen atoms. Unfortunately, a detailed mechanism cannot be proposed due to the complexity of the chemical composition near the surface.

According to the XPS and SIMS results, lithium nitrate seems to play a minor role in the formation of the SEI during the first cycle, also indicated by the subsequently executed examinations of the negative electrode in which the nitrogen signals rise to a significantly higher level. In contrast to lithium nitrate, the conducting salt is observed both in the organic and in the inorganic layer. An enrichment in the inorganic layer suggests an excellent stability against the close-by lithium electrode which is further proven by the opposing steady decline of the LiF signal in this region of the depth profile. For the XPS depth profile, this cannot be observed due to the radiation damage that leads to the decay of the $TFSI^-$ anion. There, it is

only characterized by a rise of lithium fluoride similar to lithium carbonate which is consistent with the SIMS results in turn. At last, the high fraction of lithium carbide cannot be explained by the sputtering alone as well considering the previously shown sputtering experiments (compare table 4.3). A resultant depiction of the formed SEI is shown in figure 5.5.
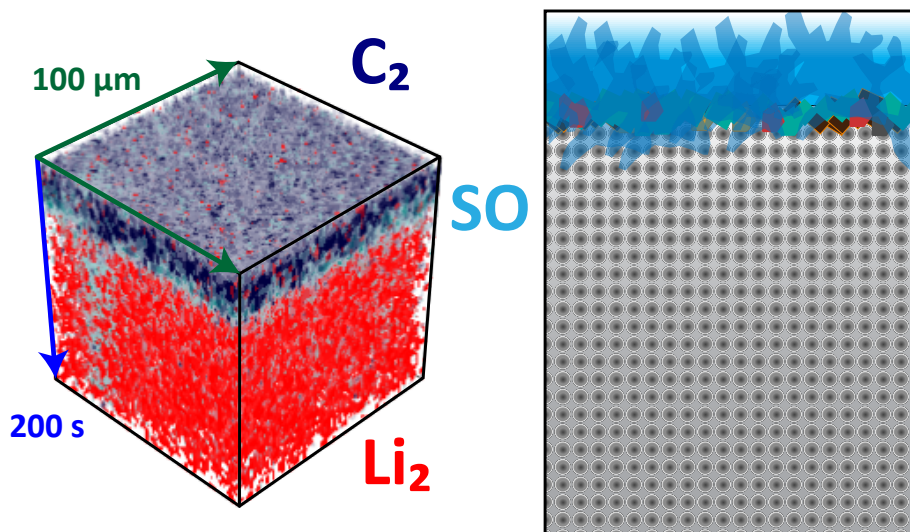

Figure 5.5.: On the left side a 3D reconstruction, created by the SIMS data, is depicted that exhibits a homogeneous distribution of the carbon (dark blue) and the inorganic salts, represented by the SO signal (light blue), on top of the lithium electrode (red) in the layered structure. According to this, the expansion and the prevailing carbonaceous character of the SEI layer is depicted in the schematic of the proposed SEI on the right side. The blue shapes resemble the polymeric character of the SEI while the stained areas illustrate deposited salt species.

Although the conducting salt and sulfur species are observed within the inorganic layer, the products formed by the solvent seem to be pronounced overall. It appears that the conducting salt is stable against the native lithium surface and, in contrast to the electrolyte additive lithium nitrate, the occurrence is much more significant. The small fraction of sulfur species in the XPS as well as SIMS depth profiles leads to the conclusion that the restraining mechanism of the carbon-sulfur electrode operated excellently. The prevailing existence of lithium oxide, lithium hydroxide, lithium carbonate, hydrocarbons and lithium carbide discloses a more explicit view on the reduction process of the solvent, however, a complete and fully assured mechanism can not be proposed yet. Lithium carbide occurs in a rather high mole fraction that may contribute to an improved electronic and ionic conductivity of the SEI allowing it to grow further on.

5.1.2. The SEI after the Second Cycle

During the second cycle, the preceding SEI composition and structure after the first cycle are affected by several processes. During the discharge, the electric field, directed from the negative to the positive electrode, may foster the desorption of cationic molecules that have been adsorbed physically to the surface in the previous charging process; whereas anionic molecules are retained at the surface. Furthermore, the migrating lithium ions probably react on their way through the SEI, particularly if the electronic conductivity of this interphase provides electrons or anions for the reaction for the charge conservation. Presumably, this leads to a further reduction of the SEI species. Besides, the electrolyte gets into contact with the chemically altered surface composition due to the surface reaction in the first cycle. Therefore, the surface yields a changed surface potential and novel surface reactions may take place. Also, the adsorption ability or interactions at the surface change significantly.
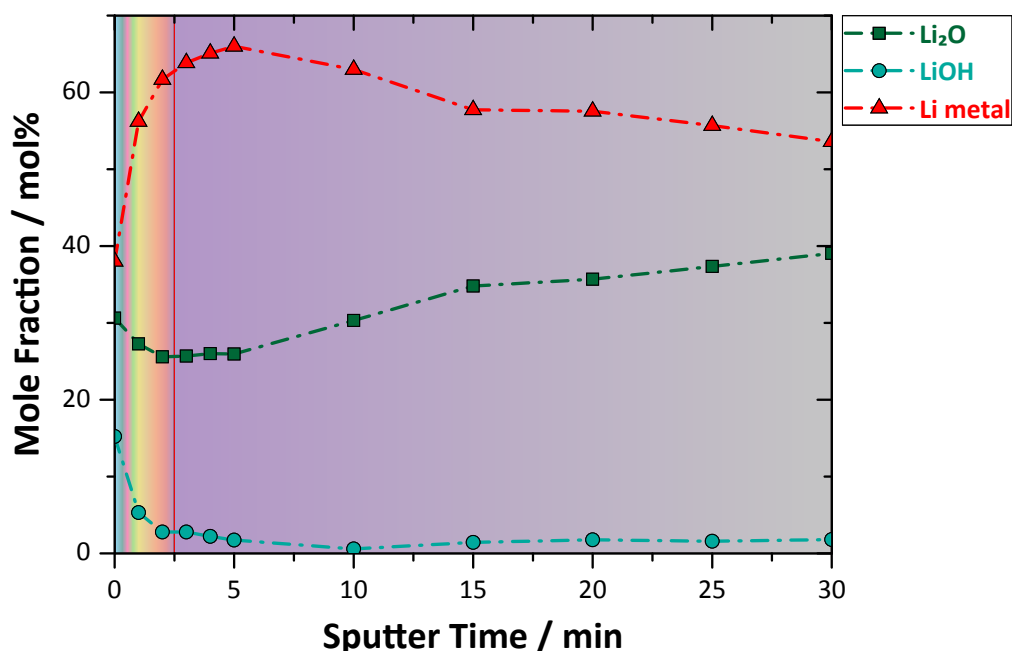
Figure 5.6.: In the XPS depth profile after the second cycle lithium metal, lithium oxide, and lithium hydroxide are visible. These lithium species display a drastically change in the SEI composition compared to the constituents after the first cycle by disclosing a lithiation of the SEI compounds most likely.

In comparison to the XPS depth profile after the first cycle, the distribution of the major phases changed by a lithium enrichment (see figure 5.6). Also, the inner boundary between the outer and the inner layer was difficult to be determined because the detected phases did not point out remarkable mole fraction changes. Eventually, it was set after 2 min of sputtering under consideration of the courses of all the phases. The prevailing compounds were lithium metal and lithium oxide

that both together resembled nearly 100 % of the surface in large part of the depth profile. Lithium hydroxide was also observed explicitly at the top surface region with a fraction of about 30 %, rapidly decreasing to less than 3 % after two minutes of sputtering. Afterwards, the mole fraction of lithium hydroxide dropped rather smoothly to 1.5 % during additional three minutes of sputtering, then reaching a constant mole fraction till the the end of the depth profile. Meanwhile, lithium metal ascended steeply from less than 40 % to about 60 %, peaked after 5 min of sputtering with a fraction of 65 %, and finally dropped steadily to circa 55 % after 30 min sputter time exhibiting the highest mole fraction over the whole depth profile. In contrast, the fraction of lithium oxide yielded an opposing trend: first it dropped from 30 % to about 25 % after 2 min of sputtering, then steadily increasing to about 40 %.
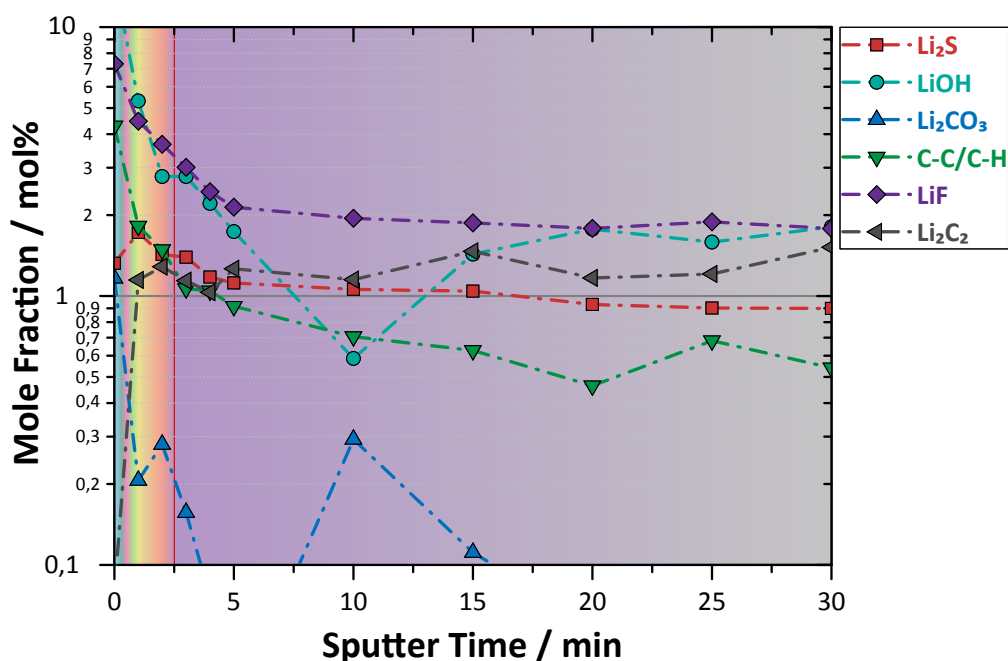
Figure 5.7.: All signals besides lithium carbide in the depth profile depiction of the minor phases are enriched at the surface and decline during the sputtering of the sample.

In the depth profile of the minor phases (figure 5.7), the prevailing compounds were lithium fluoride, hydrocarbons, lithium sulfide, and lithium carbide. Lithium carbonate was found at the top surface with a mole fraction of about one percent but it decreased immediately to the ppt range and even less after sputtering. Also, hydrocarbons were enriched with about 5 % at the surface and then dropped to 1.5 % in a similar manner as lithium hydroxide. In contrast, the amount of lithium carbide increased from the sub-ppt range by orders of magnitude to about one percent after the first sputtering step. Furthermore, lithium fluoride had a fraction of about 7 % at the top surface, then dropped to about 2 % after 5 minutes of sputtering.

In contrast to all other signals, lithium sulfide exhibited a peak after the the first sputtering step. Indeed, this peak was very swallow with only 2 %, however, it indicated a pointed depth enrichment and, generally, the fraction of lithium sulfide was greater in comparison to the first cycle.

Once again, no significant fraction of lithium nitrate and its decomposition products were observed. Also, the mole fraction of lithium salts besides lithium oxide strongly decreased compared to the depth profile of the first cycle. For instance, lithium carbonate was hardly observed after the second cycle. The fraction of carbide decreased likewise but was still above one percent and, therefore, contributed notably to the SEI.

The layer system and its boundaries were not clearly determinable in the SIMS depth profile (figure 5.8). The sample seemed to have a rougher surface so that the layers were not well defined and their interfaces smeared out. However, the organic layer and inorganic layer could be separated by the trace signals of TFSI, CO_3, and sulfur-containing signals like SO and S_2 that all peaked around a sputter time of about 180 s with a rather flat decline afterwards. The organic signals C_2 and CH_3O peaked just right before this at about 150 to 160 s, however, the intensity drop after the peak was slight as well impeding a distincter delimitation of the layers . Beyond the inorganic layer, a transition layer was plotted into the depth profile in which the Li_2 signal rose and the sulfur- and carbon-containing signals fell continuously till they reached an assumed steady state level at the end of the depth profile.

In comparison to the SIMS depth profile after the first cycle, the intensity of C_2 increased throughout the sample considering the lithium signal Li_2 as reference signal. A similar behavior was observed for the LiC signal as additional carbon-containing signal. Furthermore, the F signal remained in the mid-10^4 range while the TFSI signal decreased by over one order of magnitude. Also, a slight increment of the LiF intensity was observed for the second cycle analysis. In general, all inorganic salt resembling signals like NO_z, S_xO_y, and also CO_3 decreased for the inorganic layer. In contrast to the decrements of these oxygen-containing signals, the LiO signal remained relatively unaltered.
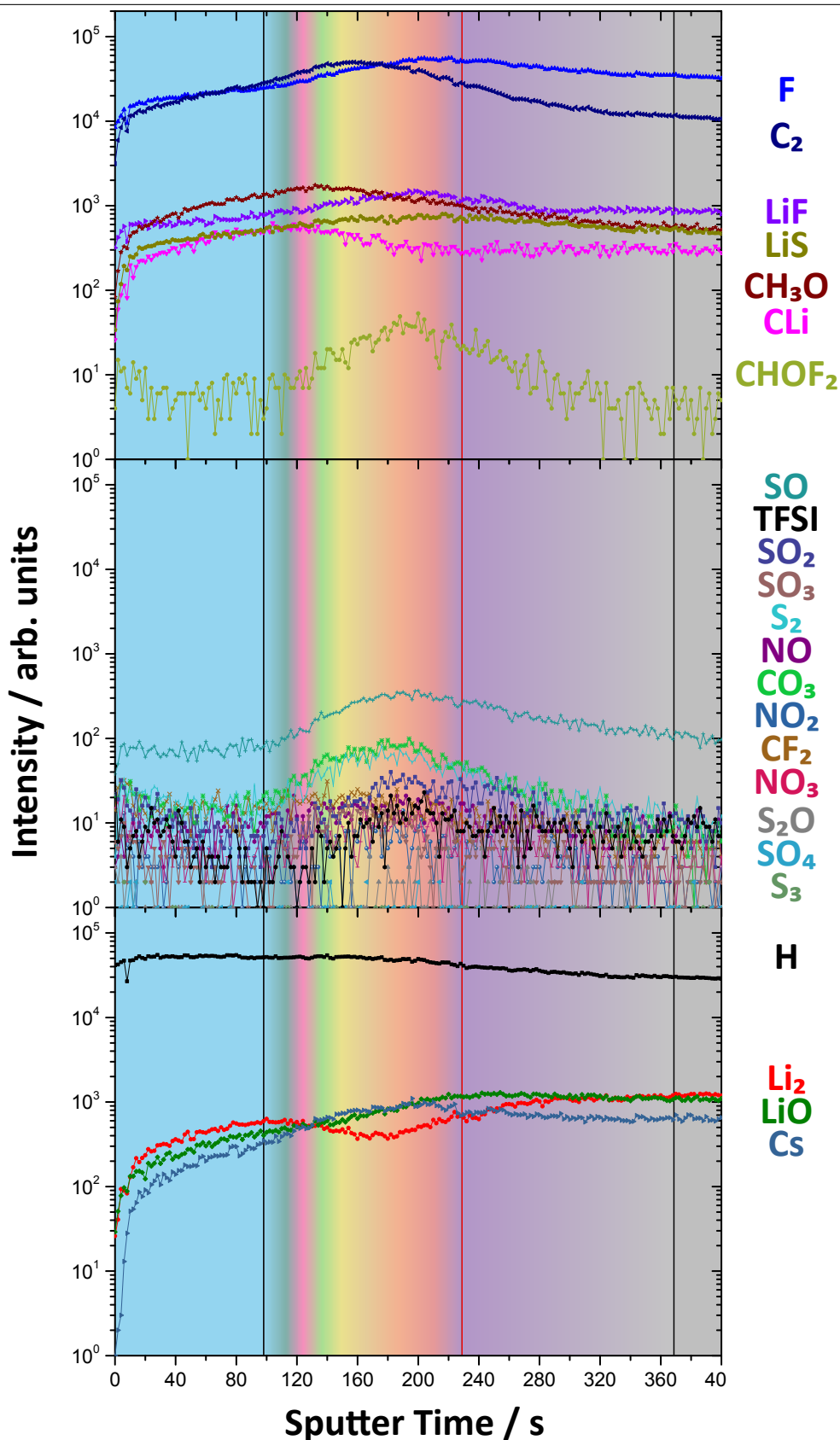
Figure 5.8.: After the second cycle, the SIMS depth profile exhibits a broad layered structure. The salt signals (middle) exhibit a low intensity level while the carbon and lithium signals are still high. This supports the perception of a reduction of the SEI constituents chemically adsorbed at the electrode after the first cycle.

Eventually merging the XPS and SIMS results after cycling the cell for two cycles together, they exhibit a remarkable change in structure and composition compared to the first cycle examination. While after one cycle no lithium metal is observed in the XPS depth profile, lithium metal is detected already at the top surface in the electrode examination after two cycles. Also, the inner boundary is reached after a shorter sputter time compared to the previous measurement after one cycle. Meanwhile, the SIMS depth profile takes a greater sputter time to reach a steady state level for the second cycle due to the analysis of a rough surface area or layer thickening, presumably. The shorter sputter time for the inner boundary in XPS and the greater sputter time for SIMS to reach the end of the inorganic layer is contradictory for both techniques. However, a possible explanation for this may be the formation of a very porous carbonaceous organic layer after the first cycle, most likely formed due to polymerization of the solvent species at the electrode surface. Since porous layers may be sputtered not so efficiently during the XPS depth profiling, the removal of the surface by the incident ions becomes very slow. This prevents the depth profile from reaching the lithium metal surface in the first cycle measurement. During the second cycle, this porous carbonaceous organic layer becomes more dense and thinner which is also substantiated by the lower hydrocarbon fraction in the XPS depth profiles. Also, the X-rays can permeate this compact carbon-rich layer even at the top surface and detect lithium metal. Indeed, no systematic observation approves the assumption of a porous SEI during the first cycle since the following examinations of all the electrodes after the first cycle are believed to hold a rather dense appearance. Though, the build-up of the initial SEI layer has a similar appearance to the ones of samples with higher cycle number, e.g. 51 and 90 cycles. For those samples, a comparable layer system with a mossy structure may arise from the lack of SEI forming compounds in the electrolyte.

For the consideration of the SIMS analysis, the choice of the analysis area is also decisive. For instance, a more distinctive layer structure including spatial features is depicted in figure 6.5 in the following chapter for the same cell after two cycles. Though, these features distort the intensities in the depth profile by yielding higher intensities for the signals of the features in the depth. Figure 5.8 shows a measurement with no features but with a wide layered structure which is assumed to be caused by a rough surface at the analysis spot. A rough surface leads to a smooth ascending or declining of all signals due to the spread distribution of the compounds over a greater depth range. However, a significantly expanded and broadened layer structure is likewise reasonable due to subsequent reactions at the surface after the first cycle SEI formation.

Examining the SEI layer composition in more detail, the salt resembling signals or fractions are very small in both SIMS and XPS depth profiles, respectively. In the XPS depth profile, the composition of the SEI changes from compounds like carbonate, lithium hydroxide, and lithium polysulfides in the first cycle, which can clearly

be assigned to the solvent and dissolved sulfur species respectively, to more lithiated or reduced compounds like lithium oxide, lithium carbide, and lithium sulfide. This transformation of the SEI is most likely caused by the lithium ablation and deposition during the second cycle reducing the present compounds at the surface by the lithium migration and the electrode surface polarization. Likewise, signals like LiO, LiC, LiS, and also SO stand out in the SIMS depth profile in comparison to the other S_xO_y and NO_z signals substantiating this observation of more lithiated or reduced species. Since the intensity of the conducting salt decreases significantly after the second cycle in the SIMS depth profile as well as in the XPS analysis, a formation of lithium fluoride seems to occur which is not rendered by radiation damage. Though, only a small amount is observed at the surface.
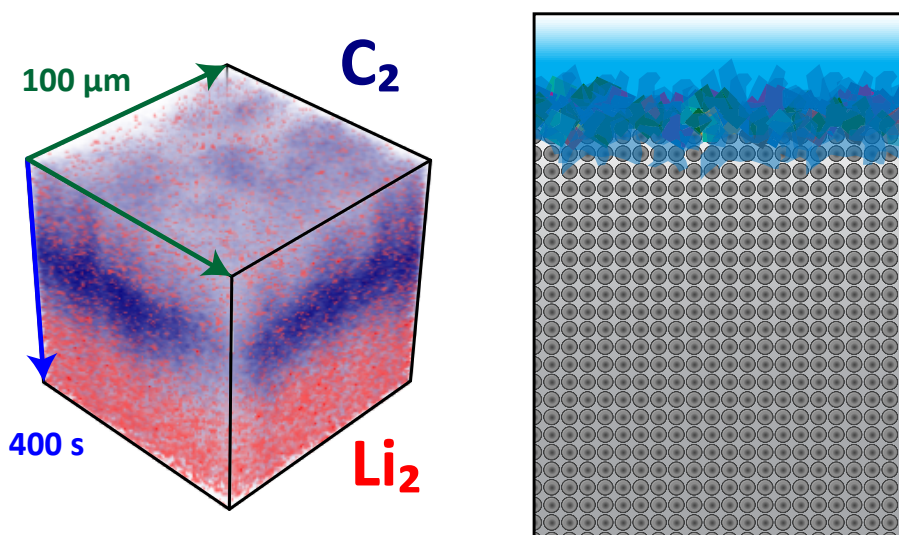
Figure 5.9.: The 3D SIMS reconstruction depicting the measurement of the second cycle on the left side shows strong intensity variation for the C_2 signal at the surface. Thereby, light blue intensity resembles a low C_2 intensity and the dark blue a high C_2 intensity. The thickness of the layer structure increased compared to the first cycle, however, it is still assumed to be relatively thin compared to the successive measurements. This is rendered by the schematic of the proposed passivation layer structure on the right side.

Concluding the results, the developed SEI as it is probed is illustrated by the second cycle analysis in figure 5.9. The high fractions of lithium metal and lithium carbide within the top surface region suggest that the surface remains electronically conducting. Indeed, lithium oxide and lithium carbide are formed casually, however, the fraction of lithium oxide relative to the overall surface coverage is supposed to be insufficient for the electronically insulation of the interface to the electrolyte. Therefore, the SEI growth of the electrode continues. In particular, the second cycle

analysis points out that the reduction mechanism of the precedingly adsorbed SEI constituents will also occur in the succeeding cycles.

5.1.3. The SEI after the Fifth Cycle

After five cycles, the development of the SEI has progressed as described by the previously shown results. Thereby, the surface gets repeatedly influenced by the adsorption of electrolyte decomposition products or polysulfides like it is described in the first cycle analysis and by a subsequently continuous reduction or lithiation of the chemically adsorbed species as it is elaborated in the second cycle examination in particular. This leads to the formation of an inner layer with strongly reduced or lithiated species developed from all previous cycles and an outer layer that primarily consists of reaction products originating from the last cycle. Hereby, the analysis after the fifth cycle resembles a short-termed evolution of these reaction sequences of adsorption and reduction.
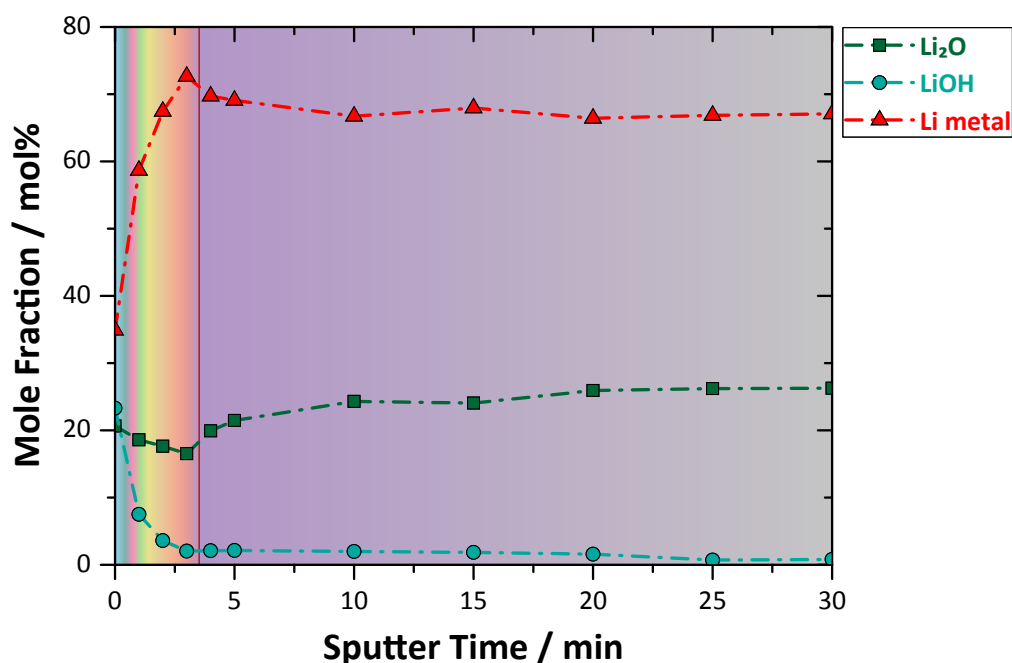
Figure 5.10.: In the XPS analysis of the five cycle electrode lithium metal is prevailing at the surface. Likewise, lithium hydroxide is observed at the top surface. In the depth, lithium metal and lithium oxide exhibit a relatively constant mole fraction while lithium hydroxide dropped significantly after 20 minutes of sputtering (compare figure 5.11).

In the depth profile of the phases with an elevated mole fraction (figure 5.10), the major changes could be observed within the the first three minutes of sputtering, respectively resembling the outer layer. There, the intensity for lithium metal rose from about 35 % abruptly to a peak of over 70 % at 3 min of sputtering, instantly falling to a constant concentration of about 65 % in the inner layer afterwards. Still, lithium metal was the prevailing compound for the whole depth profile with an even higher fraction than in the previous measurement. Analogously, the intensity for

lithium oxide decreased significantly comparing the whole depth profiles. Thereby, the minimum concentration of about 15 % was also reached at 3 minutes of sputtering, likewise indicating the end of the outer layer. Furthermore, the concentration of lithium hydroxide yielded over 20 % at the top surface, then dropped to about 2 % until the inner boundary, remained constant till 20 min of sputtering, and finally declined to less than one percent for the last two sputtering steps (also compare figure 5.11).
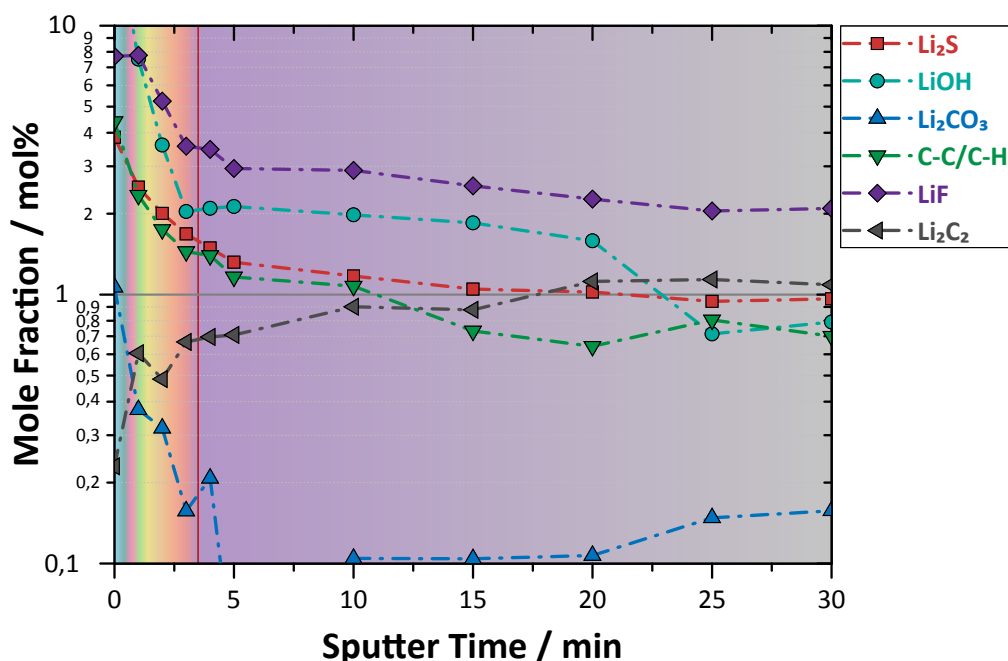
Figure 5.11.: The XPS depth distributions of the minor phases for a lithium metal electrode after five cycles yield a general trend like lithium hydroxide: the observed phases lithium fluoride, lithium sulfide, hydrocarbons, and lithium carbonate drop steadily in the outer layer and remain relatively constant in the inner layer. Another discontinuity for these signals may be observed between 20 and 25 min presumably indicating the intersection from the transition layer to the electrode in the SIMS depth profile (compare figure 5.12). Only lithium carbide shows an opposing trend in this XPS depth profile.

A similar trend like for lithium hydroxide was observed for lithium fluoride by inspecting the depth profile for the minor fractions of the SEI layer (figure 5.11). Starting with a fraction of about 8 % at the surface, the lithium fluoride amount dropped to about 3 % within the first 3 minutes, declined furthermore to about 2.5 % after 5 min of sputtering, and then steadily decreased to a mole fraction of 2 % at the end of the depth profile. Hydrocarbons and lithium sulfide exhibited an identical distribution in the depth profile that was comparable to the trend of lithium fluoride: both of them fell from a fraction of about 3 % to about 1.5 to 2 % in the outer layer, then decreased again at the fifth sputtering step to just over one per-

centage, and finally decreased steady till the end of the depth profile. Additionally, lithium carbonate was detected in the ppt range within the first 5 min of sputtering. Again, in contrast to most other compounds, the mole fraction of lithium carbide was steadily increasing from the ppt range to just over one percent at the end of the depth profile.

In comparison to the previous measurements, the lithium sulfide fraction rose furthermore. Apart from that, the depth profiles are quite alike in their constituents and their trends. Again, the electrolyte additive lithium nitrate could not be detected with the XPS technique.

A deeper look into the layered structure and composition was provided by the SIMS depth profile illustrated in figure 5.12. Thereby, the layers could be separated far more distinctively than for the last-shown SIMS depth profile because the TFSI intensity and the salt-indicating signals like S_xO_y and NO_3 reached an outstanding high plateau between 90 and about 200 seconds of sputtering time, dropping off very steeply immediately afterwards. Thereby, the distinctively measured inorganic layer contributed to a definite separation to the organic layer above and the transition layer beneath. This abrupt drop off at the end of the inorganic layer was followed by a plateau till about 320 seconds sputter time; then the salt signals declined steadily till about 700 seconds. Consequentially, the section between 200 and about 700 seconds of sputtering characterized the transition layer from the SEI to the lithium metal electrode. The latter one was represented by the constant values for all the signals indicating a steady state. Furthermore, the organic layer above the inorganic was also observed very clearly. A closer look revealed that this layer could be further split into two layers (compare figure 5.12); the first one between 0 s and about 30 s and a second between 30 s and 90 s sputter time. In the first layer, the lithium signal Li_2, the hydrogen signal H, and the carbon-containing signals C_2 and CH_3O exhibited a small maximum and the above described salt signals remained on a low level. These aforementioned salt signals (SO_2, SO_3 CO_3, and NO_3) began to rise in the second organic layer and exhibited a small shoulder at about 40 to 50 sputter seconds. The only signal that peaks in the second region of the organic layer was LiS. After the small peak of the carbon-containing signals and of the lithium signals in the first layer the signals remained relatively high on a respective plateau in the second layer. All these signals together with hydrogen declined afterwards within the inorganic layer and rose slightly in the subsequent transition layer again.

Besides, the LiF signal exhibited an individual trend that was quite different from all other signals and yielded a significantly higher intensity than the other salt signals within the organic layer. Also, in comparison to the first cycle analysis, this signal shows a higher intensity for the whole depth profile. Furthermore, the CO_3 and NO_z signals were enhanced for the inorganic layer.
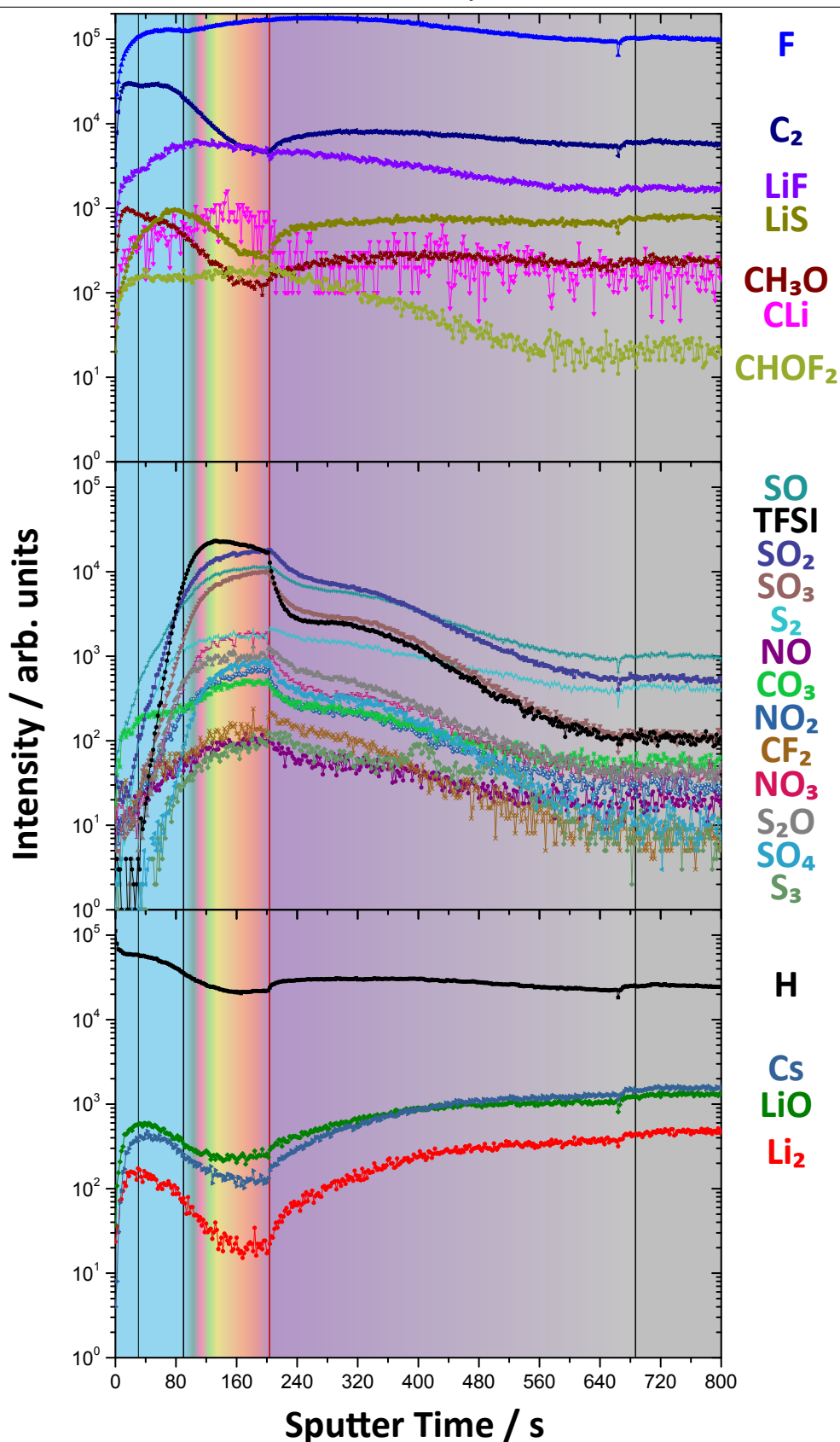
Figure 5.12.: The SIMS depth profile after the fifth cycle illustrates a distinctive layer structure. This is reflected by the carbonaceous signals (top) at the surface, by the salt signals TFSI, S_xO_y, and NO_z (middle) in the inorganic layer with consecutive drop off during the transition layer, and by the steady lithium-resembling signal Li_2 at the end of the depth profile.

In conclusion, the XPS and SIMS results complement one another so that the layer structure and its composition can be elucidated clearly. The outer layer as probed by XPS reflects the organic and inorganic layer, excellently probed by SIMS as well. Both methods show an enrichment of hydrocarbons at the surface that represents the organic layer. Furthermore, the maximum of the LiF signal and LiS signal before the appearance of the inorganic layer in the SIMS depth profile reveals the deposition of salts that can be dissolved in the electrolyte and that are physically adsorbed at the polar inorganic layer. Also, the LiF signal shows a steady decline through the inorganic and transition layer suggesting a likewise steady deposition on the electrode surface. At the surface, the concentration of lithium fluoride is supposedly related to the concentration in the electrolyte. Therefore, the deposition at the electrode surface may be more related to diffusion processes than to migration processes during cycling. The XPS results confirm a greater mole fraction of lithium sulfide and lithium fluoride within the outer layer. However, the high lithium fluoride mole fractions likewise reflects the high LiTFSI fraction that is detected as TFSI signal in the inorganic layer by the SIMS technique. Still, the top surface is believed to be enriched with previously dissolved products like lithium fluoride as the characteristics of LiF and LiS in SIMS suggests. Additionally, the distribution of the TFSI signal emphasizes the conclusion that the conducting salt gets buried beneath the surface layers and, thereby, becomes incorporated into the SEI layer of the electrode persistently. In particular, this is expressed by the the plateau intensity of the TFSI signal within the transition layer in the SIMS depth profile (figure 5.12). This illustrates a significant deposition of LiTFSI that presumably originates from the prior cycles. Also, it seems like that the SIMS transition layer is well resembled by the range from $3\,\mathrm{min}$ to $20\,\mathrm{min}$ of sputter time in the XPS depth profile. In favor for this, the fraction of lithium fluoride initially exhibits a plateau at 3 and 4 minutes sputter time in the XPS depth profile, then a drop at 5 minutes afterwards a steady decline till 25 minutes of sputtering; this trend is similar to the TFSI signal in the SIMS depth profile.

Likewise, the lithium hydroxide concentration exhibits strong discontinuities at these interval boundaries. Concerning the inorganic layer in the SIMS depth profile, it can be further noted that many signals like S_xO_y and NO_z, particularly SO_3 and NO_3, exhibit a similar profile like the TFSI signal. Thereby, the similar distribution of S_xO_y and NO_z suggests that the deposition of polysulfides leads simultaneously to the oxidation of these polysulfides by the electrolyte additive lithium nitrate. In equal measure, these species are incorporated into the SEI layer persistently.
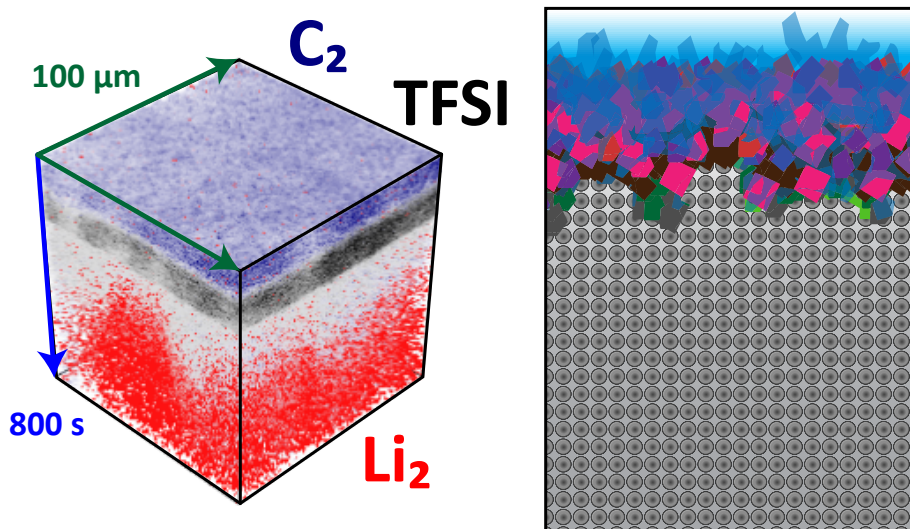
Figure 5.13.: The SIMS 3D reconstruction of the fifth cycle analysis reveals a distinct layered structure in which the carbon signal C_2 (dark blue) resembles the organic layer and the TFSI signal (black) resembles the inorganic layer. Both layers are spatially homogeneously distributed compared to the transition layer where a lower intensity of the TFSI signal (grey) and the lithium signal Li_2 (red) are inhomogenously and complementary distributed. This is also expressed by the illustration of the proposed passivation layer. There, the ongoing passivation by the conducting salt LiTFSI (pink) as well as by oxidized sulfur species (dark brown for sulfite) by simultaneous deposition of lithium nitrite (light green) are illustrated.

In combination with the previously shown analysis of the first and second cycle measurements, a first comprehensive view on the progressive surface reactions and their effects on the cell behavior emerges from the fifth cycle analysis. The ongoing formation of organic and inorganic species within the SEI layer (see figure 5.13) leads to a drying process of the electrolyte; including the burial of the conducting salt LiTFSI, this causes the later failure of the lithium-sulfur cell by the lithium metal electrode. Also, the persistent loss of active material by oxidation of the adsorbed sulfur species, diffusing or migrating from the positive to the negative electrode, to sulfur-oxygen compounds like lithium sulfite is reflected by the resulting layered structure depicted in figure 5.13. Apparently, lithium fluoride can be dissolved into the electrolyte and deposits on top of the inorganic layer with unknown consequences for the cell performance.

5.1.4. The SEI after the Twenty-Fourth Cycle

The analysis of the twenty-fourth cycle is motivated as a mid-term instance of the progressive SEI formation. While the SEI is still relatively fresh after five cycles and the layer structure and composition has just begun to build up, this mid-term instance exhibits a structure and composition in a moderate evolution state. This state resembles the progressing layer formation and alteration consecutively to the five cycle analysis, however, failure mechanisms become more relevant at this point and have a significant influence on the SEI.

Unfortunately, the XPS measurements failed due to machine problems and the samples were contaminated. The separately conducted SIMS analysis was not affected by this; so there was still a satisfactory evaluation of the structural changes possible. Admittedly, the composition could therefore only be reconsidered in a qualitative way. Indeed, the SIMS analysis was also corrupted by small dropouts of the ion source, visible at around 225 and 1200 seconds of sputtering in the depth profile after twenty-four cycles (figure 5.14), however, they could be neglected for the investigation of the depth profile since the distortion is marginal.

Considering the measurements of the fifth and twenty-fourth cycle, both depth profiles disclosed a broadening of the inorganic layer from about 120 seconds of sputtering after the fifth cycle to about 400 seconds of sputtering after the twenty-fourth cycle. Meanwhile, the thickness of the organic layer seemed to remain relatively constant with a total sputter time of circa 80 to 90 s indicated by the peaking of the C_2 signal, the H signal, and the minor or absent intensity of the lithium salts in the same range like for the fifth cycle. Additionally, the transition layer increased significantly in sputter time, however, the boundary with the inorganic could not be determined accurately because the drop off behind the inorganic layer was not as distinct as for the fifth cycle measurement. Therefore, the limits were chosen the way that the plateau of the salt-resembling signals TFSI, SO_y, and NO_z were completely included within this interval. Taking the fifth cycle analysis into account, the decline of these signals beyond the inorganic layer were fully assigned to the transition layer contributing to the plateau concentration from the prior cycle, the 23rd cycle. Once again, a closer look at the organic layer revealed that the organic layer can be separated into two layers where one was salt-free and the other contained presumably dissolved salts that adsorbed on the inorganic layer.
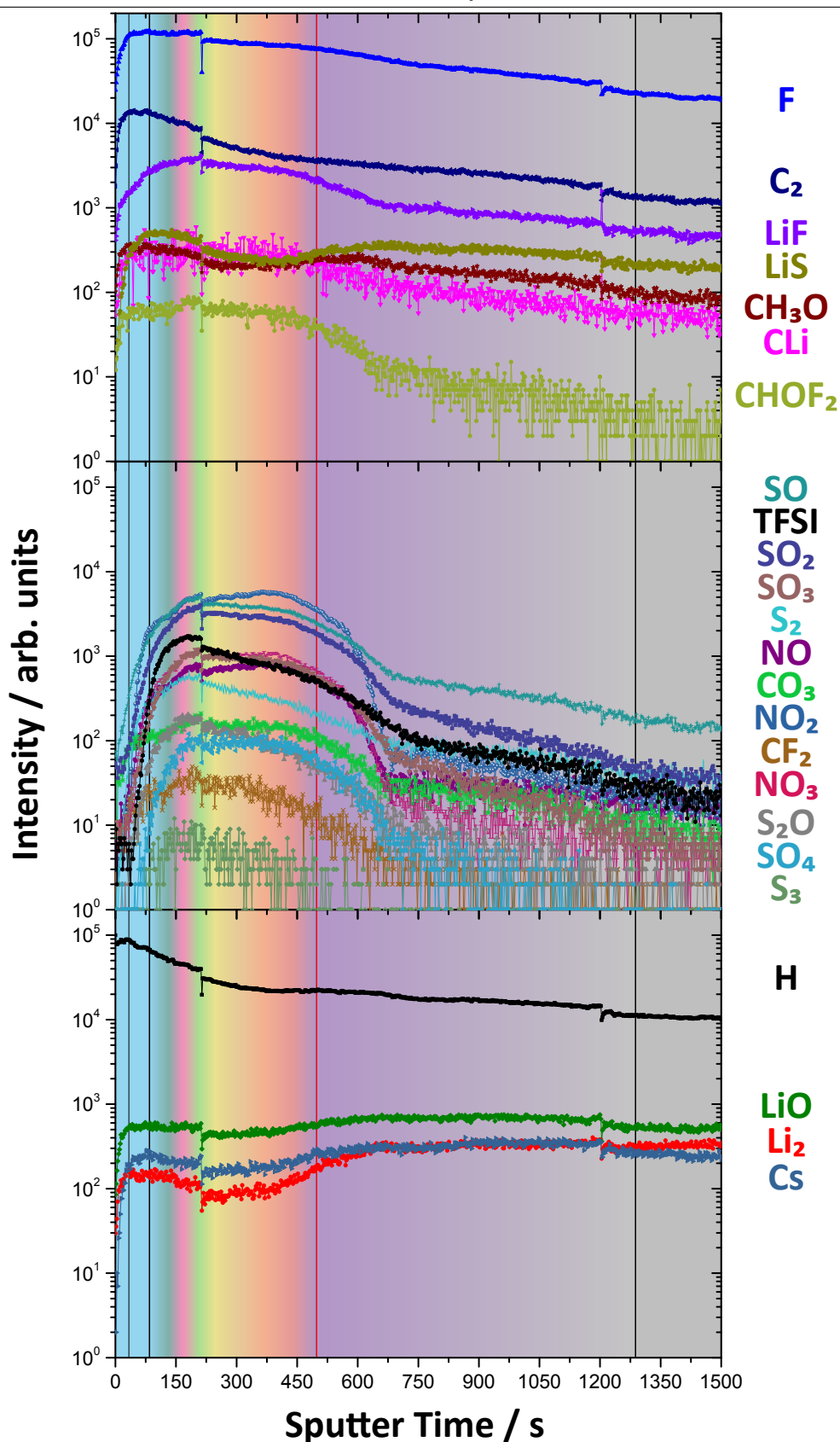
Figure 5.14.: In the SIMS depth profile after twenty-four, a thickening of the inorganic layer is indicated by the salt signals while the thickness of the organic layer remains the same. Like the inorganic layer, the transition layer grows due to the cycling.

Under consideration of the H signal as reference intensity, the intensity of the conducting salt, the TFSI signal, decreased by over one order of magnitude within the inorganic layer in comparison to the previous depth profile (figure 5.12). In contrast, the NO_2 signal increased by the same proportion in the same region. Furthermore, both NO_2 and TFSI signals exhibited opposing trends: while the NO_2 signal rose slightly, the TFSI signal declined steadily within the inorganic layer. Despite the increment of the NO_2 signal, the sulfur-oxygen signals and the CO_3 signal yielded lower intensities. Examining the transition layer, the drop off at the beginning of the range was more intense for the NO_z signals than for the TFSI signal and the S_xO_y signals. In the constant region at the end of the depth profile, the intensities of all signals, considered relatively to each other, were nearly the same as for the fifth cycle measurement. Another important observation was the lesser depth of the intensity valley for Li_2 signal in the inorganic valley.

This shallow valley of the Li_2 signal can be best explained by a stronger mixing of the deposited lithium cations with the deposited salts. Likewise less conducting salt seems to be incorporated within the inorganic layer compared to the previous measurement. Moreover, the elevated NO_2 signal reveals the ongoing behavior of lithium nitrate as an oxidizing agent that is reduced to lithium nitrite. This increment of the NO_2 signal indicates the participation of lithium nitrate in the lithium transport that leads to an enhanced adsorption at the surface of the electrode. However, the strong drop off at the beginning of the transition layer for all NO_z signals may disclose a re-dissolution during the cycling of the cell. In contradiction to the inorganic and transition layer, the extent and composition for the organic layer appears to remain the same as in the previously shown analysis (compare subsection 5.1.3). This indicates that the electronic potential of the inorganic layer presumably remains identical so that similar organic compounds are adsorbed for both measurements. The broadening of the transition layer emphasizes the ongoing fixation of active material and electrolyte species on the electrode surface. Thereby, the high SO intensity in the transition layer supports the idea that the chemically adsorbed sulfur-oxygen species are less likely dissolved into the electrolyte again during cycling. Finally pointed out, the indistinct boundary between the inorganic layer and the transition layer leads to the conclusion that the surface and the bulk of the SEI layer align each other in chemical composition and physical properties. This is caused by the the repetitive ablation and deposition process during cycling.

A summarizing picture of the SEI and the respective SIMS illustration is depicted in figure 5.15. The diminishment of conducting salt and sulfur-oxygen species within the inorganic layer may indicate less adsorption at the surface. A reason for this can be a decline of their concentration within the electrolyte so that the sulfur species or the conducting salt LiTFSI can diffuse to the electrode surface to a lesser extent. In exchange, the lithium cation migration between the electrolytes is presumably
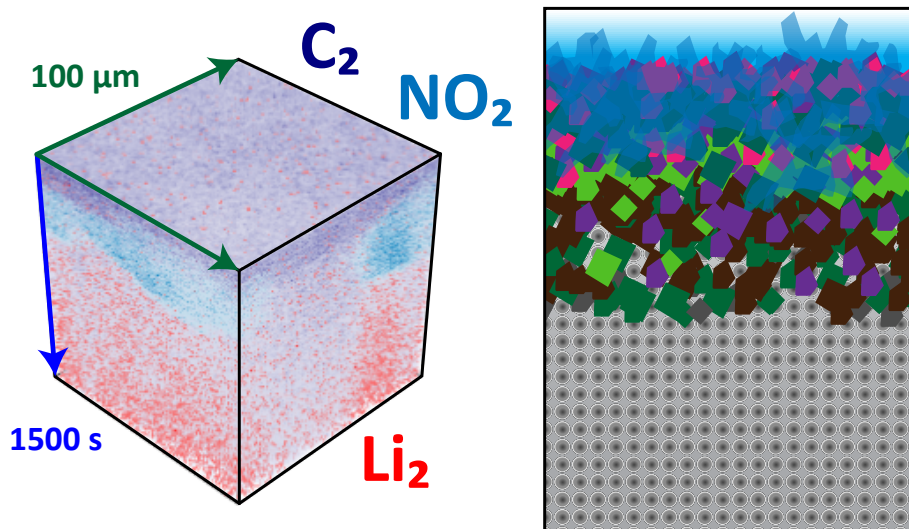
Figure 5.15.: Concluding the results of the twenty-fourth cycles, the 3D reconstruction of the SIMS data shows a thin but distinct organic layer at the top represented by the C_2 signal (dark blue). In constrast, the inorganic layer below, represented by the NO_2 (light blue), is not spatially distributed homogeneously. The resulting passivation layer exhibits conducting salt at the top. In the bulk, NO_z, S_xO_y, and lithium fluoride are the prevailing compounds.

maintained by the electrolyte additive lithium nitrate and lithium nitrite to a greater extent, therefore. That idea is also supported by the greater proportion of nitrogen-oxygen species within the SEI layer. This particular alteration of the SEI layer may indicate a change in the direction to the malfunction of the cell chemistry: Indeed, the parasitic processes described in the previous analysis degrade the cell progressively that results in a steady decay of the physical cell properties. However, the turn-over in the electrolyte conductance by the vanishing of the conducting salt is a crucial factor that may lead to an instant cell failure. The forecited steady decay is particularly resembled by the broadening of the inorganic layer and the transition layer that may cause the already mentioned issues: a notably higher overpotential due to a greater ion resistance of the SEI layer and a decline in active material as well.

5.1.5. The SEI after the Fifty-First Cycle

After cycling the cell fifty-one times, the examination of the negative electrode's surface represents the long-term evaluation of the SEI. Since the cell is at a progressed state, the finite amount of electrolyte, especially the salts LiTFSI and LiNO$_3$, plays a decisive role for the cell chemistry. Therefore, this analysis resembles the preceding observation before the cell is going to malfunction or stall. Together with the subsequent measurement of the ninetieth cycle cell that comprises a malfunction process, a deeper view into the failure mechanism can be disclosed.
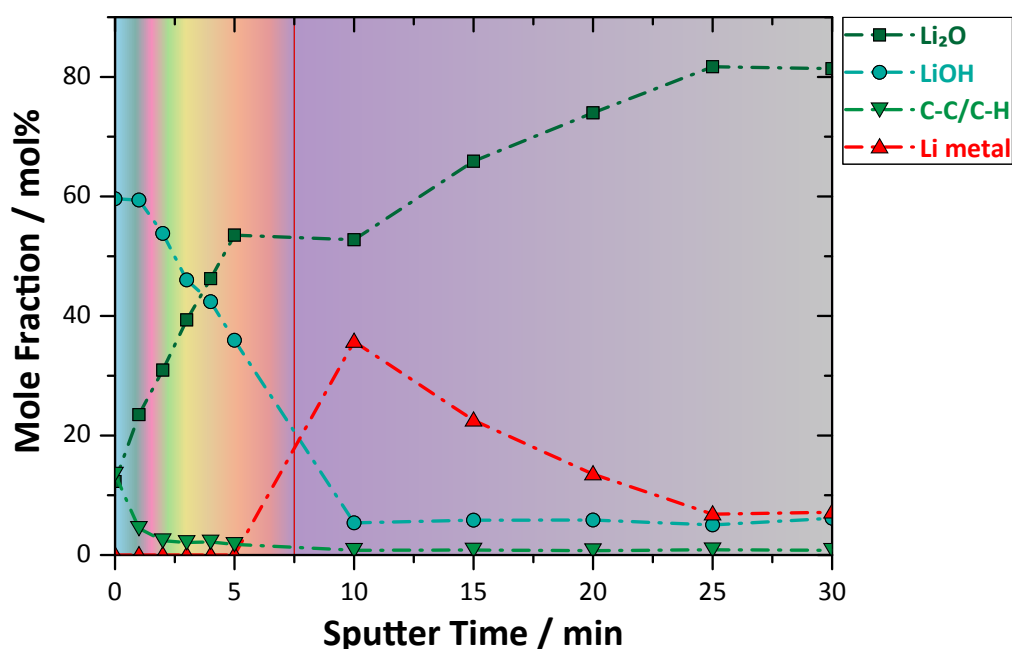
Figure 5.16.: In the depth profile after fifty-one cycles, a remarkable mole fraction of about 35 % for lithium metal is detected just beneath the outer layer within the SEI of the electrode. This high fraction is observed despite its reactivity and possible sputter effects like mixing. Again, high mole fractions of lithium hydroxide and hydrocarbons are found at the surface while lithium oxide prevails in the inner layer.

In particular, the detection of lithium metal with a peak mole fraction of over 30 % below the outer layer at 10 minutes of sputtering was notable in the XPS depth profile that depicts the major fraction range (figure 5.16). Before this maximum, the mole fraction was underneath the detection limit and afterwards it dropped steadily to just below 10 % for both sputter breakpoints at 25 and 30 minutes rendering the limited occurrence for the inner layer. Simultaneously, the first five minutes of sputtering exhibited a decline of lithium hydroxide from about 60 % to about 35 % and a rising of lithium oxide from just over 10 % to about 55 %. At 10 minutes the mole fraction of lithium hydroxide decreased to about 5% and remained constant afterwards. Additionally, the mole fraction of lithium oxide stagnated from 5 to 10 min of

sputtering and then steadily increased to over 80 % till reaching a sputter time of 25 minutes. This fraction also remained constant at the end of the depth profile. Thus, it was the prevailing compound within the inner layer. Due to these observations and also the examination of compounds with minor mole fraction, the inner boundary was set between 5 and 10 minutes of sputtering. Furthermore, hydrocarbons were observed at the top surface with a high fraction of about 15 % that was comparable with the first cycle analysis.
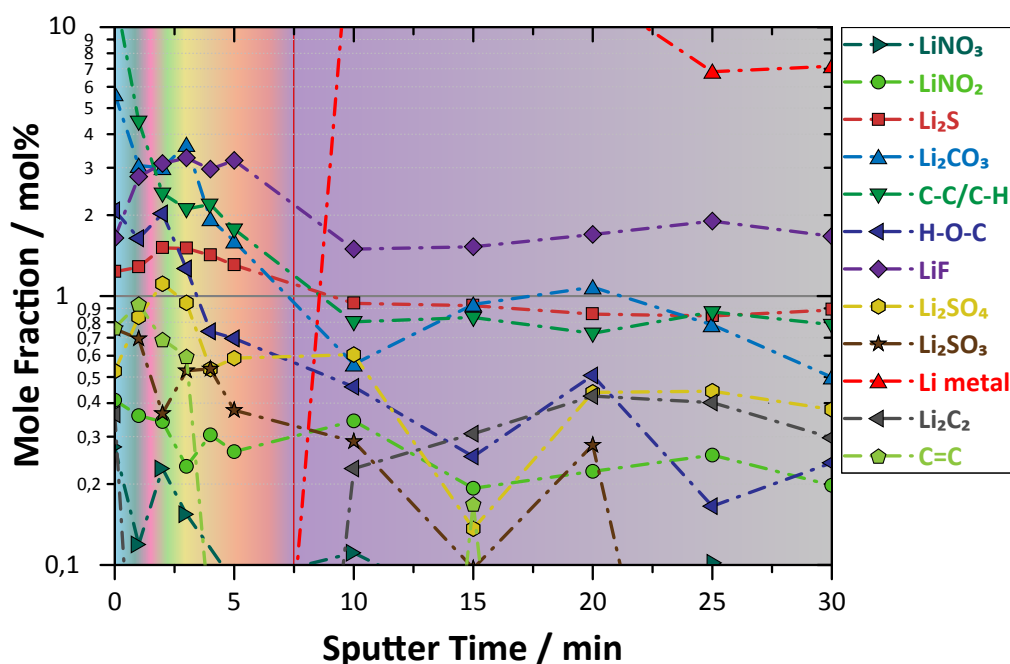
Figure 5.17.: After the fifty-first cycle, the fraction and the diversity of the salts increases in the XPS depth profile of SEI constituents with minor mole fraction. Besides the commonly present compounds lithium sulfide, lithium fluoride, and solvent decomposition products, nitrogen-oxygen and sulfur-oxygen are visible in the depth profile. The electrolyte additive lithium nitrate is visible for the first time presumably indicating a major participation in the lithium transport as already discussed in the previous analysis of a cell after twenty-four cycles.

Meanwhile, the depth profile of the minor components (see figure 5.17) revealed an overall enhancement of the salt fraction. Lithium fluoride, lithium sulfide, lithium carbonate, lithium nitrate, lithium sulfate, lithium sulfite, alcoholic groups, and aromatic carbons yielded elevated fractions, particularly till 5 minutes of sputtering. Lithium carbonate had a concentration of about 6 % at the top surface that steadily dropped down during the sputtering of the outer layer. After a sputter time of 10 minutes, it reached a fraction that fluctuated around one percent till the end of the depth profile. Along the drop-off in the outer layer, the fraction of lithium carbonate peaked with 4 % at 3 min of sputtering. Likewise, lithium fluoride exhibited its high-

est fraction at this point, however, it only stood out slightly in relation to a plateau of its fraction in the depth profile yielding a fraction of about 3% from 1 to $5\,\text{min}$ of sputtering (see figure 5.17). At the top surface and after $10\,\text{min}$ of sputtering, the mole fraction of lithium fluoride remained just below 2% indicating the layered structure even more. On the contrary, lithium carbide was primarily observed at the top surface and beyond 10 minutes sputter time in the inner layer respectively with a fraction in the mid-ppt range. Several sulfur- and nitrogen-containing signals like lithium sulfide, lithium sulfate, lithium nitrate, lithium nitrite were enriched till five minutes of sputtering in their depth profiles. Likewise, aromatic carbons were examined till 3 minutes of sputtering in the outer layer comprising a fraction in the upper ppt range. Therefore, the appearance of aromatic carbons exhibited a comparable appearance like lithium carbonate.

In comparison to the previously described measurements, the built-up of the depth profile changed drastically. Particularly, the distinctively peaking of lithium metal within the SEI stood out and will be discussed in detail later on. Additionally, the increased concentration of various salts like lithium nitrate and lithium sulfate was notably considering the analysis for low cycle numbers. Lithium nitrate or lithium nitrite were detected for the first time in this serial analysis of the SEI, however, only with a small fraction.

While the XPS depth profile yielded various features, the SIMS depth profile (see figure 5.18) appears to be less rich. There were no significant signal changes till 3000 seconds of sputtering, however, the following signals were still notable: many sulfur and nitrogen containing signals like SO, SO_2, NO_2, and S_2 were relatively high above the lithium signal Li_2. Furthermore, the S_3 fragment was almost exclusively observed in the inorganic layer considering the preceding measurements; for the depth profile after fifty-one cycles, it was detected deep throughout the sample beginning at the inception of the transition layer. Also, the CO_3 signal and the SO_3 signal were increased along the whole depth profile. Additionally noted, a defined ending of the transition layer could not be determined even after 3000 seconds of sputtering. Therefore, the extent of the transition layer was assumed to be far greater then the total sputter time. In figure 5.18, a small feature was observed at about 2200 to 2600 seconds of sputtering within the transition layer: whereas the LiF and the NO_3 signal exhibited a small increment, the S_2O and the NO_2 signal showed a small decrement. The same behavior was observed at about $2800\,\text{s}$ to a lesser extent. Furthermore, from the beginning of the transition layer at about 300 seconds of sputter time on all signals changed only smoothly that endorsed the open end of the transition layer as well. The boundary from the inorganic layer to the transition layer was set to the end of the peaking for the signals SO_y, and alike the ending of the plateau intensity of the LiF signal. To reveal the structure and composition within the surface region on a closer look, the first 800 seconds are resolved

separately in figure 5.19.

There, the organic and inorganic layers were not as differentiable as for the preceding measurements due to minor changes of the intensities at the interface of these layers. However, the depth profile yielded a discontinuity for several signals at about $80\,\mathrm{s}$: signals like F, SO, NO_2, CO_3, and even Cs, resembling the cesium sputter source, exhibited an unsteady behavior at this point. Therefore, the boundary between the organic and inorganic layer was set there. This assumption is in good agreement with the previous measurements that showed an invariant thickness of the organic layer (compare figure 5.12 and figure 5.14). For the organic layer, the C_2 and the CH_3O signal were significant once again although they did not exhibit a plateau or a continuously elevated intensity like in the previous measurements. Within the first 20 seconds, the intensity of these signals dropped and afterwards rose again in the inorganic layer. On the contrary, signals like LiF, NO_3 and S_2 peaked slightly within the intensity valley of C_2 and CH_3O at about $20\,\mathrm{s}$ of sputtering. Furthermore, the conducting salt could be observed at the top surface decreasing instantly from $5{\cdot}10^2$ to the detection limit within the first 20 seconds of sputtering. No signal yielded any significant abnormality in the measurement curve between 20 and $80\,\mathrm{s}$, however, this region is still assigned as organic layer due to the yet high C_2 signal relatively to the Li_2 signal. Deeper in the sample at the inorganic layer, the sulfur-oxygen containing signals SO_y peaked around a sputter time of $150\,\mathrm{s}$ with a tail intensity till about $300\,\mathrm{s}$ of sputtering. In contrast, the nitrogen-oxygen signals NO_z exhibited a smooth increase in this area that also approached a threshold value towards the end of the inorganic layer at $300\,\mathrm{s}$. The Li_2, LiO, and Cs signals behaved similarly, however, to a steeper extent. Therefore, the end of the inorganic layer was set by the suggested steady state of those signals and the aforementioned signal characteristics of SO_y.
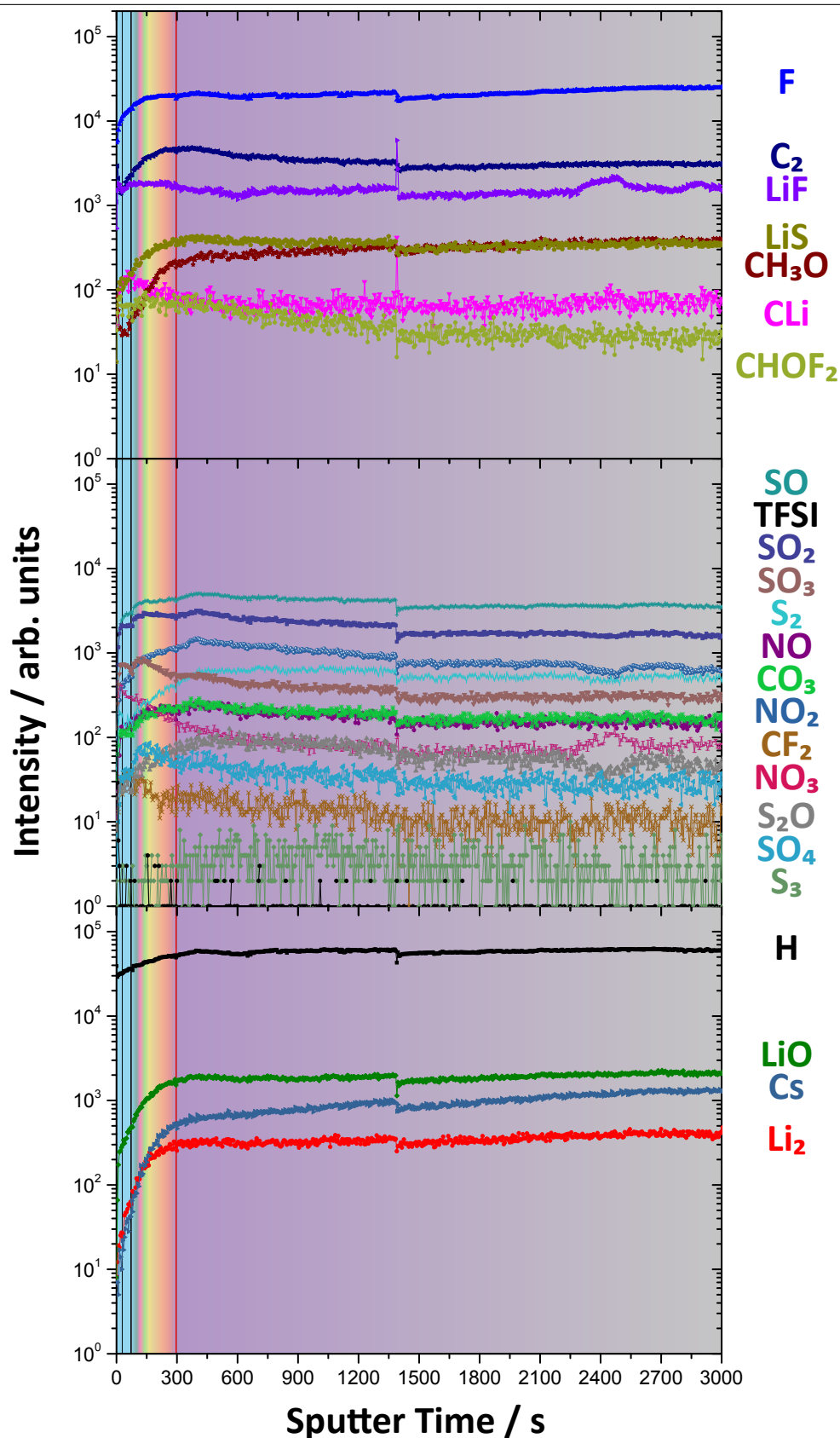
Figure 5.18.: The organic and inorganic layer resemble only a small fraction of the whole depth profile after fifty-one cycles. In contrast, the assigned transition layer excels in thickness and it does not necessarily end together with the depth profile. The artifact at about 1400 s sputter time presumably originates from a temporary instability of the bismuth ion source.
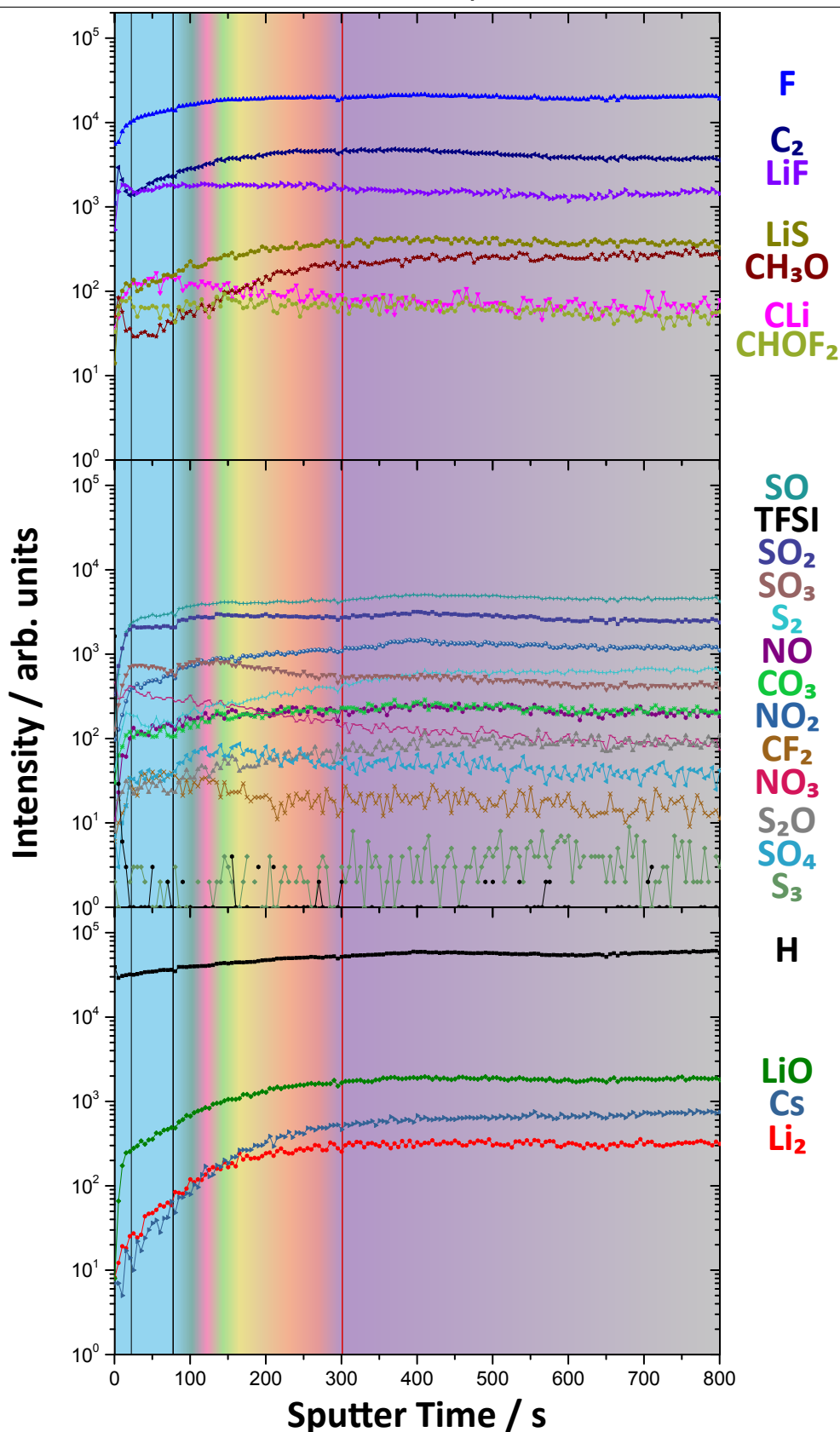
Figure 5.19.: The detailed depiction of the SIMS depth profile illustrates the layered structure close to the surface of the electrode. All intensities exhibit no changes over several orders of magnitude for a short period of time as they are observed for the previous measurements. This shows that the layer structure of SEI is not well defined anymore.

Concluding the XPS and SIMS results, the SEI of the electrode surface changed once again. Interestingly, there are some similarities compared to the first cycle analysis. Both analyses exhibit an enrichment of lithium hydroxide at the beginning of the outer layer and then drops significantly within this layer in the XPS depth profile. Likewise, for both measurements the H signal overtops the other signals in the SIMS depth profile indicating a intensified deposition of solvent decomposition products for both cases. Also, lithium oxide is the prevailing compound within the inner layer of both XPS analyses. However, the transition layer of the first cycle is negligibly thick while the transition layer after fifty-one cycles is exceedingly large in the SIMS depth profile. This evolution of the transition layer is caused by the progressive stripping and deposition of lithium and its ongoing reaction with the electrolyte. Thereby, the decomposition products and the conducting salt LiTFSI are buried underneath the inorganic layer simultaneously. This expansion of the transition layer is only possible if the layer is electric conductive. After fifty-one cycles, the transition layer becomes large to such an extent that its dimension cannot be determined by the already extensive measurement anymore. Indeed, there still has to be ionic conductivity, however, strongly reduced by the poor conductivity of the SEI. This is presumably caused by the high fraction of oxide species like lithium oxide and sulfate as well as by the decrement of lithium carbide and sulfite. This is notable since the XPS depth profile also yields a remarkable deposition of lithium metal within the SEI layer forming a kind of metal interlayer. On the one hand, this suggests a hindered diffusion to the electrode in combination with a sufficient electronic conductivity through the transition layer most likely maintained by the incorporation of this lithium metal within the SEI. On the other hand, the reactivity of this lithium metal interlayer must be suppressed by a passivation coating because the concentration of oxidized species like hydrocarbons and lithium sulfate is greater than the concentration of their respective reduced species, lithium carbide and sulfite. The evaluation of the SIMS depth profile supports this thesis by a comparatively high SO_4 signal considering the previously shown measurements. Another indicator for the lower ionic conductivity may be the minor incorporation of the conducting salt into the SEI layer that is expressed by the low LiF concentration in the XPS and the low TFSI intensity in the SIMS depth profile, also in comparison to the the preceding depth profiles. Inevitably, this leads to an enhanced deposition of oxide and sulfate species that may rather block the electrode than the incorporated conducting salt. Also, it seems like that small inclusions, reflected by the LiF and the NO_3 signals, are observed in the SEI where simultaneously the oxidation of the sulfur seems to be suppressed; this is reflected by an opposing declining trend of the S_2O and NO_2 signals to the rising LiF and NO_3 signals in the SIMS depth profile at about $2500\,s$.

Elaborating on the structure of the outer layer in the XPS depth profile, the salt fraction above the lithium metal interlayer is elevated significantly, specifically ren-

dered by the fraction of LiF, Li$_2$S, Li$_2$SO$_4$, Li$_2$CO$_3$, and the alcohol group (H-O-C). Respectively, LiF, S$_2$, Li$_2$SO$_4$, CO$_3$, and CHOF$_2$ are likewise observed in the SIMS depth profile within the inorganic layer. Thereby, CHOF$_2$ presumable indicates alcohol compounds within the sample. However, the slight peaking in both techniques point out that the intersection to the transition layer with the inorganic layer becomes rather smooth reflecting an alignment of the chemical composition between these layers. Again, this alignment is only possible if the reduction capability of the SEI layer is lowered so that the chemisorbed salts are no further changed within the SEI. On the other hand, an enrichment of hydrocarbon species is observed at the top surface by both analysis techniques, pointed out by C-C/C-H and C$_2$ respectively. However, the C$_2$ intensity yields no plateau for the SIMS depth profile and appears to a smaller extent in comparison to the previous measurements. This may be explained by a decreased physisorption due to the more polar character of ionic species like lithium sulfate within the inorganic layer that enhances the adsorption of polar species. Hence, this prevents the adsorption of non-polar species in the same manner. Furthermore, the high NO$_3$ signal in both methods confirms the assertion of the 24th cycle analysis that the electrolyte additive plays a more decisive role and presumably maintains the lithium transport through the electrolyte instead of the conducting salt LiTFSI for higher cycle numbers. Still, there seems to be some conducting salt existing as it can be seen in the detailed SIMS depth profile at the top surface (compare figure 5.19).
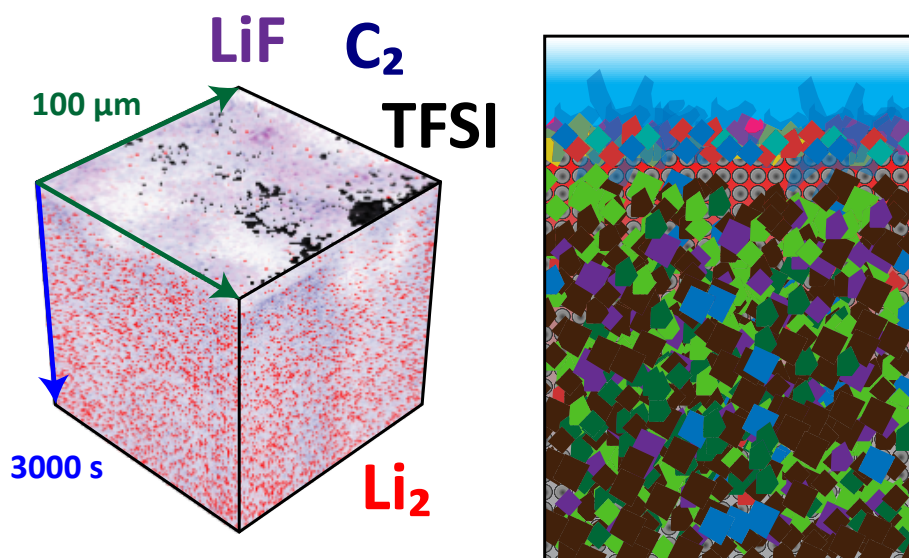
Figure 5.20.: At the top surface of the 3D reconstruction for the fifty-first cycle, some residual conducting salt is observed. In general, there is a homogeneous distribution of all other signals that emphasize the alignment of the layer structure. The proposed SEI structure points out the intermediate lithium layer as well as the oxidic character of the SEI in the depth.

In figure 5.20, the proposed SEI scheme is illustrated as well as the 3D reconstruction of the SIMS data. The electrode is vastly covered by oxidic species that lead to deposition of the lithium metal interlayer within the layer system. This is presumably caused by the diminishment of the ionic conductivity through the SEI to the native lithium electrode. The lithium metal interlayer may resemble the phenomenon lithium-plating which is usually observed at the top surface of a graphite electrode. When lithium-plating occurs, the cell reaches a nascent state for the growth of dendrites. Also, the diminishment of the conducting salt LiTFSI within the layer structure affirms that the transport through the SEI layer as well as through the whole cell may be hindered. By this, the cell resistance as well as the overpotential increase which substantially leads to a reduced energy density and, above all, to a reduced power density due to retarded electrode kinetics. However, the auxiliary of lithium nitrate may maintain the lithium transport to a certain extent. Both the emerging lithium-plating with the consequentially inevitable dendrite growth and the cumulative SEI, impeding the access to the native electrode, are potential causes for the stall of the reversible chemistry and, thereby, lead to the malfunction of the cell. This final case concerning the electrochemical breakdown of the cell is treated in the following subsection completing the insight into the formation mechanism of the solid electrolyte interphase.

5.1.6. The SEI after the Ninetieth Cycles

To conclude the whole section, the measurement of a long-term running cell with malfunction process is evaluated. This malfunction cell did not work correctly after thirty-two cycles exhibiting only a charge and a discharge capacity of about $240\,\text{mAh}\,\text{g}^{-1}$ (compare figure 3.8). The already described failure mechanisms are pronounced for such a malfunction cell. This final examination shows the sources of disintegration directly on the surface structure and composition.
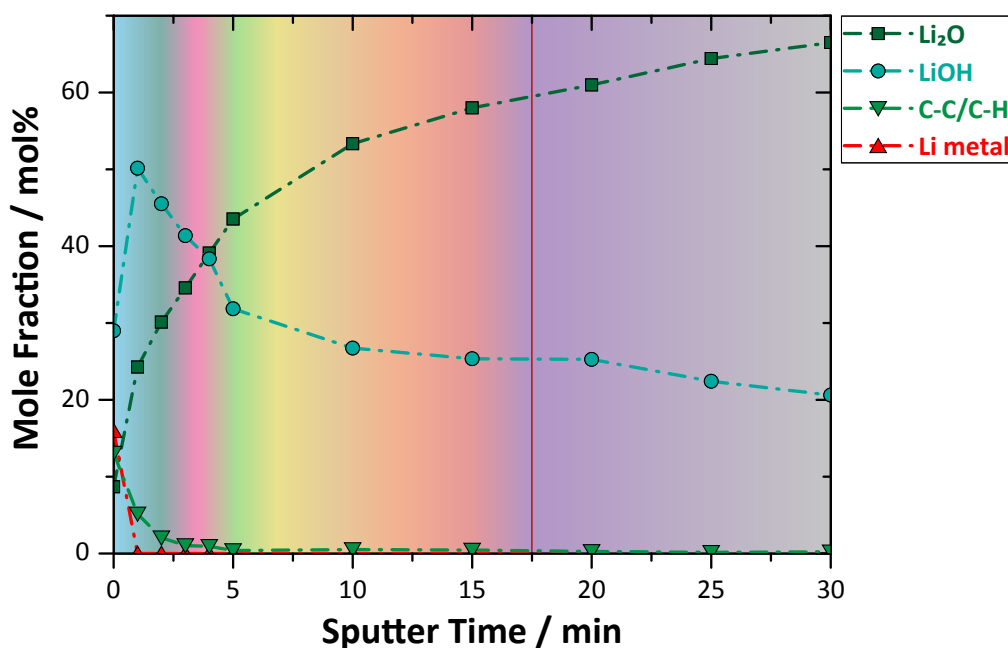
Figure 5.21.: The XPS depth profile after ninety cycles exhibits the typical opposing trend of lithium oxide and lithium hydroxide and hydrocarbons at the top surface, however, lithium metal is also observed at the top surface which is remarkable since the surface stands in contact with the electrolyte.

The XPS depth profile in figure 5.21 revealed that the major compound within the depth of the sample was lithium oxide. Its mole fraction rose from below 10 % to over 30 % after the first sputter step, then still increased substantially to about 55 % till 10 minutes of sputtering, and afterwards more steadily to over 65 % at the end of the depth profile. Meanwhile, the mole fraction of lithium hydroxide dropped steeply from about 50 % after the first sputter step to about 30 % after 5 minutes of sputtering. Afterwards, its fraction remained constant till the end of the depth profile where it reached a fraction of just over 20 %. At the top surface, the fraction of lithium hydroxide was below the measurement after the first cycle and contributed only with 30 % to the detail spectra. Instead, hydrocarbons and, remarkably, lithium metal were observed for the top surface measurement by the XPS examination. The

appearance of hydrocarbons with a fraction of about 15 % at the top surface was consistent with the previously examined measurements, however, the appearance of lithium metal with a significant mole fraction of 15 % at the top surface close to the electrolyte was quite unusual. Lithium metal could not be detected after the first sputter step anymore whereas hydrocarbons dropped to about 5 %, then the mole fraction ceased to the low ppt range till the end of the depth profile.

The depth profile for the phases of minor mole fraction (figure 5.22) yielded even higher fractions of lithium sulfide, lithium sulfite, lithium sulfate, lithium nitrite, lithium nitrate, and aromatic carbons compared to the preceding measurement after fifty-one cycles. On the contrary, the amount of lithium carbide became negligible. Still, the fractions of highly oxidized species like lithium sulfate and lithium carbonate were prevailing over the whole depth profile. Besides lithium sulfide that exhibited the highest mole fraction within the inner layer for all measurements in this chapter, all signals decreased smoothly after 5 minutes of sputtering. Indeed, all these signals were slightly elevated in the range between 2 and 5 minutes, however, no distinctive layer structure could be determined due to an alignment of the layer composition over the whole period of the depth profile. In spite of this appearance, the inner boundary was set between 15 and 20 minutes tentatively because most salt signals remained constant after 20 minutes of sputtering.
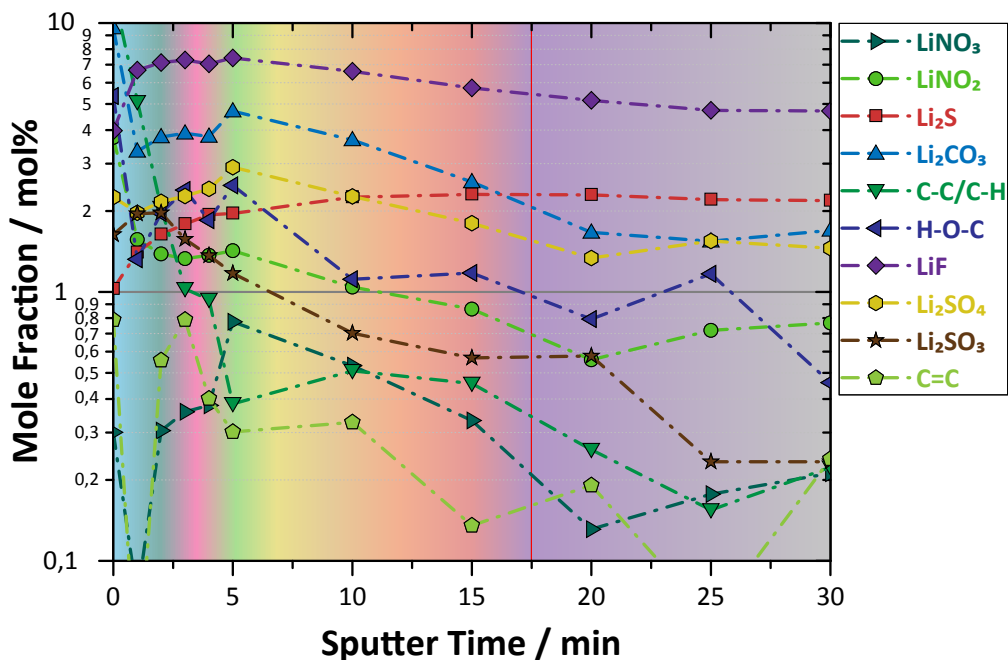
Figure 5.22.: After ninety cycles, primarily oxidized species like lithium carbonate and lithium sulfate are visible in the XPS depth profile of the phases with minor mole fraction. Also noted, lithium sulfide yields an elevated mole fraction in the depth in comparison to the previously illustrated XPS depth profiles.

In conclusion, the mole fraction of several salt compounds increased in the depth profile after ninety cycles compared to the examination after fifty-one cycles. Notably, the overall concentration of carbon-containing phases like Li_2CO_3, H-O-C, and $C=C$ dropped significantly in the depth; hydrocarbons and carbide vanished and were barely detected in the inner layer. Furthermore, lithium hydroxide exhibited a continuously high fraction, only comparable with the first cycle analysis. However, the reduced or lithiated species dominated for the first cycle, while oxidized species prevailed in the XPS depth profile for this analysis of a malfunction cell. Also, fractions of lithium nitrate and its potential decomposition product $LiNO_2$ could not be detected after the first cycle but they could be observed within the SEI layer after the ninetieth cycle.

For the SIMS analysis, the evaluation of the depth profile (see figure 5.23) was generally complicated due to an unforeseen malfunction of the bismuth emitter during the data acquisition. This resulted in a decreasing intensity for all signals and punctual dropouts of the source due to the instability of the primary ion current. Therefore, the attention was set on relative ratios with the H signal as reference because this signal exhibited the greatest steadiness concerning all measurements. A normalization to this signal would have been appropriate, however, the application of a normalized illustration of figure 5.23 was discarded to enable the comparability to the other measurements. At the end of the depth profile, all sulfur-oxygen compounds S_xO_y exhibited a high intensity as well as the intensities of S_2, S_3, and NO_z. However, no major changes were identified for the wider part of the depth profile. Despite of this, a layered structure was proposed under consideration of the slope changes at the beginning of the depth profile.

To resolve this layered structure in detail, the top 800 seconds of figure 5.23 are depicted separately in figure 5.24 similar to the measurement after fifty-one cycles. In this detailed illustration, there was a first discontinuity at about 30 seconds and a second one at about 300 seconds. The first discontinuity was described by the C_2, the F, the H, the Cs, and the CO_3 signal while the second one was rendered by SO, SO_2, S_2O, NO_2, and S_2 in particular. Similar to the previous measurements, the organic layer could be subdivided into a polymer layer and into a layer where the precipitation of dissolved sulfur and salt species were presumably observed. This inner interface of the organic layer was described by the first discontinuity. At the top surface, the polymer layer was resembled by all carbon-containing signals like LiC, C_2, CO_3, CH_3O, CF_2, and $CHOF_2$ yielding a peak within the first 30 seconds. Deeper into the sample at the boundary between the polymer and the layer with precipitated species, the intensities of S_2, S_2O, and LiS exhibited also a sharp peak. Then, the layer with precipitated species was primarily characterized by oxidized sulfur and nitrogen species. Specifically, NO_3, SO_3, and LiF were slightly peaking within the precipitation layer. The boundary between the organic and inorganic layer

was assigned to the second discontinuity at 300 seconds of sputtering. However, this assignment of the layered structure was not indisputable. Therefore, there will be a more detailed discussion later on in this subsection.

There are several similarities to the SIMS depth profile after fifty-one cycles. In principle, the layered structure was the same, however, the organic layer enlarged from 80 to about 300 seconds sputter time according to the proposed layered structure. Also, the inorganic and transition layer showed even less magnitude differences for the signals' intensity so that the assigned inorganic layer could be partially merged into the transition layer or even overlayed this layer till the end of the depth profile. Also noted, the intensities of all signals at the end of the depth profile exhibited nearly the same intensity ratios to each other like for the depth profile after fifty-one cycles.
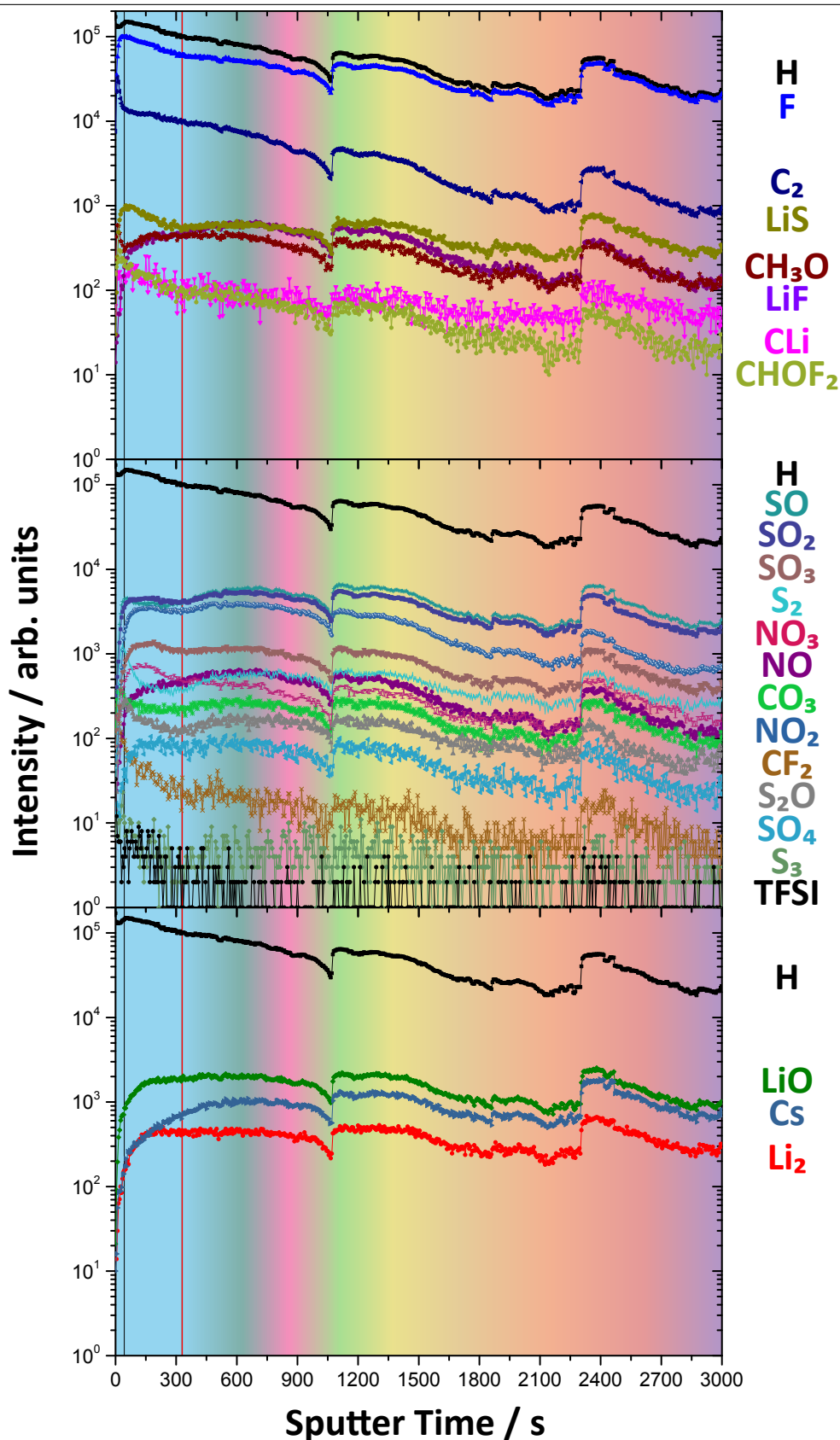
Figure 5.23.: The SIMS depth profile after ninety cycles is distorted due to the expiration of the bismuth analysis gun. A throughout high intensity of the various inorganic signals can sill be seen in the middle while the intensity of Li_2 declines to a lower level.
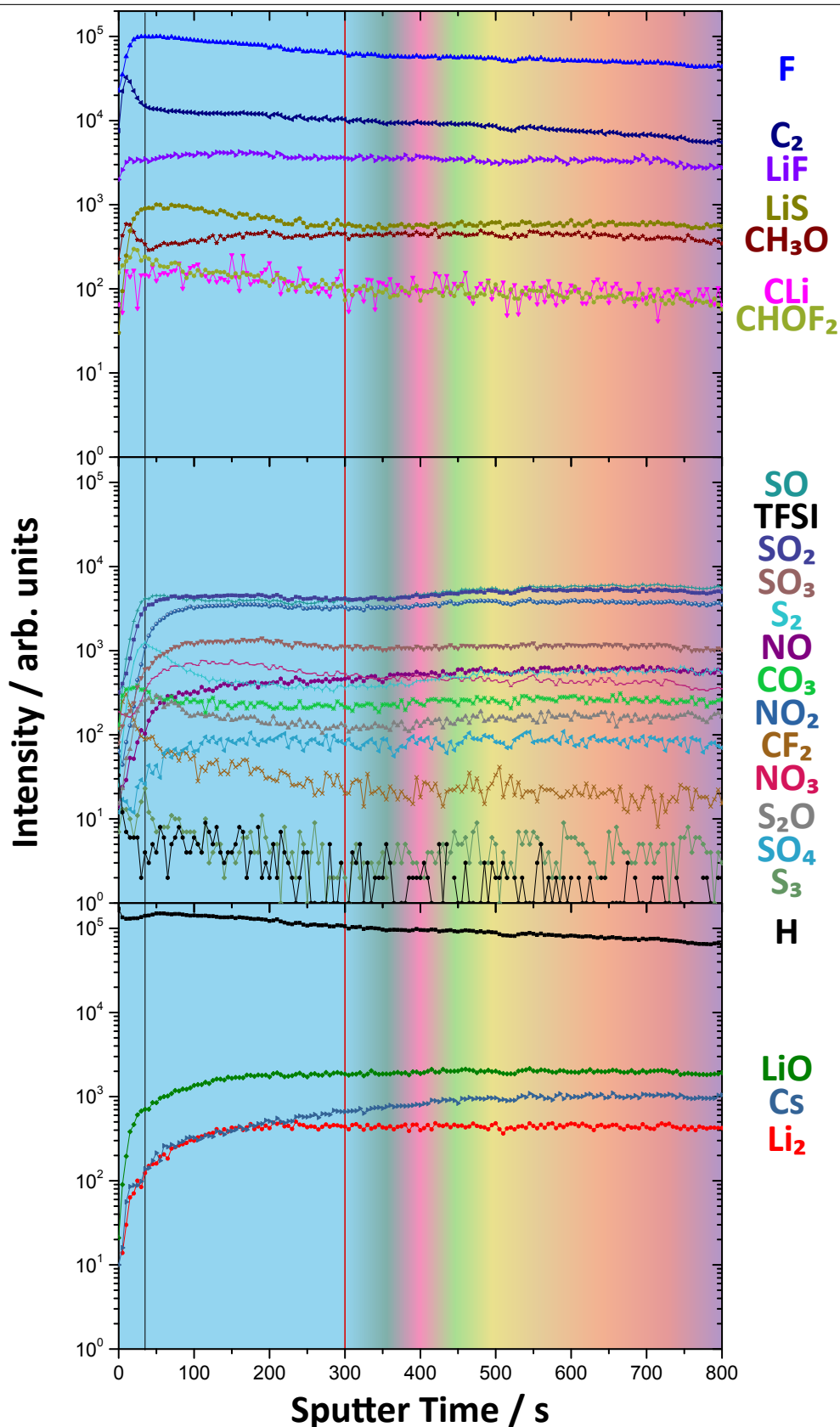
Figure 5.24.: In the detailed depiction of figure 5.23, the primary changes are visible within the first 100 seconds of sputtering. The organic layer for carbonaceous and sulfuric signals comprise the polymer and the subsequent layer consisting of precipitated species, respectively. The boundary with the inorganic layer is proposed due to the slightly increment of the sulfur- and nitrogen-oxygen signals.

Reviewing the SIMS and XPS results together, the layered structure will be discussed in detail. To begin with, the inner and outer layer, found in the XPS measurement, resemble the organic and inorganic layer, found in the SIMS profile, respectively. Thereby, the XPS exhibits an evolution of the fifty-first cycle by yielding even higher mole fractions for the formed salts. Likewise, the respective salt signals decrease only smoothly in the depth of the sample describing a stronger passivation of the electrode surface that is observed in the SIMS depth profile as well. The assignment of the inorganic layer in the SIMS measurement relates to the observation that the intensity of SO, SO_2, CO_3, and other oxygen-containing salt signals rise in all the previously illustrated inorganic layers. This can be seen also for the measurement after the ninetieth cycle, particularly under consideration of the H signal as reference. Admittedly, the organic layer then exhibits some features like peaking of the SO_3 and NO_3 signal that indicate the inorganic layer instead for the preceding measurements. However, the C_2 signal remains relatively high to these signals in the range to 300 seconds so that this applied range sill seems to be reasonable. Also, the H-O-C group exhibits a high intensity within the whole XPS depth profile that further supports the idea of a wide organic layer. A look at the end of the SIMS depth profile reveals that it is still part of the inorganic layer. The end of this layer is not reached by the measurement similar to the transition layer in the fifty-first cycle analysis. After ninety cycles, the surface is intensively covered and the whole extent of the SEI is out of scale and, therefore, cannot be determined in a qualitative way. Likewise, the high fraction of sulfuric or sulfur-oxygen species, reflected by both methods, may imply a blocking character of the SEI. Remarkably, lithium metal seems to be stably deposited at the top surface indicating the occurrence of lithium plating at the surface.

As closing experiment, the analysis of a malfunctioned, long-term cycled lithium-sulfur cell discloses the chemical properties of the terminal state (see figure 5.25). The layered structure vanishes nearly completely so that a protective SEI cannot be assumed anymore. Overall, the thickness and the composition of the whole SEI layer has become crucial for the cell performance that may cause the failure of the cell directly or indirectly. Thereby, the ion transport through the SEI is most likely hindered which also leads to the deposition of lithium metal at the top surface assuming a still sufficient electronic conductivity of the SEI layer. Furthermore, the appearance of lithium plating indicates a potential initial step for the growth of lithium dendrites that may short-circuit the negative and the positive electrode and, therefore, it leads to the stall of the cell.
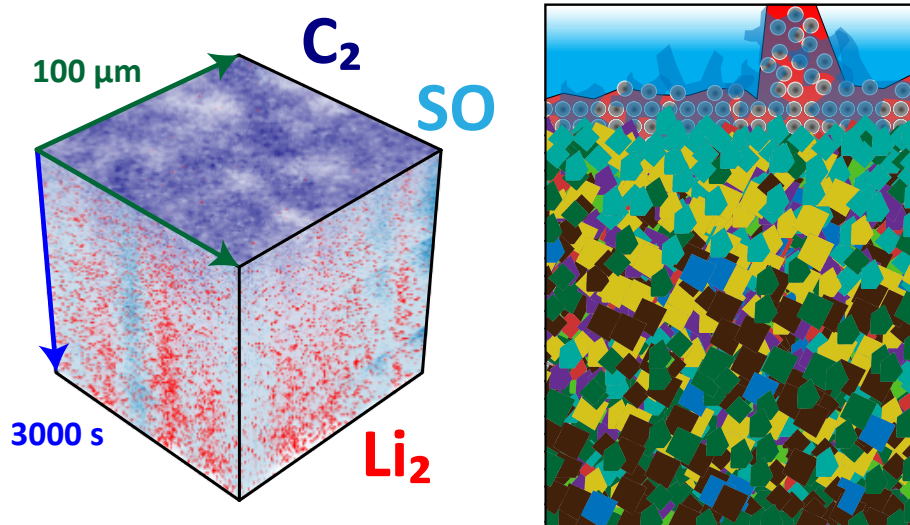
Figure 5.25.: In the SIMS reconstruction after ninety cycles, the layer structure vanishes almost completely. Indeed, carbonaceous species still prevail at the top surface but a distinct organic layer cannot be determined anymore. Due to the roughness of the surface, the Li_2 signal (red) and the SO signal (light blue) exhibit a complementary distribution. The high fraction of sulfur species, also reflected by the proposed SEI, indicates a blocking of the electrode in all probability. This failure mechanism may be entailed by the absence of a stable layered structure, consisting of a distinct organic and inorganic layer at the top surface. Due to this, lithium metal deposits on top of the blocking SEI which leads to the growth of dendrites at the end.

5.2. Conclusion and Discussion – Formulation of an Advanced SEI Model

In this section, the results of the individual examinations are combined to develop a comprehensive model of the SEI formation and aging mechanism. Before this, the appearing distortion effects during the analysis are evaluated that may mislead to a false illustration of the results. Afterwards, the evolution of the SEI is discussed in detail, whereas the individual chemical components within the cell are reviewed subsequently. A schematic illustration of the evolution is depicted in figure 5.28 and the gradual SEI evolution is also evaluated in this subsection as well. Finally, the results of this microscopic view are reconsidered on a macroscopic level to render the malfunction principles for a lithium-sulfur cell.

5.2.1. Significant Distorting Effects during the Analysis

Some remarks on the analysis in the previous section have to be made to get a better view of the results. First of all, the sputter-induced alteration of the surface composition has to be pointed out. As the previous analysis in chapter 4 shows, the oxygen-containing compounds are reduced which leads to a substantial formation of reduced oxygen species like lithium oxide or lithium sulfite. Some of these oxygen species can also vaporize into the UHV and, thereby, they are ablated from the sample surface. For the analysis of the lithium electrode, the sputtering process primarily leads to the detection of remaining lithium oxide and lithium hydroxide in the XPS depth profiles. For instance, the decomposition of sulfur-oxygen species may lead to an enhanced appearance of lithium sulfide and lithium oxide by sputtering the lithium electrode so that the actually depicted mole fraction of all these compounds may be misleading in the XPS depth profile. Therefore, the previously proposed schematics of the SEI barely contain any lithium sulfide. Likewise, the formation of lithium carbide close to the electrode surface in the inner layer is more suggested than an occurrence at the top surface. There, an appearance of lithium carbide may be caused by the sputtering of lithium alkoxides or other organolithium compounds formed at the electrode surface during cycling. Furthermore, the decomposition of LiTFSI to lithium fluoride is already pronounced after the first sputtering step that is already evidenced by the preliminary XPS experiments in the previous chapter. However, the SIMS depth profile clearly exhibits a remarkable signal of the complete TFSI molecule. The lesser extent of sputtering damaged has to be emphasized for the complementary SIMS measurements here again. Despite the radiation damage cause by the XPS depth profiling, this fact renders a comprehensive illustration of the SEI composition and structure possible.
In addition, the mixing of constituents represents another effect induced by the
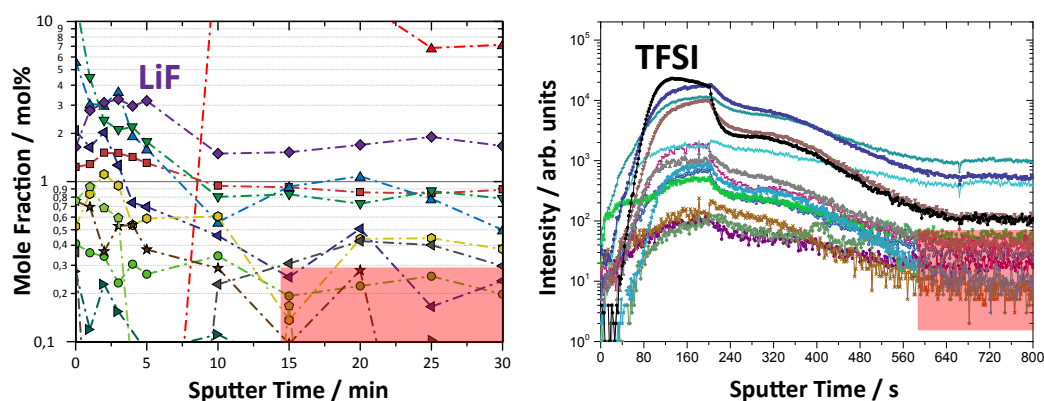
Figure 5.26.: The characteristic regions for the mixing effect are emphasized by the red boxes within the XPS and SIMS depth profiles. Furthermore, the higher sputter damage during the XPS analysis leads to the formation of lithium fluoride while the whole TFSI molecule can be detected excellently with the SIMS technique.

ion-bombardment of the sample which leads to intensity fluctuations in the depth profile (compare Ref. [90]). Due to the generally discontinuous course of the XPS breakpoint measurements (compare section 3.3), however, the mixing effect cannot be estimated precisely. Also, SIMS is a very sensitive method for low concentrations in contrast to XPS so that the signals close to the detection limit exhibit a similar fluctuation like for a mixing effect (see figure 5.26). The effect is less pronounced and signals that exhibit a fluctuation are not considered in their behavior in this thesis.

Another distorting effect is given by the surface roughness. In the SIMS 3D reconstructions of the second, fifty-first, and ninetieth cycle (compare figure 5.27), the lateral distribution of the C_2 signal is nonuniform that indicates a rough surface. Particularly, the measurement after the ninetieth cycle exhibits an inhomogeneous lateral distribution of the Li_2 and SO signal over the whole depth that suggests a nonuniform spatial deposition of lithium and electrolyte decomposition products. Therefore, a rough surface can be assumed due to this spatial distribution. A similar assumption can be made for the fifth-first cycle measurement where a distinct layer structure is absent as well and an inhomogeneous distribution of the LiF and C_2 signal is visible. As mentioned in the detailed consideration of the second cycle (compare subsection 5.1.2) the roughness of the sample surface leads to a depth broadening of all signals.

For the first, fifth, and twenty-forth cycle analysis, the C_2 signal is homogeneously distributed in space so that the surface layer is assumed to be planar for these measurements. Since comparable lateral images of the XPS technique are unfeasible due to the lack of lateral resolution or energy resolution, the influence of the roughness

on the depth resolution cannot be estimated by this technique in a reasonable manner. Also, the features like the deposition of holes or fissures (compare section 6.3) are included into the XPS depth profiles and supposedly distorted the depth profile by a small extent.

5.2.2. Aging Mechanism of the SEI Film

Thickness Evolution of the SEI Film

One direct consequence out of the distortion effects is the difficulty to define a depth scaling. Besides the inhomogeneous composition, the assumed vaporization of oxygen-containing signals leads to biased sputtering yields which even impedes a proper estimation of the depth scale. Therefore, only the sputter time is depicted as depth axis and a scaling has to be handled with care. Comparing the layered structure and the composition, a continuous growth of the SEI film is particularly suggested by the SIMS measurements (see figure 5.27 and previously illustrated SIMS depth profiles). Likewise, the inner boundary in the XPS depth profiles shifts to increasing sputter times with progressive cycle number excluding the measurement of the first cycle in which the surface is proposed to be porous and, therefore, is sputtered rather tardily in the XPS machine. Particularly, the inorganic and transition layer expand during the evolution of the SEI while the thickness of the organic layer remains constant in most instances which is reflected specifically by the SIMS depth profiles.

Constituents of the SEI Film

Concerning the composition, **lithium oxide** and **lithium hydroxide** are significantly observed by the XPS technique after the first, the fifty-first, and the ninetieth cycle for which a functional SEI is not present according to the SIMS measurements. Both compounds reflect the decomposition of the solvents that is enhanced due to the reactivity of the native lithium electrode during the first cycle or the deposition of lithium metal at the upper surface region of the SEI for the fifty-first and ninetieth cycle. However, the carbonaceous signals drop in the SIMS measurements for these long-term measurements due to the decline of the solvent concentration within the cell. Likewise, the mole fraction of lithium carbonate is substantial at the surface for these three measurements indicating the appearance of carbon-oxygen compounds that further supports the thesis of decomposed solvent species in the surface region. The XPS measurements cannot resolve the ambiguity of lithium alkoxides and lithium carbonate due to the sputtering damage (compare subsection 4.1.2), however, the CO_3 signal in the SIMS measurements rather supports the occurrence of lithium carbonate. The appearance of lithium carbonate in the outer layer in XPS as well as in the organic layer in SIMS indicates that lithium carbonate is formed

at the top surface or that it is precipitated from the electrolyte.

The oxidation of the solvent species to lithium carbonate can supposedly be explained by a reaction with the oxidizing agent **lithium nitrate**. Though, the deposition of nitrogen compounds is negligible till the mid-term evolution of the twenty-forth cycle in which the NO_2 signal is the prevailing salt-indicating signal in the SIMS depth profile. Thereby, the 3D illustration of the NO_2 intensity exhibits a nonuniform distribution (compare figure 5.27). The long-term XPS examinations substantiate the appearance of lithium nitrate and lithium nitrite within the electrode SEI. This trend together with a decline of the TFSI signal in the SIMS depth profile militates for an increased participation of lithium nitrate in the lithium-ion transport within the cell. The burial of the conducting salt **LiTFSI** is explicitly depicted by the SIMS measurement of the fifth cycle and the twenty-forth cycle analyses of the respective SIMS depth profiles. In the later one, it exhibits a co-existing high intensity of the NO_2 signal describing the changeover from LiTFSI to lithium nitrate as paramount conducting salt. This is also disclosed by the 3D reconstruction of the SIMS measurement for the cell operated over fifty-one cycles (see figure 5.27) where only a residual amount of the conducting salt is observed at the top surface layer while the NO_2 signal is throughout elevated over the whole depth profile. Lithium nitrate does not only oxidize carbonaceous species but also precipitated sulfur species at the electrode. Therefore, a reduction to lithium nitrite is a reasonable assertion, however, the restrained deposition within the SEI for many cycles may also hint that lithium nitrite is primarily solved in the electrolyte till it participates in the ion transport and then is deposited on the surface as well. In the XPS depth profiles of the long-term cells, lithium nitrate itself only appears at the top surface.

The signal of **lithium sulfate** exhibits a similar profile as lithium nitrate in the XPS analysis, however, lithium sulfate holds a higher mole fraction than its reduced state lithium sulfite for the long-term measurements. This indicates that the deposition of lithium nitrate is fostered when the amount of already oxidized species is enhanced concurrently. Particularly, this is noticeable for the fifty-one cycles analysis where a highly oxidized outer layer exists that most likely leads to the deposition of lithium metal within the SEI. Furthermore, **lithium sulfide** is primarily observed in the outer layer besides for the ninety cycles analysis where it is enriched deep within the sample. The LiS signal in SIMS also endorse the deposition of sulfuric species in the organic layer where other salt species precipitate from the electrolyte as well. Another detected compound is **lithium fluoride** which deposition at the surface is believed to be driven rather by diffusion than by migration. The only source for the detection of lithium fluoride is the conducting salt LiTFSI as it is the only compound comprising the element fluorine. There are two ways lithium fluoride is formed: On the one hand, it may be formed by reaction with the surface of the negative or positive electrode and eventually precipitates at the electrode surface by a diffusion
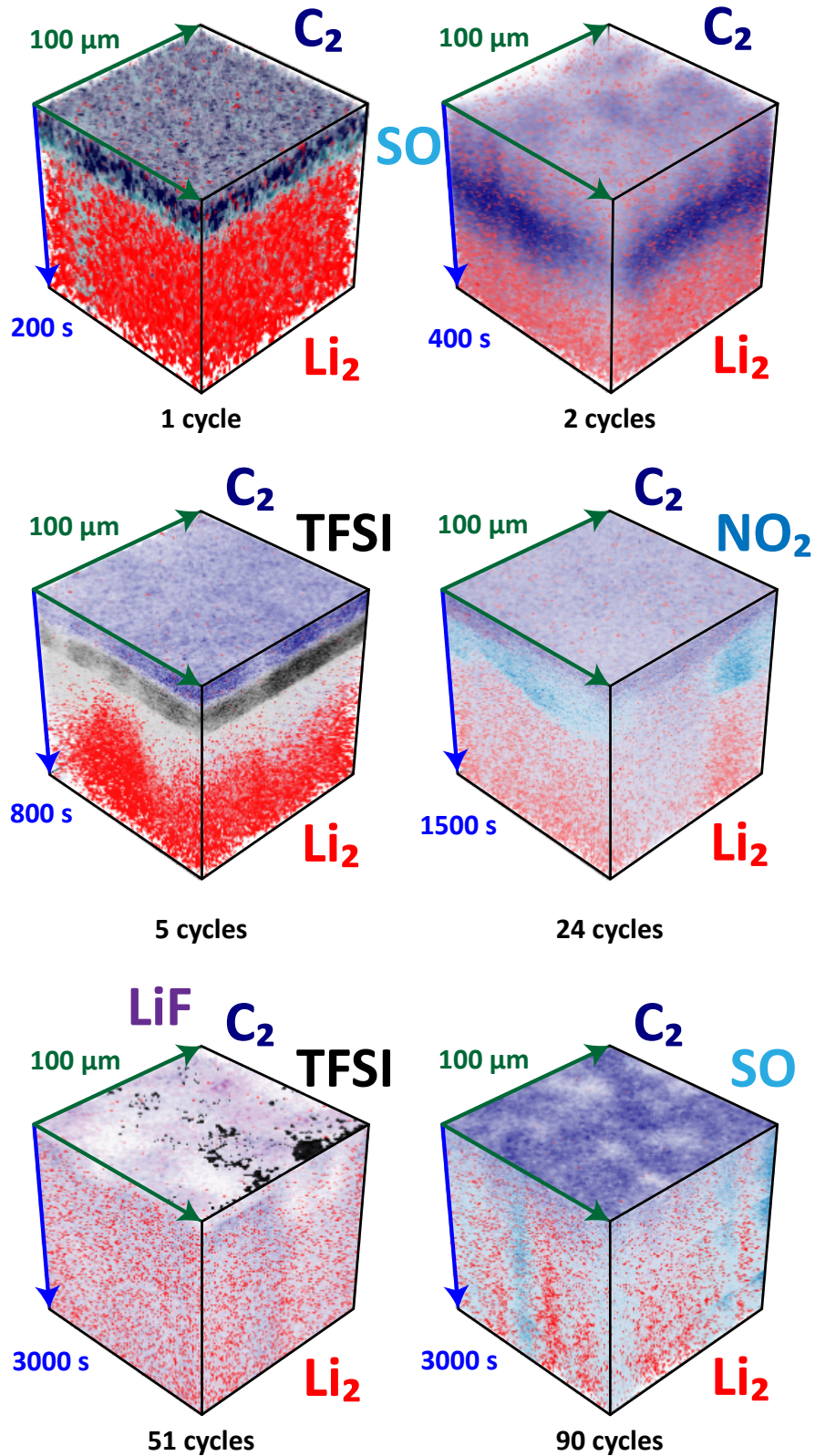
Figure 5.27.: The sequential illustration by 3D SIMS reconstructions depicts the evolving SEI layer structure. Thereby, the depth axis of the cubes (blue) enlarges from 200 to 3000 seconds as the SEI thickens. For the measurements up to twenty-four cycles, a distinct SEI layer structure is observed at the surface.

process. On the other hand, it is formed due to radiation damage (compare section 4.2). However, as it can be seen in the 3D reconstruction of the electrode surface after fifty-one cycles (figure 5.27), they occur at a different lateral position. Indeed, the buried conducting salt supposedly decays in the consecutive cycles after the deposition, however, it is also observed significantly in the organic layer like LiS which leads to the equal conclusion that it is presumably dissolved in the electrolyte. The rather smooth and steady decline in the transition layer suggests that the fluorine anion F^- may be able to diffuse through the SEI; then the concentration gradient obeys Fick's second law of diffusion that is also supported by the depicted exponential decline in the SIMS depth profiles, particularly for the analysis after five cycles. For the long-term measurements a constant saturation seems to be reached.

As already mention for these measurements after the fifty-first and ninetieth cycle, the reduction capability is suppressed in the upper surface region and throughout the whole depth respectively as it is illustrated by the according XPS depth profiles. This leads to the detection of aromatic carbon species whereas **lithium carbide** is detected for the short-term measurements after one, two, and five cycles for which the complete reduction of carbonaceous species by the stripping and deposition of lithium is part of the SEI formation mechanism.

5.2.3. The Influence of the SEI Evolution on the Cell Functionality

The summarized picture of a proposed layer evolution is illustrated in figure 5.28 which takes the abovementioned evaluation of the structure and composition into account. The different inorganic compounds are depicted with a polycrystalline character and organic compounds are illustrated as polymer clusters.

For the **first cycle** analysis, a porous organic layer with a thin inorganic layer below is assumed to be formed at the surface of the electrode. The composition of the SEI is dominated by carbonaceous compounds which resemble the favored decomposition of the solvent.

After the **second cycle**, the SEI becomes more dense, however, it still consists of carbonaceous species. By the stripping and deposition of lithium the SEI species get reduced which also leads to the formation of lithium oxide due to the reduction of the electrolyte like the conducting salt or to the formation of lithium sulfide due to the reaction with the dissolved polysulfides that are both incorporated into the SEI. The fraction of these salt species becomes more pronounced in the analysis after the **fifth cycle**. Here, a distinct layered structure is observed consisting of an organic, an inorganic layer, and a transition layer. The organic layer is enriched with carbonaceous species while the distinct inorganic layer comprises the mentioned salt species. Both layers are supposedly formed by the last discharge and charge cycle. Also, the ongoing SEI growth is particularly resembled by the defined transition
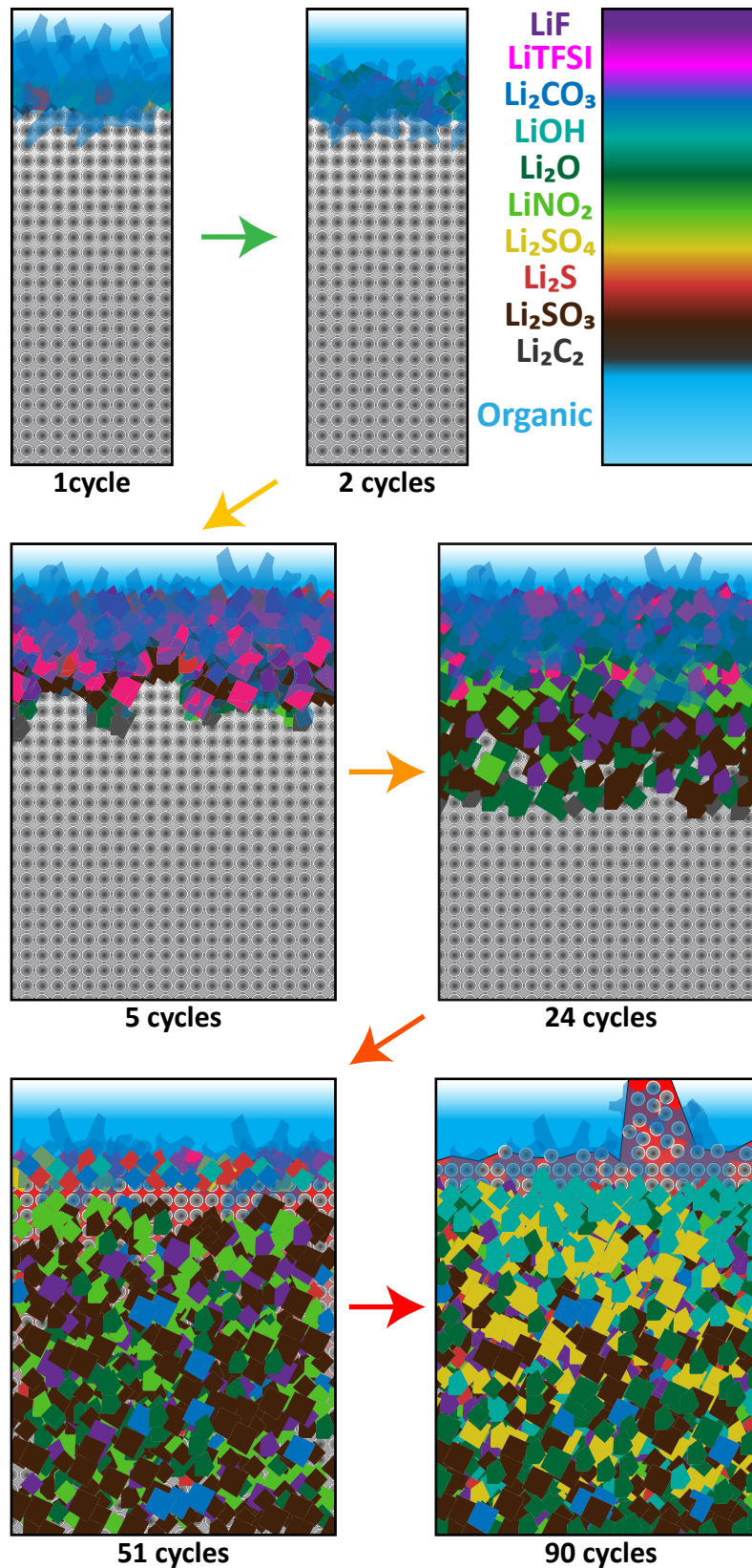
Figure 5.28.: The concluding schematic illustrates the proposed SEI formation that progressively covers the electrode surface. The composition and structure of the SEI results from the concluding evaluation of the XPS and SIMS measurements.

layer below these layers in the SIMS depth profile. By this, the transition layer presumably comprise the SEI formation of the first four cycles. Therefore, a decline of the active material and a loss of electrolyte occurs by the burial of the decomposition products within the transition layer.

In the analysis after **twenty-four cycles**, the SEI enlarges furthermore. Thereby, LiTFSI is on the verge of getting replaced by lithium nitrate as the conducting salt. The layered structure is still distinct, however, the inorganic layer is not homogeneously distributed in space anymore so that the protective character of the SEI starts to diminish.

After **fifty-one cycles**, this aging of the SEI results in a complete passivation of the electrode. Furthermore, lithium metal is observed within the SEI that is protected against the electrolyte by a high concentration of oxidized species at the surface. Only a residual fraction of LiTFSI is observed at the top surface so that lithium nitrate supposedly prevails as conducting salt at this state of the cell. Also, the surface roughness increases which leads to a laterally heterogeneous distribution, however, no significant composition changes are detected over the depth.

The layered structure completely vanishes after **ninety cycles**. Here, the SEI becomes extremely large as well. Concerning the composition, primarily oxidized compounds are observed within the surface region. Remarkably, lithium metal is deposited at the top surface indicating a blocking of the ion transport by the massive SEI.

By this evaluation of the described XPS and SIMS measurements the most important failure effects are pointed out that lead to the cell stalling. The cumulative SEI growth by sulfuric species leads to a loss of active material. Furthermore, the conducting salt LiTFSI gets buried within the SEI which is supposedly compensated by the electrolyte additive lithium nitrate as replacement conducting salt. However, the progressively incorporation of these species or their decomposition products within the SEI leads to the drying of the electrolyte. The passivation film works as a physical barrier for the ion transport to the lithium metal electrode. Therefore, the cell resistance or the overpotential rises with incremental SEI thickness. Finally, this blockage of the ion transport leads to the deposition of lithium metal at the top surface. This lithium-plating is a nascent state for the growth of dendrites that may short-circuit the cell chemically, the demise of the cell.

6. Important Phenomena of the SEI Analysis

In this chapter ,the observation of specific features concerning the SEI analysis are described briefly. First, the effect of washing the sample with the electrolyte is rendered by systematically XPS and SIMS measurements. Afterwards, the observation of a fissure in the electrode surface is illustrated by 3D SIMS reconstructions. Finally, the examination of clusters and holes is depicted likewise by 3D illustration of the SIMS data.

These findings were coincidentally detected during the measurement of several areas on every sample and, hence, no systematically evaluation could be conducted. Also, the determination of the distribution for those effects was not feasible so that the impact on the whole electrode surface could not be estimated quantitatively.

6.1. The Effect of Sample Washing

After dismantling the cell for the ex-situ analysis of the electrode (compare section 3.4), the SEI surface may be covered by an undesired precipitation of conducting salt from the residual electrolyte that is still wetting the electrode surface. This precipitation affects the SEI analysis in a negative way. For instance, the previous chapters show that the conducting salt is extremely unstable during sputtering and, therefore, influences the depth profiling. For this reason, electrodes are sometimes washed or rinsed with a solvent or solvent mixture to dissolve the precipitated conducting salt (compare Ref. [50][64][83]). However, the washing process with electrolyte may additionally dissolve constituents of the SEI, particularly carbonaceous species, which cannot be dissolved due to the saturation of the solvent with sorbates within the assembled cell. On this account, an utilization of a washing step is controvertible.

Analogous to the previous chapter 5, cells with different cycle numbers were examined with XPS and SIMS. Figure 6.1 depicts the XPS depth profiles after one, two, and five cycles. Again, the measurement of the washed sample with twenty-four cycles failed due to the machine malfunction that led to the contamination of the samples. Meanwhile, the concluding SIMS depth profile of the surface in figure 6.2 shows the courses of specific signals for one, two, five, and twenty-four cycles.

The XPS investigation (figure 6.1) revealed a reduction to lithium metal and lithium oxide as prevailing compounds with a mole fraction of about 95 %. Thereby, their respective mole fractions yielded above 70 % for lithium metal and below 30 % for

1 Cycle
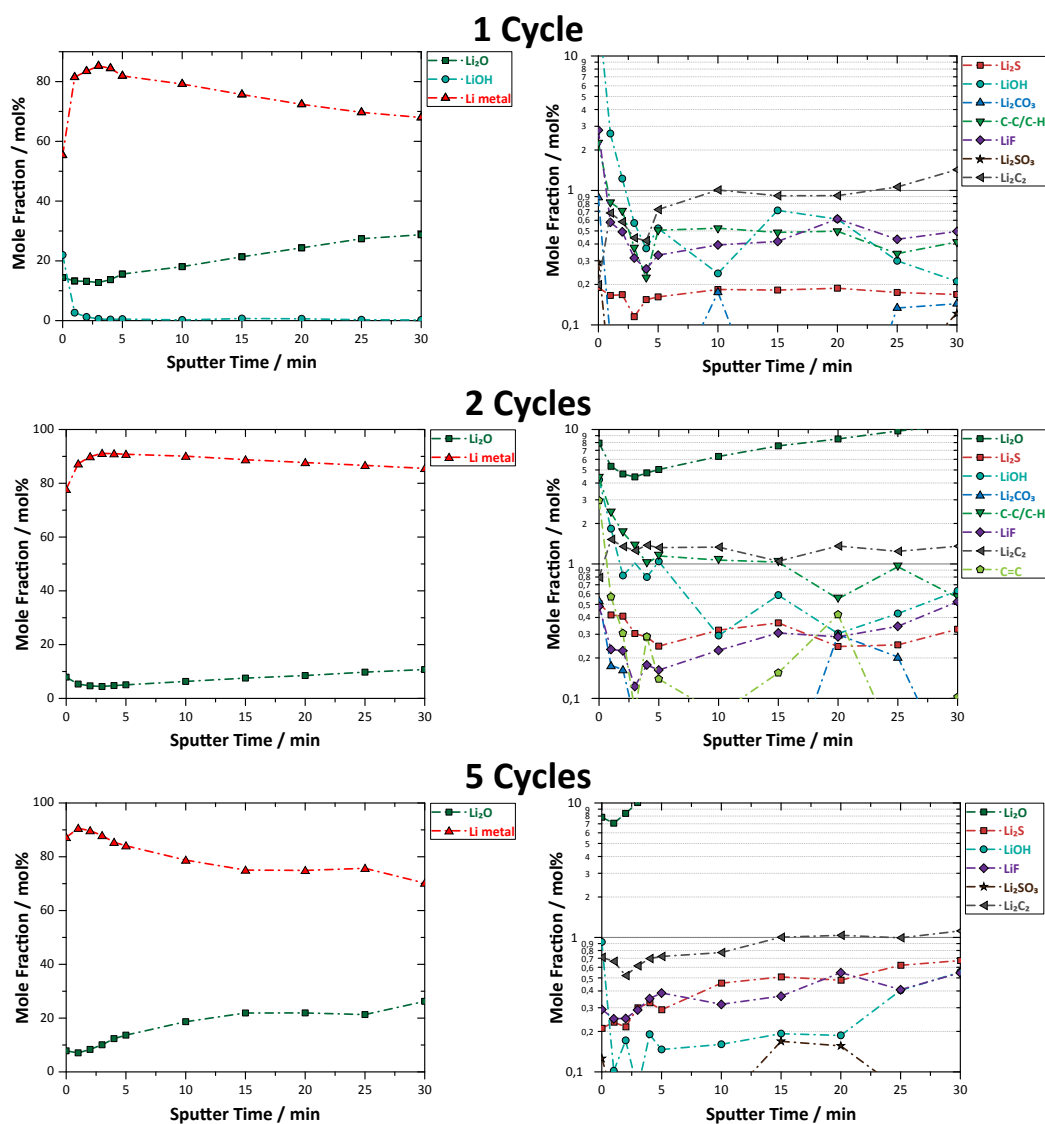
2 Cycles

5 Cycles

Figure 6.1.: The figure shows the depth profiles for one, two, and five cycles. Both major (left) and minor (right) mole fraction graphs of all respective samples are very similar to each other. The washing step seems to reduce the signals to a few constituents and no significant layer structure like for the unwashed samples is visible (compare section 5.1).

lithium oxide in the depth for all measurements. While lithium metal exhibited a decreasing trend towards the end of the depth profile lithium oxide increased coincidentally. Only lithium hydroxide was also observed at the top surface with a significant amount of just above 20 % for the first cycle. In contrast to the measurements of unwashed samples, lithium hydroxide or lithium peroxide did not exhibit an important role in the overall surface composition for the washed sample. As further constituents of the remaining SEI, lithium carbide, lithium fluoride, and lithium sulfide were observed with a total mole fraction in the percentage range. Also, in comparison to the unwashed samples, the amount of lithium sulfate and lithium fluoride declined significantly. Furthermore, the mole fraction for each of them yielded

a constant or slightly increasing trend towards the end of the depth profile. Most of the salt signals like lithium sulfate, lithium nitrate or nitrite, and LiTFSI that were detected during the analysis of the unwashed samples were not observed with a detectable fraction for the washed samples. A distinction between an outer and an inner layer was not applied due to the lack of reasonable tracer signals that would have made a distinguishing possible.

In the SIMS depth profiles most sulfur-oxygen and nitrogen-oxygen signals decreased as well. Therefore, only the relevant signals are depicted in figure 6.2 for the different measurements. Similarly to the XPS results, an actual layer structure could not be detected besides for the first cycle measurement. Here, the signals C_2, CH_3O, SO, NO_2 peak within the first sixty seconds while the Li_2 and LiO signal exhibit a depletion similar to the first cycle of the unwashed samples. The TFSI signal resembling the conducting salt was below the detection limit.

Concluding the XPS and SIMS results, most salt signals like TFSI for the conducting salt vanish due to the dissolution into the electrolyte during the washing step. Especially for the fifth cycle analysis, this represents a significant difference between the washed and the unwashed sample, for which an organic layer, an inorganic layer, and a transition layer could be determined distinctively by the salt signals in the SIMS depth profile. For the washed samples, no layer structure is visible anymore. Also the signals of each measurement align to each other for all the SIMS measurements which impedes the evaluation of reduction and oxidation processes. This is specifically exemplified by the salt signals. However, the rising trends for lithium sulfide and lithium fluoride with increasing depth may endorse the dissolution of them into the electrolyte which leads to a smaller mole fraction at the surface. This affirms the solubility of lithium fluoride and lithium sulfide into the electrolyte like it is proposed in the previous chapter. Furthermore, lithium carbide does not seem to be dissoluble at all since it exhibits a comparable mole fraction to the unwashed samples in the XPS depth profiles.

In general, the washing of the samples resembles a grave loss of information in every respect. For this reason, the here depicted measurements highly emphasize not to wash or rinse the electrodes with a solvent to gain a complete image of the structure and composition by the SEI analysis. The measurements of the unwashed samples exhibit no significant coverage of precipitated LiTFSI at the top surface in this cell system (compare figure 5.27).
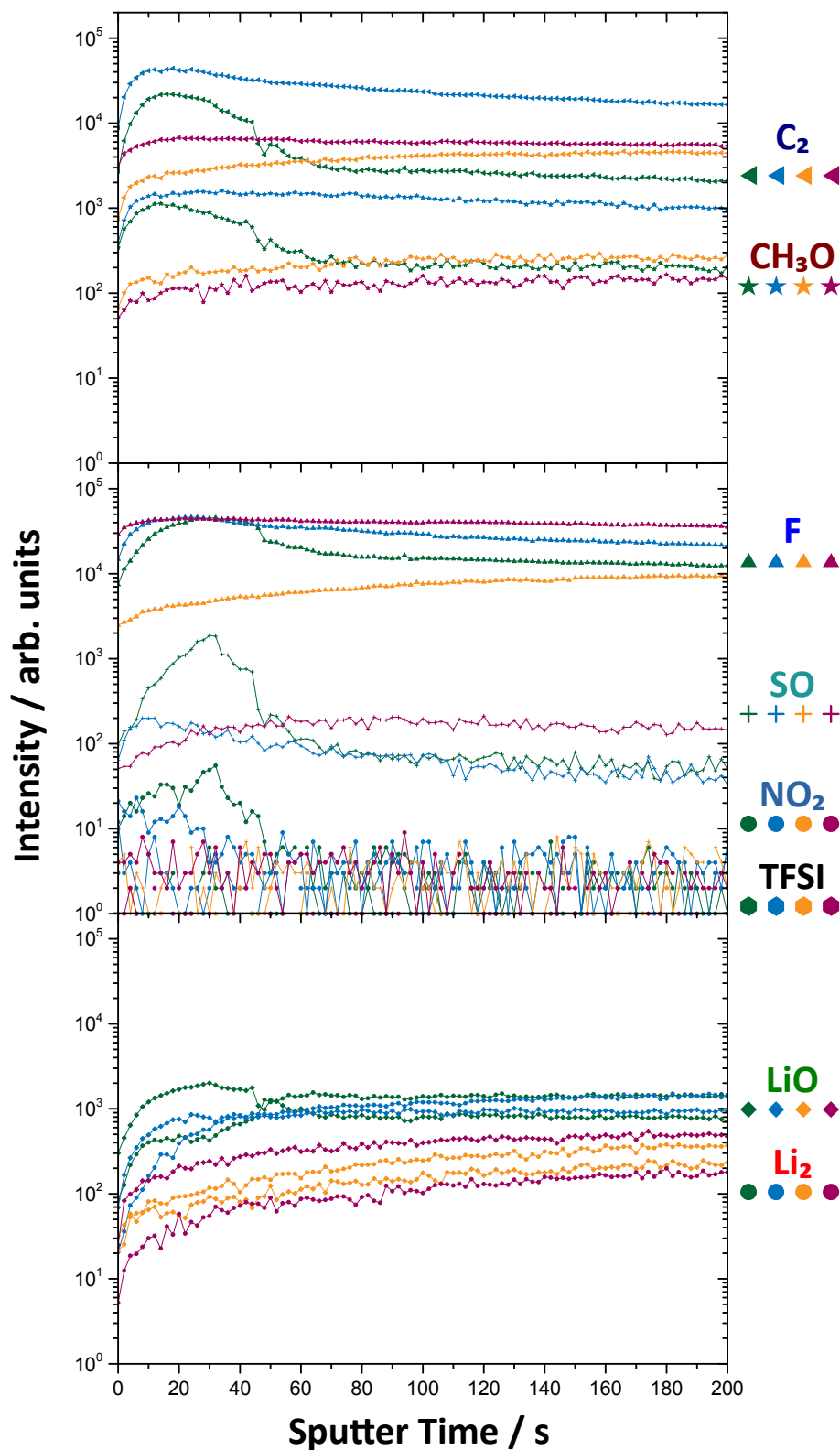
Figure 6.2.: The SIMS depth profiles of the washed samples disclose that the layer structure vanishes by washing except for the first cycle analysis (green). For the analysis of the second cycle (blue), of the fifth cycle (orange), and of the twenty-fourth cycle (violet) just a steady course can be determined.

6.2. The Observation of Surface Fissures

In this section, the detection of a fissure is illustrated by 3D SIMS reconstructions. As already mentioned, the lateral resolution of XPS is not sufficient enough to reveal features on the surface in detail. However, fissures can also be observed by other imaging techniques like Scanning Electron Microscopy (SEM).

The exemplary SEM image (figure 6.3) revealed connecting fissures that were several hundred micrometers long altogether and a few micrometers wide. The fissures were clearly distinguishable from the rest of the surface which was planar to a greater or lesser extent; this was also due to the washing of the sample that was applied before the imaging. At the junction of the fissures, deep holes appeared that might also emerge from the conducting salt clusters (compare section 6.3). The cross-section of these holes amount to about 10 μm.
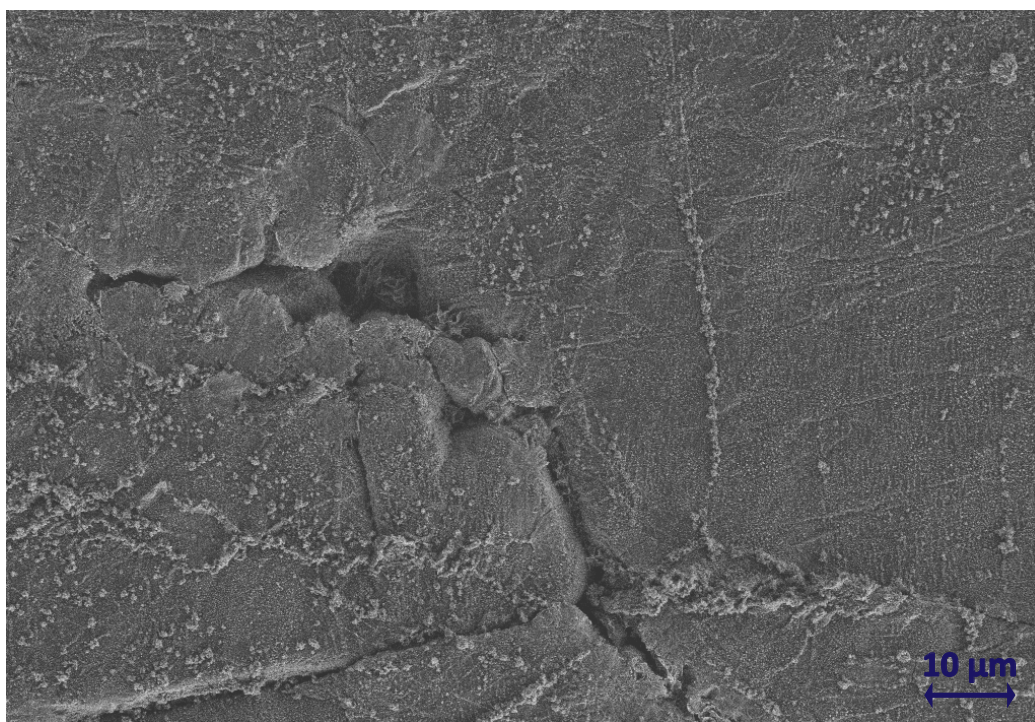
Figure 6.3.: The depicted surface area belongs to a negative electrode after one cycle that was washed with the electrolyte. On the left of the image, long dark fissures and deep holes are observed while the surface is considered as planar on the right side of the image.

While the intensity contrast in SEM is feasible for the determination of the difference in altitude, it is not intuitively determinable in an equal measure for the SIMS technique. There, the intensity is not an unambiguous parameter for the altitude due to the dependence of the intensity on plenty other parameters. However, the
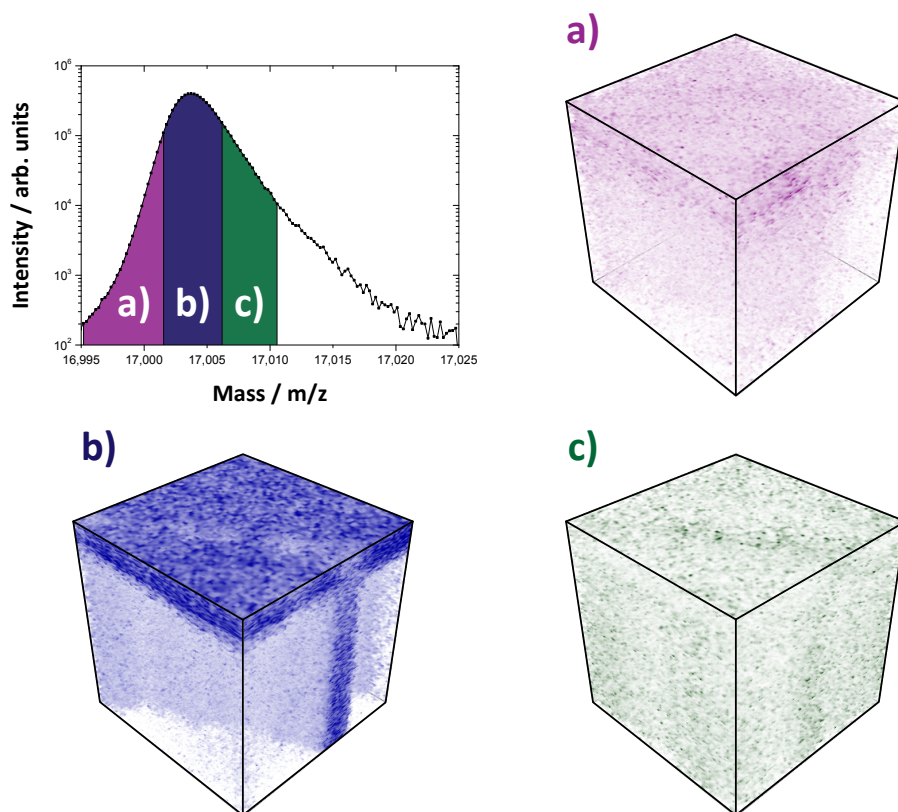
Figure 6.4.: On the top left, the OH peak in the mass spectrum is depicted. The subdivision of the peak into three parts enables the resolution in altitude due to the dependence of the the flight-time on the covered distance for the secondary ions. The greater intensities at higher mass per charge ration for the figures b) and c) indicate that the origin of the signals come from a greater depth than for the planar surface characterized by the figure a).

altitude changes the flight-time for the masses which is depicted in figure 6.4. For a high altitude, the distance and hence the flight-time of the secondary ions decreases and the detected atoms or molecules shift to a lower mass. Contrarily, the distance and likewise the flight-time increases for an fissure and therefore the detection of the secondary ions shifts to a higher mass. However, the difference of the altitude for the feature compared to the residual surface has to be significant so that a difference in flight-time is also observable.

As it can be seen in figure 6.4, the peak in the mass spectrum was separated into three parts: one was assigned little before the region of the maximum, another one was assigned round the maximum, and the last one was assigned after the maximum region. In figure 6.4 b), the maximum region is illustrated as 3D reconstruction. A long line (light blue) was detected from the left corner to the right side at the surface. The intensity for this feature was low within the surface layer and high in the depth of the sample. The region before the maximum (figure 6.4 a)) just reflected

the surface layer while the region after the maximum (figure 6.4 c)) exhibited an increased intensity at the position of the feature line. That means the surface ions at a) were firstly detected and the feature plus the background ions at b) and c) were later detected. Therefore, these results confirmed the formation of a fissure that was detected with the SIMS technique.

To get a deeper look into the constituents of the fissure, several mass signals were plotted as 3D reconstructions as it can be seen in figure 6.5. While the lithium signal Li exhibited a slightly depressed intensity along the fissure line the H, the C_2, and the SO_2 signal held an elevated intensity in the area of the fissure like for the OH signal before. Furthermore, the C_2 signal presumably illustrated the appearance of the already mention holes that were resembled by the two pillars with an increased intensity from the surface to the bulk. Particularly, these pillars were observed in the 3D reconstructions of the S signal and the F signal.

As a concluding outcome, the observed signals at the fissure resemble the electrolyte decomposition products which is substantiated by the C_2, the OH, and the H signal. These are also detected at the surface so that an intrusion of the electrolyte into the fissure structure is supposedly occurring. The origin of fissures may be an increased surface tension due to the appearing of the SEI. When the surface constricts itself due to the reaction with the electrolyte or sulfur species the surface cracks at the weakest spot. Thereby, the observed holes play a decisive role. The conducting salt LiTFSI and the sulfur species are proposed as cause for the holes since the F and S signal exclusively exhibit high pillar intensities. Supposedly, the surface cracks along the perforation formed by these holes. The influence on the cell performance by these fissures and holes cannot be estimated because no distribution of the size and quantity is yielded in this analysis, however, the occurrence of fissures resembles a mechanical instability of the SEI so that a continuous protection of the electrode is less likely and a breakdown in the future cycles may be imminent.
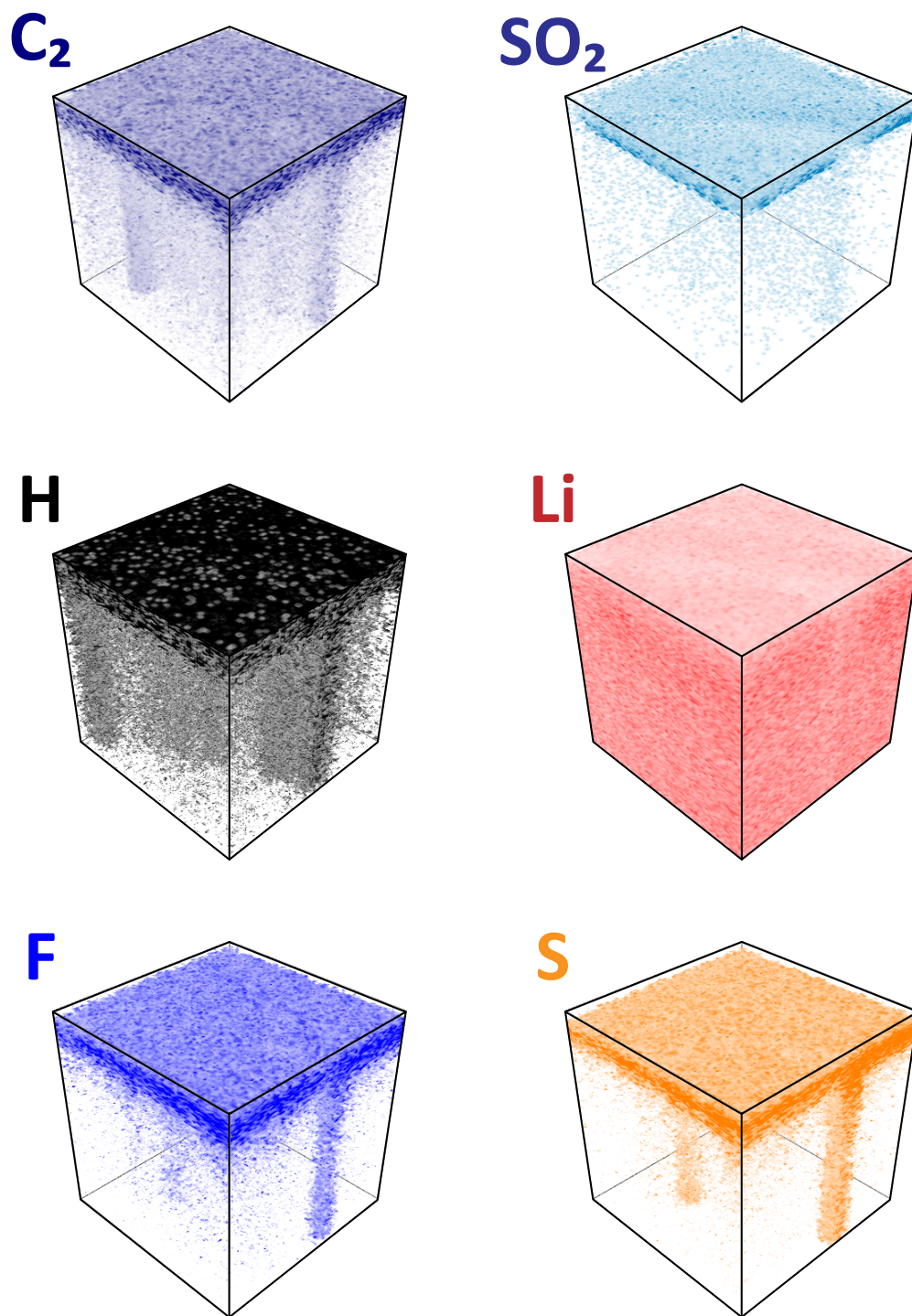
Figure 6.5.: In this figure, the 3D SIMS reconstructions of several signals illustrate a fissure structure that is observed for an unwashed sample after two cycles. While the top and middle signals document the fissure structure, the bottom signals also exhibit the occurrence of holes along the fissure (compare figure 6.3).

6.3. The Formation of Holes and LiTFSI Clusters

In this last section of this chapter the formation of holes with the simultaneous appearance of LiTFSI clusters are investigated in detail. Two measurements, exhibiting a single spot and multiple spots respectively, are disclosed and discussed afterwards. Analogously to the previous section, a suitable mass was selected and divided into different segments with slightly different masses (compare figure B.1). This was applied to the measurement with a single spot for the same sample after one cycle as in subsection 5.1.1. Again, the intensity of the feature appeared at higher masses, hence, from a deeper sample depth. By this, the presence of a hole was identified while the existence of sticking out grains or dendrites were denied at the same time. For the multiple holes, there was barely any evidence of the formation of holes due to the lack of intensity contrast for the mass segments, however, the occurrence of holes were likewise assumed due to the similar composition in comparison to the single hole.

As illustrated in figure 6.6, a hole singularity was distinctively observed by the 3D SIMS reconstructions of the sample after one cycle. Thereby, the diameter of the hole was over $10\,\mu m$. The composition of the hole was characterized by the conducting salt LiTFSI on the one hand and electrolyte plus sulfur species on the other hand. Thereby, the conducting salt, which is resembled by the TFSI signal, clusters at the surface and declines towards the depth of the electrode. On the contrary, the solvent, the dissolved sulfur species, and the conducting salt decomposition products are illustrated by the C_2 and OH signals, the S signal, and the F signal, respectively. These signals prevailed in the depth of the electrode surface. Meanwhile, the Li signal exhibited a lesser intensity at the spot of the hole.

After two cycles, one SIMS measurement revealed a surface region with multiple spots where those LiTFSI cluster were observed (see figure 6.7). Here, the observed clusters had a smaller diameter than for the first measurement. Also, such a cluster was visible deep inside the surface at about the middle level of the 3D cube. Similar to the single spot measurement, the OH, F, and S signal were intensified beneath the elevated TFSI signal. However, the C_2 signal exhibited a stronger intensity from the surface to about the middle level of the 3D model complementary to these three signals that exhibited a higher intensity below the medium level. For both measurements, a definite layer structure was absent at the surface.

To conclude the results from both measurement, holes or channels into the electrode surface can be observed with LiTFSI cluster at the top of them. These holes presumably consist of reaction products from the lithium metal with the electrolyte. As a possible explanation for the formation of this hole structure, a suppressed deposition of lithium may occur at single spots during the charging process. Comparable to the fissure structure analysis (section 6.2), the F and S signal are observed deep in the surface. Therefore, the conducting salt is supposedly the cause for the hole formation or at least contributes to its appearance. The LiTFSI cluster at the middle level of the second cycle analysis may origin from a deposition of the first cylcle. Notably, no fissures are visible for the multiple cluster analysis, however, the absence of the SEI layer supports the previously mentioned thesis that fissures are formed most likely due to the increased surface tension cause by the SEI.
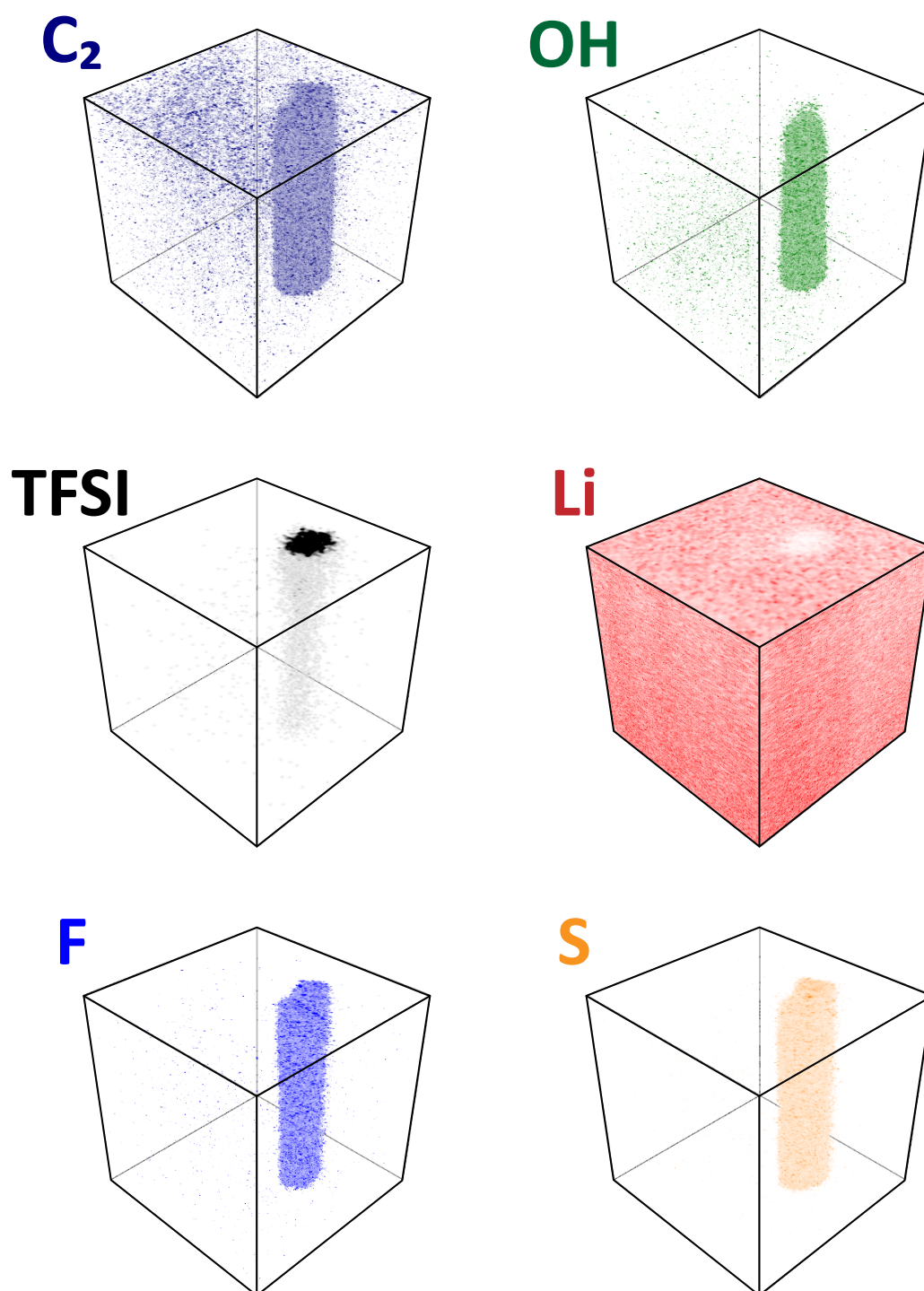
Figure 6.6.: After the first cycle, one SIMS measurement reveals the structure and composition of a hole illustrated by the 3D reconstructions of the depicted signals. While the TFSI signal is intensified at the top surface the other signals, resembling the electrolyte (C_2) or the sulfur (S), and the electrolyte decomposition products (OH, F), prevail in the depth. Also, the Li signal exhibits a complementary trend to the TFSI signal. The z-axis of the cube corresponds to 2000 seconds of sputtering.
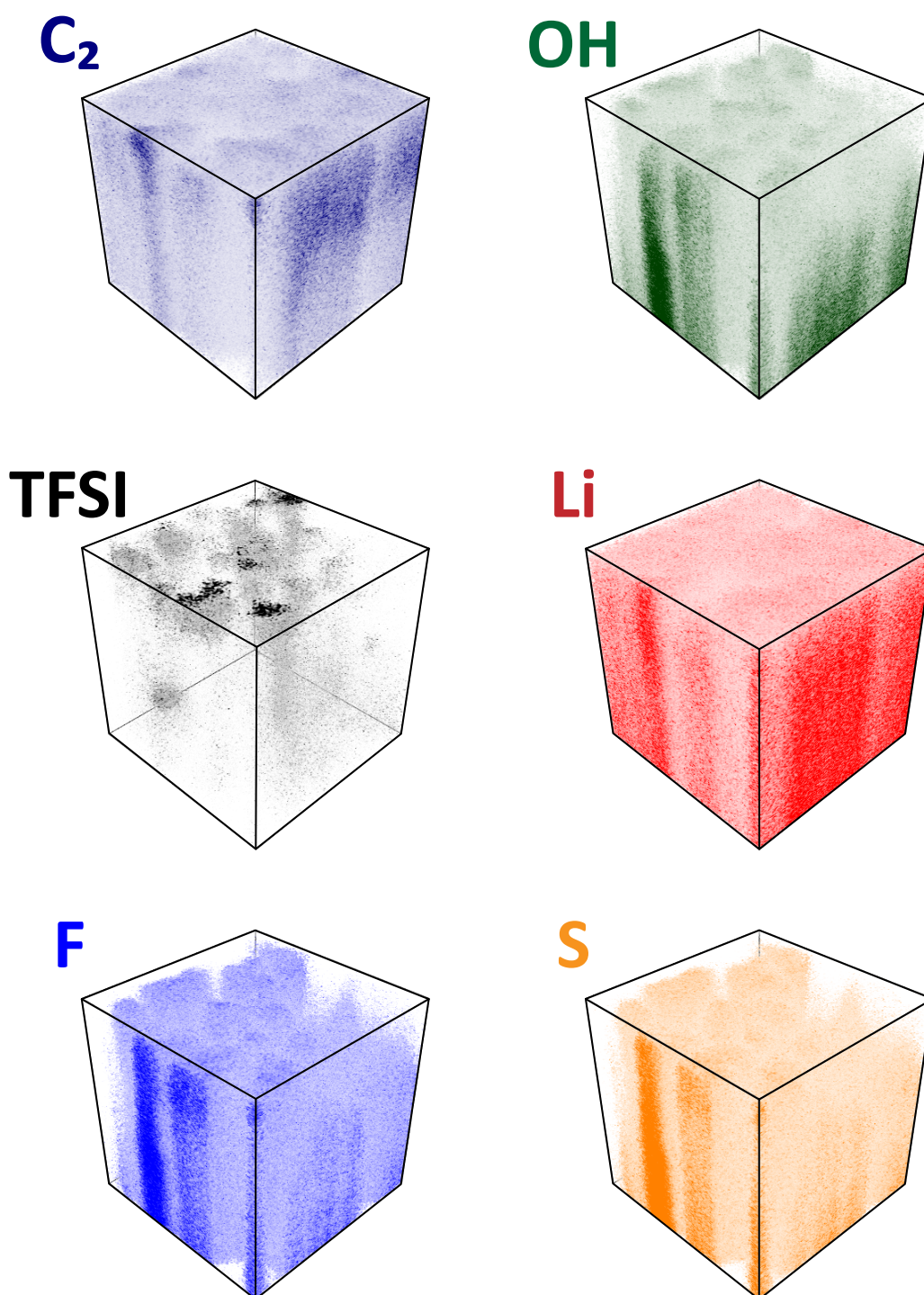
Figure 6.7.: The here depicted 3D reconstructions show the occurrence of several TFSI cluster after the second cycle. Notably, a TFSI cluster can be seen on at the middle level of the according cube (front left). Similar to the single hole measurement, the OH, F, and S signal exhibit a higher intensity in the depth, however, C_2 shows an elevated intensity at the top. Here, the z-axis of the cube corresponds to a sputter time of 3000 seconds.

7. Summary and Outlook

In this thesis, a detailed and consistent approach to investigate the SEI of the negative electrode in lithium-sulfur cells is proposed. An up-to-date overview of literature is given in chapter 2, the experimental fundamentals in chapter 3, the preliminary investigation of the radiation damage with the XPS technique in chapter 4, the systematic measurements of the negative electrode's surface for cells of different cycle numbers with the complementary techniques XPS and SIMS in chapter 5, and notable features for the described analysis in chapter 6.
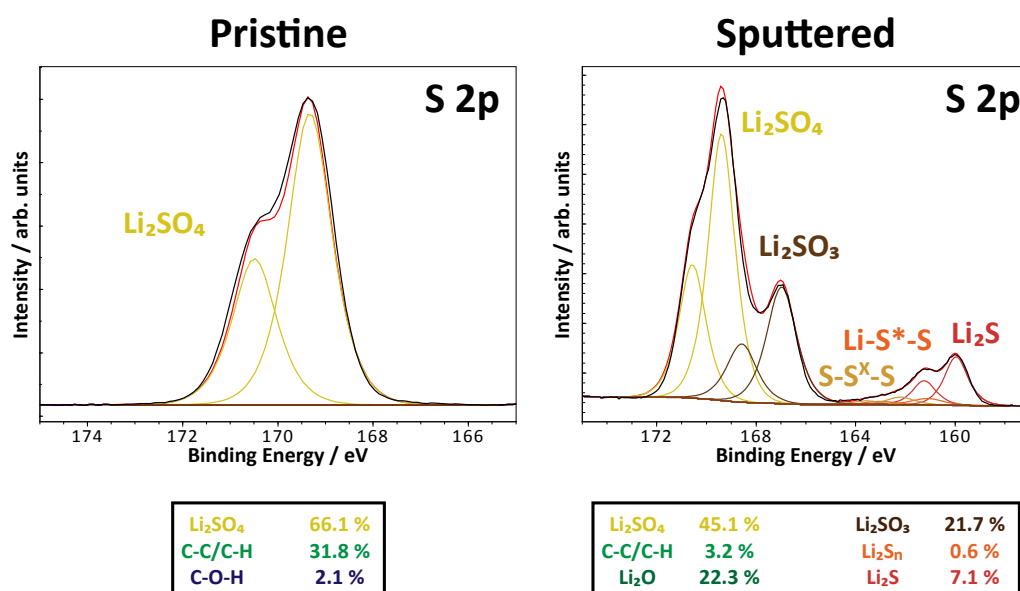
Figure 7.1.: The depicted XPS measurement of the sulfur S 2p line for a pristine and sputtered sample exemplarily shows the obtained insights for the reference measurements. The different peaks are assigned according to the literature and quantified with the peak coupling method. By this, precise reference values are obtained for the binding energy of the respective peaks. Also, the influence of radiation damage is examined by sputtering the pristine sample. Due to the peak coupling method, the quantification is illustrated in mole fraction instead of the commonly applied elemental or component quantification. This leads to a concise presentation of the XPS data in the depth profiles.

In summary, the XPS analysis stands out due to the application of the peak coupling method (compare section 3.4) which provides a concise presentation of the extensive spectra data for the XPS measurements. Thereby, the single peaks of a distinct compound in the different detail spectra are connected with each out so that the peak intensities can be translated to mole fraction. This leads to a more comprehensive illustration of the XPS data for the composition distribution of a surface.

By preliminary reference experiments, the precise peak positions and the quantification of the decomposition of the pristine compounds due to radiation damage are obtained for the depth profiling of the SEI. Therefore, selected compounds have to be investigated in the pristine and the sputtered state. For the lithium-sulfur battery cell system, the sulfur species lithium sulfide, lithium tetrasulfide, and lithium sulfate are considered to be a constituent in the SEI of the negative electrode. Furthermore, the behavior of the electrolyte components LiTFSI and lithium nitrate along with the potential solvent decomposition products lithium carbonate, lithium methoxide, and lithium ethoxide are examined for the same sputter condition as well. In conclusion, an extensive view on the surface decomposition due to sputtering is yielded by these measurements of lithium-sulfur battery specific compounds. Thereby, the analyses provide quantitative results about the sputter decomposition (table 4.3). For instance, the almost complete conversion of the conducting salt LiTFSI to lithium fluoride is remarkable for the sputtering experiments. However, these results about the sputter decomposition are considered only qualitative for the later SEI analysis due to the additional interactions of the compounds during the depth profiling of the SEI. Also, precise peak positions are obtained for the pristine compounds and several decomposition products (table 4.2) which are utilized as template in the subsequent SEI analysis.

A systematic investigation of the SEI is provided by the analysis of the surface with the XPS and SIMS techniques for cells with different cycle numbers. The first and the second cycle represent the initial SEI formation processes and mechanisms where the lithium electrode is processed electrochemially for the first time and then the formed SEI is traversed by lithium ions likewise for the first time. Afterwards, the five, twenty-four, fifty-one, and ninety cycle analyses respectively disclose the short-term, mid-term, long-term, and malfunction state analyses of the SEI evolution.

Thereby, the 3D reconstructions of the SIMS data give new insights into the spatial distribution of the SEI constituents which allows a qualitative description of the SEI evolution. The layered system of the SEI is directly revealed by the data. This layered system consists of an organic layer at the top plus an inorganic and a transition layer below. The thickness of the SEI, particularly of the inorganic and the transition layer, increases with progressive cycle number while the thickness of the organic layer remains constant. With progressive cycle numbers, the spatial distribution of firstly
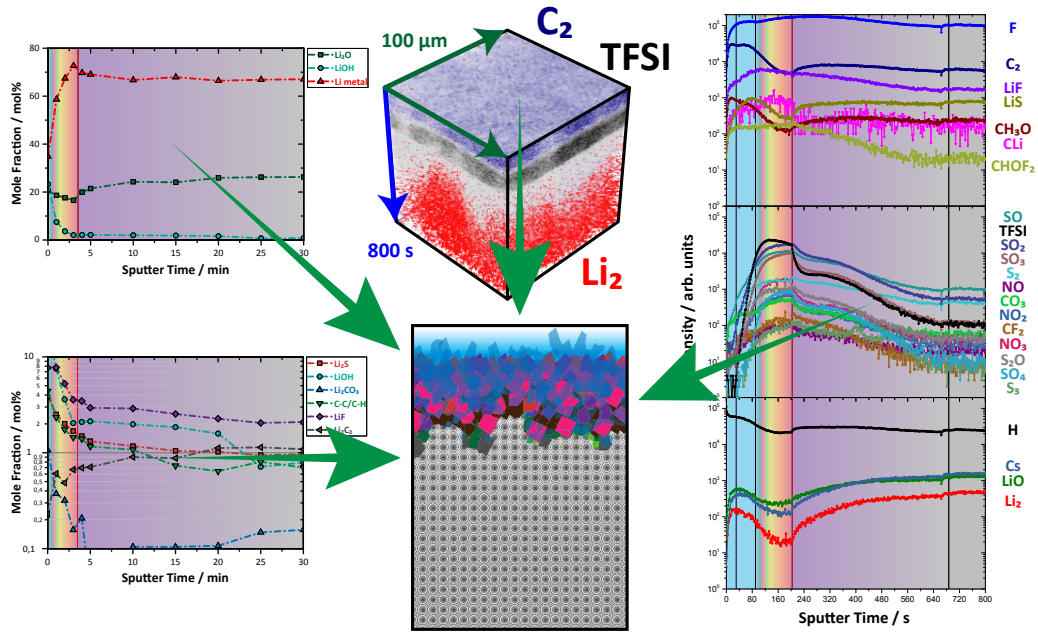
Figure 7.2.: By considering the XPS depth profiles of the major and minor phases (left), the significant signals in the SIMS depth profile (right), and the 3D distribution of those signals in the 3D SIMS reconstructions (top middle), a concluding image of the SEI can be proposed.

the transition layer, later also the inorganic layer becomes heterogeneous which may indicate the instability of the SEI as protective film for the electrode.

Also, qualitative conclusions about the composition of the SEI are yielded by the quantitative analyses with the XPS technique and intensity considerations of the SIMS measurements. It is observed that the conducting salt LiTFSI is buried beneath the inorganic layer within the transition layer which leads to a decline of the conducting salt within the electrolyte. By this, the fraction of LiTFSI within the SEI also decreases and the fraction of lithium nitrate increases for greater cycle numbers. Therefore, an adoption process of lithium nitrate as conducting salt seems to occur within the cell system. Furthermore, lithium metal is detected at the surface in the long-term cycling and the malfunction state examinations. This presumably indicates the lithium-plating process that resembles a nascent state for dendrite growth and thus the failure of the cell.

Summarizing these results, the evolution of the SEI is comprehensively rendered by the spatial distribution of the constituents and by the examination of the composition. By this, concluding images of SEI can be proposed as it is depicted in figure 7.2. In addition, several processes are observed that lead to the stall of the cell. Therefore, this analysis method allows a qualitative consideration of the SEI evolution.
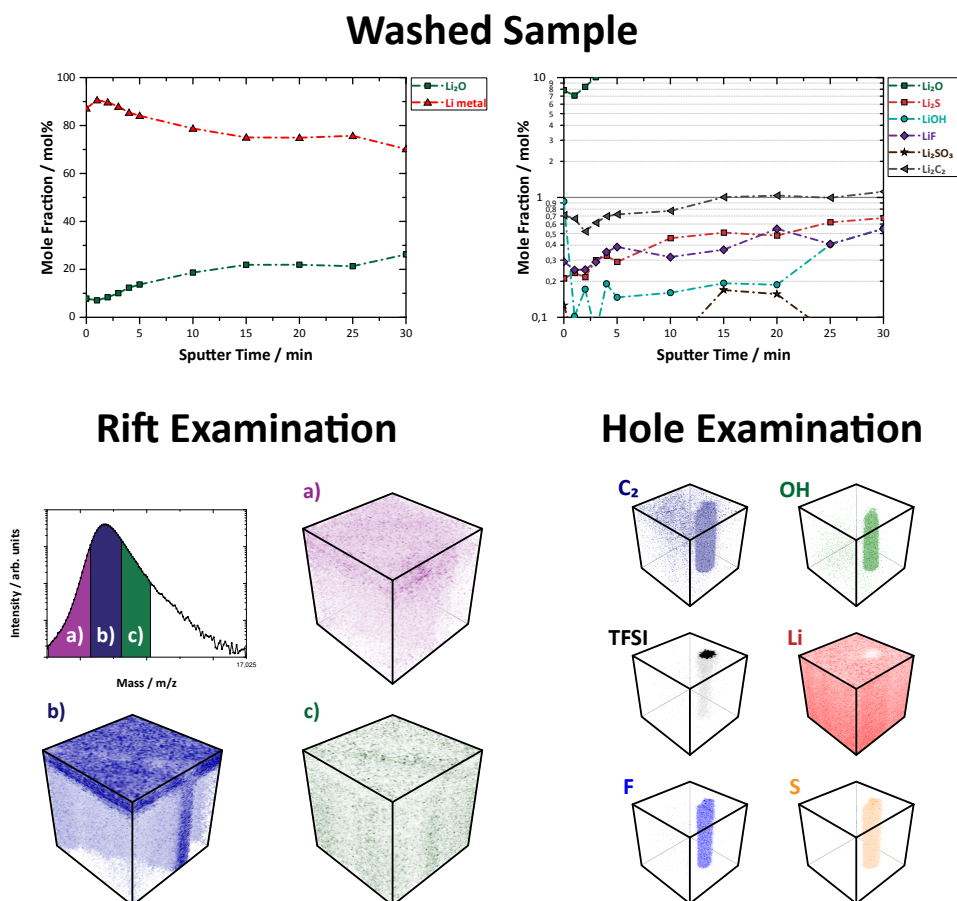
Figure 7.3.: The figure summarizes the important features observed by additional measurements for the SEI analysis. After washing of the samples with electrolyte, there is barely any information yielded about the SEI film. Therefore, washing is proposed to be inappropriate for the SEI analysis. Furthermore, the existence of fissures and holes are verified by examined a tracing mass in the SIMS technique. Also, the composition of those fissures and holes is investigated by considering important tracer masses.

This systematic analysis is proposed to be unfeasible if the samples are washed with the electrolyte or influenced by surface features (compare figure 7.3). Indeed, the washing process is a common procedure in the SEI analysis to remove the precipitated conducting salt, however, it is asserted to significantly influence the XPS and SIMS depth profiles. Thereby, the washing process removes relevant information about the SEI composition and layered structure for the cells utilized in this work. It is also pointed out that additional features at the surface can contribute to the SEI as well. For instance, the occurrence of fissures and holes is detected by the 3D illustrations of the respective SIMS data. For the systematical analysis of the SEI, however, selected areas with no features are chosen to avoid their superposing influence on the SEI evolution.

Emanating from the here presented analysis for lithium-sulfur cells, there are several novel investigation possibilities imaginable for the SEI. Thereby, several aspects of the SEI analysis like for the sample preparation, for the data record, and the data processing are addressed in this thesis. These aspects concern the XPS and SIMS technique respectively as well as their complementary interplay leading to the developed comprehensive illustration of the SEI structure and composition. Thus, this analysis concept is likewise transferable to the analysis of the SEI with different external parameters like temperature, stack pressure, or injected vibrations. Particularly, the analysis of a surface modified either by electrolyte additives or by a pretreatment before the cell construction is interesting to develop and improve the physical properties of the SEI like electronic insulation, ion conductivity, and mechanical stability. Naturally, this analysis concept is also adaptable for other battery systems besides the treated lithium-sulfur battery system in this thesis.

For instance, the influence of electrolyte additives like lithium nitrate on the surface composition is exemplarily described in this thesis and may be assigned to various other electrolyte additives. The surface composition can be tuned according to the utilized electrolyte additives to achieve a dense surface layer and to suppress the growth of the SEI film beyond the current state. Also, the surface structure may be further enhanced so that no holes or fissures may occur in the surface topography. In conclusion, the SEI can be tuned to enhance the physical properties like electronic insulation, ion conductance, and mechanical stability which will be resembled by the SEI structure and composition and, therefore, may be monitored by the presented analysis concept.

Furthermore, the preliminary modification of the lithium metal surface and the development of this treatment during the cycling process may be examined by this concept. Here, the conservation of the preliminary treatment and the interaction of the treatment with the electrolyte are of particular significance. The treated surface has to be insoluble for the utilized electrolyte and likewise should not diffuse to the positive electrode. If only the surface of the negative electrode is modified the treatment components should not diffuse into the bulk of the electrode as well. Also, the treatment should not be buried beneath the deposited lithium during charging. By the presented analysis procedure, these requirements for the surface treatment of lithium metal may be monitored as well and therefore verify the success of the treatment.

As last conclusion, it has to be noted that indeed the presented results provide an extensive view on the SEI analysis, however, no deeper insight into the organic species of SEI is revealed in this thesis. For this, the analysis has to be expanded to other analysis techniques like FTIR and Raman spectroscopy or requires a different approach for the measurement settings. Furthermore, the spatial resolution is restricted to the microscale; a nanoscale analysis of the SEI is not achievable with the

utilized techniques so that other techniques like Auger spectroscopy are required. The application of complementary techniques additionally to the presented analysis may further enhance the insight on the SEI film and render a more comprehensive and precise reproduction of the SEI.

Bibliography

[1] Balogun, Muhammad-Sadeeq ; Qiu, Weitao ; Luo, Yang ; Meng, Hui ; Mai, Wenjie ; Onasanya, Amos ; Olaniyi, Titus K. ; Tong, Yexiang: A review of the development of full cell lithium-ion batteries: The impact of nanostructured anode materials. In: *Nano Research* 9 (2016), 7, Nr. 10, S. 2823–2851. `http://dx.doi.org/10.1007/s12274-016-1171-1`. – DOI 10.1007/s12274–016–1171–1

[2] Hagen, Markus ; Hanselmann, Dominik ; Ahlbrecht, Katharina ; Maça, Rudi ; Gerber, Daniel ; Tübke, Jens: Lithium–Sulfur Cells: The Gap between the State-of-the-Art and the Requirements for High Energy Battery Cells. In: *Advanced Energy Materials* 5 (2015), Nr. 16

[3] Padbury, Richard ; Zhang, Xiangwu: Lithium-oxygen batteries-Limiting factors that affect performance. In: *Journal of Power Sources* 196 (2011), Nr. 10, 4436 - 4444. `http://dx.doi.org/http://dx.doi.org/10.1016/j.jpowsour.2011.01.032`. – DOI http://dx.doi.org/10.1016/j.jpowsour.2011.01.032. – ISSN 0378–7753

[4] Wu, Borong ; Ren, Yonghuan ; ; Ning, Li ; Soylu, Seref (Hrsg.): *Electric Vehicles: The Benefits and Barriers.* InTech, 2011. `http://dx.doi.org/DOI:10.5772/717`. `http://dx.doi.org/DOI:10.5772/717`

[5] Lide, David R.: *CRC Handbook of Chemistry, 84th.* CRC Press, 2003

[6] Rauh, R. D. ; Abraham, K. M. ; Pearson, G. F. ; Surprenant, J. K. ; Brummer, S. B.: A Lithium/Dissolved Sulfur Battery with an Organic Electrolyte. In: *Journal of The Electrochemical Society* 126 (1979), Nr. 4, 523-527. `http://dx.doi.org/10.1149/1.2129079`. – DOI 10.1149/1.2129079

[7] Yamin, H. ; Gorenshtein, A. ; Penciner, J. ; Sternberg, Y. ; Peled, E.: Lithium Sulfur Battery. In: *Journal of The Electrochemical Society* 135 (1988), Nr. 5, 1045-1048. `http://dx.doi.org/10.1149/1.2095868`. – DOI 10.1149/1.2095868

[8] Peled, E. ; Sternberg, Y. ; Gorenshtein, A. ; Lavi, Y.: Lithium-Sulfur Battery: Evaluation of Dioxolane-Based Electrolytes. In: *Journal of The Electrochemical Society* 136 (1989), Nr. 6, 1621-1625. `http://dx.doi.org/10.1149/1.2096981`. – DOI 10.1149/1.2096981

[9] Akridge, James R. ; Mikhaylik, Yuriy V. ; White, Neal: Li/S fundamental chemistry and application to high-performance rechargeable batteries. In: *Solid State Ionics* 175 (2004), Nr. 1-4, 243 - 245. `http://dx.doi.org/10.1016/j.ssi.2004.07.070`. – DOI 10.1016/j.ssi.2004.07.070. – ISSN 0167–2738. – <ce:title>Fourteenth International Conference on Solid State Ionics</ce:title>

[10] Teran, Alexander A. ; Balsara, Nitash P.: Effect of Lithium Polysulfides on the Morphology of Block Copolymer Electrolytes. In: *Macromolecules* 44 (2011), Nr. 23, 9267-9275. `http://dx.doi.org/10.1021/ma202091z`. – DOI 10.1021/ma202091z

[11] Zheng, Dong ; Zhang, Xuran ; Wang, Jiankun ; Qu, Deyu ; Yang, Xiaoqing ; Qu, Deyang: Reduction mechanism of sulfur in lithium-sulfur battery: From elemental sulfur to polysulfide. In: *Journal of Power Sources* 301 (2016), 312 -

316. http://dx.doi.org/http://dx.doi.org/10.1016/j.jpowsour.2015.10.002. – DOI http://dx.doi.org/10.1016/j.jpowsour.2015.10.002. – ISSN 0378–7753

[12] *Kapitel* 4. In: STEUDEL, Ralf: *Inorganic Polysulfides S_n^{2-} and Radical Anions S_n^-*. Berlin, Heidelberg : Springer Berlin Heidelberg, 2003. – ISBN 978–3–540–44951–5, 127–152

[13] MIKHAYLIK, Yuriy V. ; AKRIDGE, James R.: Low Temperature Performance of Li/S Batteries. In: *Journal of The Electrochemical Society* 150 (2003), Nr. 3, A306-A311. http://dx.doi.org/10.1149/1.1545452. – DOI 10.1149/1.1545452

[14] LI, Jingfa ; YANG, Liuqing ; YANG, Shiliu ; LEE, Jim Y.: The Application of Redox Targeting Principles to the Design of Rechargeable Li-S Flow Batteries. In: *Advanced Energy Materials* 5 (2015), Nr. 24, n/a–n/a. http://dx.doi.org/10.1002/aenm.201501808. – DOI 10.1002/aenm.201501808. – ISSN 1614–6840. – 1501808

[15] PAN, Huilin ; WEI, Xiaoliang ; HENDERSON, Wesley A. ; CHEN, Junzheng ; SHAO, Yuyan ; XIAO, Jie ; LIU, Jun: Understanding and Controlling of Solution Chemistry of Lithium Polysulfide to Enable High Energy Li-S Redox Flow Battery. In: *Meeting Abstracts* MA2015-01 (2015), Nr. 3, 703. http://ma.ecsdl.org/content/MA2015-01/3/703.abstract

[16] BUSCHE, Martin R. ; DROSSEL, Thomas ; LEICHTWEISS, Thomas ; WEBER, Dominik A. ; FALK, Mareike ; SCHNEIDER, Meike ; REICH, Maria-Louisa ; SOMMER, Heino ; ADELHELM, Philipp ; JANEK, Jü rgen: Dynamic formation of a solid-liquid electrolyte interphase and its consequences for hybrid-battery concepts. In: *Nat Chem* 8 (2016), Mai, Nr. 5, 426–434. http://dx.doi.org/10.1038/nchem.2470. – ISSN 1755–4330

[17] CAO, Ruiguo ; XU, Wu ; LV, Dongping ; XIAO, Jie ; ZHANG, Ji-Guang: Anodes for Rechargeable Lithium-Sulfur Batteries. In: *Advanced Energy Materials* 5 (2015), Nr. 16, n/a–n/a. http://dx.doi.org/10.1002/aenm.201402273. – DOI 10.1002/aenm.201402273. – ISSN 1614–6840. – 1402273

[18] YAMADA, Takanobu ; ITO, Seitaro ; OMODA, Ryo ; WATANABE, Taku ; AIHARA, Yuichi ; AGOSTINI, Marco ; ULISSI, Ulderico ; HASSOUN, Jusef ; SCROSATI, Bruno: All Solid-State Lithium-Sulfur Battery Using a Glass-Type P2S5-Li2S Electrolyte: Benefits on Anode Kinetics. In: *Journal of The Electrochemical Society* 162 (2015), Nr. 4, A646-A651. http://dx.doi.org/10.1149/2.0441504jes. – DOI 10.1149/2.0441504jes

[19] CHEN, Maohua ; ADAMS, Stefan: High performance all-solid-state lithium/sulfur batteries using lithium argyrodite electrolyte. In: *Journal of Solid State Electrochemistry* 19 (2015), Nr. 3, 697–702. http://dx.doi.org/10.1007/s10008-014-2654-1. – DOI 10.1007/s10008–014–2654–1. – ISSN 1433–0768

[20] HAN, Fudong ; YUE, Jie ; FAN, Xiulin ; GAO, Tao ; LUO, Chao ; MA, Zhaohui ; SUO, Liumin ; WANG, Chunsheng: High-Performance All-Solid-State Lithium-sulfur Battery Enabled by a Mixed-Conductive Li₂S Nanocomposite. In: *Nano Letters* 16 (2016), June, Nr. 7, 4521–4527. http://dx.doi.org/10.1021/acs.nanolett.6b01754. – DOI 10.1021/acs.nanolett.6b01754. – PMID: 27322663

[21] ISMAIL, Iqbal ; NODA, Akihiro ; NISHIMOTO, Atsushi ; WATANABE, Masayoshi: {XPS} study of lithium surface after contact with lithium-salt doped polymer electrolytes. In: *Electrochimica Acta* 46 (2001), Nr. 10-11, 1595 - 1603. http://dx.doi.org/http://dx.doi.org/10.1016/S0013-4686(00)00758-1. – DOI http://dx.doi.org/10.1016/S0013-4686(00)00758–1. – ISSN 0013–4686

[22] BARGHAMADI, Marzieh ; BEST, Adam S. ; BHATT, Anand I. ; HOLLENKAMP, Anthony F. ; MAHON, Peter J. ; MUSAMEH, Mustafa ; RÜTHER, Thomas: Effect of LiNO$_3$ additive and pyrrolidinium ionic liquid on the solid electrolyte interphase in the lithium-sulfur battery. In: *Journal of Power Sources* 295 (2015), 212 - 220. `http://dx.doi.org/http://dx.doi.org/10.1016/j.jpowsour.2015.06.150`. – DOI http://dx.doi.org/10.1016/j.jpowsour.2015.06.150. – ISSN 0378–7753

[23] BOULINEAU, Sylvain ; COURTY, Matthieu ; TARASCON, Jean-Marie ; VIALLET, Virginie: Mechanochemical synthesis of Li-argyrodite Li6PS5X (X = Cl, Br, I) as sulfur-based solid electrolytes for all solid state batteries application. In: *Solid State Ionics* 221 (2012), 1 - 5. `http://dx.doi.org/http://dx.doi.org/10.1016/j.ssi.2012.06.008`. – DOI http://dx.doi.org/10.1016/j.ssi.2012.06.008. – ISSN 0167–2738

[24] SHIM, Joongpyo ; STRIEBEL, Kathryn A. ; CAIRNS, Elton J.: The Lithium/Sulfur Rechargeable Cell. In: *Journal of The Electrochemical Society* 149 (2002), Nr. 10, A1321-A1325. `http://dx.doi.org/10.1149/1.1503076`. – DOI 10.1149/1.1503076

[25] CHANG, Duck-Rye ; LEE, Suck-Hyun ; KIM, Sun-Wook ; KIM, Hee-Tak: Binary electrolyte based on tetra(ethylene glycol) dimethyl ether and 1,3-dioxolane for lithium-sulfur battery. In: *Journal of Power Sources* 112 (2002), Nr. 2, 452 - 460. `http://dx.doi.org/10.1016/S0378-7753(02)00418-4`. – DOI 10.1016/S0378–7753(02)00418–4. – ISSN 0378–7753

[26] SONG, Min-Sang ; HAN, Sang-Cheol ; KIM, Hyun-Seok ; KIM, Jin-Ho ; KIM, Ki-Tae ; KANG, Yong-Mook ; AHN, Hyo-Jun ; DOU, S. X. ; LEE, Jai-Young: Effects of Nanosized Adsorbing Material on Electrochemical Properties of Sulfur Cathodes for Li/S Secondary Batteries. In: *Journal of The Electrochemical Society* 151 (2004), Nr. 6, A791-A795. `http://dx.doi.org/10.1149/1.1710895`. – DOI 10.1149/1.1710895

[27] GAO, Jie ; LOWE, Michael A. ; KIYA, Yasuyuki ; ABRUÑA, Héctor D.: Effects of Liquid Electrolytes on the Charge-Discharge Performance of Rechargeable Lithium/Sulfur Batteries: Electrochemical and in-Situ X-ray Absorption Spectroscopic Studies. In: *The Journal of Physical Chemistry C* 115 (2011), Nr. 50, 25132-25137. `http://dx.doi.org/10.1021/jp207714c`. – DOI 10.1021/jp207714c

[28] CHOI, Y J. ; JUNG, B S. ; LEE, D J. ; JEONG, J H. ; KIM, K W. ; AHN, H J. ; CHO, K K. ; GU, H B.: Electrochemical properties of sulfur electrode containing nano Al$_2$O$_3$ for lithium/sulfur cell. In: *Physica Scripta* 2007 (2007), Nr. T129, 62. `http://stacks.iop.org/1402-4896/2007/i=T129/a=014`

[29] RAUH, R.D. ; SHUKER, F.S. ; MARSTON, J.M. ; BRUMMER, S.B.: Formation of lithium polysulfides in aprotic media. In: *Journal of Inorganic and Nuclear Chemistry* 39 (1977), Nr. 10, 1761 - 1766. `http://dx.doi.org/10.1016/0022-1902(77)80198-X`. – DOI 10.1016/0022–1902(77)80198–X. – ISSN 0022–1902

[30] GUTMANN, V.: Empirical parameters for donor and acceptor properties of solvents. In: *Electrochimica Acta* 21 (1976), Nr. 9, 661 - 670. `http://dx.doi.org/http://dx.doi.org/10.1016/0013-4686(76)85034-7`. – DOI http://dx.doi.org/10.1016/0013–4686(76)85034–7. – ISSN 0013–4686

[31] HERR, T. ; FISCHER, P. ; TÜBKE, J. ; PINKWART, K. ; ELSNER, P.: Increasing the energy density of the non-aqueous vanadium redox flow battery with the acetonitrile-1,3-dioxolane-dimethyl sulfoxide solvent mixture. In: *Journal of Power Sources* 265 (2014), 317 - 324. `http://dx.doi.org/http://dx.doi.org/10.1016/j.jpowsour.2014.04.141`. – DOI http://dx.doi.org/10.1016/j.jpowsour.2014.04.141. – ISSN 0378–7753

[32] Institut für Arbeitsschutz der Deutschen Gesetzlichen Unfallversicherung (IFA): *GESTIS-Stoffdatenbank.* `http://www.dguv.de/ifa/GESTIS/GESTIS-Stoffdatenbank/index.jsp`. Version: June 2016

[33] ZHANG, Sheng S.: A review on electrolyte additives for lithium-ion batteries. In: *Journal of Power Sources* 162 (2006), Nr. 2, 1379 - 1394. `http://dx.doi.org/http://dx.doi.org/10.1016/j.jpowsour.2006.07.074`. – DOI http://dx.doi.org/10.1016/j.jpowsour.2006.07.074. – ISSN 0378–7753. – Special issue including selected papers from the International Power Sources Symposium 2005 together with regular papers

[34] AURBACH, Doron ; TALYOSEF, Yosef ; MARKOVSKY, Boris ; MARKEVICH, Elena ; ZINIGRAD, Ella ; ASRAF, Liraz ; GNANARAJ, Joseph S. ; KIM, Hyeong-Jin: Design of electrolyte solutions for Li and Li-ion batteries: a review. In: *Electrochimica Acta* 50 (2004), Nr. 2-3, 247 - 254. `http://dx.doi.org/http://dx.doi.org/10.1016/j.electacta.2004.01.090`. – DOI http://dx.doi.org/10.1016/j.electacta.2004.01.090. – ISSN 0013–4686. – Polymer Batteries and Fuel Cells:Selection of Papers from First International Conference

[35] MEINI, Stefano ; ELAZARI, Ran ; ROSENMAN, Ariel ; GARSUCH, Arnd ; AURBACH, Doron: The Use of Redox Mediators for Enhancing Utilization of Li_2S Cathodes for Advanced Li-S Battery Systems. In: *The Journal of Physical Chemistry Letters* 5 (2014), Nr. 5, 915-918. `http://dx.doi.org/10.1021/jz500222f`. – DOI 10.1021/jz500222f. – PMID: 26274088

[36] LIANG, Xiao ; HART, Connor ; PANG, Quan ; GARSUCH, Arnd ; WEISS, Thomas ; NAZAR, Linda F.: A highly efficient polysulfide mediator for lithium-sulfur batteries. In: *Nat Commun* 6 (2015), Januar, –. `http://dx.doi.org/10.1038/ncomms6682`

[37] GERBER, Laura C. H. ; FRISCHMANN, Peter D. ; FAN, Frank Y. ; DORIS, Sean E. ; QU, Xiaohui ; SCHEUERMANN, Angelique M. ; PERSSON, Kristin ; CHIANG, Yet-Ming ; HELMS, Brett A.: Three-Dimensional Growth of Li_2S in Lithium-Sulfur Batteries Promoted by a Redox Mediator. In: *Nano Letters* 16 (2016), Nr. 1, 549-554. `http://dx.doi.org/10.1021/acs.nanolett.5b04189`. – DOI 10.1021/acs.nanolett.5b04189. – PMID: 26691496

[38] QIAN, Jiangfeng ; HENDERSON, Wesley A. ; XU, Wu ; BHATTACHARYA, Priyanka ; ENGELHARD, Mark ; BORODIN, Oleg ; ZHANG, Ji-Guang: High rate and stable cycling of lithium metal anode. In: *Nat Commun* 6 (2015), Februar, –. `http://dx.doi.org/10.1038/ncomms7362`

[39] DEMIR-CAKAN, Rezan ; MORCRETTE, Mathieu ; NOUAR, Farid ; DAVOISNE, Carine ; DEVIC, Thomas ; GONBEAU, Danielle ; DOMINKO, Robert ; SERRE, Christian ; FÉREY, Gérard ; TARASCON, Jean-Marie: Cathode Composites for Li-S Batteries via the Use of Oxygenated Porous Architectures. In: *Journal of the American Chemical Society* 133 (2011), Nr. 40, 16154-16160. `http://dx.doi.org/10.1021/ja2062659`. – DOI 10.1021/ja2062659

[40] KOLOSNITSYN, V. ; KUZ'MINA, E. ; KARASEVA, E. ; MOCHALOV, S.: Impedance spectroscopy studies of changes in the properties of lithium-sulfur cells in the course of cycling. In: *Russian Journal of Electrochemistry* 47 (2011), 793-798. `http://dx.doi.org/10.1134/S1023193511070093`. – ISSN 1023–1935. – 10.1134/S1023193511070093

[41] SU, Yu-Sheng ; FU, Yongzhu ; COCHELL, Thomas ; MANTHIRAM, Arumugam: A strategic approach to recharging lithium-sulphur batteries for long cycle life. In: *Nat Commun* 4 (2013), Dezember, –. `http://dx.doi.org/10.1038/ncomms3985`

[42] AURBACH, Doron ; POLLAK, Elad ; ELAZARI, Ran ; SALITRA, Gregory ; KELLEY, C. S. ; AFFINITO, John: On the Surface Chemical Aspects of Very High Energy Density, Rechargeable Li–Sulfur Batteries. In: *Journal of The Electrochemical Society* 156 (2009), Nr. 8, A694-A702. `http://dx.doi.org/10.1149/1.3148721`. – DOI 10.1149/1.3148721

[43] Babu, Ganguli ; Ababtain, Khalid ; Ng, K. Y. S. ; Arava, Leela Mohana R.: Electrocatalysis of Lithium Polysulfides: Current Collectors as Electrodes in Li/S Battery Configuration. In: *Scientific Reports* 5 (2015), März, 8763–. `http://dx.doi.org/10.1038/srep08763`

[44] Li, Bin ; Li, Songmei ; Xu, Jingjing ; Yang, Shubin: A new configured lithiated silicon-sulfur battery built on 3D graphene with superior electrochemical performances. In: *Energy Environ. Sci.* 9 (2016), 2025-2030. `http://dx.doi.org/10.1039/C6EE01019A`. – DOI 10.1039/C6EE01019A

[45] Kulisch, Jörn ; Sommer, Heino ; Brezesinski, Torsten ; Janek, Jürgen: Simple cathode design for Li-S batteries: cell performance and mechanistic insights by in operando X-ray diffraction. In: *Phys. Chem. Chem. Phys.* 16 (2014), 18765-18771. `http://dx.doi.org/10.1039/C4CP02220C`. – DOI 10.1039/C4CP02220C

[46] Jozwiuk, Anna ; Sommer, Heino ; Janek, Jürgen ; Brezesinski, Torsten: Fair performance comparison of different carbon blacks in lithium-sulfur batteries with practical mass loadings - Simple design competes with complex cathode architecture. In: *Journal of Power Sources* 296 (2015), 454 - 461. `http://dx.doi.org/http://dx.doi.org/10.1016/j.jpowsour.2015.07.070`. – DOI http://dx.doi.org/10.1016/j.jpowsour.2015.07.070. – ISSN 0378–7753

[47] Chung, Woo J. ; Griebel, Jared J. ; Kim, Eui T. ; Yoon, Hyunsik ; Simmonds, Adam G. ; Ji, Hyun J. ; Dirlam, Philip T. ; Glass, Richard S. ; Wie, Jeong J. ; Nguyen, Ngoc A. ; Guralnick, Brett W. ; Park, Jungjin ; Somogyi, Árpád ; Theato, Patrick ; Mackay, Michael E. ; Sung, Yung-Eun ; Char, Kookheon ; Pyun, Jeffrey: The use of elemental sulfur as an alternative feedstock for polymeric materials. In: *Nat Chem* 5 (2013), Juni, Nr. 6, 518–524. `http://dx.doi.org/10.1038/nchem.1624`. – ISSN 1755–4330

[48] Diao, Yan ; Xie, Kai ; Xiong, Shizhao ; Hong, Xiaobin: Insights into Li-S Battery Cathode Capacity Fading Mechanisms: Irreversible Oxidation of Active Mass during Cycling. In: *Journal of The Electrochemical Society* 159 (2012), Nr. 11, A1816-A1821. `http://dx.doi.org/10.1149/2.020211jes`. – DOI 10.1149/2.020211jes

[49] Schneider, Artur ; Weidmann, Christoph ; Suchomski, Christian ; Sommer, Heino ; Janek, Jürgen ; Brezesinski, Torsten: Ionic Liquid-Derived Nitrogen-Enriched Carbon/Sulfur Composite Cathodes with Hierarchical Microstructure-A Step Toward Durable High-Energy and High-Performance Lithium-Sulfur Batteries. In: *Chemistry of Materials* 27 (2015), Nr. 5, 1674-1683. `http://dx.doi.org/10.1021/cm504460p`. – DOI 10.1021/cm504460p

[50] Markevich, E. ; Salitra, G. ; Rosenman, A. ; Talyosef, Y. ; Chesneau, F. ; Aurbach, D.: The effect of a solid electrolyte interphase on the mechanism of operation of lithium-sulfur batteries. In: *J. Mater. Chem. A* 3 (2015), 19873-19883. `http://dx.doi.org/10.1039/C5TA04613K`. – DOI 10.1039/C5TA04613K

[51] Ji, Xiulei ; Nazar, Linda F.: Advances in Li-S batteries. In: *J. Mater. Chem.* 20 (2010), 9821-9826. `http://dx.doi.org/10.1039/B925751A`. – DOI 10.1039/B925751A

[52] Lee, Song H. ; Rasaiah, Jayendran C.: Molecular Dynamics Simulation of Ion Mobility. 2. Alkali Metal and Halide Ions Using the SPC/E Model for Water at 25 °C. In: *The Journal of Physical Chemistry* 100 (1996), Nr. 4, 1420-1425. `http://dx.doi.org/10.1021/jp953050c`. – DOI 10.1021/jp953050c

[53] Wilkinson, D.P. ; Wainwright, D.: In-situ study of electrode stack growth in rechargeable cells at constant pressure. In: *Journal of Electroanalytical Chemistry* 355 (1993), Nr. 1-2, 193 - 203. `http://dx.doi.org/http://dx.doi.org/10.1016/0022-0728(93)80362-L`. – DOI http://dx.doi.org/10.1016/0022–0728(93)80362–L. – ISSN 1572–6657. – An International

Journal Devoted to all Aspects of Electrode Kinetics, Interfacial Structure, Properties of Electrolytes, Colloid and Biological Electrochemistry

[54] HIRAI, Toshiro ; YOSHIMATSU, Isamu ; YAMAKI, Jun-ichi: Influence of Electrolyte on Lithium Cycling Efficiency with Pressurized Electrode Stack. In: *Journal of The Electrochemical Society* 141 (1994), Nr. 3, 611-614. `http://dx.doi.org/10.1149/1.2054778`. – DOI 10.1149/1.2054778

[55] GOODMAN, Johanna K. S. ; KOHL, Paul A.: Effect of Alkali and Alkaline Earth Metal Salts on Suppression of Lithium Dendrites. In: *Journal of The Electrochemical Society* 161 (2014), Nr. 9, D418-D424. `http://dx.doi.org/10.1149/2.0301409jes`. – DOI 10.1149/2.0301409jes

[56] STARK, Johanna K. ; DING, Yi ; KOHL, Paul A.: Nucleation of Electrodeposited Lithium Metal: Dendritic Growth and the Effect of Co-Deposited Sodium. In: *Journal of The Electrochemical Society* 160 (2013), Nr. 9, D337-D342. `http://dx.doi.org/10.1149/2.028309jes`. – DOI 10.1149/2.028309jes

[57] DING, Fei ; XU, Wu ; GRAFF, Gordon L. ; ZHANG, Jian ; SUSHKO, Maria L. ; CHEN, Xilin ; SHAO, Yuyan ; ENGELHARD, Mark H. ; NIE, Zimin ; XIAO, Jie ; LIU, Xingjiang ; SUSHKO, Peter V. ; LIU, Jun ; ZHANG, Ji-Guang: Dendrite-Free Lithium Deposition via Self-Healing Electrostatic Shield Mechanism. In: *Journal of the American Chemical Society* 135 (2013), Nr. 11, 4450-4456. `http://dx.doi.org/10.1021/ja312241y`. – DOI 10.1021/ja312241y. – PMID: 23448508

[58] KOZEN, Alexander C. ; LIN, Chuan-Fu ; PEARSE, Alexander J. ; SCHROEDER, Marshall A. ; HAN, Xiaogang ; HU, Liangbing ; LEE, Sang-Bok ; RUBLOFF, Gary W. ; NOKED, Malachi: Next-Generation Lithium Metal Anode Engineering via Atomic Layer Deposition. In: *ACS Nano* 9 (2015), Nr. 6, 5884-5892. `http://dx.doi.org/10.1021/acsnano.5b02166`. – DOI 10.1021/acsnano.5b02166. – PMID: 25970127

[59] TIRADO, José L.: Inorganic materials for the negative electrode of lithium-ion batteries: state-of-the-art and future prospects. In: *Materials Science and Engineering: R: Reports* 40 (2003), Nr. 3, 103 - 136. `http://dx.doi.org/http://dx.doi.org/10.1016/S0927-796X(02)00125-0`. – DOI http://dx.doi.org/10.1016/S0927–796X(02)00125–0. – ISSN 0927–796X

[60] JESCHULL, Fabian ; BRANDELL, Daniel ; EDSTROM, Kristina ; LACEY, Matthew J.: A stable graphite negative electrode for the lithium-sulfur battery. In: *Chem. Commun.* 51 (2015), 17100-17103. `http://dx.doi.org/10.1039/C5CC06666B`. – DOI 10.1039/C5CC06666B

[61] PELED, E. ; YAMIN, H.: Solid Electrolyte Interphase (SEI) Electrodes. Part 1. The Kinetics of Lithium in LiAlCl4-SOCl2. In: *Israel Journal of Chemistry* 18 (1979), Nr. 1-2, 131–135. `http://dx.doi.org/10.1002/ijch.197900016`. – DOI 10.1002/ijch.197900016. – ISSN 1869–5868

[62] BALBUENA, Perla B. ; WANG, Yixuan: *Solid–Electrolyte Interphase: Lithium-ion batteries.* World Scientific, 2004 `http://www.worldscientific.com/worldscibooks/10.1142/p291`

[63] NIEHOFF, Philip ; PASSERINI, Stefano ; WINTER, Martin: Interface Investigations of a Commercial Lithium Ion Battery Graphite Anode Material by Sputter Depth Profile X-ray Photoelectron Spectroscopy. In: *Langmuir* 29 (2013), Nr. 19, 5806-5816. `http://dx.doi.org/10.1021/la400764r`. – DOI 10.1021/la400764r. – PMID: 23586847

[64] HEINE, Jennifer ; HILBIG, Peter ; QI, Xin ; NIEHOFF, Philip ; WINTER, Martin ; BIEKER, Peter: Fluoroethylene Carbonate as Electrolyte Additive in Tetraethylene Glycol Dimethyl Ether Based Electrolytes for Application in Lithium Ion and Lithium Metal Batteries. In:

Journal of The Electrochemical Society 162 (2015), Nr. 6, A1094-A1101. `http://dx.doi.org/10.1149/2.0011507jes`. – DOI 10.1149/2.0011507jes

[65] HAN, Yamiao ; DUAN, Xiaobo ; LI, Yanbing ; HUANG, Liwu ; ZHU, Ding ; CHEN, Yungui: Improved cycling performances with high sulfur loading enabled by pre-treating lithium anode. In: *Ionics* 22 (2016), Nr. 2, 151–157. `http://dx.doi.org/10.1007/s11581-015-1543-7`. – DOI 10.1007/s11581–015–1543–7. – ISSN 1862–0760

[66] AURBACH, Doron: Review of selected electrode-solution interactions which determine the performance of Li and Li ion batteries. In: *Journal of Power Sources* 89 (2000), Nr. 2, 206 - 218. `http://dx.doi.org/http://dx.doi.org/10.1016/S0378-7753(00)00431-6`. – DOI http://dx.doi.org/10.1016/S0378–7753(00)00431–6. – ISSN 0378–7753

[67] AURBACH, D. ; DAROUX, M. L. ; FAGUY, P. W. ; YEAGER, E.: Identification of Surface Films Formed on Lithium in Propylene Carbonate Solutions. In: *Journal of The Electrochemical Society* 134 (1987), Nr. 7, 1611-1620. `http://dx.doi.org/10.1149/1.2100722`. – DOI 10.1149/1.2100722

[68] TASAKI, Ken ; GOLDBERG, Alex ; LIAN, Jian-Jie ; WALKER, Merry ; TIMMONS, Adam ; HARRIS, Stephen J.: Solubility of Lithium Salts Formed on the Lithium-Ion Battery Negative Electrode Surface in Organic Solvents. In: *Journal of The Electrochemical Society* 156 (2009), Nr. 12, A1019-A1027. `http://dx.doi.org/10.1149/1.3239850`. – DOI 10.1149/1.3239850

[69] GOFER, Y. ; ELY, Y. E. ; AURBACH, D.: Surface chemistry of lithium in 1,3-dioxolane. In: *Electrochimica Acta* 37 (1992), Nr. 10, 1897 - 1899. `http://dx.doi.org/http://dx.doi.org/10.1016/0013-4686(92)85096-4`. – DOI http://dx.doi.org/10.1016/0013–4686(92)85096–4. – ISSN 0013–4686

[70] PELED, E. ; GOLODNITSKY, D. ; ULUS, A. ; YUFIT, V.: Effect of carbon substrate on SEI composition and morphology. In: *Electrochimica Acta* 50 (2004), Nr. 2-3, 391 - 395. `http://dx.doi.org/http://dx.doi.org/10.1016/j.electacta.2004.01.130`. – DOI http://dx.doi.org/10.1016/j.electacta.2004.01.130. – ISSN 0013–4686. – Polymer Batteries and Fuel Cells:Selection of Papers from First International Conference

[71] ZU, Chenxi ; AZIMI, Nasim ; ZHANG, Zhengcheng ; MANTHIRAM, Arumugam: Insight into lithium-metal anodes in lithium-sulfur batteries with a fluorinated ether electrolyte. In: *J. Mater. Chem. A* 3 (2015), 14864-14870. `http://dx.doi.org/10.1039/C5TA03195H`. – DOI 10.1039/C5TA03195H

[72] XIONG, Shizhao ; XIE, Kai ; DIAO, Yan ; HONG, Xiaobin: On the role of polysulfides for a stable solid electrolyte interphase on the lithium anode cycled in lithium-sulfur batteries. In: *Journal of Power Sources* 236 (2013), 181 - 187. `http://dx.doi.org/http://dx.doi.org/10.1016/j.jpowsour.2013.02.072`. – DOI http://dx.doi.org/10.1016/j.jpowsour.2013.02.072. – ISSN 0378–7753

[73] WAGNER, M.W. ; LIEBENOW, C. ; BESENHARD, J.O.: Effect of polysulfide-containing electrolyte on the film formation of the negative electrode. In: *Journal of Power Sources* 68 (1997), Nr. 2, 328 - 332. `http://dx.doi.org/http://dx.doi.org/10.1016/S0378-7753(97)02586-X`. – DOI http://dx.doi.org/10.1016/S0378–7753(97)02586–X. – ISSN 0378–7753

[74] XIONG, Shizhao ; XIE, Kai ; DIAO, Yan ; HONG, Xiaobin: Characterization of the solid electrolyte interphase on lithium anode for preventing the shuttle mechanism in lithium-sulfur batteries. In: *Journal of Power Sources* 246 (2014), 840 - 845. `http://dx.doi.org/http://dx.doi.org/10.1016/j.jpowsour.2013.08.041`. – DOI http://dx.doi.org/10.1016/j.jpowsour.2013.08.041. – ISSN 0378–7753

[75] KIM, Hyung ; JEONG, Chang-Sik ; KIM, Yong-Tae: Shuttle inhibitor effect of lithium perchlorate as an electrolyte salt for lithium-sulfur batteries. In: *Journal of Applied Electrochemistry* 42 (2012), 75-79. `http://dx.doi.org/10.1007/s10800-011-0373-1`. – ISSN 0021–891X. – 10.1007/s10800-011-0373-1

[76] ROSENMAN, Ariel ; ELAZARI, Ran ; SALITRA, Gregory ; MARKEVICH, Elena ; AURBACH, Doron ; GARSUCH, Arnd: The Effect of Interactions and Reduction Products of LiNO3, the Anti-Shuttle Agent, in Li-S Battery Systems. In: *Journal of The Electrochemical Society* 162 (2015), Nr. 3, A470-A473. `http://dx.doi.org/10.1149/2.0861503jes`. – DOI 10.1149/2.0861503jes

[77] VETTER, J. ; NOVÁK, P. ; WAGNER, M.R. ; VEIT, C. ; MÖLLER, K.-C. ; BESENHARD, J.O. ; WINTER, M. ; WOHLFAHRT-MEHRENS, M. ; VOGLER, C. ; HAMMOUCHE, A.: Ageing mechanisms in lithium-ion batteries. In: *Journal of Power Sources* 147 (2005), Nr. 1-2, 269 - 281. `http://dx.doi.org/http://dx.doi.org/10.1016/j.jpowsour.2005.01.006`. – DOI http://dx.doi.org/10.1016/j.jpowsour.2005.01.006. – ISSN 0378–7753

[78] VERMA, Pallavi ; MAIRE, Pascal ; NOVÁK, Petr: A review of the features and analyses of the solid electrolyte interphase in Li-ion batteries. In: *Electrochimica Acta* 55 (2010), Nr. 22, 6332 - 6341. `http://dx.doi.org/http://dx.doi.org/10.1016/j.electacta.2010.05.072`. – DOI http://dx.doi.org/10.1016/j.electacta.2010.05.072. – ISSN 0013–4686

[79] EDSTRÖM, Kristina ; HERSTEDT, Marie ; ABRAHAM, Daniel P.: A new look at the solid electrolyte interphase on graphite anodes in Li-ion batteries. In: *Journal of Power Sources* 153 (2006), Nr. 2, 380 - 384. `http://dx.doi.org/http://dx.doi.org/10.1016/j.jpowsour.2005.05.062`. – DOI http://dx.doi.org/10.1016/j.jpowsour.2005.05.062. – ISSN 0378–7753. – Selected papers presented at the 2004 Meeting of the International Battery Association2004 International Meeting of the International Battery Association

[80] MALMGREN, S. ; CIOSEK, K. ; HAHLIN, M. ; GUSTAFSSON, T. ; GORGOI, M. ; RENSMO, H. ; EDSTRÖM, K.: Comparing anode and cathode electrode/electrolyte interface composition and morphology using soft and hard X-ray photoelectron spectroscopy. In: *Electrochimica Acta* 97 (2013), 23 - 32. `http://dx.doi.org/http://dx.doi.org/10.1016/j.electacta.2013.03.010`. – DOI http://dx.doi.org/10.1016/j.electacta.2013.03.010. – ISSN 0013–4686

[81] PHILIPPE, B. ; HAHLIN, M. ; EDSTRÖM, K. ; GUSTAFSSON, T. ; SIEGBAHN, H. ; RENSMO, H.: Photoelectron Spectroscopy for Lithium Battery Interface Studies. In: *Journal of The Electrochemical Society* 163 (2016), Nr. 2, A178-A191. `http://dx.doi.org/10.1149/2.0051602jes`. – DOI 10.1149/2.0051602jes

[82] PELED, E. ; TOW, D. B. ; MERSON, A. ; GLADKICH, A. ; BURSTEIN, L. ; GOLODNITSKY, D.: Composition, depth profiles and lateral distribution of materials in the SEI built on HOPG-TOF SIMS and XPS studies. In: *Journal of Power Sources* 97 (2001), 52 - 57. `http://dx.doi.org/http://dx.doi.org/10.1016/S0378-7753(01)00505-5`. – DOI http://dx.doi.org/10.1016/S0378–7753(01)00505–5. – ISSN 0378–7753. – Proceedings of the 10th International Meeting on Lithium Batteries

[83] LU, Peng ; HARRIS, Stephen J.: Lithium transport within the solid electrolyte interphase. In: *Electrochemistry Communications* 13 (2011), Nr. 10, 1035 - 1037. `http://dx.doi.org/http://dx.doi.org/10.1016/j.elecom.2011.06.026`. – DOI http://dx.doi.org/10.1016/j.elecom.2011.06.026. – ISSN 1388–2481

[84] SCHINDLER, Volker ; GREINER, Guenter: Vakuumtechnische Voraussetzungen der Oberflaechenphysik. In: *Physik in unserer Zeit* 14 (1983), Nr. 4, 116–124. `http://dx.doi.org/10.1002/piuz.19830140404`. – ISSN 1521–3943

[85] BRIGGS, David ; SEAH, Martin P.: *Practical surface analysis by Auger and X-ray photoelectron spectroscopy.* John Wiley & Sons, 1983

[86] TAGLAUER, E ; VICKERMAN, John C.: *Surface Analysis-The Principle Techniques.* Wiley, New York, 1997

[87] MOULDER, John F. ; CHASTAIN, Jill ; KING, Roger C.: *Handbook of X-ray photoelectron spectroscopy: a reference book of standard spectra for identification and interpretation of XPS data.* Physical Electronics Eden Prairie, MN, 1995

[88] SEAH, M. P. ; DENCH, W. A.: Quantitative electron spectroscopy of surfaces: A standard data base for electron inelastic mean free paths in solids. In: *Surface and Interface Analysis* 1 (1979), Nr. 1, 2–11. http://dx.doi.org/10.1002/sia.740010103. – DOI 10.1002/sia.740010103. – ISSN 1096–9918

[89] VICKERMAN, J. C. ; BROWN, A ; REED, N.M.: *Secondary Ion Mass Spectrometry: Principles and Applications.* Oxford University Press, 1989

[90] WILSON, R.G. ; STEVIE, F.A. ; MAGEE, C.W.: *Secondary Ion Mass Spectrometry: A Practical Handbook for Depth Profiling and Bulk Impurity Analysis.* John Wiley & Sons, Ltd, 1989

[91] YU, Ming L.: A bond breaking model for secondary ion emission. In: *Nuclear Instruments and Methods in Physics Research Section B: Beam Interactions with Materials and Atoms* 18 (1986), Nr. 1-6, 542–548. http://www.sciencedirect.com/science/article/B6TJN-4KMBGNN-31/2/5402525eafd68b2eccdc64eb1cff760d. – ISSN 0168–583X

[92] YU, Ming L. ; LANG, Norton D.: Mechanisms of atomic ion emission during sputtering. In: *Nuclear Instruments and Methods in Physics Research Section B: Beam Interactions with Materials and Atoms* 14 (1986), April, Nr. 4-6, 403–413. http://www.sciencedirect.com/science/article/B6TJN-470VG7N-1JP/2/b22ef7d78c8898143b754b520a02c25d. – ISSN 0168–583X

[93] GERHARD, W. ; PLOG, C.: Secondary ion emission by nonadiabatic dissociation of nascent ion molecules with energies depending on solid composition. In: *Zeitschrift fuer Physik B Condensed Matter* 54 (1983), Nr. 1, 59–70. http://dx.doi.org/10.1007/BF01507950. – ISSN 0722–3277

[94] FREY, Hartmut: *Vakuumbeschichtung, Bd.1 : Plasmaphysik, Plasmadiagnostik, Analytik.* Springer, Berlin; VDI, 1995

[95] MOELLER, Wolfhard: *Fundamentals of Ion-Surface Interaction.* http://iktp.tu-dresden.de/KP/presentations/downloads/Fundam_ISI.pdf. Version: 2004

[96] SMART, Roger St. C. ; SKINNER, William M. ; GERSON, Andrea R.: XPS of sulphide mineral surfaces: metal-deficient, polysulphides, defects and elemental sulphur. In: *Surface and Interface Analysis* 28 (1999), Nr. 1, 101–105. http://dx.doi.org/10.1002/(SICI)1096-9918(199908)28:1<101::AID-SIA627>3.0.CO;2-0. – DOI 10.1002/(SICI)1096–9918(199908)28:1<101::AID–SIA627>3.0.CO;2–0. – ISSN 1096–9918

[97] MYCROFT, J.R. ; BANCROFT, G.M. ; McINTYRE, N.S. ; LORIMER, J.W. ; HILL, I.R.: Detection of sulphur and polysulphides on electrochemically oxidized pyrite surfaces by X-ray photoelectron spectroscopy and Raman spectroscopy. In: *Journal of Electroanalytical Chemistry and Interfacial Electrochemistry* 292 (1990), Nr. 1, 139 - 152. http://dx.doi.org/http://dx.doi.org/10.1016/0022-0728(90)87332-E. – DOI http://dx.doi.org/10.1016/0022–0728(90)87332–E. – ISSN 0022–0728

[98] Oei, Djong-Gie: Sodium-sulfur system. II. Polysulfides of sodium. In: *Inorganic Chemistry* 12 (1973), Nr. 2, 438-441. http://dx.doi.org/10.1021/ic50120a039. – DOI 10.1021/ic50120a039

[99] Contarini, Salvatore ; Rabalais, J.Wayne: Ion bombardment-induced decomposition of Li and Ba sulfates and carbonates studied by X-ray photoelectron spectroscopy. In: *Journal of Electron Spectroscopy and Related Phenomena* 35 (1985), Nr. 2, 191 - 201. http://dx.doi.org/http://dx.doi.org/10.1016/0368-2048(85)80056-6. – DOI http://dx.doi.org/10.1016/0368–2048(85)80056–6. – ISSN 0368–2048

[100] Wenzel, Sebastian ; Metelmann, Hauke ; Raiss, Christine ; Dürr, Anna K. ; Janek, Jürgen ; Adelhelm, Philipp: Thermodynamics and cell chemistry of room temperature sodium/sulfur cells with liquid and liquid/solid electrolyte. In: *Journal of Power Sources* 243 (2013), 758 - 765. http://dx.doi.org/http://dx.doi.org/10.1016/j.jpowsour.2013.05.194. – DOI http://dx.doi.org/10.1016/j.jpowsour.2013.05.194. – ISSN 0378–7753

[101] Stephan, Arul M. ; Prem Kumar, Thiruvikraman ; Thomas, Sabu ; Bongiovanni, Roberta ; Nair, Jijeesh R. ; Angulakshmi, Natarajan ; Pollicino, Antonino: $Ca_3(PO_4)_2$-incorporated poly(ethylene oxide)-based nanocomposite electrolytes for lithium batteries. Part II. Interfacial properties investigated by XPS and a.c. impedance studies. In: *Journal of Applied Polymer Science* 124 (2012), Nr. 4, 3255–3263. http://dx.doi.org/10.1002/app.34710. – DOI 10.1002/app.34710. – ISSN 1097–4628

[102] Yao, Koffi P. C. ; Kwabi, David G. ; Quinlan, Ronald A. ; Mansour, Azzam N. ; Grimaud, Alexis ; Lee, Yueh-Lin ; Lu, Yi-Chun ; Shao-Horn, Yang: Thermal Stability of Li_2O_2 and Li_2O for Li-Air Batteries: In Situ XRD and XPS Studies. In: *Journal of The Electrochemical Society* 160 (2013), Nr. 6, A824-A831. http://dx.doi.org/10.1149/2.069306jes. – DOI 10.1149/2.069306jes

[103] Beamson, G. ; Briggs, D.: *High Resolution XPS of Organic Polymers.* John Wiley & Sons, 1992

[104] Aduru, Subhodaya ; Contarini, Salvatore ; Rabalais, J. W.: Electron-, x-ray-, and ion-stimulated decomposition of nitrate salts. In: *The Journal of Physical Chemistry* 90 (1986), Nr. 8, 1683-1688. http://dx.doi.org/10.1021/j100399a045. – DOI 10.1021/j100399a045

[105] Nyten, Anton ; Stjerndahl, Marten ; Rensmo, Hakan ; Siegbahn, Hans ; Armand, Michel ; Gustafsson, Torbjorn ; Edstrom, Kristina ; Thomas, John O.: Surface characterization and stability phenomena in Li_2FeSiO_4 studied by PES/XPS. In: *J. Mater. Chem.* 16 (2006), 3483-3488. http://dx.doi.org/10.1039/B605578H. – DOI 10.1039/B605578H

[106] Kanamura, Kiyoshi ; Tamura, Hiroshi ; Takehara, Zen ichiro: XPS analysis of a lithium surface immersed in propylene carbonate solution containing various salts. In: *Journal of Electroanalytical Chemistry* 333 (1992), Nr. 1, 127 - 142. http://dx.doi.org/http://dx.doi.org/10.1016/0022-0728(92)80386-I. – DOI http://dx.doi.org/10.1016/0022–0728(92)80386–I. – ISSN 1572–6657. – An international journal devoted to all aspects of electrode kinetics, interfacial structure, properties of electrolytes, colloid and biological electrochemistry

[107] Nord, A. G.: Crystal structure of β-Li_2SO_4. In: *Acta Crystallographica Section B* 32 (1976), Mar, Nr. 3, 982–983. http://dx.doi.org/10.1107/S0567740876004433. – DOI 10.1107/S0567740876004433. – Out of Diamond

[108] Y.-Y. Lin, M.-P. Z. H.-Q. Zhang Z. H.-Q. Zhang: The Crystal Structure of Zabuyelite. In: *Chinese Science Bulletin* 35 (1990), S. 489–492. – Out of Diamond

[109] D'ANS, Jean ; LAX, Ellen: *Taschenbuch für Chemiker und Physiker.* Springer-Verlag, 2013

[110] ROCKWOOD: *Lithium Methoxide.* online. `http://www.rockwoodlithium.com/pdf/401711.pdf`. Version: 03 2015

[111] CHEMICALBOOK.COM: *Lithium Ethoxide Basic Information.* online. `http://www.chemicalbook.com/ProductChemicalPropertiesCB5136595_EN.htm#MSDSA`

Acknowledgment

Declaration of Authorship

I, Hauke Metelmann, declare that I have completed this dissertation single-handedly without the unauthorized help of a second party and only with the assistance acknowledged therein. I have appropriately acknowledged and cited all text passages that are derived verbatim from or are based on the content of published work of others, and all information relating to verbal communications. I consent to the use of an anti-plagiarism software to check my thesis. I have abided by the principles of good scientific conduct laid down in the charter of the Justus Liebig University Giessen „Satzung der Justus-Liebig-Universität Gießen zur Sicherung guter wissenschaftlicher Praxis" in carrying out the investigations described in the dissertation.

Gießen, February 5, 2018

‾‾‾‾‾‾‾‾‾‾‾‾‾‾‾‾‾‾‾‾‾‾‾‾‾‾

Hauke Metelmann

A. Appendix

A.1. Crystallographic Data

Lithium Sulfate
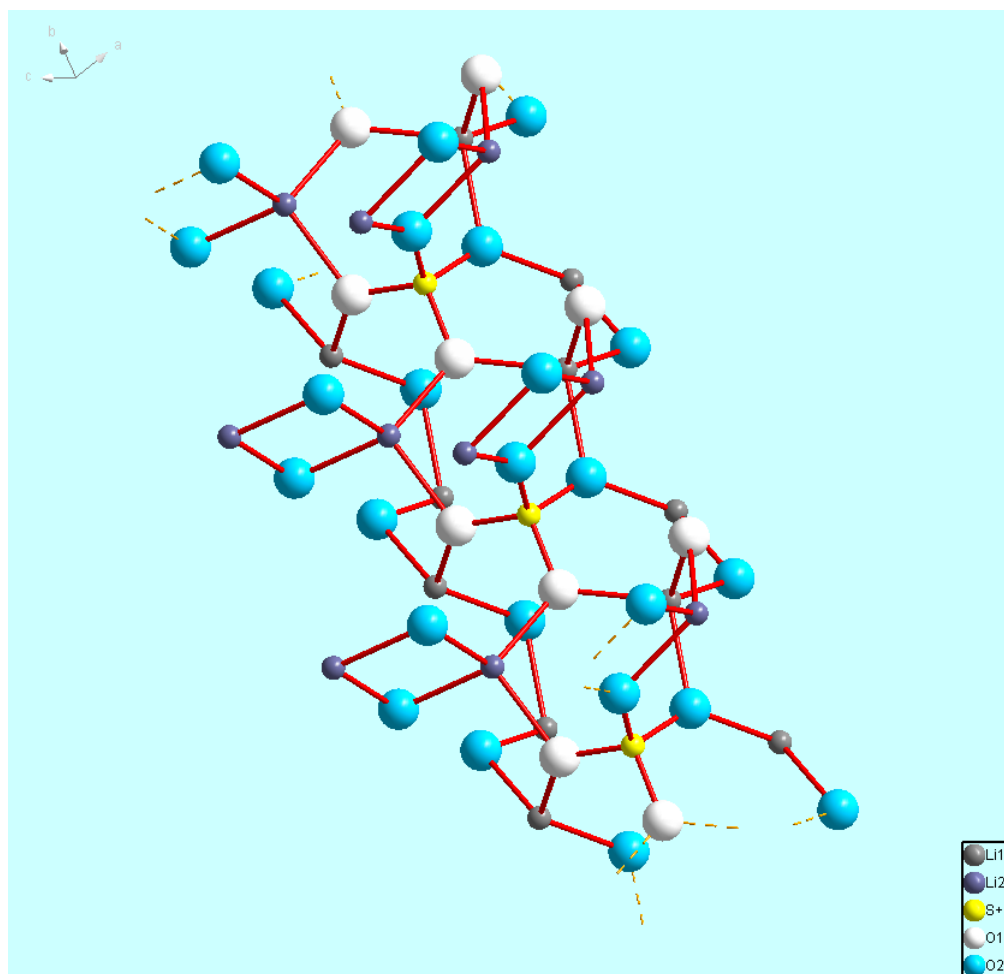
Figure A.1.: The crystal structure of Li_2SO_4 after Ref. [107] exhibited two distinguishable lithium (grey and violet) and oxygen (white and light blue) atoms within the compound.

Lithium Carbonate
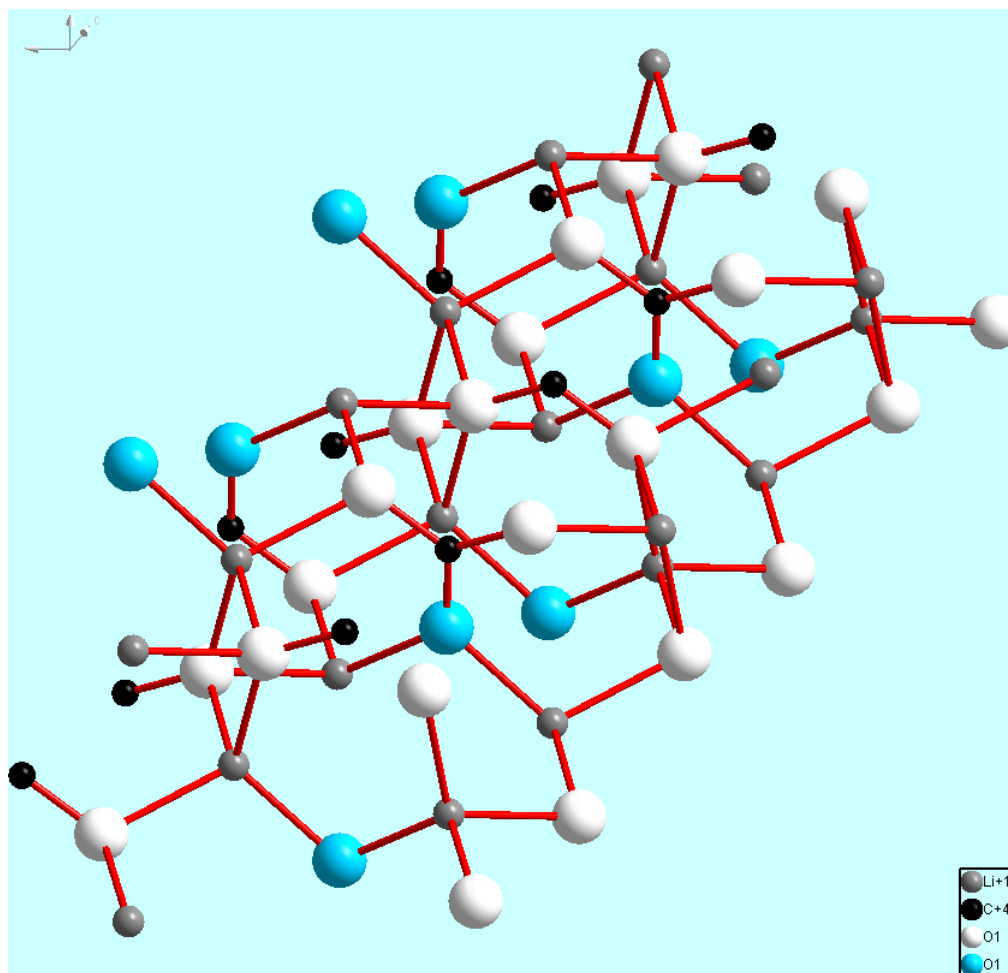
Figure A.2.: The crystal structure of Li_2SO_3 after Ref. [108] exhibited two differentiable oxygen atoms; one white spheres resembles the oxygen in the alkoxide group and the light blue one the oxygen of the carbonyl group.
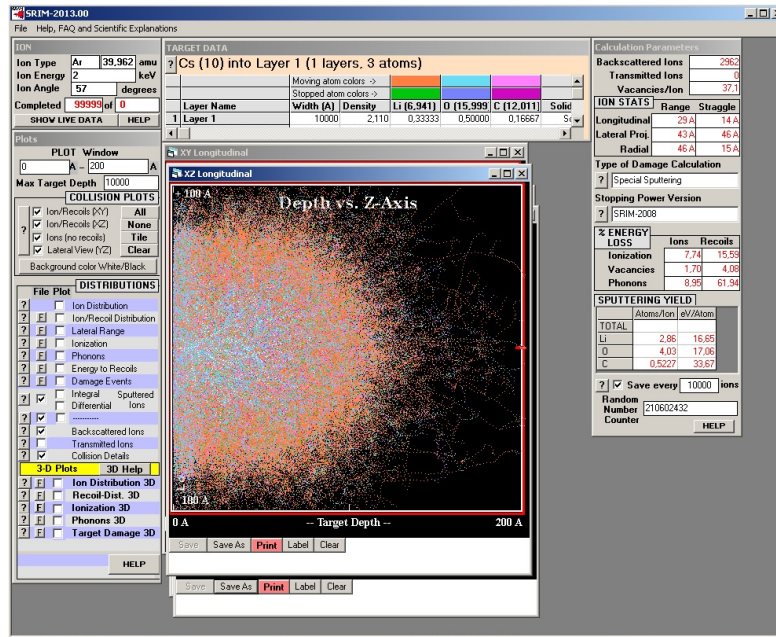
A.2. SRIM Simulation Data
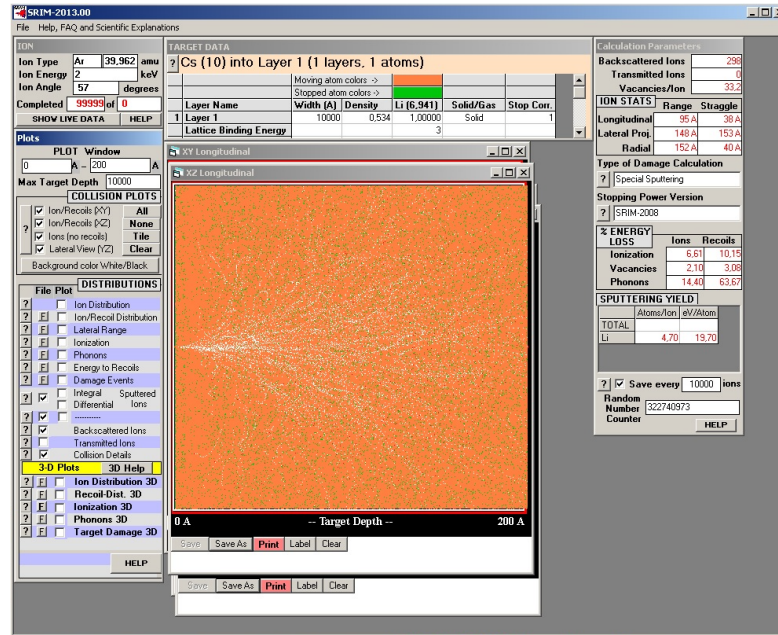
Figure A.3.: SRIM simulation of lithium; density from ref. [5]
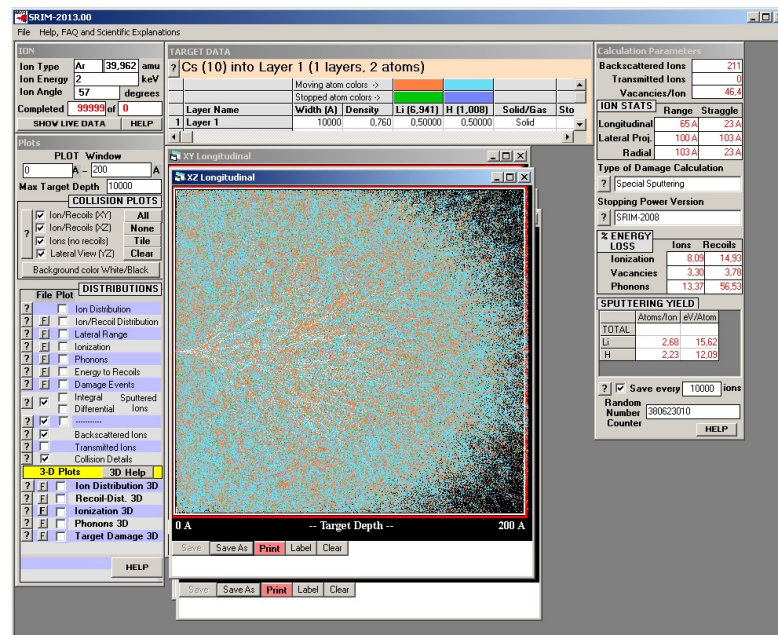
Figure A.4.: SRIM simulation of lithium hydride; density from ref. [5]
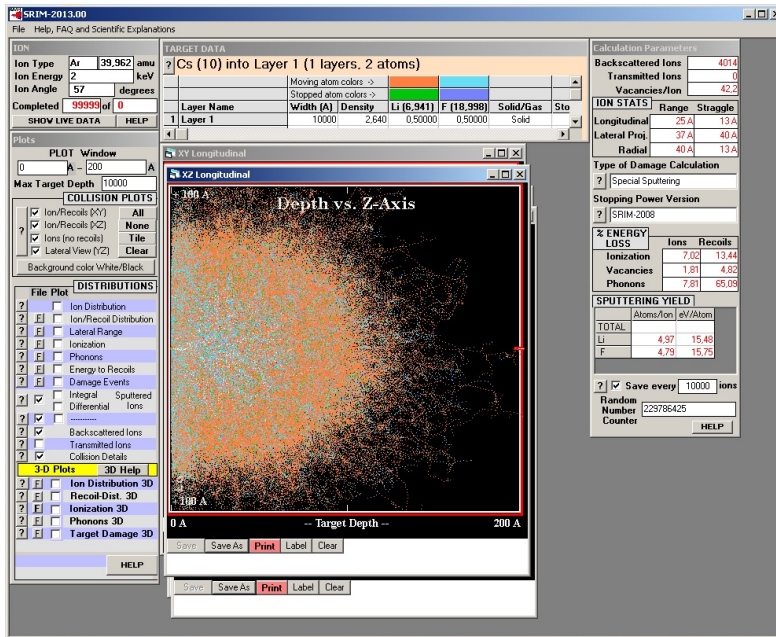
Figure A.5.: SRIM simulation of lithium fluoride; density from ref. [5]
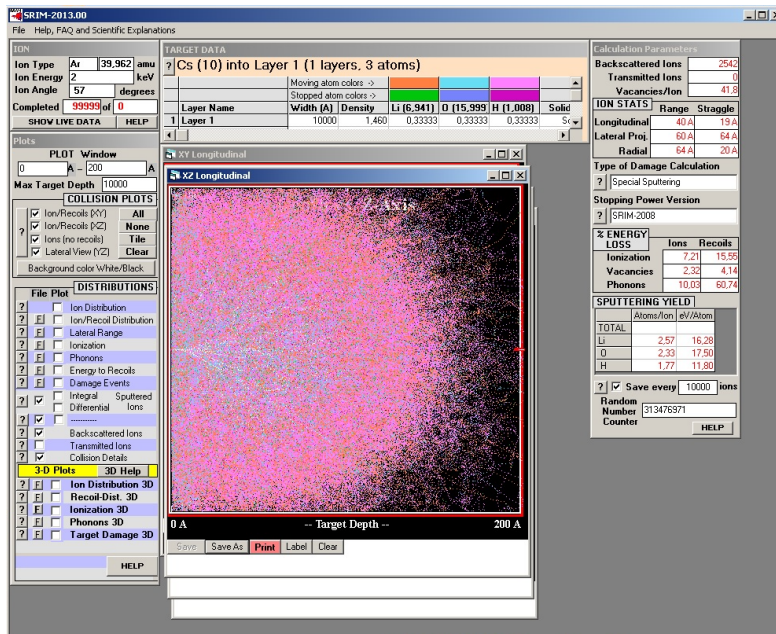
Figure A.6.: SRIM simulation of lithium hydroxide; density from ref. [5]
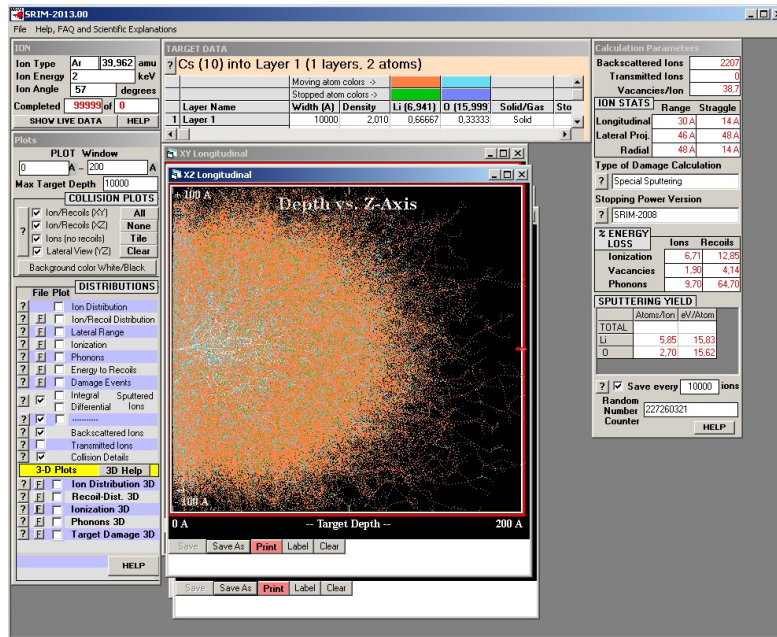
Figure A.7.: SRIM simulation of lithium oxide; density from ref. [5]
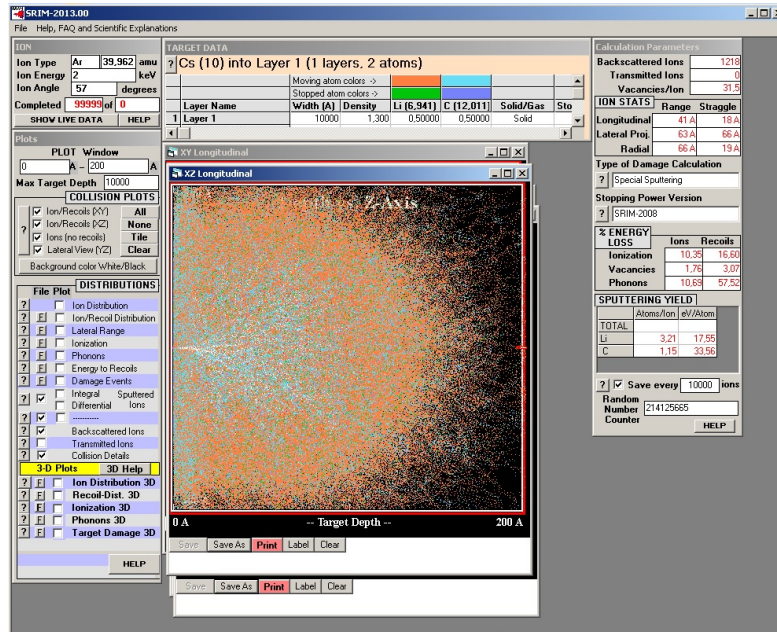
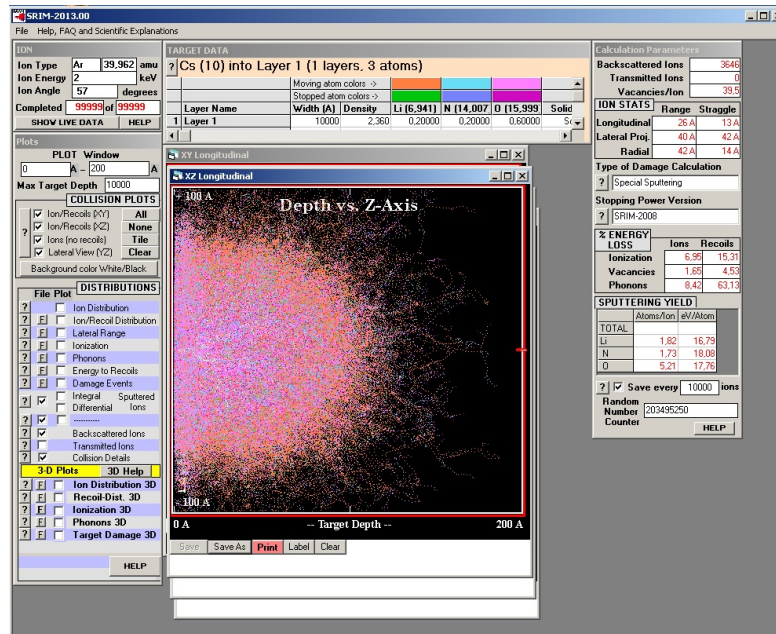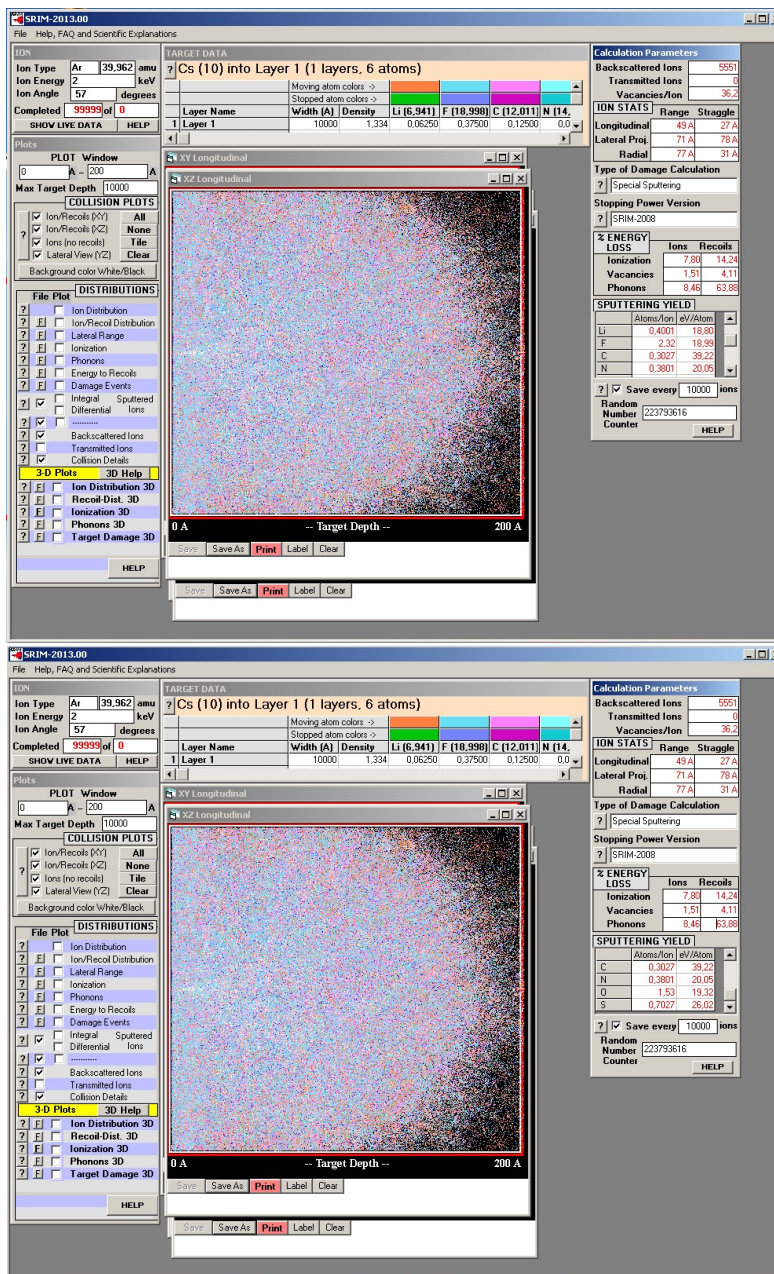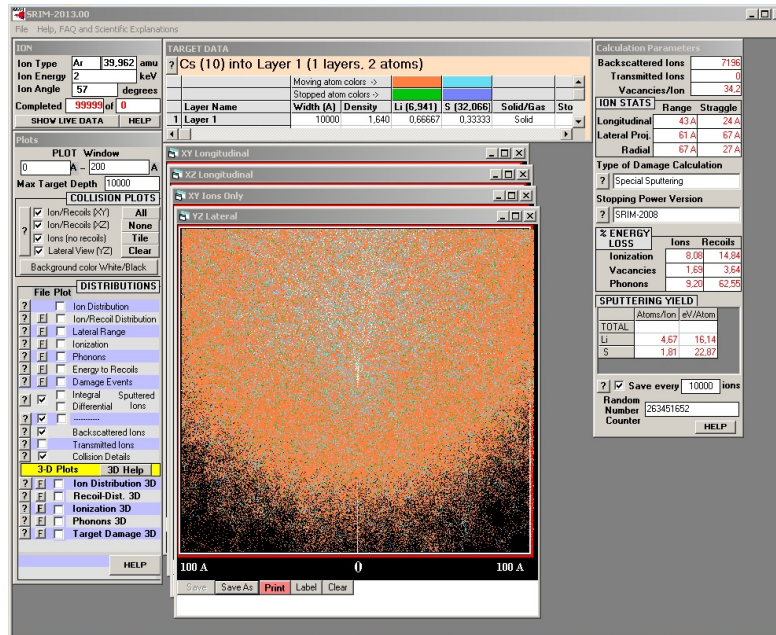Figure A.8.: SRIM simulation of lithium carbide; density from ref. [109]
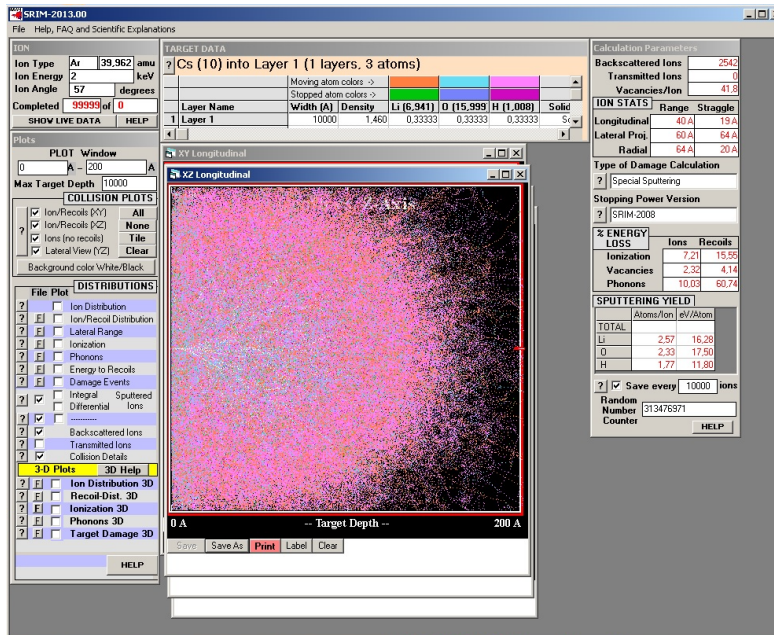
Figure A.9.: SRIM simulation of lithium methoxide; density from ref. [110]
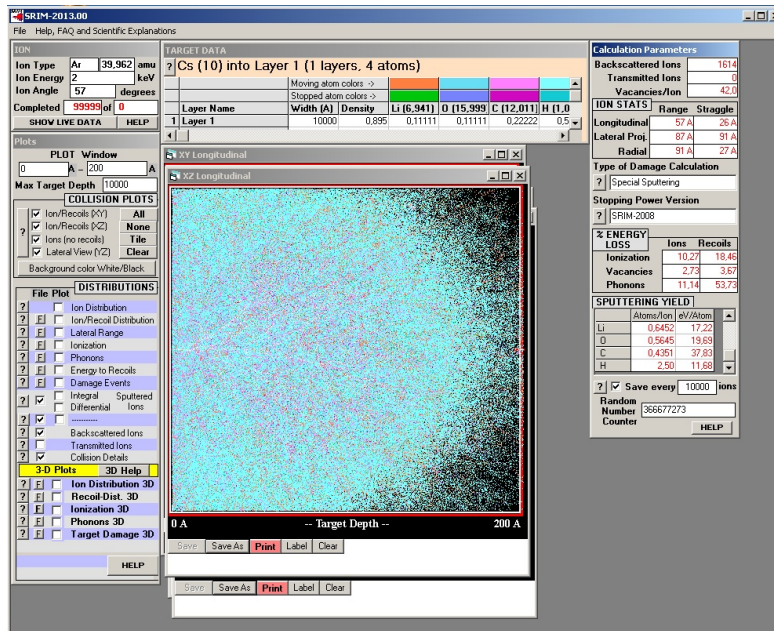
Figure A.10.: SRIM simulation of lithium ethoxide; density from ref. [111]

Figure A.11.: SRIM simulation of lithium carbonate; density from ref. [5]

Figure A.12.: SRIM simulation of lithium nitrate; density from ref. [5]

Figure A.13.: SRIM simulation of LiTFSI; density from ref. [111]

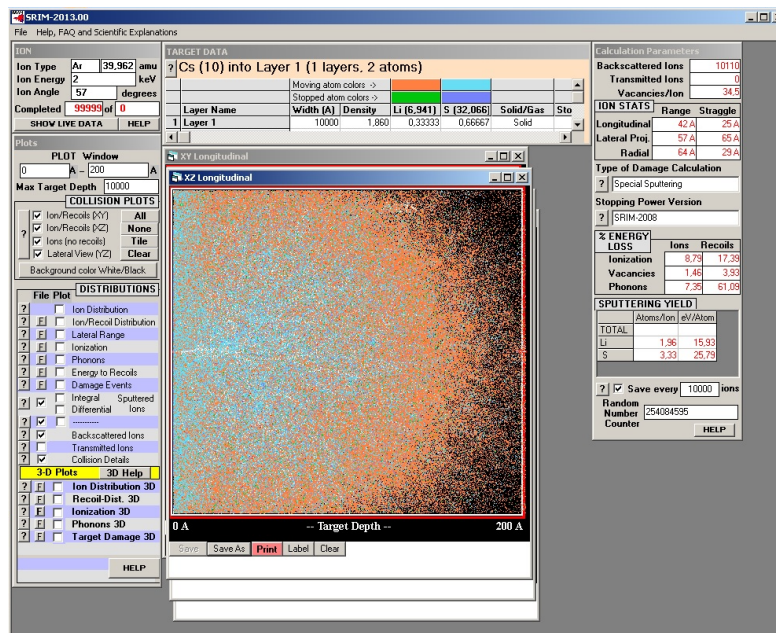Figure A.14.: SRIM simulation of lithium sulfide; density from ref. [5]

Figure A.15.: SRIM simulation of lithium tetrasulfide; density interpolated between Li_2S and S_8 from ref. [5]
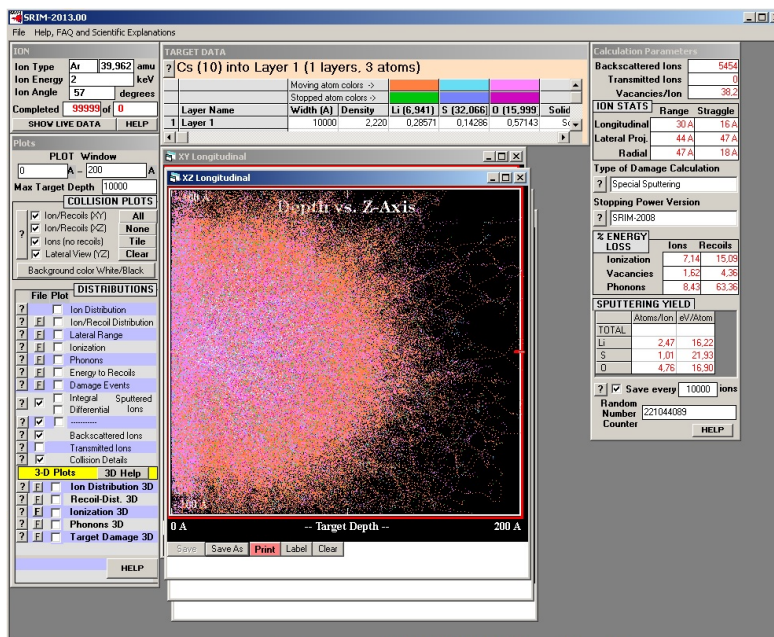
Figure A.16.: SRIM simulation of lithium sulfate; density from ref. [5]
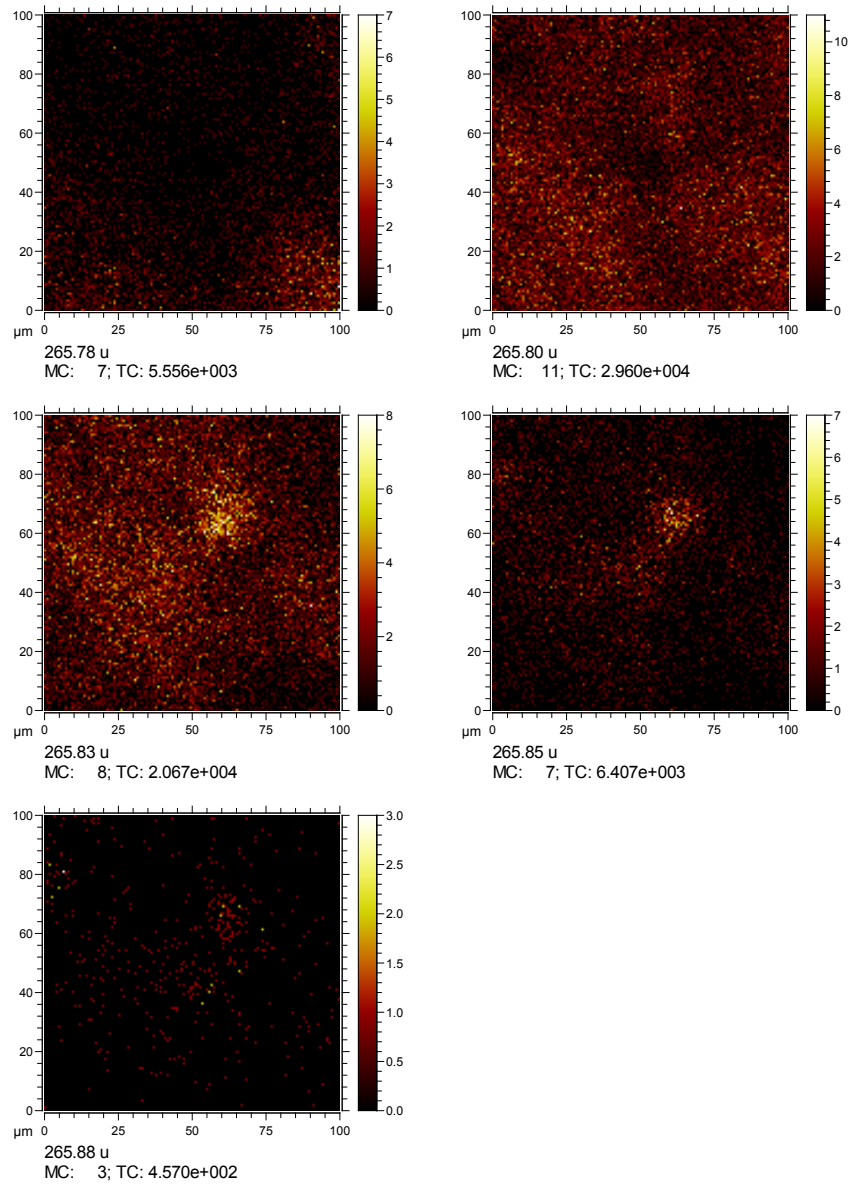
B. Appendix 2

Figure B.1.: The SIMS maps of the Cs$_2$ signal for the sample after one cycle reveal that the increased intensity of the single spot is found primarily at higher masses. This leads to the conclusion that this spot resembles a hole.